

Performance Analysis of a Retrofitted Reversible Solid Oxide Cell and a Combined Cycle Gas Turbine

An assessment of exergy efficiencies, greenhouse gas emissions, and gross profits.

Pieter-Bas Draijer



DELFT UNIVERSITY OF TECHNOLOGY

**Performance Analysis of a Retrofitted Reversible
Solid Oxide Cell and a Combined Cycle Gas
Turbine**

An assessment of exergy efficiencies, greenhouse gas emissions, and
gross profits.

by

Pieter-Bas Draijer

To obtain the degree of Master of Science
at the Delft University of Technology,
to be defended publicly on Monday August 31 October, 2022 at 02:00 PM

Student number:	4595262	
Thesis committee:	Prof.dr. Ad van Wijk	TU Delft, supervisor
	Prof.dr.ir. Sikke Klein	TU Delft
	Ir. Theo Woudstra	TU Delft
	Prof.dr. Hans Geerlings	TU Delft
	Edwin van Ruijven	Vattenfall, supervisor



Acknowledgements

When I first encountered hydrogen in a practical setting during my part-time job at NEN, I already became fascinated by the molecule and its potential. This interest was one of the main reasons for starting my MSc in Energy, Flow, and Process Technology at the Delft University of Technology. My interest only grew during my study and my internship at Nobian, where I researched the degradation of alkaline electrolyzers. When I had to choose a topic for my MSc research, I knew I wanted to include hydrogen.

My thesis supervisor, Prof.dr. Ad van Wijk, helped me in shaping this research. I am grateful that he took the time to read my work and provide me with valuable feedback. Our pleasant conversations were of great help, as these discussions have often led me to new insights during the research process.

I would also like to thank Edwin van Ruijven, for his support from within Vattenfall. The space he has given me while writing this research has ensured that this work contributes to both Vattenfall and the broader academic field. Furthermore, I would like to thank him for connecting me with his colleagues at Vattenfall, who helped me in the different stages of this research.

Finally, I would like to thank my reviewers Ir. Theo Woudstra and Prof.dr.ir. Sikke Klein for the feedback they gave me during the writing of this research, even though they were under no obligation to do so. Their constructive feedback took my research to a higher level.

This research marks the end of eight challenging years in which I was able to finish a BSc in Economics at Erasmus University, a BSc in Mechanical Engineering and an MSc in Energy, Flow, and Process Technology at the Delft University of Technology. Writing this research was the final step in completing my degree. I hope it reflects the time and effort I spent on it.

Pieter-Bas Draijer
Delft, 2022

Summary

The vast amounts of greenhouse gas (GHG) emissions, surging gas prices, and increasing proportion of intermittent energy sources force the energy sector to structurally modify the energy system. The reversible Solid Oxide Cell (rSOC) is considered to be part of the solution due to its high efficiency, good scalability, and ability to balance the energy grid. The rSOC is a high-temperature, electrochemical device that can convert both power-to-gas and gas-to-power during its Solid Oxide Fuel Cell (SOFC) and Solid Oxide Electrolysis Cell (SOEC) modes. The integration of the SOFC with a combined cycle gas turbine (CCGT) features exceptional synergies. Although the synergies of the SOFC and CCGT have already been widely reviewed, the combination of an rSOC and a CCGT has remained unexplored.

The research objective of this study is to assess the benefits of retrofitting an rSOC to an existing CCGT by simulating its exergetic performance, relative GHG emissions and gross profit, and comparing these results to those of an existing CCGT. During the integration of the rSOC (operating in SOFC mode) with the CCGT, the performance of the reversed SOEC mode must be taken into account because it will have to operate with the same operating conditions and the same system components. In order to decrease the system investment cost, this work examines to what extent the rSOC can be retrofitted into the currently deployed CCGTs.

This research optimizes the process plant design and scrutinizes the effect of various operating conditions on the system performance. The optimization is performed through exergy analyses of a zero-dimensional Aspen Plus model. A case study, in which the proposed system is inserted into an energy resource allocation model of the Amsterdam metropolitan area, is used to examine the gross profit of the proposed multi-energy system.

The optimization of the SOFC-CCGT system results in an exergy efficiency of 61.5%, generating 518 MW_e, which enhances the performance of the existing CCGT by 3.8% and decreases the GHG emissions [CO_{2e} t/MWh] by 21.3%. When the combined heat and power (CHP) mode of the CCGT is considered, the resulting SOFC-CCGT CHP system achieves an exergy efficiency of 61.2%, while generating 474 MW_e and 103 MW_{th}. The SOFC-CCGT CHP outperforms the exergy efficiency of the original CCGT CHP with 4.2%, while emitting 13.2% less GHG emissions. The same operating conditions of the SOFC were applied to the SOEC, which manages to operate with an exergy efficiency of 84.3%.

Implementing the rSOC-CCGT CHP system into the energy resource allocation model results in a 118% increased net present value (NPV) of the gross profit compared to the original CCGT. The proposed multi-energy system is able to adjust its operating mode to anticipate the price variations in the energy grid and thereby increases the gross profit. Adding a thermal energy storage system decouples the consumption and production of heat, which enhances the NPV of the gross profit by an additional 1.4%.

Contents

Acknowledgements	i
Summary	ii
Nomenclature	vi
List of Figures	ix
List of Tables	xiii
1 Introduction	1
1.1 Background	1
1.2 Solutions	1
1.3 Goal & Contribution	2
1.4 Methodology	3
1.5 Structure	4
2 Theoretical Background	5
2.1 rSOC	5
2.1.1 Working Principle	5
2.1.2 Voltage Losses	7
2.1.3 Heat Management	10
2.2 Gas Turbine.	11
2.2.1 Compressor	11
2.2.2 Combuster Model.	12
2.2.3 Turbine Model	12
2.2.4 Combined Model	12
2.3 Steam Turbine	13
2.3.1 Heat Recovery Steam Generator.	14
2.4 SOFC-CCGT	14
2.4.1 Integration Methods	14
2.5 District Heating Network.	16
2.5.1 CCGT and District Heating	16
2.6 Multi Energy System	17
2.6.1 Imbalance	17
2.6.2 Storage	17
2.7 Exergy.	18
3 Literature study	21
3.1 Reversible SOC	21
3.1.1 Cell Level	21
3.1.2 System Level	22
3.1.3 Transient Response	22
3.1.4 Summary	23
3.2 SOFC-CCGT	23
3.2.1 Summary	25
3.3 MES.	26
3.3.1 SOC-based MES	26
3.3.2 Non-SOC-based MES.	26
3.3.3 Storage	27
3.3.4 Summary	27

3.4	Literature Gap and Proposed System	28
3.4.1	Assessing the Benefits Based on Exegetic Performance (Sub-objective 1)	28
3.4.2	Assessing the Benefits Based on GHG Emissions (Sub-objective 2)	29
3.4.3	Assessing the Benefits Based on Gross Profit (Sub-objective 3)	29
4	Methodology	31
4.1	Retrofitted CCGT	31
4.1.1	Computer Model CCGT	32
4.1.2	Computer Model CCGT CHP	37
4.2	rSOC	39
4.2.1	Stack Assumptions	39
4.2.2	Power	39
4.2.3	Operating Conditions.	40
4.2.4	Cell Parameters.	40
4.2.5	SOFC Computer Model	41
4.2.6	SOEC Computer Model	42
4.2.7	Validation	43
4.3	System level.	44
4.3.1	System Modules	44
4.3.2	Resulting flowsheet	48
4.4	Aspen Solution Sequence.	48
4.5	Performance Indicators.	50
4.5.1	Exergy Efficiency	50
4.5.2	Energy Efficiency	52
4.5.3	GHG Emissions.	53
4.6	Optimization Sequence	53
5	Optimization	55
5.1	Operating Conditions Analysis.	55
5.1.1	Stack Level	55
5.1.2	System Level	60
5.1.3	Conclusion Operating Conditions	65
5.2	Flowsheet Optimization	67
5.2.1	Flowsheet Optimization 1: Cell Heat Integration	68
5.2.2	Flowsheet Optimization 2: Air Circulation	69
5.2.3	Flowsheet Optimization 3: Downstream Turbines	74
5.2.4	Flowsheet Optimization 4: System Heat Integration	76
5.2.5	Revised: Optimal Operating Conditions.	80
5.2.6	Conclusion SOC Optimization	84
5.3	SOFC CCGT	85
5.3.1	SOFC-CCGT HRSG	85
5.3.2	SOFC-CCGT Preheater	87
5.3.3	Part Load SOFC-CCGT	88
5.4	SOFC CCGT CHP	89
5.4.1	Model Modification	89
6	Results and Discussion	92
6.1	Assessing the Benefits Based on Exegetic Performance (Sub-objective 1)	92
6.1.1	Results Optimization Case 1A: Full Load	92
6.1.2	Results Optimization Case 2A: Part Load	95
6.1.3	Results Optimization Case 1B: Full Load	97
6.1.4	Results Optimization Case 2B: Part Load.	99
6.1.5	Summary	100
6.2	Assessing the Benefits Based on GHG Emissions (Sub-objective 2)	101
7	Multiple Energy System: Case Study	102
7.0.1	Dispatch Model	102

7.1	Assessing the Benefits Based on Gross Profit (Sub-objective 3)	105
7.2	Conclusion	109
8	Conclusion	110
8.1	Research Objectives	110
8.2	Summary and Conclusion of Research Process	110
8.2.1	Summary and Conclusion of rSOC Optimization Process	110
8.2.2	Summary and Conclusion of SOFC-CCGT Coupling.	111
8.2.3	Summary and Conclusion about MES.	111
8.3	Main Findings	112
8.3.1	Assessing the Benefits Based on Exegetic Performance (Sub-objective 1)	112
8.3.2	Assessing the Benefits Based on GHG Emissions (Sub-objective 2)	112
8.3.3	Assessing the Benefits Based on Gross Profit (Sub-objective 3)	112
8.3.4	Assessing the Benefits Based on All Performance Parameters (Main Research Objective).	113
8.4	Research limitations and recommendations for future research	113
8.4.1	Simulation software.	113
8.4.2	Model	113
	References	114
A	Appendix Tables	120
A.1	Theoretical Background	120
A.2	Appendix Optimization	120
A.3	MES analysis	123
A.4	Appendix Results and discussion	123

Nomenclature

Abbreviations

Abbreviation	Definition
CAPEX	Capital Expenditures
CCGT	Combine Cycle Gas Turbine
CHP	Combined Heat and Power
CO ₂ e	Carbon dioxide equivalent
DHN	District Heating Network
FC	Fuel Cell
FE	Fuel Electrode
GHG	Greenhouse Gas
GT	Gas Turbine
GWP	Global Warming Potential
HEX	Heat Exchanger
HHV	Higher Heating Value
HRSG	Heat Recovery Steam Generator
LHV	Lower Heating Value
MES	Multi Energy System
NPV	Net Present Value
OE	Oxygen Electrode
ORC	Organic Rankine Cycle
RES	Renewable Energy Source
rSOC	reversible Solid Oxide Cell
RTE	Round Trip Efficiency
SOC	Solid Oxide Cell
SOEC	Solid Oxide Electrolysis Cell
SOFC	Solid Oxide Fuel Cell
SRC	Steam Rankine Cycle
ST	Steam Turbine
TES	Thermal Energy Storage
TPB	Triple Phase Boundary

Variable

Variable	Definition
C _p	Heat capacity [J/K]
D	Diffusion coefficient [m ² /s]
d_p	Pore diameter [m]
$\dot{E}x_d$	Exergy destruction [W]
$\dot{E}x$	Exergy transfer rate [W]
F	Faraday constant [C/mol]
FU	Fuel utilization factor
g	Gibbs free energy [kJ/mol]
G ⁰	Gibbs free energy at standard conditions [kJ]
G	Gibbs energy [kJ]
h	Enthalpy [kJ/mol]

Variable	Definition
J	Current [A]
j	Current density [A/m ²]
j ₀	Exchange current density [A/m ²]
M	Molecular weight [g/mol]
\dot{m}	Mass flow [kg/s]
N	Number of cells [-]
\dot{n}	Fuel flow [mol/s]
P	Generated power [W]
p	Pressure [bar]
\dot{Q}	Heat transfer [W]
R	Gas constant [J/K mol]
r	Specific resistance [Ωm^2]
s	Entropy [J/mol]
SF	Split factor [-]
T	Temperature [C]
V ⁰	Voltage standard equilibrium potential [V]
V	Voltage [V]
v	volume [m ³]
X	Gas species [-]
x	Normalized load factor [-]
y	Load correlation factor [-]
α	Butler Volmer transfer coefficient [-]
γ	Heat capacity ratio [-]
Γ_f	Exergy grade [-]
η	Energy efficiency [%]
σ	Internal irreversibilities [W/K]
σ_i	Pre-exponential factor of the exchange current density [A/cm ²]
σ_{el}	Ionic conductivity [$\Omega^{-1} m^{-1}$]
δ	Electrolyte layer thickness [m]
ϵ	Electrode porosity [-]
τ	Porosity [-]
ψ	Exergy efficiency [%]

Subscripts

Symbol	Definition
<i>a</i>	Air
<i>AB</i>	Afterburner
<i>ap</i>	Approach point
<i>act</i>	Activation
<i>b</i>	Bulk
<i>C</i>	Compressor
<i>ch</i>	Chemical
<i>Comp</i>	Compressor
<i>con</i>	Concentration
<i>Cond</i>	Condensed
<i>cold</i>	Cold side
<i>eff</i>	Effective
<i>el</i>	Electric
<i>env</i>	Environmental
<i>f</i>	Fuel
<i>FE</i>	Fuel electrode

Symbol	Definition
<i>GtS</i>	Grid to Stack module
<i>hot</i>	Hot side
<i>id</i>	Ideal
<i>in</i>	Incoming
<i>m</i>	Binary indexation for molecules 1
<i>n</i>	Binary indexation for molecules 2
<i>o</i>	Oxygen
<i>ohm</i>	Ohmic
<i>Pur</i>	Purification module
<i>PtG</i>	Purification to Grid module
<i>return</i>	Return stream
<i>R</i>	Released
<i>SG</i>	Sweep gas
<i>supply</i>	Supply stream
<i>sys</i>	System
<i>T</i>	Temperature
<i>th</i>	Thermal
<i>tn</i>	Thermoneutral
<i>tot</i>	Total
<i>tpd</i>	Triple-phase boundary
<i>Turb</i>	Turbine
<i>z</i>	Indication for both fuel and oxygen electrode

List of Figures

1.1	The original and proposed CCGT systems.	3
1.2	The original and proposed CCGT CHP systems.	3
2.1	Planar SOC model [1].	6
2.2	Fuel electrode and oxygen electrode operation. Retrieved and adjusted from [2].	6
2.3	Heat ($q = \Delta g - \Delta h = T\Delta s$) and power (Δg) production during reaction conversion of water [3]. The jump at 100 °C represents the f heat of vaporization of water Δh_{evap}	7
2.4	Relation rSOC with Current density [A/m ²] and Voltages [V] [4].	10
2.5	Energy balance of an rSOC [4]. The Oxidant and Fuel are heated to the temperature ± 100 [C] by electric heaters (\dot{Q})[W]. The produced or required heat is absorbed or supplied by the Oxidant. \dot{W} (P) is the generated electricity[W].	11
2.6	a) Schematic overview of the GT system. b) T-s diagram for Brayton cycle with isentropic efficiency [5].	11
2.7	Relation GT power output and exergy efficiency with the Turbine inlet Temperature and compression ratio [6] at an ambient temperature of 27 °C.	13
2.8	a) Schematic overview of the ST system. b) T-s diagram for Rankine cycle with turbine isentropic efficiency correction [7].	13
2.9	HRSG temperature distribution and exergy destruction.	14
2.10	Comparison of performance between several types of power units: Combustion-based cycles, alternative fuel cell technologies and the fuel cell combustion cycles [8].	15
2.11	(a) SOFC GT directly coupled, (b) SOFC GT indirectly coupled. [9].	15
2.12	District heating network supplied by industrial centralized processes and renewable energy sources [10].	16
2.13	Simplistic schematic overview of ST bleed supplying the District heating network. Component: 1) Boiler, 2) High-Pressure Turbine, 3) Intermediate-Pressure Turbine, 4) Low-Pressure Turbine, 5) Condenser, 6) District Heating heat exchanger, 7) District Heating heat exchanger, 8) DHN return water, 9) DHN supply water, 10) Bypass [11].	17
4.1	Aspen Gas Turbine system overview.	32
4.2	Heat and mass balance of GT.	33
4.3	Steam Turbine Aspen system overview.	33
4.4	Heat and mass balance of ST.	34
4.5	Sankey exergy diagram of Hemweg 9 CCGT full load, used in Base case 1A and 2A. *Net = The power consumption subtracted from the power generation.	37
4.6	Schematic visualization of the planned CCGT CHP Hemweg 9 which defines Base case 1B and 2B.	38
4.7	Sankey exergy diagram Hemweg 9 CCGT CHP full load, used in Base Case 1B and 2B. *Net = The power consumption subtracted from the power generation.	39
4.8	SOFC schematic overview.	41
4.9	SOEC schematic overview.	43
4.10	Comparison model and experiments [1].	44
4.11	Grid to Stack system overview.	45
4.12	Purification system overview.	46
4.13	Purification to Grid module system overview.	47
4.14	Afterburner system overview.	47
4.15	Schematic SOFC system overview. During the optimization, the SOFC exhaust flow is connected to the CCGT.	48
4.16	Schematic SOEC system overview.	48

4.17	Model convergence and solution sequence. Before the heat integration of the SOFC-CCGT the 'SOFC-CCGT heat transfer' is equal to zero indicating that the systems operate separately.	49
5.1	Current density [A/m^2] versus a) Cell voltage [v], b) Overpotentials [V]. The graph depicts the current density during SOFC mode as positive, the reverse is true during SOEC mode.	56
5.2	Operating temperature versus Cell voltage, Overpotentials, and Nernst voltage for a) SOFC and b) SOEC.	57
5.3	Pressure versus the cell voltage, overpotentials, and Nernst voltage for a) SOFC, and b) SOEC.	58
5.4	a) SOFC - Cell voltage versus Temperature and Pressure. b) SOEC - Cell voltage versus Temperature and Pressure. The black plane represents the thermoneutral region at a specified Temperature and Pressure.	58
5.5	SOEC Cell Voltage vs concentration of fuel.	59
5.6	SOC - Cell voltage versus Current Density at different sweep gasses.	60
5.7	SOEC Pressure versus System Power. The four system modules are depicted: SOEC, Grid to Stack, Purification, and Purification to Grid. During the SOEC analysis, power consumption is defined as positive, and power production as negative. The cumulative of the bars is the total power consumption.	60
5.8	SOEC Pressure versus System Exergy Destruction and Exergy Efficiency. The exergy destruction of the four system modules is depicted (left y-axis): SOEC, Grid to Stack, Purification and Purification to Grid. Ψ_{sys} represents the exergy efficiency of the SOEC system including the Balance of plant, and Ψ_{SOEC} and represents the exergy efficiency of the cell. The cumulative equals the total exergy losses.	61
5.9	SOFC Pressure versus Power. P_{SOFC} and P_{GtS} represent the power production of the SOFC and the Grid to Stack module. During the SOFC analysis, power consumption is defined as negative, and power production as positive. The total of the bars equals the cumulative power production.	62
5.10	SOFC Pressure versus System Exergy Destruction and Exergy Efficiency. The cumulative of the bars is the total exergy destruction [MW].	62
5.11	SOEC Temperature versus System Power. Power consumption is defined as positive.	63
5.12	SOEC Temperature versus system Exergy Destruction and Exergy Efficiency.	63
5.13	SOFC Temperature versus System Power. Power generation is defined as positive.	64
5.14	SOFC Temperature versus system exergy destruction and exergy efficiency.	64
5.15	SOEC Molar Fraction [H_2O] versus a) System Power, b) System Exergy Destruction and Exergy Efficiency.	65
5.16	SOFC Molar Fraction [H_2] versus a) System Power, b) System Exergy Destruction and Exergy Efficiency.	65
5.17	SOEC Optimization 1: Cell heat integration.	68
5.18	SOFC Optimization 1: Cell heat integration.	68
5.19	Results and improvement of optimization 1: Cell heat integration. The blue bars indicate the results from the previous flowsheet, the grey bars indicate the results after the applied heat integration.	69
5.20	SOEC Optimization 2: Air recirculation.	70
5.21	SOEC Air recirculation ratio versus Compressor power of the recirculation compressor and the Grid to Stack compressor P (Orange y-axis), and the heating/cooling duty of the air preheating Q (Blue y-axis).	70
5.22	SOEC Air recirculation factor versus a) System Power, b) System Exergy Destruction and Exergy Efficiency.	71
5.23	SOEC - Air recirculation ratio versus Oxygen concentration and Nernst Voltage.	71
5.24	SOFC Optimization 2: Air recirculation.	71
5.25	Air recirculation ratio versus Compressor power of the recirculation compressor and the Grid to Stack compressor P (Orange y-axis), and the heating/cooling duty of the air preheating Q (Blue y-axis). A negative Q means the cooling which is pure exergy loss.	72
5.26	Air recirculation ratio versus Oxygen concentration and Nernst Voltage.	73

5.27	SOEC Air recirculation factor versus a) System Power, b) System Exergy Destruction and Exergy Efficiency.	73
5.28	Reduction of fresh air. The current air consumption (grey) is compared to the system after Flowsheet optimization 1: Cell heat integration (blue).	74
5.29	SOEC Optimization 3: Downstream turbine	75
5.30	SOFC Optimization 3: Downstream turbine. Comparison position of Option 1 and 2. The heat integration is included in the flowsheet to substantiate the explanation of the dependency on the following heat integration.	75
5.31	Power generation or consumption, and decreased environmental exergy losses of optimization 3: Downstream turbine (grey) vs optimization 2:ARR (blue).	76
5.32	Current ARR and corresponding Oxygen Electrode inlet temperature [C].	77
5.33	Redesigning the SOC heat integration.	77
5.34	SOEC Optimization 4: Cell heat integration.	77
5.35	SOFC Optimization 4: Cell heat integration.	78
5.36	Resulting flowsheet SOEC Pinch analysis. Heat exchanger <i>HEX_{opt4}</i> represents the simplified heat exchanger network resulting from the Pinch analysis.	79
5.37	Resulting flowsheet SOFC system heat integration. Heat exchanger optimization 4 represents the simplified heat exchanger network. The position of the heat transfer between the SOFC and the CCGT is already indicated but the transfer equals zero.	79
5.38	Results and improvement of optimization 4: System heat integration (grey) vs. optimization 3: Downstream Turbines.	80
5.39	SOEC Temperature versus a) System Power, b) System Exergy Destruction and Exergy Efficiency.	80
5.40	SOFC Temperature versus a) System Power, b) System Exergy Destruction and Exergy Efficiency.	81
5.41	SOEC effect of Pressure on a) Power and b) Exergy.	82
5.42	SOFC Pressure versus a) System Power, b) System Exergy Destruction and Exergy Efficiency.	82
5.43	Final operating conditions after optimized SOC. Concentration definition is dependent on the SOC mode: SOFC mode; [H ₂], SOEC mode; [H ₂ O].	84
5.44	SOFC-CCGT flowsheet with heat transfer to from the SOFC exhaust flow to the HRSG.	86
5.45	SOFC-CCGT flowsheet with heat transfer to from the SOFC exhaust flow to the HRSG and fuel preheater. The fuel preheater is positioned after the HRSG.	88
5.46	Resulting SOFC-CCGT CHP flowsheet. DHN1 receives heat from the bleed between the IP- and LP- ST, and from the CPH splitted water flow. DHN2 utilizes the SOFC's downstream exhaust gas.	89
5.47	Comparison between the decoupled SOFC and CCGT CHP systems (Base case 2B), and the optimized SOFC-CCGT CHP. The latter defines Optimization case 1B. All units are in [MW].	90
6.1	Sankey exergy diagram Optimization case 1A: SOFC-CCGT full load. *Net = The power consumption subtracted from the power generation.	93
6.2	Sankey exergy diagram Optimization case 2A: SOFC-CCGT part load. *Net = The power consumption subtracted from the power generation.	95
6.3	Sankey exergy diagram Optimization case 1B: SOFC-CCGT CHP full load. *Net = The power consumption subtracted from the power generation.	97
6.4	Sankey exergy diagram Optimization case 2B: SOFC-CCGT CHP part load. *Net = The power consumption subtracted from the power generation.	99
7.1	a) District Heating Network Metropolitan area Amsterdam and Almere. b) Interconnected nodal representations of DHN of the Heating Network Metropolitan area Amsterdam and Almere by the dispatch model.	103
7.2	a) PQ diagram of SOFC-CCGT CHP system. The highlighted area shows the operating zone of the proposed system b) PQ coordinates and SOEC input/output in LHV. The SOEC can operate at any point between 130 and 0 MW which is determined by an interpolation.*First-order LHV efficiency which includes power and heat.	104

7.3	Utilization of energy carriers by the rSOC-CCGT CHP in the first two weeks of January 2030. 1) Hydrogen, 2) Power, 3) Heat, 4) Natural Gas.	105
7.4	Adaptability of the rSOC-CCGT system to the APX price. The price is normalized for confidentiality purposes.	106
7.5	Production of hydrogen HHV [MW] (light green, left y-axis), heat [MW] (dark green, left y-axis) and total heat stored (blue, right y-axis). Arrows indicate the regions of interest.	109
A.1	Pinch analysis for SOEC system, cooling water at cold utility and electric heating at hot utility	120
A.2	Pinch analysis for SOEC system, Temperature vs. heat load diagram	120
A.3	SOEC system optimization rounds results	121
A.4	SOFC system optimization rounds results	122
A.5	SOFC Graphs	122

List of Tables

2.1	Reactions at fuel and air electrodes [12]. Released energy $\Delta h = 285.83$ kJ/mol (ambient conditions).	6
3.1	Summary Base case 1A, Base case 2A, Optimization case 1A and Optimization case 2A with the expected outcomes of exergy efficiency Ψ	29
3.2	Summary Base case 1B, Base case 2B, Optimization case 1B and Case 2B with the expected outcomes of exergy efficiency Ψ	29
4.1	Gas turbine system input.	32
4.2	GT validation. The Δ [%] shows the biggest difference. The underlined value denotes with which Δ [%] calculates the difference. *CA = Confidential Appendix **Difference is calculated in Kelvins [K]. ***Model uses low calorific natural gas. Sources on sequential order: Appendix Page 2, 13 and 15, [13], [14].	33
4.3	Steam turbine input and design parameters retrieved from the reference model Confidential Appendix Page 2. *The isentropic efficiency was calculated to match the outlet temperature of the reference model. **The mechanical efficiency was retrieved from Oudenalder [14].	34
4.4	Aspen model output in comparison with the provided reference model. The output is defined as gross power. $\Delta\%$ is calculated based on to the reference model. *Gross power including the Balance of Plant power consumption **The exhaust temperature was retrieved from the heat and mass balance of the Diemen 34 CCGT CHP plant. . .	35
4.5	Aspen model output in comparison with the provided 288 MW reference model. The output is defined as gross power. *Gross power including Balance of Plant's power consumption.	35
4.6	Efficiency of the CCGT Aspen model compared to the provided reference THERMOFLEX model during part load operating with the applied load correction curve of Brouwer et al.[15].	36
4.7	Aspen model output with heat production compared with the provided reference heat model. The output is defined as gross power. *The CCGT total power is including Balance of Plant power consumption.	38
4.8	Operating conditions validation SOC.	40
4.9	Input parameters SOC [16], except of the A_{tot} [17].	41
4.10	Assumptions components and storage conditions.	44
4.11	Overview of system modules with the consisting system components.	45
4.12	Input and output conditions of streams entering and leaving the system.	48
4.13	Exergy efficiency and exergy destruction of the SOFC-CCGT system.	51
4.14	Exergy efficiency and exergy destruction of the SOEC system	52
5.1	Variations of the operating conditions. The constant operating conditions are based on the experiments of Kamzempoor et al. [1]. * Fuel utilization factor determines the current density. ** Concentration definition is dependent on the SOC mode: SOFC mode; [H ₂], SOEC mode; [H ₂ O].	56
5.2	Results SOC voltages and power output. Input Stack temperature 850 C, pressure 5 bar, Current density 5000 A/m ² , Fuel Utilization 0.8, Fuel composition 0.97 & 0.9 for SOFC and SOEC respectively, Sweep gas Air.	66
5.3	Preliminary results after examining the operating conditions: Input and output, exergy efficiency, and exergy destruction.	67
5.4	Comparison positions downstream turbine. DST end is positioned all the way downstream, and DST Aftb is positioned directly after the afterburner.	76

5.5	SOEC pinch analysis input.	78
5.6	Comparison of the current system after the five optimization rounds and the systems prior to the flowsheet optimization.	84
5.7	Comparison between the system of Base case 1A (two SOFC and CCGT decoupled systems), the integration with HRSG, and the integration with the HRSG and the fuel preheater (FPH). The latter defines Optimization case 1A. All units are in [MW]. CF is the isentropic correction factor of the turbomachinery.	88
5.8	Fuel input, Turbine power output and applied turbomachinery isentropic efficiency for the original CCGT simulation and optimized Cases 1A and 2A.	89
5.9	Fuel input, Turbine power output and applied turbomachinery isentropic efficiency for the original CCGT CHP simulation and optimized Cases 1B and 2B.	91
6.1	Comparisons overview with system power and heat output.	92
6.2	Absolute exergy differences of Base case 1A and Optimization case 1A.	94
6.3	Absolute exergy differences of Base case 2A and Optimization case 2A.	96
6.4	Absolute exergy differences of Base case 1B and Optimization case 1B.	98
6.5	Absolute exergy differences of Base case 2B and Optimization case 2B.	100
6.6	Summary of exergy efficiency results of all Cases.	101
6.7	Summary of CO ₂ e results of all Cases. The variable CO ₂ e includes the total of the heat and electricity generation of the system. *Relative to Base case 2A and Base case 2B for the Cases A and B respectively.	101
7.1	Results 2030 rSOC-CCGT CHP in comparison to CCGT Hemweg 9. *Listed in HHV.	107
7.2	NPV, gross profit, revenue, and costs of examined years of the rSOC-CCGT CHP and the original Hemweg 9 plant. The absolute numbers are confidential (Confidential Appendix Page 19), the relative difference is provided.	107
7.3	Total generated energy [TWh] of the two systems and energy carrier over the years 2025 to 2045.	108
7.4	NPV, gross profit, revenue and costs of examined years of the rSOC-CCGT CHP and rSOC-CCGT CHP + TES. The absolute numbers are confidential (Confidentiality Appendix Page 19), the relative difference is provided.	109
8.1	Concluding results Sub-objective 2 Cases A: Exergy efficiency and relative GHG emissions	112
8.2	Concluding results Sub-objective 2 Cases B: Exergy efficiency and relative GHG emissions	112
8.3	Concluding results Sub-objective 3: NPV of gross profit [M€], Total energy of carriers generated [TWh], Weighted NPV [€/MWh]	112
A.1	Relevant molecules in the system and the molecule standard exergy [18]	120
A.2	Results 2030 rSOC-CCGT CHP with and without TES. *Listed in HHV	123
A.3	Relative exergy differences of Base case 1A and Case 1A	123
A.4	Relative exergy differences of Base case 2A and Case 2A	124
A.5	Relative exergy differences of Base case 1B and Case 1B with the decoupled SOFC	125
A.6	Relative exergy differences of Base case 2B and Case 2B without the decoupled SOFC	126

1

Introduction

1.1. Background

In the past decade, the world has been awakened to the visible damage of the increasing temperature of Earth's atmosphere due to increasing Green House Gas concentrations caused by human activity by burning carbon-based fuels. The continuation of burning carbon-based fuels will continue to cause severe irreversible damage to the environment if no structural changes are implemented [19]. Therefore, in 2015, the Paris Agreement was signed by 196 countries, including the Netherlands, to collectively work on limiting global warming by 2 °C comparable to pre-industrial levels [20]. But even more recently, the Council of the European Union agrees to regulate the reduction of gas consumption by 15% in 2022 [21]. Over the past year, the supply of gas appears to be deployed as a geopolitical weapon. The dependency on gas could lead to a European energy crisis and skyrocketing gas prices [22].

The heat and electricity generation sector is the biggest consumer of natural gas and one of the biggest emitters of Greenhouse Gases (GHGs), accounting for 24% of the global GHG emission [23]. In the Netherlands, natural gas accounted for 90% of the residential heating and 51% of electricity generation [24]. The perspective of fueling these CCGTs with natural gas is becoming less appealing due to their contribution to global warming, the simultaneously increasing gas price [25] and Carbon Tax [26].

Structurally changing the energy system of the heat and electricity sector is not without challenges. Because the current CCGTs are still far from amortized, early phasing out of these CCGTs would cause capital asset destruction. From a financial point of view, the energy sector is bounded to the use of CCGTs. Consequently, the energy sector requires solutions that enhance the CCGT performance to decrease the emission intensity¹ while reducing the cost price. Increasing the proportion of renewable energy sources will also lead to many challenges regarding the reliability and availability of the energy system [27]. The intermittent behavior of renewable energy sources and the periodic nature of energy consumption leads to discrepancies in the energy grid resulting in an unbalance between energy production and consumption [28].

1.2. Solutions

Multi-Energy systems (MESs) are gaining interest in the development of sustainable urban energy systems [29]. An MES utilizes multiple energy carriers which optimally interact with each other at various system levels to enhance the performance on a technical, economic and environmental level, relative to classical energy systems whose sectors interact at a lesser extent [30]. The expansion of the number of energy carriers results in a higher degree of freedom during the system optimization, which leads to increased system efficiency and contributes to decarbonizing the energy sector [29].

¹GHG emissions per kilowatt-hour

Switching from carbon-based energy carriers to renewable fuels would significantly decrease or even eliminate GHG emissions. One promising alternative to carbon-based fuels is green hydrogen [31]. Green hydrogen is produced by the electrical loading of water molecules, using electricity generated by renewable energy sources, that splits the molecule into hydrogen and oxygen. Even though the alternatives to carbon-based fuels are not yet competitive from an economical and technical perspective, they are expected to become competitive when the proportion of renewable energy sources in the energy mix is increased [32].

Reversible, electrochemical systems have the potential to absorb a considerable amount of surplus renewable energy by converting it to chemical energy carriers (such as hydrogen) in a sustainable manner. The reversible Solid Oxide Cell currently gains interest due to the high round-trip efficiency, good scalability, and exceptional SOFC-CCGT integration synergies [2]. The rSOC is a single, bifunctional, high-temperature, electrochemical system that is able to convert power to gas during Solid Oxide Electrolysis Cell (SOEC) mode and gas to power during Solid Oxide Fuel Cell (SOFC) mode. The bifunctional model should reduce the investment costs per operating hour and increase the capacity factor compared to the separate electrochemical devices [2][16]. During the SOFC mode, it is advantageous to integrate its high-temperature exhaust gas with a CCGT, which results in superior performance, both energetic and environmental, compared to the standalone CCGT [33].

Recent research has focused on complex and expensive hybrid SOFC and CCGT systems rather than financially attractive systems [34], while few studies take into account the existing turbines [35]. To the best of this author's knowledge, no research on the integration of an rSOC with a CCGT has been performed.

1.3. Goal & Contribution

The discussed problems and gaps in the current literature led to the formation of the following research objective:

The research objective is to assess the benefits of retrofitting an rSOC to an existing CCGT by simulating its exergetic performance, relative GHG emissions and gross profit, and comparing these results to those of the existing CCGT.

The performance is measured in the system's exergy efficiency, the GHG per unit of energy [$\text{CO}_2\text{e t/MWh}$], and the net present value (NPV) of the predicted gross profit per unit of energy [$\text{€}/\text{MWh}$]. The performed exergetic optimization results in the optimal operating conditions and process design that maximizes the synergies of the rSOC and CCGT, while respecting the original operating conditions of the existing CCGT.

The main research objective can thus be divided into 3 sub-objectives:

- *The first research sub-objective is to assess the benefits of retrofitting an rSOC to an existing CCGT based on the exergetic performance.*
- *The second research sub-objective is to assess the benefits of retrofitting an rSOC to an existing CCGT based on the GHG emissions.*
- *The third research sub-objective is to assess the benefits of retrofitting an rSOC to an existing CCGT based on the gross profit.*

This research provides insight into the optimization of an rSOC in an existing energy system and the understanding of the added value of rSOC-CCGT integration. During the integration of the rSOC (operating in SOFC mode) with the CCGT, the performance of the SOEC mode must be taken into account. The bifunctional unit will have to operate with the same operating conditions and the same system components. In order to decrease the investment costs of the system and to extend the lifetime of existing CCGTs. This work examines to what extent the rSOC can be retrofitted into the currently deployed CCGTs and if the integration leads to improved system performances. The entire energy system involved in this integration includes the hydrogen grid, electricity grid, gas grid and district

heating network.

1.4. Methodology

This work optimizes the rSOC-CCGT process plant design and scrutinizes the effect of various operating conditions on the system performance. The optimization is performed through exergetic and electrochemical modeling of a zero-dimensional Aspen Plus model [36]. The Aspen Plus model simulates the existing 440 MW_e Hemweg 9 CCGT which is integrated with a 100 MW SOFC while also being able to operate in SOEC mode. The original CCGT system and the proposed SOFC-CCGT system are visualized in Figure 1.1.

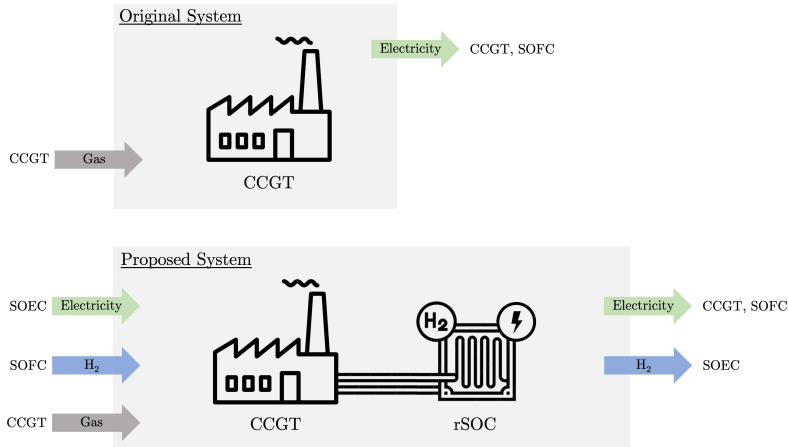


Figure 1.1: The original and proposed CCGT systems.

The owner of the CCGT, Vattenfall, plans to convert the CCGT to a combined heat and power (CHP) plant with a generation capacity of 100 MW_{th}. To keep up with these developments, the integration of the CHP and the rSOC is also examined. The original CCGT CHP system and the proposed SOFC-CCGT CHP system are visualized in Figure 1.2.

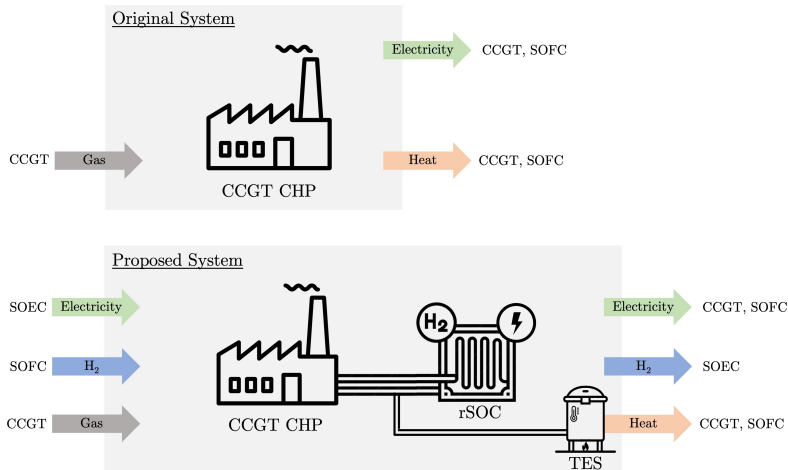


Figure 1.2: The original and proposed CCGT CHP systems.

To make a valid comparison between the proposed optimized SOFC-CCGT and the existing CCGT, only one parameter should be altered for each comparison. Because the system produces heat and electricity, multiple comparisons should be examined. Ultimately, four comparisons are made where either both the systems are running at full load, or both systems generate the same amount of power

or heat. These comparisons are elaborated on in Chapter 3.

Even though the proposed system may be more efficient, the price of the same amount of energy for hydrogen is higher than that of natural gas, so the NPV of the gross profit per unit of energy is not guaranteed to go down. To test the advantages of implementing the SOEC, a case study was performed in which the optimized system is inserted into an optimal energy resource allocating model that simulates the energy network of the Amsterdam metropolitan area. The model is used to examine the practical implication of the system by providing insights into the comparison of the NPV of the gross profit. The results of the proposed system are compared with the existing CCGT. The case study also examines whether the addition of thermal energy storage leads to an increased NPV. The thermal energy storage would decouple the production and consumption of heat, allowing the system to operate at its design point rather than operating at a sub-optimal part load point. In addition, the system could respond to price volatility while still being able to meet heat demand, increasing the gross profit per MWh.

1.5. Structure

First, the theoretical background, which is required to understand the rest of the work, is discussed in Chapter 2. The working principle of the rSOC and CCGT, and the definition of an MES are elaborated on. The existing studies that have provided insights into the proposed systems are examined in Chapter 3. After this analysis, the gaps in the current literature are identified and the activities in this research to fill these gaps are elaborated on. Chapter 4 discusses the construction of the model in Aspen Plus and defines the base case systems. The optimization process and the effect of the operating conditions on the performance are discussed in Chapter 5. The optimized proposed systems are compared with the simulation of the existing model in Chapter 6. Thereafter, in Chapter 7, the proposed multi-energy system is inserted into the optimal energy resource allocating model to compare the system gross profit with the current setup. The work concludes the results in Chapter 8. The research ends with discussing the limitations and accompanied recommendations for future work.

2

Theoretical Background

The theoretical background of this paper builds a foundation that enhances the understanding of the upcoming chapters. This section separates the author’s own research from the theory that it requires. This chapter elaborates on the thermodynamic and electrochemical models of the rSOC and CCGT, the various ways in which the individual components can be linked, what a Multi Energy System defines, and finally how the exergy analysis is applied.

2.1. rSOC

The reversible electrochemical cell consists of a single unit with bifunctional electrochemical modes able to convert electrochemical energy into power and heat in fuel cell mode, or vice-versa in the electrolysis mode. Research on these cells has been increasing for the past decade because of the potential to absorb a considerable amount of surplus energy by converting it to chemical energy in a sustainable manner [2], while during a shortage of energy converting the chemical energy back to power and heat, with an exceptional round trip efficiency [37]. The rSOC is an example of such a system that is characterized by a high operating temperature, using an oxygen-ion permeable ceramic structure which eliminates the need for precious metal catalysts [38].

The rSOC can accomplish high efficiencies: the energy conversion round trip efficiency, excluding storage losses, is 70%Based on the Lower Heating Value (LHV). The Higher Heating Value (HHV) is maintained throughout this work unless mentioned otherwise. The LHV is used when the results stem from the literature that applies LHV. [2]. The rSOCs are flexible in their scalability, allowing them to scale without affecting the efficiency of the system, and has high fuel flexibility. The rSOC is adaptable because of multiple integration methods (e.g. heat and mass) making it applicable to many processes. The rSOC is perfectly capable of adjusting to different power and storage capacities because the two modes can be sized independently of each other. The startup time is sufficiently fast to comply with the intermittent behavior of the energy grid due to the heat inertia of the stack [39]. The next Chapter 3 will further elaborate on the research on the transient response of the rSOC.

2.1.1. Working Principle

In a non-reversible electrochemical cell, the terms anode and cathode are used for the oxidation and reduction electrode, respectively. However, in an rSOC, the anode and cathode electrodes switch polarity during the switch of cell mode. To avoid misunderstandings when calling the correct electrode during the switch of polarity, an alternative terminology is implemented leading to a consistent identification of the electrode. Figure 2.1 visualizes the planar configuration of a SOC and Figure 2.2 depicts the working principle and terminology of a hydrogen-based rSOC. The SOC electrodes are classified by the Fuel Electrode (FE) and the Oxygen Electrode (OE). Although the OE uses the word “oxygen”, the inserted Sweep Gas (SG) is not limited to pure oxygen.

During SOFC mode, the fuel (hydrogen) enters the FE, and an oxygen-containing gas at the OE.

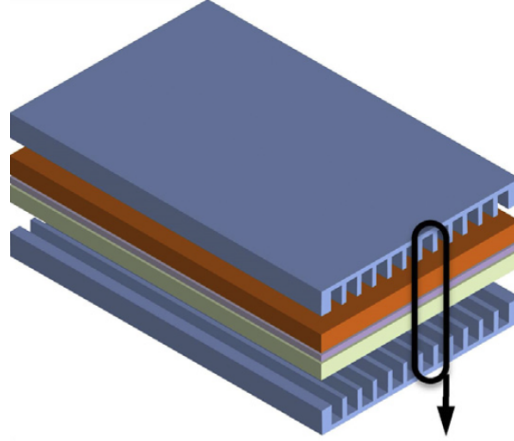


Figure 2.1: Planar SOFC model [1].

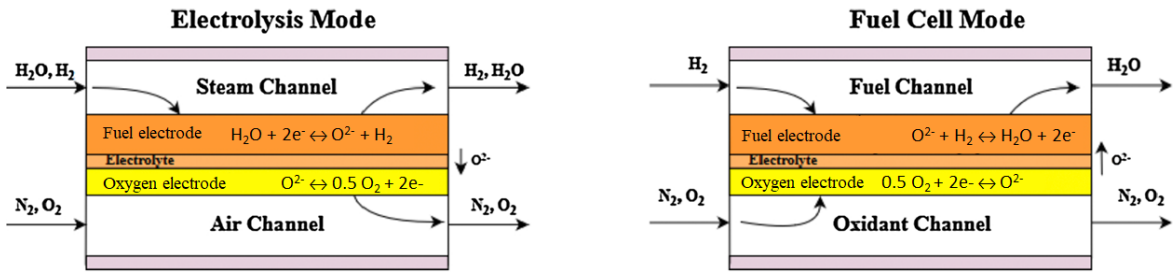


Figure 2.2: Fuel electrode and oxygen electrode operation. Retrieved and adjusted from [2].

The positive potential difference between the two half-reactions splits the oxygen O_2 into two oxygen ions O^{-2} which migrate through the electrolyte to the FE at the other side of the cell (Table 2.1). The electrolyte prevents the permeation of molecules other than oxygen such as nitrogen when using air as the sweep gas. The migrating O^{-2} ions form an ionic current that activates an electric current to close the circuit. The oxygen ions together with hydrogen gas react to water at the FE. The resulting combined reaction forms the net reaction.

The reversed reaction during SOEC works similarly. However, during SOEC mode, water instead of hydrogen enters the FE. The applied load splits water into hydrogen and oxygen ions. Again, the oxygen ions permeate through the electrolyte to form oxygen. The hydrogen and oxygen leave the FE and OE respectively. The current is defined as negative during SOFC mode and positive during SOEC mode. With this definition, the model can easily cope with the alternating electrode polarity by switching the sign of the electrical current.

Table 2.1: Reactions at fuel and air electrodes [12]. Released energy $\Delta h = 285.83$ kJ/mol (ambient conditions).

Reaction	SOFC	SOEC
Anodic	$\text{H}_2 + \text{O}^- \rightarrow \text{H}_2\text{O} + 2\text{e}^-$ (fuel electrode)	$\text{O}^- \rightarrow \frac{1}{2}\text{O}_2 + 2\text{e}^-$ (air electrode)
Cathodic	$\frac{1}{2}\text{O}_2 + 2\text{e}^- \rightarrow \text{O}^-$ (air electrode)	$\text{H}_2\text{O} + 2\text{e}^- \rightarrow \text{H}_2 + \text{O}^-$ (fuel electrode)
Global	$\text{H}_2 + \frac{1}{2}\text{O}_2 \leftrightarrow \text{H}_2\text{O}$	

The heat management of the rSOC is of particular importance due to the respective highly exothermic or endothermic reaction during SOFC and SOEC mode Δh of 285.83 kJ/mol [16]. The heat and power production of the reaction depends on the operating conditions. The understanding of the com-

plex heat management requires the knowledge of how the operating conditions of the cell affect the cell's operating Voltage. This is explained using the following voltage analysis

Voltage Analysis

The Gibbs free energy of the reaction Δg [kJ/mol] defines the electrical work that can be extracted from the net reaction during SOFC mode or is required during the SOEC mode. The Gibbs free energy is dependent on the specific reaction enthalpy Δh [kJ/mol], the reaction entropy Δs [kJ/mol K] and the temperature of the cell T (see Figure 2.3). Equation 2.1 defines the inverse relation of temperature with the electrical power output or power consumption when voltage losses are not considered. During SOFC mode, an increasing temperature reduces the Δg resulting in a reduction of generated electric energy. The same relation applies to the SOEC, however, in this case, less electrical energy is required to split the same amount of water. Voltage losses produce heat which can be utilized during SOEC mode resulting in high efficiencies [16] but deteriorates the efficiency during the SOFC mode. First, these voltage losses will be discussed before this latter effect is explained in more detail.

$$\Delta g = \Delta h - T \cdot \Delta s \quad (2.1)$$

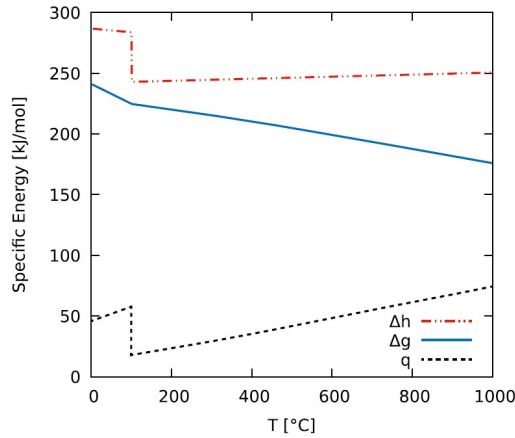


Figure 2.3: Heat ($q = \Delta g - \Delta h = T\Delta s$) and power (Δg) production during reaction conversion of water [3]. The jump at 100 °C represents the f heat of vaporization of water Δh_{evap} .

The standard equilibrium potential V_{Nernst}^0 in its turn is dependent on the ΔG^0 which represents the Gibbs free energy at standard pressure. The amount of electrons n transferred during the net reaction equals 2. Equation 2.3 defines the Nernst Equation that expresses the Nernst voltage under non-standard conditions V_{Nernst} . This expression takes into account the cell temperature T_{stack} , the operating pressure P_{stack} , and the mole fractions of the gas species X_{H_2} , X_{O_2} and X_{H_2O} ¹.

$$V_{Nernst}^0 = \frac{-\Delta g^0}{n \cdot F} \quad (2.2)$$

$$V_{Nernst} = V_{Nernst}^0 + \frac{R \cdot T}{2 \cdot F} \ln \left(\frac{X_{H_2,b} \cdot \sqrt{X_{O_2,b}}}{X_{H_2O,b}} \right) + \frac{R \cdot T}{2 \cdot F} \ln \left(\sqrt{\frac{P_{stack}}{P_0}} \right) \quad (2.3)$$

2.1.2. Voltage Losses

The Nernst voltage describes the ideal system without voltage losses. In reality, voltage losses occur during operation originating from the underlying mechanisms: migration of charge, diffusion of gas, and activation of the reaction [17]. These voltage losses are generally defined as the ohmic overpotential η_{ohmic} , concentration overpotential η_{con} and the activation overpotential η_{act} respectively. The assumptions regarding these losses are discussed in the coming sections.

¹The subscript n stands for the species used; H₂O, H₂, O₂ and N₂ when air is used. The subscript z stands for both the FE and OE.

The extra resistance - represented by the voltage losses - lowers the SOFC's cell voltage by adding the losses to V_{Nernst} and thus decreases the generated electrical power. During SOEC mode, the voltage losses are added to the V_{Nernst} resulting in a higher cell voltage, requiring more electrical power (Equation 2.4).

$$V_{cell} = V_{Nernst} \pm (\eta_{act} + \eta_{ohm} + \eta_{con}) \quad (2.4)$$

Activation Losses

The Butler Volmer equation, in (Equation 2.5) describes the effect of the current density j [A/cm²] and the η_{act} . In this work, the hyperbolic sine approach Butler Volmer equation, in Equation 2.5, is applied because it is effective throughout a large scope of operating conditions [16]. In literature, the exchange current density j_0 [A/cm²] is generally based on an Arrhenius relation which specifies the relation between the temperature and the reaction rate (Equation 2.6).

The empirical values of the activation energy $E_{act,i}$ and pre-exponential factor of the exchange current density σ_i were retrieved from Buttler et al. [3] conforming to the model of Hauck et al. [16]. The index i stands for either the fuel or the oxygen electrode. The n_i defines the number of transferred electrons per mole during the reaction which equals 2 for the half-reaction at the FE and 4 for the half-reaction at the OE (Table 2.1). The α [-] is the transfer coefficient which is set to 0.5 to achieve the hyperbolic sine Butler Volmer equation [16].

$$\eta_{act,i} = \frac{R \cdot T}{F \cdot n_i \cdot \alpha} \cdot asinh \left(\frac{j}{2 \cdot j_{0,i}} \right) \quad (2.5)$$

$$j_{0,i} = \frac{R \cdot T}{2 \cdot F} \sigma_i \cdot exp \left(-\frac{E_{act,i}}{R \cdot T} \right) \quad (2.6)$$

Ohmic Losses

Ohmic losses occur due to the resistance of transporting the current e^- , and of the transportation of ionic current O^{-2} through the electrolyte. In the rSOC, the ionic voltage losses dominate over the electric voltage losses because of the relatively high transportation resistance of O^{-2} ions through the electrolyte compared to the resistance encountered by electrons [40].

The Ohmic voltage loss η_{ohmic} [V] is calculated by multiplying the specific resistance r [Ωm^2] by the current density j [J/m²]. Equation 2.7 expresses the σ_{el} , δ_{el} , $r_{ohmic,const}$ and $r_{ohmic,el}$ as the ionic conductivity of the electrolyte [$\Omega^{-1} m^{-1}$], the electrolyte layer thickness [m], the combined resistance of the interconnectors and wires [Ωm^2], and the specific Ohmic resistance of the electrolyte layer [Ωm^2], respectively.

$$\eta_{ohmic} = j \cdot \left(\frac{\delta_{el}}{\sigma_{el}} + r_{ohmic,const} \right) = j \cdot (r_{ohmic,el} + r_{ohmic,const}) \quad (2.7)$$

The effects of temperature on the resistance of interconnectors and wires are negligible compared to the effect on the Ohmic resistance of the electrolyte layer. Therefore, the $r_{ohmic,const}$ is assumed independent of temperature [16]. The dependency of σ_{el} on temperature is defined in Equation 2.8. The pre-exponential empirical factor $\sigma_{0,el}$ [$\Omega^{-1} m^{-1}$] and the activation energy $-E_{act,el}$ [J/mol] are empirically fitted [1].

$$\sigma_{el} = \sigma_{0,el} \cdot exp \left(\frac{-E_{act,el}}{R \cdot T} \right) \quad (2.8)$$

Diffusion Losses

The diffusion losses occur due to the diffusion limitations of the reactants from the bulk flow to the reaction zone, thereby, slowing down the formation of the product. Additionally, the limited diffusion of formed products moving back to the bulk flow blocks the reaction zone. The total diffusion loss η_{con} , in Equation 2.9, is defined by the diffusion losses at the FE $\eta_{con,FE}$ and OE $\eta_{con,OE}$, which are calculated Equation 2.10 and 2.11 respectively. These losses are dependent on the gas compositions of the species in the bulk flow $X_{n,b}$ and of a species in the triple-phase boundary $X_{n,tpb}$ [41][16].

$$\eta_{con} = \eta_{con,FE} + \eta_{con,OE} \quad (2.9)$$

$$\eta_{con,FE} = \frac{R \cdot T_{stack}}{2 \cdot F} \cdot \ln \left(\frac{X_{H_2O,b} \cdot X_{H_2,tpb}}{X_{H_2O,tpb} \cdot X_{H_2,b}} \right) \quad (2.10)$$

$$\eta_{con,OE} = \frac{R \cdot T_{stack}}{4 \cdot F} \cdot \ln \left(\frac{X_{O_2,b}}{X_{O_2,tpb}} \right) \quad (2.11)$$

The triple-phase boundary (TPB) is the electrochemical active site within the SOC. Equation 2.12 calculates the gas compositions at the TPB - $X_{O_2,tpb}$ and $X_{n,tpb}$ - by applying Fick's laws of diffusion using the mole fractions at the electrode surface ($X_{O_2,s}$ and $X_{n,s}$) and the bulk flow ($X_{O_2,b}$ and $X_{n,b}$). The subscript n stands for the molecules H_2 and H_2O . The $X_{n,s}$ and $X_{n,b}$ are defined in Equation 2.14 and 2.13 respectively.

$$X_{O_2,tpb} = 1 + (X_{O_2,s} - 1) \cdot \exp \left(\frac{R \cdot T_{cell} \cdot j \cdot \delta_o}{4 \cdot F \cdot P_o \cdot D_{O_2,eff}} \right) \quad (2.12)$$

$$X_{n,tpb} = X_{n,s} + K \frac{R \cdot T_{cell} \cdot j \cdot \delta_f}{2 \cdot F \cdot P_f \cdot D_{eff,FE}} \quad \text{where } n \in [H_2 \Rightarrow K = -1 \ \& \ H_2O \Rightarrow K = 1] \quad (2.13)$$

$$X_{O_2,s} = 1 + (X_{O_2,b} - 1) \cdot \exp \left(\frac{R \cdot T_o \cdot j}{4 \cdot F \cdot P_o \cdot D_{O_2,N_2}} \frac{H_{ch,OE}}{2} \right) \quad (2.14)$$

$$X_{n,s} = X_{n,b} + K \frac{R \cdot T_f \cdot j}{2 \cdot F \cdot P_f \cdot D_{n,eff}} \frac{H_{ch,FE}}{2} \quad \text{where } m \in [H_2 \Rightarrow K = -1 \ \& \ H_2O \Rightarrow K = 1] \quad (2.15)$$

The effective diffusion coefficient $D_{n,eff}$ is constructed by scaling the Knudsen diffusion coefficient $D_{n,Kn}$. The $D_{n,Kn}$ describes the gas diffusion in a porous media and is dependent on the binary diffusion coefficient of the gasses $D_{n,m}$ [41]. $D_{n,m}$ is the binary diffusion coefficient between the two relevant species pairs n and m ; H_2O and H_2 at the FE, and O_2 and N_2 at the OE. This method also takes the electrode porosity ϵ [-], porosity τ [-], the molecular weight of the species M_n and the diffusion volumes $v_{d,n}$ into account. $H_{ch,z}$ is the electrode channel height [m], d_p is the pore diameter [m]. When pure oxygen is used, the $D_{O_2,eff}$ can be simplified as Equation 2.19.

$$D_{n,m} = \frac{1.43 \cdot 10^{-2} T_{stack}^{1.75}}{2 P_{stack} \sqrt{\frac{2}{M_n^{-1} + M_m^{-1}}}} (v_{d,n}^{1/3} + v_{d,m}^{1/3}) \quad (2.16)$$

$$D_{n,Kn} = \frac{2 d_{p,FE}}{3} \sqrt{\frac{8 R T_{stack}}{\pi M_{H_2O}}} \quad (2.17)$$

$$D_{n,eff} = \frac{\epsilon}{\tau} \frac{D_{H_2,H_2O} D_{Kn,H_2O}}{(D_{H_2,H_2O} + D_{Kn,H_2O})} \quad (2.18)$$

$$D_{O_2,eff} = \frac{\epsilon}{\tau} D_{O_2,Kn} \text{ Using pure oxygen} \quad (2.19)$$

2.1.3. Heat Management

The heat production or consumption to maintain the cell's operating temperature is proportional to difference between the cell voltage and the thermoneutral voltage V_{tn} . The thermoneutral voltage is the voltage to attain zero heat flux in the cell. The sum of the heat production $T\Delta s$ and the electricity generation Δg makes the total released energy Δh_R per mole by the electrochemical conversion. At ambient conditions, the oxidation of hydrogen is highly exothermic; the specific reaction enthalpy Δh of 285.83 kJ/mol [16]. The reverse is true for the splitting of water, characterized by the endothermic reaction under similar conditions. The thermoneutral voltage is deducted by dividing the total released energy per mole of the reaction with the stoichiometric factor of the reaction and the Faraday constant [C/mol] in Equation 2.20.

$$V_{tn} = \frac{\Delta h_R F}{2} = 1.287 \text{ at } 800 \text{ }^\circ\text{C} \quad (2.20)$$

Not only the reaction determines the heat duty of the cell but also the energy lost by the voltage losses is converted into heat. Therefore, the total heat duty of the cell is the sum of the heat of reaction and the heat generation of the losses. Equation 2.21 summarizes this relation. The heat production or requirement \dot{Q} to maintain the temperature in the cell depends on the operating conditions. The rSOC electrochemical and thermal relation of the current density, voltage, temperature, and exothermic or endothermic behavior is depicted in Figure 2.4.

$$\dot{Q} = (V_{tn} - V_{cell}) J \quad (2.21)$$

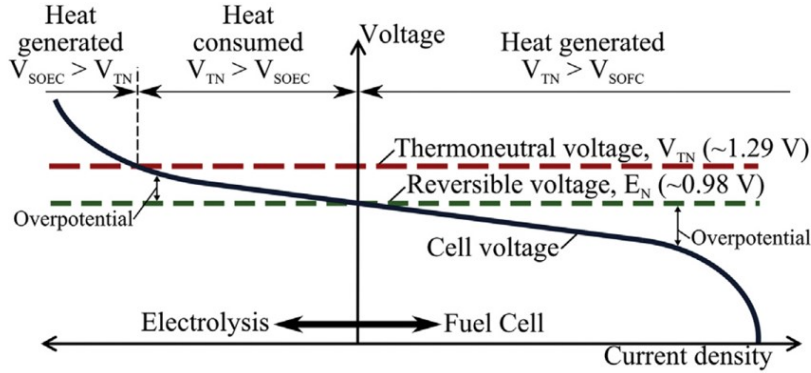


Figure 2.4: Relation rSOC with Current density [A/m²] and Voltages [V] [4].

During the endothermic operation of the SOEC, the cell utilizes the heat produced by the voltage losses. Thus, the heat generated by the losses subsides the heat required to maintain the reaction resulting in a reduction of the required additional energy. When sufficient heat is present within the control volume, the endothermic operation will be preferred over the exothermic operation to maximize the system performance by minimizing either power consumption or environmental exergy losses.

The SOFC operates generally in exothermic mode. In this case, the losses increase the heat production of the cell and thus decrease the generated electrical power. Besides, the SOFC produces a substantial amount of heat during operation especially when hydrogen is used as fuel. There is no reformer required if pure hydrogen instead of hydrocarbons or ammonia is used. Consequently, all generated heat is converted into a temperature increase of the exhaust gasses and thus an increase in cell temperature. A large temperature gradient will lead to greater thermal stresses which are harmful to the brittle material of the SOC, and decrease the lifetime of the SOC [42].

The required heat can be delivered by either an external heat source or by the losses' generated heat, or a combination of both. The temperature of the cell can be maintained to a specific temperature change, by increasing the sweep gas (oxygen or air) flow at the Oxygen Electrode. Feeding the rSOC with a sweep gas with a temperature difference, is generally applied to equal the energy balance [43][16][17].

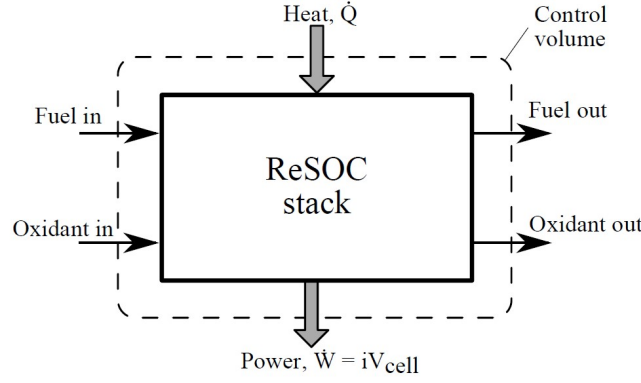


Figure 2.5: Energy balance of an rSOC [4]. The Oxidant and Fuel are heated to the temperature ± 100 [C] by electric heaters (\dot{Q})[W]. The produced or required heat is absorbed or supplied by the Oxidant. \dot{W} (P) is the generated electricity[W].

2.2. Gas Turbine

The power industry widely employs gas turbines because of their great thermal efficiency, quick delivery time, high flexibility, and variable capacity [44]. The high-temperature exhaust gasses provide extra power when coupled to a downstream steam cycle. Such a system is called a CCGT power plant. A Gas Turbine (GT) generates work based on the Brayton cycle by combining a compressor, a combustion chamber, and an expansion turbine. The simplified schematic overview of a GT system is depicted in Figure 2.6.

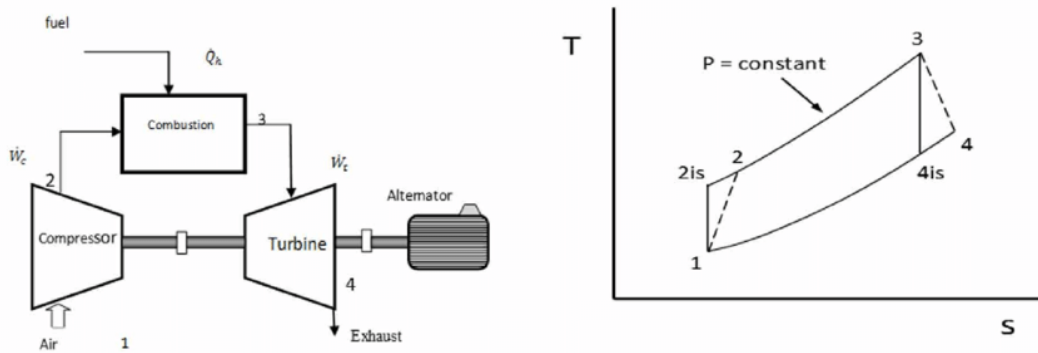


Figure 2.6: a) Schematic overview of the GT system. b) T-s diagram for Brayton cycle with isentropic efficiency [5].

2.2.1. Compressor

The compressor is fed with ambient air after which this air is compressed. The pressure ratio P_e/P_i of the outgoing flow P_e and incoming flow P_i is an important design parameter [45]. The pressure ratio determines the required power of the compressor, calculated by the difference of enthalpy of the ingoing and outgoing stream (Equation 2.23). Additionally, the temperature of the incoming stream T_i is an important variable because the required work is dependent on the volume of the gas, which in its turn, is dependent on the gas temperature (Equation 2.22). The exit temperature is calculated with the ideal gas law and an isentropic efficiency η_c . The $\gamma_a = C_{p,a}/C_{v,a}$ is the ratio of specific heats of air.

$$T_e = T_i + \frac{T_i}{\eta_c} \left(\left(\frac{P_e}{P_i} \right)^{(\gamma_a - 1)/\gamma_a} - 1 \right) \quad (2.22)$$

$$\Delta h_{c, in} = C_{p,a} T_i \left(\frac{P_e}{P_i} \right)^{R/C_{p,a}} - 1 \quad (2.23)$$

The compressor's required power is calculated by multiplying the air mass flow \dot{m}_{air} with the enthalpy difference of the incoming airflow $h_{air,in}$ and the outgoing compressed air stream $h_{air,out}$.

$$P_C = \dot{m}_{air}(h_{c,out} - h_{c,in}) \quad (2.24)$$

2.2.2. Combuster Model

The GT combustion chamber oxidizes the supplied fuel, at constant pressure, with the oxygen provided by the incoming compressed air. The chemical energy of the fuel is converted into heat which increases the volume. The heated and pressured exhaust gasses enter the turbine for expansion. When natural gas is used, the following set of oxidation reactions occurs during the combustion. The fuel heating value [kJ/kg] and thus the efficiency depends on the fuel composition [38].



2.2.3. Turbine Model

The turbine generates mechanical power by simultaneously expanding the exhaust gasses and residual air. The pressure and temperature are simultaneously decreased by the expansion of the gas. The ratio of specific heats of the turbine $\gamma_g = C_{p,g}/C_{v,g}$ is, therefore, a combination of the exhaust and air gas.

$$\Delta h_T = C_{p,g} T_i \left(\frac{P_e}{P_i} \right)^{R/C_{p,g}} - 1 \quad (2.30)$$

The produced power is calculated similar to the required power of the compressor, by multiplying the flue gas mass flow \dot{m}_{flue} with the enthalpy difference of the incoming stream $h_{flue,in}$ and the outgoing compressed air stream $h_{flue,out}$. Again, the idealized required power is corrected by an isentropic- and mechanical efficiency $\eta_{c,i}$ and $\eta_{c,m}$ respectively.

$$P_T = \dot{m}_{air} \Delta h_T \quad (2.31)$$

The bleed of the turbine cools the turbine blades, therefore this fraction of the stream does not generate electricity. The bleed guarantees optimal performance in regard to plant configuration and operational conditions [46]. The bleed stream rejoins with the GT exhaust stream through after the turbine expands the residual stream.

2.2.4. Combined Model

The net power delivered $P_{GT,net}$ is the difference between the compressor power consumption P_C and the turbine power production P_T , multiplied the generator efficiency η_{gen} .

$$P_{GT,net} = \eta_{gen} (P_T - P_C) \quad (2.32)$$

Figure 2.7 emphasizes the importance of the Turbine inlet Temperature (TIT) and the compression ratio (CR). The figure shows the relationship of the TIT and CR on the exergy efficiency and P_{net} . Although the effects of the TIT and CR on the cycle performance are highly dependent on the specific cycle and implemented boundary conditions, the general findings agree with the exergy efficiency and P_{net} increase at higher TITs but decrease at lower CRs [6]. Also, as the load increases, the energy destroyed decreases. Pattanayak [6] concludes that due to the significant impact - of the TIT and CR on the exergy efficiency and exergy destruction make the TIT and CR the most crucial design specification in GT cycle construction. Therefore, the specific consequence of the TIT and CR on the applied GT must be well identified.

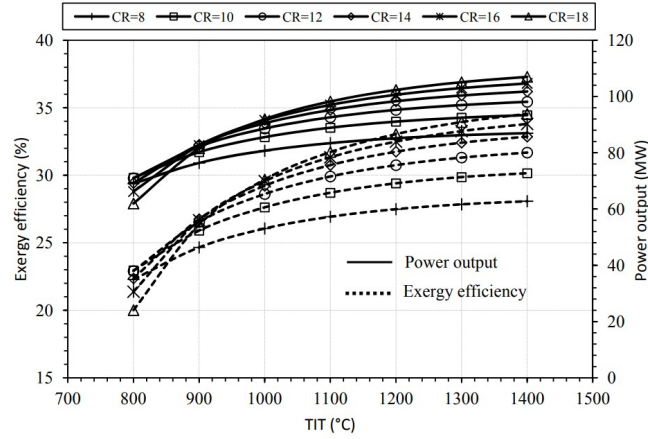


Figure 2.7: Relation GT power output and exergy efficiency with the Turbine inlet Temperature and compression ratio [6] at an ambient temperature of 27 °C.

2.3. Steam Turbine

The residual heat of the GT in the exhaust gas is recovered in the steam turbine (ST) which applies a Rankine cycle which is schematically depicted in Figure 2.8. The utilization of heat increases the exergy efficiency and the power output [38]. The hot GT exhaust gas provides heat through the HRSG (depicted by a boiler in the figure) to the circulating water which is then converted to steam (1 → 2). Expanding the hot steam generates the work (2 → 3). After the heat is extracted and the steam is converted to water in the condenser (3 → 4), the pump pressurizes the water by inserting work (4 → 1).

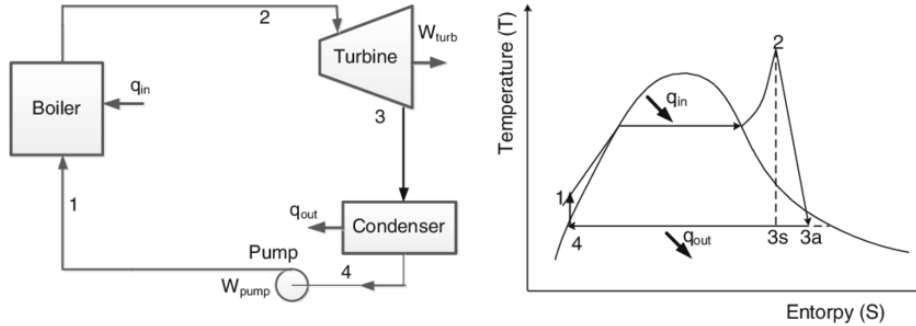


Figure 2.8: a) Schematic overview of the ST system. b) T-s diagram for Rankine cycle with turbine isentropic efficiency correction [7].

Droplet formation in the turbine decreases the turbine efficiency and causes erosion that degrades the turbine making the turbine prone to maintenance. To avoid droplet formation, the minimum amount of steam quality of 90% must be maintained [47]. The cycle is augmented by applying a superheater and reheaters to ensure the necessary vapor quality. The superheater increases the average temperature, which improves the quality and increases the performance. The reheater supplies heat to the steam exiting a turbine to allow the direct insertion to the sequential turbine. Multi-pressure stage turbines increase efficiency by providing additional work by utilizing lower-temperature heat sources. The net generated power of the ST $P_{net,ST}$ is the sum of the different pressure stage turbines P_{ST} and the required pumping power P_{Pump} :

$$P_{net,ST} = \eta_{gen} (P_{ST} - P_{Pump}) \quad (2.33)$$

The performance of a CCGT at part load conditions needs to be considered because the maximum or optimal design load of the plants is frequently not retained during their lifespan [48]. Part load conditions cause the performance to deviate from its optimal designed load, lowering the plant's ther-

mal efficiency. This results in a decrease in the overall plant performance and an increase in the CO₂e [t/MWh] emissions [44].

2.3.1. Heat Recovery Steam Generator

The residual heat of upstream power cycles is recovered by the Heat Recovery Steam Generator (HRSG). The HRSG consists of three distinctive sections; the economizer, evaporator and superheater. Figure 2.9a shows the sequence and relative temperature level of the three sections. The incoming water is heated to saturated water in the economizer after which it enters the evaporator. In the evaporator, the saturated water is heated until the water is converted to saturated steam. Lastly, the superheater increases the temperature of the steam resulting in superheated steam.

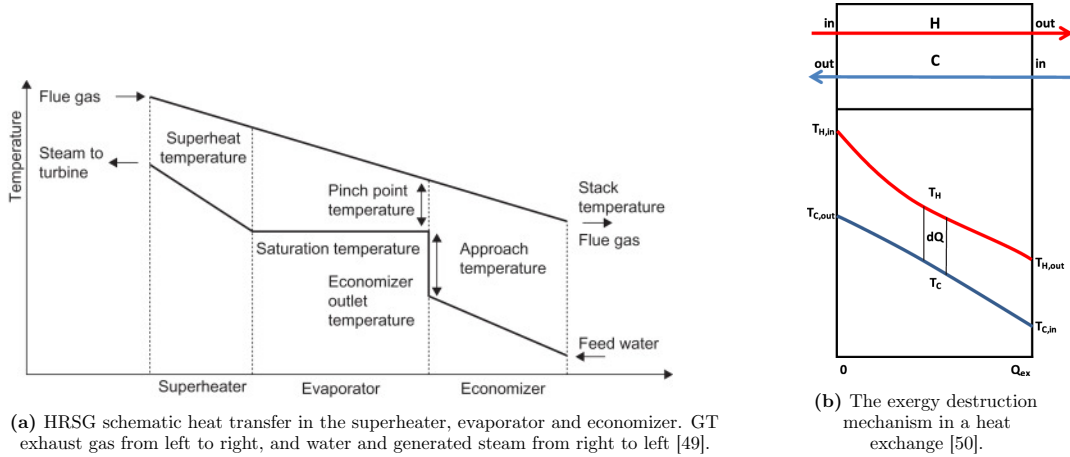


Figure 2.9: HRSG temperature distribution and exergy destruction.

To minimize losses, the area between the lines in Figure 2.9b needs to be minimized by aligning the temperatures of the streams. A multi-stage ST minimizes the area by varying the operating pressure of the cold stream with a resulting varying saturation temperature of the steam. This principle can be applied multiple times at different pressure stages to maximize the power output.

2.4. SOFC-CCGT

The high-temperature exhaust streams of the SOFC can be utilized to drive downstream thermodynamic cycles [34]. The SOFC-CCGT integrated plant has superior performance, both energetic and environmental, compared to the standalone cycles [33]. Coupling the SOFC exhaust gasses with the CCGT by heat and/or mass creates synergies. Additionally, the SOFC could offer a considerable amount of extra power. Comparing the performance under the same operating conditions, the SOFC-GT power plant has on average a 27.8% higher thermal efficiency compared to the conventional GT power plant [33] and the theoretical electric efficiency of the hybrid cycle can reach over the 70%(LHV)[34]. The electrical efficiency of the SOFC-CCGT outperforms the other large-scale power generation units [8] (which is depicted in Figure 2.10).

According to Sharaf et al.[51], the efficiency of a fuel cell is not much affected by system size, unlike combustion-based systems. In fact, fuel cells exhibit better efficiency at part loads than at full loads due to the increased voltage losses at higher loads. Combining a GT and FC results in enhanced load flexibility of the integrated system compared to the GT alone [51].

2.4.1. Integration Methods

There are several methods to integrate the SOFC with a GT and they can generally be classified as either directly or indirectly. A direct coupled SOFC-GT shares the same working fluid and can thus be defined as both thermally and chemically integrated. The indirect coupled SOFC-GT is solely

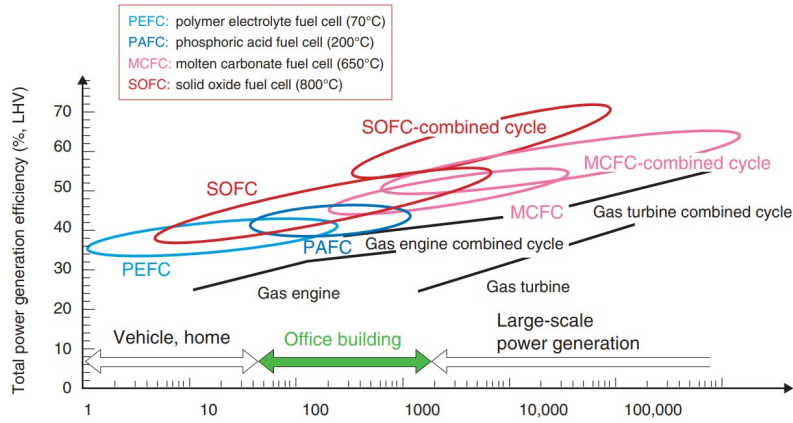


Figure 2.10: Comparison of performance between several types of power units: Combustion-based cycles, alternative fuel cell technologies and the fuel cell combustion cycles [8].

thermally integrated by heat exchangers [38]. The schematic representation of the direct and indirect coupled SOFC-GT are depicted in Figure 2.11a and 2.11b respectively. The provided heat by the SOFC substitutes the required heat to expand the GT’s oxidized fuel.

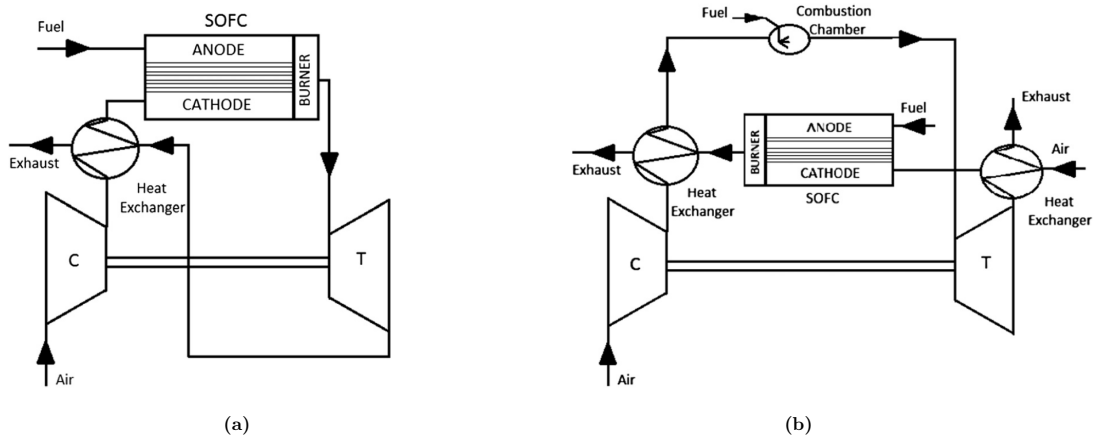


Figure 2.11: (a) SOFC GT directly coupled, (b) SOFC GT indirectly coupled. [9].

Directly Coupled

The direct coupling method is preferred over the indirect coupling method when the SOFC is pressurized. The GT generates power by expanding the SOFC’s exhaust gas in addition to the conventional gas expansion. Also on the electrochemical level is a high-pressure operation preferred; the V_{Nernst} is higher compared to the low-pressure operation (Equation 2.3), and an increased pressure reduces the activation losses by simultaneously increasing the adsorption rates and the absorbent surface coverage [1].

However, the same increase in operating pressure negatively impacts the efficiency of the SOEC mode. The increased V_{Nernst} results in a larger required electrical power to split the water molecule. Secondly, the activation losses on the Oxygen Electrode (OE) increase at higher pressure levels. Besides the disadvantageous electrochemical consequences, SOFC-GT integration encounters several drawbacks from a practical perspective during high-pressure operations. The direct coupling method causes material reliability issues related to anodic-cathodic pressure differentials which limits the operating flexibility. The associated pressure fluctuations in the GT could cause severe damage to the turbine blades [38]. Most modeled hybrid SOFC-GT assume futuristic components that currently do not exist, while few studies take into account the existing system components while considering these damaging consequences [35].

Indirectly Coupled

Indirect coupled SOFC-CCGTs are less sensitive to the disadvantages discussed above. However, Buonomano et al. [34] concluded that direct coupled SOFC-CCGT outperforms the indirect systems by generally 5% higher efficiency. The main advantage of an indirect coupled SOFC-CCGT is the strong ability of the SOFC to be integrated with a wide variety of existing CCGT types [38]. The CCGT can maintain its original operating conditions, and the integration is achieved by relatively fewer adjustments and costs.

2.5. District Heating Network

Through a system of pipes, district heating distributes hot water or steam from a central point to specific homes or blocks of buildings. The implementation of DH results in a significant reduction of CO₂ emissions, fuel consumption and costs, and an increase in system efficiency [52]. The conventional heat generated by decentralized heat production is replaced by the heat from the district heating network, fed by centralized industrial-scale processes. Figure 2.12 depicts a schematic representation of a DHN.

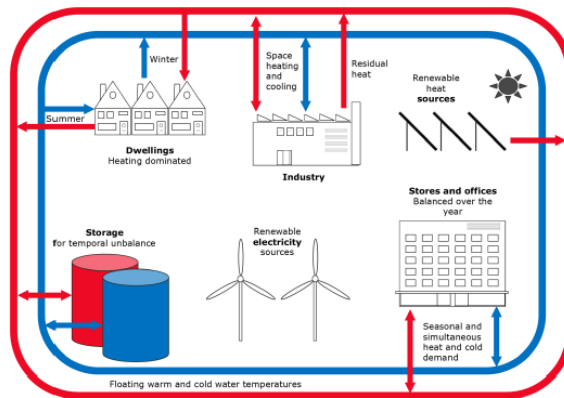


Figure 2.12: District heating network supplied by industrial centralized processes and renewable energy sources [10].

The world's district heat consumption is rapidly growing. The climate agreement of the Netherlands states that DHN will play a major role in achieving the Paris Agreement [53]. Growth targets of the Netherlands aim to connect 1.5 million houses to the district heating network by 2030 and provide 7 million houses with sustainable heat by the year 2050 [54].

2.5.1. CCGT and District Heating

The simplest form of CCGT heat recovery is the utilization of the downstream heat losses. The CHP plant utilizes the downstream environmental exergy losses by cooling down the exhaust gasses to produce useful heat which supplies the DHN. The other heat extraction method imposes a bleed at the IP of the LP turbine which temporarily extracts hot steam from the system [55]. This hot steam heats the circulating DH feedwater, after which the steam is inserted back into the system. Figure 2.13 visualizes the ST bleed.

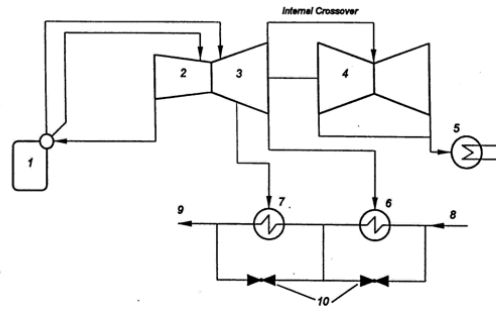


Figure 2.13: Simplistic schematic overview of ST bleed supplying the District heating network. Component: 1) Boiler, 2) High-Pressure Turbine, 3) Intermediate-Pressure Turbine, 4) Low-Pressure Turbine, 5) Condenser, 6) District Heating heat exchanger, 7) District Heating heat exchanger, 8) DHN return water, 9) DHN supply water, 10) Bypass [11].

2.6. Multi Energy System

Multi-Energy Systems (MES) are gaining interest in the development of sustainable urban energy systems [29]. An MES utilizes multiple energy carriers which optimally interact with each other at various system levels and could enhance the performance on technical, economic and environmental levels relative to classical energy systems whose sectors interact at a lesser extent [30]. The expansion of the number of energy carriers results in a higher degree of freedom for the systems' optimization which could lead to increased system efficiency [29]. An energy system should meet the energy demand, generate energy at an affordable price, operate safely, and be reliable [56]. An optimized MES contributes to enhancing the system's efficiency and energy utilization, fosters optimal deployment of the assets, decreases the energy costs and the GHG emissions [30], and stabilizes the various energy grids [57].

2.6.1. Imbalance

The discrepancy between the scheduled, offered and dispatched by a transmission provider, and the actual quantity of energy delivered to such transmission provider is understood as the energy imbalance. The energy grid must always be in balance, several sub-optimal solutions can be used to achieve this such as, anticipating at the generation side, influencing the consumption, importing or exporting energy, load shedding and energy storage. Varying the energy price is widely used to control the imbalance, which could in a volatile energy price [28]. The simultaneous expansion of RESs in the energy grid mix and the increasing heat demand promote the imbalance between the production and consumption of energy. During an imbalanced heat grid, thermal energy is prone to be wasted.

The performance of power plants depends on these imbalances [57]. An unflexible MES is unable to mitigate the unbalance in the energy sector. Matching the supply and demand of energy will result in a reduction of the generation unit size, increased system performance, increased RES exploitation, energy grid flexibility, reduction in pumping power, reduction of carbon emissions and a reduction in investment costs [28]. The variations on the production side are mainly caused by the RESs [27].

2.6.2. Storage

Expanding the MES with energy storage devices provides solutions for matching energy production and consumption. Storage systems are rated on six performance indicators [2]. These indicators are energy density, daily self-discharge, response time, lifetime, life cycles, round trip efficiencies and investment costs.

Long-term Storage by Artificial Fuels

Storing energy in artificial fuels, such as hydrogen or biofuels, is the best solution for long-term storage. By using these large-scale solutions, seasonal energy fluctuations can be managed [31]. Hydrogen has significant advantages over other storage mediums when it is used in heat-related systems [58]. Hydrogen can be transported with little loss compared to electric transportation and heat transportation.

Offsite storage is thus possible without relatively large additional losses. Furthermore, little or no losses occur during the period that hydrogen is stored. The discharge rate is an important factor to take into account when considering long-term energy storage. There is not yet an alternative solution for large-scale electricity or TES without significant losses. Hydrogen is currently considered one of the leading energy carriers to decarbonize the heat sector, while simultaneously helping to balance the seasonal discrepancy between energy production and consumption [58]. Multiple mature hydrogen storage technologies are present today.

The main arguments to choose the rSOC energy conversion device with the energy carriers hydrogen over other storage systems relate to flexibility, adaptability, capability, and high efficiency. The rSOC can accomplish high efficiencies, the energy conversion round trip efficiency is 70%² and can reach up to 80% with heat integration, which is higher than CAES (42-55%) and comparable to TES and flow batteries 72-80% and 84% respectively [2]. The foremost disadvantages are the current affordability and the technical readiness compared to the other conversion devices. However, the capital costs could shrink from 2000 to 530 €/kW_{el} by 2050 [17] due to technology commercialization, and economies of scale.

Thermal Energy Storage Comparison

The distinctive types of TES can be classified by four characteristics. The first is the physical phenomenon that underlies the technology. Generally, the physical phenomenon can be divided into sensible, latent and chemical storage. Sensible TES has the highest maturity of the three, it has been deployed in a considerable number of DHNs [28]. The second characteristic divided the TES technologies into short-term or long-term storage. TES has a relatively high discharge rate which results in substantial losses when used for long-term storage. The third classification is the degree of centralization. The storage system can exist of multiple small-size systems localized at the consumer, or one or few large-scale systems placed at strategic points in the DHN. The last characterization is mobilized or demobilized storage. Since the TES for DH is relatively large, this work will only consider demobilized Thermal Energy Storage (TES).

2.7. Exergy

Exergy can be regarded as the maximum theoretical work obtainable from a system when the system passes from a given state to the dead state that is in thermodynamic equilibrium with its environment [47]. Exergy provides information about the quality of the energy. Exergy efficiency describes the true losses of a system caused by irreversibilities, whereas energy efficiency fails to describe this. Thus, exergy efficiencies provide a measure in comparison to ideality.

Exergy Analysis

The exergy rate balance for a control volume in steady-state is formulated in Equation 2.34. The exergy destruction $\dot{E}x_d$, derived from Equation 2.34, equals the difference between the incoming exergy and outgoing exergy. The component-specific exergy analysis is further elaborated on in Chapter 4.

$$0 = \sum_j \left(1 - \frac{T_0}{T_j}\right) \dot{Q}_j - P + \sum_i \dot{E}x_i - \sum_e \dot{E}x_e - \dot{E}x_d \quad (2.34)$$

The total exergy is separated by physical Ex^{ph} and chemical exergy Ex^{ch} , and can be further classified by its origin. In this work, exergy is classified as follows [59]:

1. Physical Exergy

(a) Mechanical

- i. Origin: Kinetic
- ii. Origin: Potential

²The following efficiencies are all in LHV, excluding storage losses

(b) Thermomechanical

- i. Origin: Temperature
- ii. Origin: Pressure

2. Chemical Exergy

- i. Origin: Mixing and Separation
- ii. Origin: Chemical Reaction

Physical Exergy

The Ex^{ph} is calculated as defined in Equation 2.36. This work neglects the kinematic and potential effects, due to the negligible contribution to the total, which simplifies the Ex^{ph} to Equation 2.37 [38].

$$\dot{E}x = Ex^{ph} + Ex^{ch} \quad (2.35)$$

$$\dot{E}x^{ph} = \dot{m} \left((h - h_0) - T_0(s - s_0) + \frac{1}{2}(V^2 - V_0) + g(z - z_0) \right) \quad (2.36)$$

$$\dot{E}x^{ph} \approx \dot{m} ((h - h_0) - T_0(s - s_0)) \quad (2.37)$$

Chemical Exergy

The chemical exergy is associated with the additional work generated by the contents of the system in the dead state that is permitted to chemically react with the contents in the environment [47]. Chemical exergy is relevant in combustion and electrochemical systems. The chemical exergy of a pure species $\dot{E}x^{ch}$ is calculated by the exergy grade γ_f , the higher heating value (HHV) and the mass flow, and the chemical exergy mixture Ex_{mix}^{ch} by using the molecule standard exergy Ex_n^{ch} with the composition of the gasses y_i , stated in Equation 2.39. The exergy destruction $\dot{E}x_d$ is defined as the difference between incoming exergy and outgoing exergy and can thus be derived from Equation 2.34.

$$\dot{E}x^{ch} = \Gamma_f \dot{m}_f HHV_f \quad (2.38)$$

$$\dot{E}x_{mix}^{ch} = \sum y_n \dot{E}x_n^{ch} + RT_0 \sum y_n \ln(y_n) \quad (2.39)$$

Ex_n^{ch} is the molecule's standard exergy. Appendix A.1 summarizes the relevant molecules in the system and the molecule standard exergy [18].

Exergy Destruction

In contrast to energy, exergy destruction is not conserved but destroyed by irreversibilities [47]. Exergy destruction and losses play an important role in developing strategies to improve the system's performance. Exergy could also be lost due to exergy leaving the system boundary. This is described as Exergy losses. This work adopts the exergy destruction and losses to determine the quantity, component location and exergy type of the wasted resources. Equation 2.40 defines the Exergy destruction E_d by multiplying the environmental temperature T_0 with the entropy produced within the system by the internal irreversibilities σ .

Exergy destruction and losses form the basis of the exergy analysis. A parametric analysis is used to examine the effects of the operating conditions on the system's exergy destruction. System-level exergy and the relevant component-specific efficiencies will be discussed in Chapter 4 once the system setup is specified.

$$\dot{E}x_d = T_0 \sigma \quad (2.40)$$

Exergy Efficiency

The exergy efficiency is derived from the exergy rate balance and can be defined as a ratio of the useful recovered exergy divided by the total supplied exergy. The useful exergy and the exergy efficiency are component-specific. Chapter 4 elaborates on these component-specific exergies when the base case of the system is defined.

$$\varepsilon = \frac{\sum \dot{E}x_{out}}{\sum \dot{E}x_{in}} \quad (2.41)$$

3

Literature study

The findings of previous studies form the basis of this study. This research builds and expands upon the critical points examined in the literature. In addition, research gaps are identified, clarifying the value of this research. First, Section 3.1 elaborates on the literature related to modeling and optimizing the rSOC. The ideal coupling method of the SOFC and CCGT is highlighted in Section 3.2. Finally, Section 3.3 evaluates the MES applications that could improve the performance of the system.

3.1. Reversible SOC

What follows is an analysis of the literature that focuses on the rSOC. Of particular interest are the assumptions for modeling the system, the results of the optimization and the achieved performance.

3.1.1. Cell Level

Hauck et al. [16] modeled a zero-dimensional thermodynamic rSOC model in Aspen Plus with which a parametric analysis was conducted to investigate the relationship of different operating conditions with system performance. The model proved to perfectly represent the experimental rSOC operation that was validated with the experiments of Kazempoor and Braun [1]. In addition to the operating conditions, Hauck et al. also examined various sweep gas compositions and fuels, including hydrogen. They concluded that the increase in temperature leads to an overall improvement in performance, but that changing the gas compositions or increasing the pressure improved the performance of one mode while obstructing the other mode. The increase in pressure leads to an increase in cell voltage and reduces diffusion losses. In the SOEC, the reduction in losses appeared to outweigh the increase in Nernst voltage at current densities exceeding 1.25 A/cm^2 .

Kazempoor and his fellow researchers have greatly contributed to the thermodynamic modeling of an rSOC. First, Kazempoor et al. established two individual models for the SOFC [41] and the SOEC [60], and combined them in an rSOC model [1]. The geometric values of the model were calibrated and validated using an experimental setup. Kazempoor and Braun emphasize the relation of operating conditions with the individual losses of the rSOC: Ohmic resistance accumulates to the majority of losses, but the ratio and the magnitude of the losses vary greatly between the modes. They recommend no operating temperatures below $700 \text{ }^\circ\text{C}$ due to the increase in losses. Varying the pressure does not influence the performance so vigorously as the temperature over the examined range ($750 - 850 \text{ }^\circ\text{C}$ versus $1 - 30 \text{ bar}$).

Kazempoor and Braun emphasize the relation of operating conditions with the individual losses of the rSOC and propose solutions to minimize these losses. Activation, polarization and ohmic resistance accumulate in the majority of losses, and the ratio and the magnitude of the losses strongly vary between the modes. Temperatures below $700 \text{ }^\circ\text{C}$ are not recommended due to the increase in losses. Elevated pressures can cause the SOEC to operate in the exothermic region.

Furthermore, a zero-dimensional Aspen Plus model fueled by a mixture of water and hydrogen was configured by Bianchi et al. [12]. The results at the cell level were consistent with the experiments, thus the zero-dimensional model guarantees minimum computational power without loss of information. The cell voltage increases when a higher concentration of hydrogen is used. Therefore, the concentration should be maximized for the SOFC but minimized for the SOEC.

However, Bianchi and Bosio [17] argue that the degradation rate of the rSOC has to be considered during the maximization or minimization of the hydrogen concentration, for the SOFC and SOEC respectively. The microstructure of the SOFC shows a higher degradation rate when fueled by pure hydrogen. Besides, small quantities of steam reduce polarization losses. The same holds for a low percentage of hydrogen at SOEC mode. Therefore, to mitigate the degradation rate, the authors recommend to fuel the SOFC with a mixture of 97% / 3% $\text{H}_2/\text{H}_2\text{O}$ and the SOEC with 10% / 90% $\text{H}_2/\text{H}_2\text{O}$ on molar basis.

A small amount of hydrogen starts the electrochemical reaction immediately which results in higher power output [34]. Additionally, the use of air instead of pure oxygen is preferred since the decreased performance of the SOFC is compensated by the enhanced SOEC performance. Besides, no oxygen purification or storage unit is required. This corresponds to the findings of Hauck [16].

Bianchi and Bosio [17] also conducted a parametric study. The stacks efficiency was examined with the variation of the current density (1000 to 10000 and -1000 to -10000 $[\text{A}/\text{m}^2]$ for SOFC and SOEC respectively) and the fuel utilization 10% to 90% (H_2 and H_2O for SOFC and SOEC respectively). The round trip thermal efficiency of the system - calculated by multiplying the efficiency of both modes - was maximized at a current density of 3000 for SOFC and -6000 for SOEC at the maximum fuel utilization factor and maximum fuel concentration. Bianchi and Bosio [17] appoint that the commercialization of the rSOC has still many challenges to overcome. They conclude with a recommendation on initiating research to the incorporation of the rSOC unit in current energy grids to determine the commercial potential or the system [17].

3.1.2. System Level

The next step involves observing the performance of an rSOC-based system when the Balance of Plant is also included. The first research is by Giannoulidis et al. [61], who investigated the energy storage and conversion system using an rSOC at its core. The system converts steam electrolysis for SOEC and methanol for SOFC. The maximum cell's exergy efficiency was 72.3% and 62.6% for the SOEC and SOFC respectively. The thermal roundtrip efficiency was 98% at the applied current density of 500 A/m^2 but decreased exponentially to 75% at current densities of 10,000 A/m^2 . The maximum system round trip efficiency is 64.3%, which was achieved at a current density of 500 A/m^2 .

However, the authors recommend a current density of 5000 A/m^2 when considering the production of "a reasonable amount of power" per stack instead of having to enlarge the plant to oversized dimensions [61]. The maximum power density is also around 5000 A/m^2 for hydrogen cycles [43] which significantly decreasing the cell capital costs [62]. Higher operating pressure enhances the stack's performance but decreases the system's performance. Higher pressures cause an increase in the system's hot utility which outweighs the advantages of the stack performance.

3.1.3. Transient Response

Botta et al. [39] examined the transient response of rSOCs by investigating the limiting local temperature gradient and voltage during the switching of modes. The voltage responds to the load variation within a few seconds; a stable fuel utilization factor was achieved in 50 seconds. Changes in temperature took some longer; 10 minutes to respond to achieve a constant temperature gradient when switching from SOFC to SOEC mode while it took 18 minutes for the reverse transition. The authors concluded that the rSOC is a flexible and fast-responding system that was mainly governed by thermal inertia. They suggest that the rSOC transient response of the rSOC is sufficient for real-world grid stabilizing applications.

Motylnski et al. [63] developed an rSOC-based model with Aspen Hysys that was tested on the ability to be integrated into a power grid for power balancing. The dynamic model was tested by cou-

pling it to a wind profile after which the operating conditions in the stack were monitored. The study showed that the direct coupling to a varying power grid did not overload the stack keeping it within the pre-defined limits regarding the temperature, pressure, and concentration gradient. The variation of 40 A/min was sufficient to keep up with the grid load variations while not exceeding these limits. A fresh preheated air flow regulated the stack temperature by varying the flow rate. During the switching of modes, the fuel concentration in the rSOC (water and hydrogen) was gradually switched for two minutes time to avoid stack degradation by sudden concentration variation. During SOFC mode, the composition of 90% H₂ /10% H₂O was inserted while the reverse holds for the SOEC. The study did not assess the benefits of grid balancing by the rSOC or the profits involved.

The findings are consistent when examining the transient response at the stack level. Wehrle et al. [64] examined the transient response of the operating conditions at the stack level of 50 cells through a 3D model. The airflow rate and the cell voltage were found to be powerful tools to maintain temperature gradients. The simulations showed that, after a voltage perturbation, the current density and mole fractions of the species follow immediately, while the temperature gradient slowed the switching of modes due to the inherent thermal resistance of the stack. The authors suggest that the Balance of Plant in the system will be the limiting factor. However, in the future, near-immediate mode switching will be achieved.

The degradation effects of the rSOC during the switching of modes were reviewed by Khan et al. [65]. The main driving force of degradation was the delamination of the electrodes caused by temperature gradients. During the switching of modes, the brittle metal hydrides and metal oxides formed on the surface would erode. The SOFC degrades in 40.000 hours by 10% of the first order efficiency, while the SOEC only needs 10.000 hours to reach that same degradation. The resulting insufficient lifetime of the rSOC for is one the biggest drawbacks of the technology [17].

3.1.4. Summary

The findings can be summarized as follows:

- Zero-dimensional models may equally well approximate the actual operation of the rSOC than higher-order dimensions [16][61][12].
- Increased hydrogen concentration enhances the SOFC performance but moderates SOEC performance [12][16] due to the affected Nernst voltage. However, to prevent degradation, the concentration on molar basis is limited to the mixture of 97%/3% H₂/H₂O for SOFC mode and 10%/90% H₂/H₂O for SOEC [17][34].
- Although the maximum round trip efficiency, of converting power-to-gas-to-power excluding storage losses, is achieved at lower current densities (500 A/m²), current densities around 5000 A/m² are preferred when considering the production of a reasonable amount of power instead of enlarging the plant size [61], and to maximize the power density [43] which decreases system costs [62].
- Air is commonly used as the sweep gas [16] [17].
- Research on the incorporation of the rSOC unit in current energy grids is required to determine the commercial potential of the system [17].
- The transient response of an rSOC is sufficient to keep up with the grid load variations making the Balance of Plant the limiting factor [39][63][64].

3.2. SOFC-CCGT

The potential of integrating a SOFC and a CCGT has been widely explored over the past two decades. The following section discusses the main conclusions from these works. The goal of this work is to assess the exergy efficiency and CO₂e emissions while considering the investment costs. These costs could be significantly reduced by integrating existing system components into the new proposed system. The SOFC-CCGT integration would achieve the first two goals and a retrofitted CCGT would help to accomplish the latter. Therefore, the following section pays specific attention to the retrofitted CCGT integration.

Buonomano et al. [34] analyzed and compared a vast number of hybrid SOFC CCGT configurations. The hybrid systems were classified based on the following design parameters: Temperature and pressure level of the SOFC stack, type of fuel, type of reformer, downstream turbine inclusion, and type of Brayton cycle.

The pressure level is an important design parameter. Generally, a pressurized system enables direct integration which gives the highest efficiency. But a lower-pressure indirect connection should be chosen when simplicity, reliability and robustness are preferred. With indirect configuration, the SOFC and GT can operate independently of each other, only taking into account the amount of heat transfer required and assuring the correct Turbine inlet Temperature (TIT). Although the higher efficiency and the lower costs, the operating domain of the direct configuration is very limited due to the operating constraints of the turbomachinery, which leads to an inflexible system. Buonomano et al. [34] noted that there are generally two methods to recover heat downstream heat: re-circulating air or applying an HRSG. Oxygen electrode recirculation performed the best both economically and energetically.

Buonomano et al. [34] denote that despite the enormous amount of research on the hybrid cycles of the SOFCs, the cycle is still a long way from becoming commercially available. The price of the hybrid cycles is still orders of magnitude greater than that of traditional systems (such as GTs and reciprocating engines). Therefore, Buonomano et al. call upon academics, instead of focusing on the design of complex and expensive hybrid SOFC systems, to examine economically feasible manufacturing techniques and systems.

The consideration of combining the SOFC-GT with a low-level ST was investigated by Gandiglio et al. [66]. Two systems were compared: one a pressurized SOFC-GT-ST (20 bar) and the other an ambient SOFC-ST. The SOFC generates 220 MWe at an operating temperature of 800 °C, a fuel utilization factor of 0.85, and a current density of 6400 A/m². The net additional power provided by the turbomachinery was 54 and 65 MWe for the ambient and pressurized configurations respectively. The HHV efficiency of the ambient system was 64% and the pressurized configuration outperformed the atmospheric configuration by 6%. A fuel pre-heater and air recirculation factor of 0.55 was applied in both setups. The expansion of the pressurized exhaust gas decreased the temperature, which prevented the gas to facilitate heat to the air preheater and thereby affecting the total recovered heat.

Braun et al. [67] performed a similar study, investigating the difference between a downstream ORC and Steam Rankine Cycle (SRC) on the electric efficiency of a 100 MW directly coupled SOFC with a retrofitted Pratt & Whitney FT8-3 GT. The SOFC was fueled by syngas, and a fuel utilization factor of 0.80 was applied. The system operates at 775 °C, at 0.75 V and 4500 W/m² with a maximum of 100 °C temperature rise at the inlet and outlet of both the fuel and oxygen electrode. The bottoming cycle increased the electric efficiency from 67% to 75%. Replacing the ORC with an SRC would enhance the electrical efficiency by an additional 4 percentage points. Via an operating conditions sensitivity analysis, Braun et al. [67] concluded that the cell voltage, the SOFC fuel utilization, and the operating pressure had the biggest impact in the observed range. Pressure drops and temperature increases had only a mild effect. The power output of the SOFC had a relation with the air recirculation ratio. Also, the maximum temperature increase between the inlet and outlet of the electrode channels mildly influences the system performance (increasing from 100 to 150 resulted in a 0,1% of system efficiency) [67] but it increased thermal stresses and the thereby the degradation ratio [17].

Cheddie [68] performed a thermo-economic optimization of a direct coupled retrofitted 10 MW GT with a SOFC. Both systems were fueled by natural gas. The resulting 37 MW system enhanced the efficiency from the original GT standalone thermal efficiency from 30% to 66.2% (LHV) while the exergy efficiency increased from 13.7% to 47.0%. With the same amount of gas, the standalone GT would generate only 17 MW. The resulting system generates 270% additional power while the fuel consumption only increased by 66.8%. The entire retrofitted system would cost \$32M, which results in an NPV of \$34.9 M. Cheddie [68] did not account for the technical disadvantageous implications of the direct coupling or periodic shutdowns. However, Cheddie recommends future research to contribute to this gap. Besides, no ST was considered.

Eveloy et al. [38] did examine a retrofitted GT with a downstream Rankine Cycle. The original 9.1 MW GT was expanded by an indirect internal reforming SOFC. The combined system generated 25.3

MW at an exergy efficiency of 55.9% compared to 28% at the standalone GT. Then the system was upgraded with a downstream Rankine cycle. For this purpose, an organic Rankine cycle is compared with a steam Rankine cycle.

The SOFC-GT-Organic Rankine Cycle system's exergy efficiency was 6% higher than the SOFC-GT configuration. Replacing the ORC with a ST enhances the system by an additional 4% efficiency. However, the ORC has a less complex configuration because it does not require different pressure stages to utilize all the energy.

Eveloy et al. [38] argued that the indirect integration method was preferred to ease design complexity allowing a wider variety of retrofitted cycles to be integrated at reduced costs. The same arguments were corresponding to that of Zhao et al. [69]. The authors applied two additional optimizations. First, an afterburner was employed to burn the SOFC's unconverted fuel to generate heat (950 °C) that preheats the incoming air and fuel streams. Secondly, an air splitter, positioned after the oxygen electrode, reduced the fresh air requirement thereby reducing compression power.

The CO_{2e} emissions by the SOFC-GT compared to the GT were examined by Haseli et al. [33] and Eveloy et al. [38]. The result is strongly related to the turbine inlet temperature and the compression ratio, but Haseli et al. [33] showed a consistent result favoring the SOFC-GT plant over the GT plant. The minimum factor of $CO_{2,SOFC-GT}/CO_{2,GT}$ is 1.75 at an operating temperature of 977 °C and a compression ratio between 2 and 14. The indirect integration of the SOFC and GT has a major effect on the fuel consumption of the conventional GT. It reduces the fuel consumption by 72% by utilizing the heat of the SOFC exhaust gasses [38]. The relative fuel reduction is related to the power capacity ratio of the SOFC and the CCGT. A higher ratio in favor of the SOFC has the potential to provide more heat which substitutes the heat generated by combusting fuels.

Schouten and Klein [70] investigated multiple hydrogen oxygen cycles based on the Brayton cycle and a downstream steam low-pressure turbine. Concluding from the exergy analysis, the combustion of hydrogen in the GT accounted for the largest part of exergy destruction. The authors proposed the integration of SOFCs with the GT as the solution. Two setups were examined: A setup including SOFCs operating at a single temperature level of 700 °C, and the other, with multiple SOFCs placed in series operating at different temperature levels at 700, 850 and 1000 °C. The fuel and air were entering the fuel cell at 150 °C below the operating pressure. Additionally, two SOFC cooling techniques were compared: 1) Excess air, circulating over the cell, cools the cell to the desired outlet temperature, and 2) Diluting the air of the oxygen electrode with steam.

The addition of the three SOFCs to the upgraded Grazz cycle performed best. The LHV efficiency was increased from 75.7% to 85.1%. Air recirculation was preferred over steam dilution, which can be explained by the Nernst voltage drop due to the dilution of the oxygen. The authors end with a recommendation to study the modification of existing CCGT cycles with the insights provided by their work.

3.2.1. Summary

- The academics should focus on examining economically feasible hybrid cycles rather than complex and expensive ones [34]. Research on retrofitted CCGT with SOFC could reduce the system costs [68].
- A pressurized direct coupled system gives the highest efficiency [34][66]. However, the indirect connection should be chosen when simplicity, reliability, and robustness are preferred, which is the case in retrofitted cycles [69] [38].
- Increasing the temperature difference between the inlet and outlet of the SOFC system has a slight positive effect on the CCGT SOFC system performance [67], but it significantly increases the SOFC degradation rate [17].
- The addition of SOFC to the (CC)GT cycles enhances the system performance. This is also true for retrofitted CCGTs. In that case, the indirect coupling is preferred which results in a 4 - 6% lower efficiency compared to direct coupling [66].
- SOFC CCGT cycles emit less CO₂ t/MWh by the increased system efficiency even if the SOFC is fueled with the same fuel.

- The environmental impact of the SOFC-GT is strongly related to the turbine inlet temperature and the compression ratio [33].
- Recirculating air is the most common method for heat recovery [34]. [70]. It is more effective than a downstream heat recovery system but it does not exclude each other [34].

3.3. MES

This section specifically addresses the MESs using electrochemical conversion systems consisting of either a reversible cell or a separate fuel and electrolyzer cell. The reversible electrochemical cells are of special interest. The section elaborates on the benefits of the MES: it considers the contributions of the system to meet the energy demand, generate energy at an affordable price, operate safely, and be reliable.

3.3.1. SOC-based MES

Milewski et al. [71] compared the optimal system configuration of the Balance of Plant (turbomachinery, storage devices, and heat exchangers) and its optimal operating conditions for a hydrogen rSOC, deployed for peak-load solutions. The simplest configuration has no turbomachinery and consists of the minimum amount of components. When the system is expanded with the addition of heat exchangers, turbomachinery, and O₂ storage, the operating conditions should change accordingly, improving the performance. The system improved by strategically positioning the heat exchanger network and using water pumps instead of steam compressors.

Nevertheless, there is much to criticize about the method of analyzing the rSOC. First, Milewski et al. tested two extreme pressure levels: 1 bar and 800 bar. The latter is extremely high compared to all other studies discussed above. Second, Milewski et al. assumed a constant efficiency of 80% for the SOFC and SOEC. However, the efficiency strongly depends on the pressure [34] and differs from SOC mode under similar conditions. Lastly, the endothermic or exothermic operating of the SOEC - which affects the performance [1] - under high pressure was not considered. Therefore, only the strategic positioning of the components from Milewski et al will be used in this work.

Bin et al. [72] modeled a grid stabilization system consisting of an rSOC integrated with CO₂ methanation synthesis. Bin et al. tested the system at two control modes: Stationary mode and a mode where they linked the MES to an electricity grid and a limited capacity H₂ storage tank. The tank stored the hydrogen under ambient conditions. The rSOC operated at 10 bar at 600 °C. The 1 MW SOFC was loaded with 233.9 A/m² resulting in a cell voltage of 0.71 V, and vice versa 2308 A/m² and 1.44 V for the 2 MW SOEC. The cell voltage of 1.44 V exceeded the thermoneutral voltage of 1.29 V, which resulted in more than 20% additional energy input for heat. The resulting thermal efficiency in stationary mode was 85%. However, it dropped to 47% when the MES was linked to the simulated energy grid.

Sensoli [73] optimized an rSOC-based system including latent heat and hydrogen storage in Aspen Plus. To mimic the anticipated environment in which the cells would function, multiple realistic profiles of power generation (solar, wind and an existing power plant) and consumption on different scales and different seasons were examined by the authors. The obtained round trip efficiency from power to gas to power varies between 78% and 84%, depending on the case. Pure oxygen performed better at system performance but the economical point of view prefers air as the sweep. The author emphasizes that the system should only be manufactured for large-scale systems, exceeding 20 MW of electric power, in order to be profitable. The high-temperature heat storage at 800 °C increased the round-trip efficiency and the profitability of the system. However, the author did not correct for time-related heat losses.

3.3.2. Non-SOC-based MES

Although the system of Burer et al. [74] does not consist of a SOEC, the work included interestingly the district heating into the equation and performed an environmental analysis. The multi-criteria optimization was performed on a district heating, cooling and power-generating plant. The authors optimized the system performance with regard to costs and CO₂ emissions. The main duty of the system was to meet the heating and cooling demand all year round. The system was able to produce

solely power or a combination of heat and power depending on the needs of the energy grid. Excess electricity was utilized by generating additional heat. The MES was constructed by integrating a SOFC, a CCGT a heat pump, absorption chillers and a gas boiler. The SOFC and GT are directly connected, the SOFC acted as the combustion chamber of the GT. The heat contained in the exhaust gas preheats the incoming air stream of the SOFC and thereafter supplied the heat to the downstream steam absorption chiller and the Heat Recovery Device of the DHN.

Four best-performing system operating conditions were specified based on a Pareto-frontier. The SOFC-GT efficiency peaked at 69.3 % with a working pressure of 4 Bar at 900 °C while emitting 0.285 kg CO₂/kWh. When operating at lower temperatures (700 °C) the capacity of the GT/FC was required to decrease causing the exhaust gas temperature to increase from 218 to 239 °C. The performance deteriorated to 67.7% and the emission rate increased by 0.007 kg CO₂/kWh. Placing a simple heat exchanger downstream of the system helped prevent system environmental heat losses.

3.3.3. Storage

Storage is needed to mitigate the unbalance between energy production and consumption [28]. Short-term storage mitigates the daily fluctuations in the district heating network. Furthermore, long-term energy storage captures seasonal fluctuations. Therefore two distinct storage systems, that are optimized for distinct time periods, are required.

Short-term Storage

The relevant and scalable storage systems for daily fluctuations are Thermal Energy Storage (TES) and batteries [31]. The advantages of combining the TES with the DHN from a technical, economical and environmental perspective are listed below. These advantages become even more evident when the TES is connected to a renewable, gas-based MES [28].

1. The size of the energy-generating components in the multi-energy system is allowed to decrease [28] which reduces the system's capital costs per kWh [2]. Also, the TES reduces the operating costs such as the pumping power of a DHN, accounting for 1% of the energy requirements, by reducing mass flow rates [28]
2. A TES in combination with a CHP system increases the flexibility of the systems which maximizes the system's profit [28]
3. The capacity factor of the heat generating system is increased [28]
4. The hydraulic limitations of the heat capacity of the pipes in the DHN are decreased [28]
5. The TES helps to align the generation and consumption of heat [28] and because of it the combined system reacts faster on heat demand fluctuations [28]
6. More users can be connected to the DHN without large modifications of the network [28]

Sensible Water TES

Sensible heat TES is often used when daily storage is paired with DH systems. The heat is stored by increasing the temperature of the selected storage medium. The storage medium is selected based on physical properties, availability and pricing. Water is the most commonly used storage medium because of the following reasons:

- The low cost and technology simplicity [28]
- The similar energy carrier as the storage medium and the DHN's transfer medium [28]; Pressurizing water allows for operating conditions that satisfy the maximum supply temperature of 125 °C avoiding evaporation and allowing the direct connection with the DHN [75]
- The right thermal properties; high specific heat, density and thermal conductivity [75]

3.3.4. Summary

The following was concluded from the reviewed literature:

- rSOC is well suited for balancing the electricity grid [71] [72]
- rSOC with heat or hydrogen storage-based MESs should only be manufactured for large-scale systems in order to be profitable [73]

- The performance of the stationary mode rSOC MESs strongly differs when the MES was linked to an energy grid [72].
- A SOFC-GT based MES which includes district heating and cooling, designed to always meet the heating and cooling demand, showed superior performance with regard to costs and CO₂ emissions to the conventional system [74].
- TES is preferred in a MES when combined with a DHN on technical, economical and environmental perspective [28] [2] [76]
- Sensible TES is generally paired with the DHN for the low cost and technology simplicity of the storage technique [28] [75]

3.4. Literature Gap and Proposed System

Literature is calling for research into methods and systems to make the rSOC commercially attractive [17][68]. The transient response is not the limiting factor of following the load variations in the energy grid [64], incorporating the rSOC into an existing energy network would help determine the system's profitability. In theory, it appears that the efficiency of the SOFC-CCGT outperforms the current stand-alone CCGT [34] and that the SOEC operates at the highest thermal efficiency compared to the alternative electrolyzer [17]. But in practice, the system setups are not feasible due to cost constraints [17]. Research on adapting the SOFC to an existing CCGT may contribute to the adoption of the hybrid SOFC-CCGT system [34][70], if the system costs are found to decrease.

However, few research was found on the retrofitted hybrid system. To the best of the author's knowledge, no research examined the integration of an rSOC with an existing GT or CCGT. This study aims to determine the enhancement of performance caused by coupling the SOFC to an existing CCGT, while taking into account the bifunctional SOEC operating mode.

3.4.1. Assessing the Benefits Based on Exegetic Performance (Sub-objective 1)

Power For the simulation, the existing CCGT of the Hemweg 9 area, located in Amsterdam with a design point capacity of 440 MW, is used to which an rSOC is coupled with a capacity of 100 MW when operating in SOFC mode. The CCGT and the SOFC consume natural gas and hydrogen respectively. During reversible mode, the SOEC is able to generate hydrogen which the SOEC feeds a presumed hydrogen grid. The SOFC system receives its hydrogen from the same hydrogen grid.

The proposed system is compared with the current system by running both systems at full load, and comparing the power output and exegetic efficiency of both systems to each other. The outcomes of these comparisons will be used to make the assessment of sub-objective 1. Table 3.1 summarizes the comparisons between the Base cases (1A and 2A) and Optimization cases (1A and 2A). Due to the proven SOFC-CCGT superior performance in the discussed literature, the exergy efficiency of the combined system operating at full load (comparison 1A) is expected to be greater than the stand-alone CCGT, despite the fact that the performance of the SOEC must be taken into account when optimizing the SOFC. By comparing the uncoupled systems with the coupled systems, the synergies between the SOFC and CCGT can be explored. Although the efficiency of the CCGT will be deteriorated by part load/off-design operation, it is expected that also the efficiency of the integrated SOFC-CCGT at part load (Optimization case 2A) still exceeds the conventional CCGT at full load when both system setups generate the same electrical power output (comparison 2A). Maintaining the same power output allows the exergy analysis to compare the exergy flows on an absolute allowing better identification of differences.

Table 3.1: Summary Base case 1A, Base case 2A, Optimization case 1A and Optimization case 2A with the expected outcomes of exergy efficiency Ψ .

Comparison	Base case	Optimization case	Expected outcome
1A	CCGT & SOFC <u>full load</u> decoupled	CCGT-SOFC <u>full load</u> coupled	Ψ Optimization case 1A $>$ Ψ Base case 1A
Power [MW]	Full load ($P_e = 438$ MW)	Full load ($P_e = ?$ MW)	
Heat [MW]	No heat	No heat	
2A	CCGT full load	CCGT-SOFC part load coupled	Ψ Optimization case 2A $>$ Ψ Base case 2A
Power [MW]	Full load ($P_e = 438$ MW)	Part load ($P_e = 438$ MW)	
Heat [MW]	No heat	No heat	

Heat and Power The owner of the Hemweg CCGT (Vattenfall) considers modifying the Hemweg 9 power plant to a combined heat and power (CHP) plant that is capable of supplying heat to the DHN by tapping the hot recirculating steam and water from the CCGT. The system should be flexible enough to alternate between power (generating 440 MW_e) and combined heat and power modes (generating 413 MW_e and 100 MW_{th}) [77]. Therefore, this work also explores how integrating the rSOC with the CCGT CHP could improve exergy efficiency. The multi-energy system is thereby extended with the connection to the DHN.

The same comparisons are applied to the combined heat and power plant as in comparisons 1A and 2A: Comparison 1B is at full load and comparison 2B at part load. However, the part load operation in comparison 2B now matches the combined system's heat generation [MW] instead of power generation. The outcomes of these comparisons will also be used to make the assessment of sub-objective 1. Table 3.2 summarizes the comparisons between the planned CCGT CHP (Base case 1B and 2B) and the optimized SOFC-CCGT CHP (Optimization case 1B and 2B). Again, the full load and part load optimized system is expected to outperform their respective Base cases. Besides the exergy improvement by the synergies with the CCGT, it is expected that the exhaust flow from the SOFC can supply heat to the DHN resulting in an enhanced exergy efficiency.

Table 3.2: Summary Base case 1B, Base case 2B, Optimization case 1B and Case 2B with the expected outcomes of exergy efficiency Ψ .

Comparison	Base case	Optimization case	Expected outcome
1B	CCGT & SOFC <u>full load</u> decoupled	CCGT-SOFC <u>full load</u> coupled	Ψ Optimization case 1B $>$ Ψ Base case 1B
Power [MW]	Full load ($P_e = 413$ MW)	Full load ($P_e = ?$ MW)	
Heat [MW]	Full load ($P_{th} = 100$ MW)	Full load ($P_{th} = ?$ MW)	
2B	CCGT full load	CCGT-SOFC part load	Ψ Optimization case 2B $>$ Ψ Base case 2B
Power [MW]	Full load ($P_e = 413$ MW)	Part load ($P_e = ?$ MW)	
Heat [MW]	Full load ($P_{th} = 100$ MW)	Part load ($P_{th} = 100$ MW)	

3.4.2. Assessing the Benefits Based on GHG Emissions (Sub-objective 2)

For all eight cases, the relative GHG emissions [CO₂e t/MWh] are compared which includes the electrical and heat generation. The outcomes of these comparisons will be used to make the assessment of sub-objective 2. The emissions for the integrated system are expected to be lower than for the stand-alone systems, which should follow from the increased system efficiencies. Furthermore, incorporating hydrogen into the system should reduce the relative GHG emissions per MWh, assuming the hydrogen is generated with electricity produced by renewable energy sources.

3.4.3. Assessing the Benefits Based on Gross Profit (Sub-objective 3)

SOEC The SOEC is simultaneously optimized along with the SOFC, because the rSOC consists of a bifunctional system that has the same dimensions, Balance of Plant, and is subjected to the same operating conditions to avoid mechanical and thermal stress gradients. To test the advantages of implementing the rSOC, a case study was performed in which the optimized system is inserted into an energy resource allocation model for the energy network of the Amsterdam metropolitan. The model aims to maximize the gross profit of the energy system. The model is used to examine the practical implication of the system. The case study tests whether the implementation of the proposed multiple energy systems achieves a higher gross profit [€/MWh]. Even though the proposed system may be more efficient, the price of the same amount of energy for hydrogen is higher compared to natural gas,

so the cost per kWh produced is not guaranteed to go down. Nevertheless, by utilizing various energy carriers, the combination of these systems would hypothetically be able to respond to price fluctuations of the energy network caused by the supply and demand of these energy carriers. The relative gross profit is expected to increase because the proposed system can adjust its operating mode depending on the energy price whereas the original system was solely able to produce power. The NPV of the gross profit [€] and the weighted NPV of the gross profit [€/MWh] of the proposed systems are compared and will be used to make the assessment of sub-objective 3.

TES Lastly, it examines whether adding TES to the proposed system leads to an increased relative gross profit. The proposed system is extended with a sensible TES system because of its low cost, technology simplicity and synergies with the DHN [28] [75]. The TES is expected to decouple the production and demand of heat, giving the system more freedom to anticipate the price volatility in the energy grid while still meeting the constraint to meet heat demand. To test this, the multi-energy system is extended by adding a simulation of an existing TES system in the same dispatch model.

4

Methodology

The CCGT, rSOC and the Balance of Plant divide the system into the three main subsystems. The components in the system differ depending on the SOC mode. This chapter discusses the components in the order listed above. Each section starts with the assumptions, followed by the interpretation of the subsystem in the model, and ends with a validation. After the formulation of the individual components, they are combined and the overview of the formed systems is presented. Next, the performance indicators by which the system is valued are defined. The chapter ends with a description of the optimization process.

4.1. Retrofitted CCGT

The existing energy infrastructure, the future plans of the area, and the plant's ability to provide heat in the future make the Hemweg 9 area the perfect location for the proposed energy system. In the future, the Hemweg area is planned to become a fossil-free hub for electricity and heat [78]. The area will be used for the production, distribution and storage of renewable energy. In addition, the Hemweg area will become the center for the production of green hydrogen. The Hemweg area is connected to the DHN, electricity grid and gas grid. Moreover, the government of the Netherlands will construct a hydrogen grid that will be accessible from the Hemweg area [79]. The hydrogen will be stored in salt caverns or empty gas fields.

The constructed model approximates the operation and performance of the Hemweg 9 Gas Turbine. The CCGT of Hemweg 9 has a capacity of 440 MW_e [80]. The GT exists of the Siemens F-Class heavy-duty GT (SGT5-4000F) with a gross power output of 292 MW. For the ST, the Siemens two-flow low-pressure ST (SST5-5000) is used. The SST5-5000 consists of three STs operating at different pressure stages; High-Pressure (HP), Intermediate-Pressure (IP) and Low-Pressure (LP) ST. The power plant initially just creates electricity, but it is also planned to provide heat. The plant is equipped with a single-shaft CCGT, both the gas and STs drive the generator via a single shaft.

The system is modeled in Aspen Plus model [36]. Aspen plus is originally a chemical process simulator that allows building a process model based on building blocks. The building blocks represent modules of a process design and calculate the performance of these processes given the operating conditions. Multiple studies achieved a realistic representation of the operation of an rSOC [16] [61]. The constructed Aspen model of the CCGT will be compared with a THERMOFLEX model. THERMOFLEX covers both design and off-design simulation and is commonly used to model all types of power plants, including combined cycles [81]. However, the Aspen Plus was selected to incorporate the electrochemical model of the rSOC because THERMOFLEX is not capable of doing so. This requires making concessions in the simulation of the CCGT results. Aspen Plus does not have a standard procedure for off-design simulations of gas cycles. To still approximate these effects, an isentropic efficiency correction curve was applied which will be elaborated on in the coming section. The coming section explains the similarities as well as the differences in performance. Chapter 8 further explains the limitations and recommends

follow-up research on how to counter these limitations.

4.1.1. Computer Model CCGT

The model can be divided into three parts: compressor, combustion chamber and turbine. Because the theory was explained in Chapter 2, the following section solely focuses on the assumptions of the constructed GT model. The model is based on the design point 443.6 MW gross power THERMOFLEX model, referred to as the reference model, obtained through Vattenfall which can be found in the attached Confidential Appendix Page 1 to 3¹. The representation of the CCGT has been converted and simplified to the Aspen model which is integrated with the electrochemical model. The conversion and simplification of the CCGT model are defended in the upcoming section. The constructed GT system overview is schematically depicted in Figure 4.1.

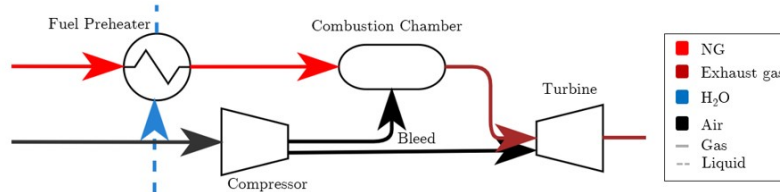


Figure 4.1: Aspen Gas Turbine system overview.

Assumptions The Aspen Plus model of the CCGT uses the standard ISO conditions 15 °C, 1.013 bar, and 60% relative humidity. The model applies an individual isotropic and mechanical efficiency for the compressor and turbine, and a complete combustion in the combustion chamber was assumed. Finally, all pressure drops in the components are conforming the reference models mentioned in the Confidential Appendix Page 2.

Table 4.1a lists the input parameters and operating conditions of the Siemens SGT5-4000F as defined in the reference model. The pressure ratio was retrieved from Siemens [13]; the isotropic efficiency, mechanical efficiency and the bleed fraction of the compressor and turbine from the work of Oudenalder [14]. Table 4.1b lists the high-calorific natural gas composition that fuels the GT, the heating values were retrieved from Aspen plus.

Table 4.1: Gas turbine system input.

(a) Input of GT model. Sources: Confidential Appendix page 1 to 3, Siemens [13] [14].

Parameter	Value
m_{fuel} [kg/s]	15.93
m_{air} [kg/s]	672.8
Pressure ratio [-]	18
$T_{\text{fuel,in}}$ [C]	156
p_{fuel} [bar]	39.6
Isentropic efficiency turbine [%]	92.5
Isentropic efficiency compressor [%]	87.0
Generator design efficiency [%]	99.0
Bleed fraction [-]	0.0779
LHV_{fuel} [kJ/kg]	45,753

(b) Molar gas composition of high-calorific natural gas [%].

Component	Composition [%]
CH4	88.4
C2H6	5.08
N2	3.24
C3H8	1.42
CO2	1.11
C4H10	0.29
C5H12	0.15
C6H14	0.09

Validation To validate the Aspen model, the design point (at maximum gross power) was compared with sources provided by Vattenfall and found in the literature. The results are listed in Table 4.2, where the last column defines the largest difference between the Aspen model and the reference models.

¹Because some of the information in this research is based on confidential information provided by Vattenfall, not every source is visible to the reader. Therefore some sources are mentioned in a Confidential Appendix so that the reviewers of this paper can verify them. Nevertheless, the key data points are mentioned in the text and are occasionally normalized which enables the results to be interpreted

Figure 4.2 shows the heat and mass balance output of the constructed Aspen model. The efficiency of the GT in the Aspen model is structurally lower than in the reference models. The absolute difference in efficiency differs the most with the outcomes of the simulation of Oudenalder [14] by -0.4% which is -1.27% relative to the efficiency of in Aspen Plus model. The difference can be explained by the accompanied higher exhaust temperature of the Aspen model or because of the different inserted fuel composition. Based on the slight deviations in the results, it can be concluded that the GT in Aspen is reasonably in agreement with the reference model and models found in the literature.

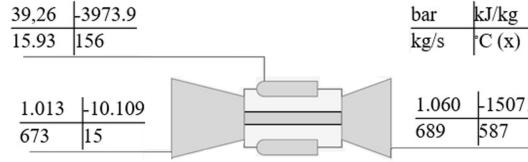


Figure 4.2: Heat and mass balance of GT.

Table 4.2: GT validation. The Δ [%] shows the biggest difference. The underlined value denotes with which Δ [%] calculates the difference. *CA = Confidential Appendix **Difference is calculated in Kelvins [K]. ***Model uses low calorific natural gas. Sources on sequential order: Appendix Page 2, 13 and 15, [13], [14].

Parameter	CA* Page 2	CA Page 15	Siemens	Oudenalder	Aspen	Δ [%]
P_{gross} [MW]	-	288	<u>288</u>	290	287	-0.35
η_{gross} [%]	-	39.5	39.5	<u>39.9</u>	39.4	-1.27
$T_{exhaust}$ [C]	-	<u>577</u>	580	579	587	1.16**
m_{fuel} [kg/s]	15.93	-	-	19.12***	15.93	-
$m_{exhaust}$ [kg/s]	689	-	<u>688</u>	690	689	0.10

Steam Turbine

The construction of the STs is divided into three main modules: the turbines, the heat recovery and the pumps. Figure 4.3 depicts the schematic system overview of the three combined modules. The design point of the CCGT is eventually validated using the reference model of the Confidential Appendix Page 2, the model of Oudenalder [14], and the data provided by Siemens [13]. Figure 4.3 shows the schematic representation of the system. The three different pressure level HRSGs (HP, IP, LP) merged the Super Heater/Reheater (SH) (RH), Evaporator (Evap), Economizer (Eco) and Degassers. The condenser is positioned sequentially to the LP ST. The condensate preheater (CPH) preheats the water before entering each pressure level HRSG

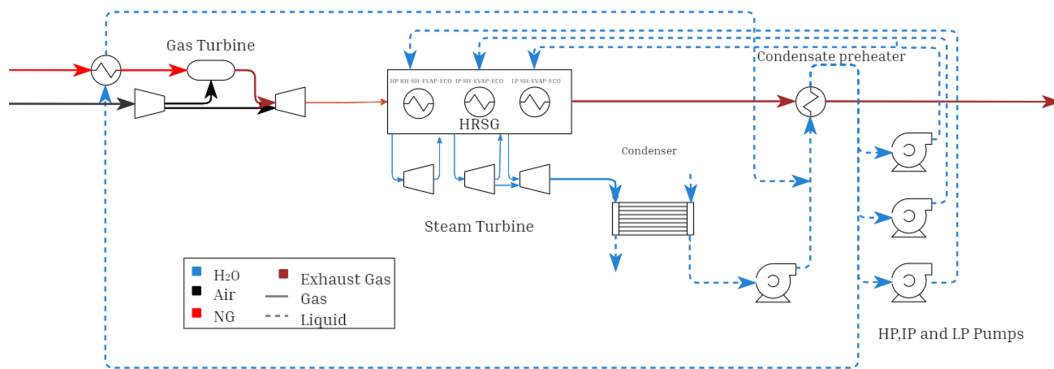


Figure 4.3: Steam Turbine Aspen system overview.

Assumptions The HRSG heat exchangers were placed in series. The pressure drops of the three pressure levels HRSGs take into account the merged systems. The total pressure drop of each pressure level HRSG was calculated by subtracting the pressure of the outgoing superheater stream from that of the incoming economizer stream, retrieved from the Confidential Appendix Page 2. This simplification was

applied to the HRSG of each ST which greatly reduced the complexity of the heat exchanger network. The heat exchanger network additionally consists of the condenser, the Condensate Preheater (CPH) and the fuel preheater.

The current setup monitors the temperature of the GT exhaust stream prior to and after the HRSG. The total extracted heat from the GT exhaust stream is calculated from the heat and mass balance. The assumption of in-series setup results in information loss of exergy losses of the individual HRSG's heat exchangers. The total exergy losses over the total HRSG module can still be measured because the model generates the heat and mass balances of the incoming and outgoing streams of the total HRSG that matches the reference model.

The low-pressure ST (LP ST) expands the steam to conditions that cause condensation of water. The maximum allowable amount of condensate is 10% which prevents droplet formations [47]. The vapor-liquid mixture is condensed to saturated water in the condenser. The condenser uses a cold water utility, functioning as a cold sink resulting in exergy losses.

After the CPH, the combined water stream is split into four streams that either enter the HRSG, at the three corresponding pressure levels or are used to preheat the GT's fuel. The Aspen model calculates the split ratios to match the mass flow reentering the STs to represent a closed system. Four pumps regulate the corresponding pressure and make up for the pressure drops in the system.

Input The inputs of the ST system are set to match the incoming and outgoing mass flows, pressures and temperatures to the reference model provided. The isentropic efficiency was adjusted to attain the same output temperatures as the reference model while maintaining the pressure ratio.

Table 4.3: Steam turbine input and design parameters retrieved from the reference model Confidential Appendix Page 2. *The isentropic efficiency was calculated to match the outlet temperature of the reference model. **The mechanical efficiency was retrieved from Oudenalder [14].

Parameter	HP	IP	LP
P_{in} [bar]	128.3	29.45	4.432
Pressure ratio [-]	3.88	6.94	127
T_{in} [C]	565	565	287
m_{steam} [kg/s]	77.56	89.99	100.6
Isentropic efficiency [%]*	91.7	94.5	92
Mechanical efficiency [%]**	99.8	99.8	99.8

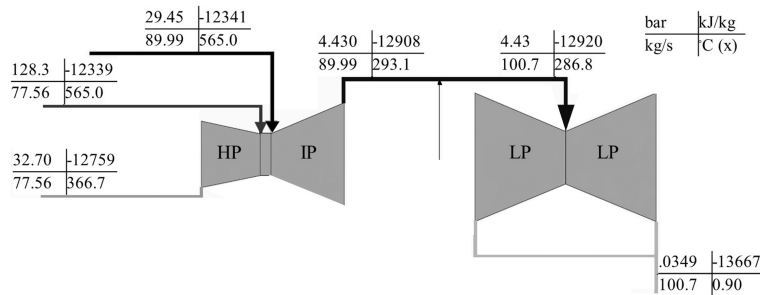


Figure 4.4: Heat and mass balance of ST.

Validation The validation is based on the reference model of the Confidential Appendix Page 2 and the THERMOFLEX of Oudenalder [14]. The output in Table 4.4 is defined as gross power, the net power of the generator can be calculated by correcting the gross power by 1% which corresponds to the generator losses of the reference model. The exhaust temperature was retrieved from the heat and mass balance of the Diemen 34 CCGT CHP plant mentioned in the Confidential Appendix Page 14.

The Diemen 34 power plant is, similar to the Hemweg 9 power plant, composed of the SGT5-4000F GT and SST5-5000 ST. When operating solely in power generating mode, the operating conditions plant is similar to the Hemweg 9 Power plant [77]. Consequently, the same exhaust temperature was assumed since no other sources were available.

The validation shows a structural surplus in the power output of the ST, especially at the first turbine. The difference may be due to the exclusion of an HP to IP bleed. In the reference model, the input and output mass flows of the HP ST do not seem to match although the flowsheet does not indicate a bleed to the IP ST. The final power output differs by 0.63% because the surplus of the ST is compensated by the deficits of the GT. The efficiency drop varies from the efficiency drop because THERMOFLEX uses a higher LHV (+0.1%) for the same gas composition.

Despite the differences in the results between the Aspen and the THERMOFLEX model, THERMOFLEX was not able to model the electrochemical rSOC. As a result, Aspen Plus had to be used with which an attempt is made to simulate the CCGT, by matching the temperature and pressure of the gas and STs. This allows examining the integration between the SOFC and CCGT with the assumption that the Aspen Plus model matches sufficiently.

Table 4.4: Aspen model output in comparison with the provided reference model. The output is defined as gross power. $\Delta\%$ is calculated based on to the reference model. *Gross power including the Balance of Plant power consumption **The exhaust temperature was retrieved from the heat and mass balance of the Diemen 34 CCGT CHP plant.

Parameter	Aspen Model	Reference model	Oudenalder	Δ [%]
$P_{ST,HP}$ [MW]	31.0	28.4	-	9.15
$P_{ST,IP}$ [MW]	50.9	49.6	-	2.62
$P_{ST,LP}$ [MW]	75.0	73.6	-	1.90
$P_{ST,tot}$ [MW]	156.9	151.6	146.1	3.50
P_{GT} [MW]	286.6	292.1	284.7	-1.88
P_{CCGT}^* [MW]	440.9	443.7	430.8	-0.63
$T_{exhaust}$ [C]**	90.8	90.2	-	0.67
η_{Gross} LHV [%]	60.5	60.6	59.3	-0.17

Off-design Operation

During the second comparison (Optimization case 2A versus Base case 2A), the proposed SOFC-CCGT system is compared to the original CCGT while the power output of the proposed SOFC-CCGT system is equalized to that of the original Hemweg 9 CCGT. For off-design performance, the Aspen model implements the operating conditions of the 288 MW THERMOFLEX reference model of the Confidential Appendix Pages 7 to 9. As in the previous construction of the full-load Aspen model, the model copied the mass and heat balances of the GT's and ST's incoming and outgoing streams. The pressure ratios and the isentropic efficiency of the STs are retrieved from the flowsheet of the Confidential Appendix pages 7 to 9.

Validation Again, the HP ST works up more power that the reference model but now in lesser proportions. The efficiency of the Aspen model differs by 1% from the THERMOFLEX model. Unfortunately, the exhaust temperature of the reference model was not provided.

Table 4.5: Aspen model output in comparison with the provided 288 MW reference model. The output is defined as gross power. *Gross power including Balance of Plant's power consumption.

Parameter	Aspen Model	Reference model	Δ [%]
$P_{ST,HP}$ [MW]	23.6	22.3	6.01
$P_{ST,IP}$ [MW]	42.6	42.4	0.42
$P_{ST,LP}$ [MW]	54.9	54.2	1.39
$P_{ST,tot}$ [MW]	121	119	1.91
P_{GT} [MW]	166	169	-1.96
P_{CCGT}^* [MW]	285	288	-1.06
$T_{exhaust}$ [C]	93.0	-	
η_{Gross} LHV [%]	56.8%	57.4%	-1.01

The power output of the part load CCGT 288 MW together with the power of the SOFC 100 MW is unlikely to add up to the required 441 MW even if the synergies are taken into account. To still approach the required power output, the capacity of the CCGT is proportionally scaled by approximately 10% depending on the additional power required, which is will be determined in the optimization process. Due to the indirect integration of the SOFC and GT, the part load performance is simpler to manage without structural changes of the system setup[34]. However, the decrease in load causes the CCGT to deviate from the optimal configuration. Unfortunately, there is no reference THERMOFLEX model that provided exactly the right power output. To still approach the deviating performance from the provided reference model, the load correction curve of natural gas-fed CCGTs of Brouwer et al. [15] was applied. The curve was determined using a regression of load-efficiency curves from multiple studies. The associated R^2 value is 0.88.

The Aspen model adopts the load correction by correcting the isentropic efficiency of the turbomachinery depending on the load. The load correction factor y corrects the isentropic efficiency of the turbine based on the normalized load factor x compared to the maximum load of the turbine. The fuel mass flow, air mass flow and recirculating steam were scaled proportionally to the load factor x . The non-proportional deviations in the heat balance were approximated with the load correction factor. The limitations of this approximation are further elaborated on during the discussion of the limitations of this work in Chapter 8.

Figure 4.6 shows the result of the implementation of the correction curve into the Aspen model compared to the reference models in the Confidential Appendix Page 1 to 9. The data points were derived from the provided THERMOFLEX models. The line between the data points is a linear interpolation that can only be used for an indication of the differences between the Aspen model and THERMOFLEX models.

The performance of the Aspen model agrees well with the data points from the reference models agrees well with the Aspen model. The largest difference between the Aspen model and the linear interpolation of the data points does not exceed 1.5%. Especially between 284 and 350 MW, the Aspen model agrees well with the data points. This range is needed for the increase of the combined SOFC CCGT capacity to the required 441 MW.

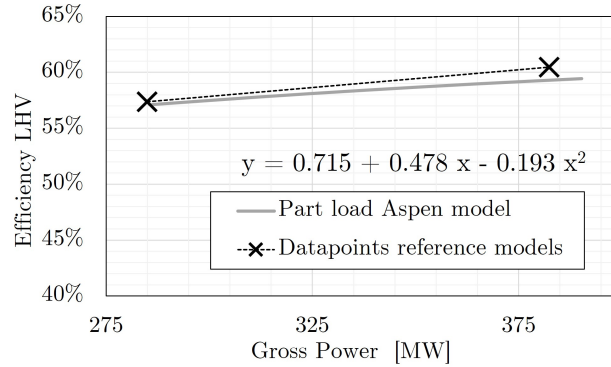


Table 4.6: Efficiency of the CCGT Aspen model compared to the provided reference THERMOFLEX model during part load operating with the applied load correction curve of Brouwer et al.[15].

Output Hemweg 9 CCGT: Full Load Operation (Used in Base Case 1A and 2A)

The simulation of the Hemweg 9 CCGT at full load has an exergy efficiency of 57.7%, it produces 440.6 [MW] electricity while emitting 0.336 CO_{2e} [t/MWh]. The exergy Sankey diagram represents the exergy flows of the full load system expressed as a ratio of the total exergy input of the fuel. This research utilizes exergy-based Sankey diagrams for the comparison of the computed cases. Sankey diagrams based on the exergy balance offer special advantages in effectively locating potential areas for improvement. Sankey energy diagrams fall short of meeting this objective [82]. At the current exergy

Sankey diagram in Figure 4.5, the exergy input of Exergy In, Fuel to Combustor, and Heat to Working Fluid/Gas are all 100%, which seems redundant but during the SOFC-CCGT integration, this notation will be useful to determine the differences between the systems.

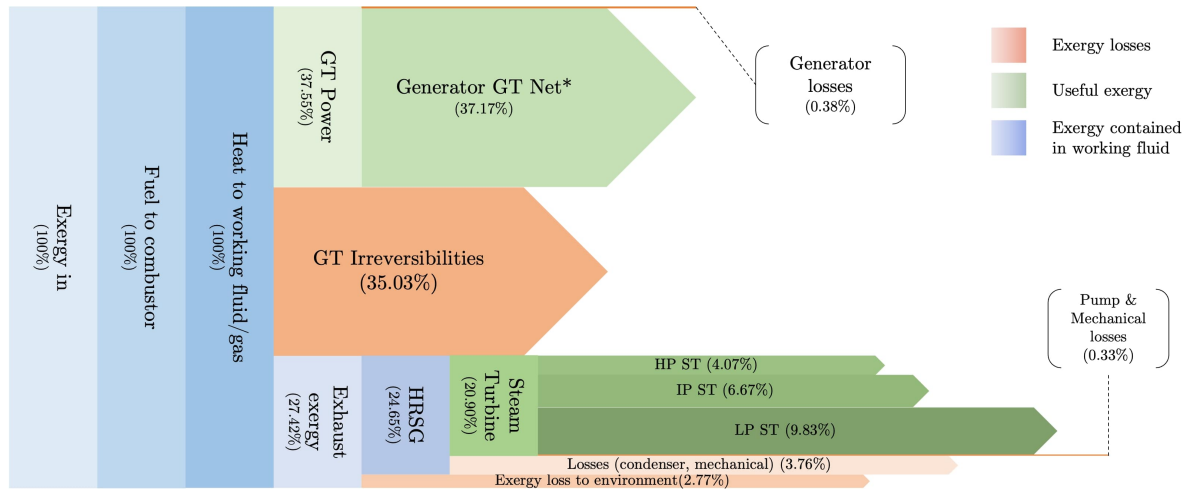


Figure 4.5: Sankey exergy diagram of Hemweg 9 CCGT full load, used in Base case 1A and 2A. *Net = The power consumption subtracted from the power generation.

4.1.2. Computer Model CCGT CHP

Siemens, in cooperation with Vattenfall, has proven that the Hemweg 9 power plant is capable of producing heat by tapping steam and water from the CCGT to heat the DHN feedwater. The system would be flexible enough to switch between CHP and power production mode. The implementation of the bleed is achievable at low costs and the system is flexible so the heat production can easily be scaled to deliver heat according to the demand [77]. The Aspen model implements the modifications of the Confidential Appendix Page 13 which represents the modifications of the full load CCGT reference model to the planned CCGT CHP plant. The CCGT CHP supplies the DHN by transferring the heat of two streams.

The first is to impose a bleed at the IP of the LP turbine which temporarily extracts hot steam from the system [55]. This hot steam heats the circulation DH feedwater, after which the condensed water is pressurized and inserted into the CPH. The second heat source is drained from the water stream outgoing from the CPH. After providing heat to the DHN, the water stream, like the bleed water stream, is pumped into the system at the CPH with equal pressure. Both returning water streams end up at 65 °C with which they are fed into the CPH. The water mass flow of the DHN feed is adjusted via an energy balance to increase the return temperature of the DHN water to the required 110 °C.

The following list of modifications to the Aspen flowsheet was implemented to represent the provided THERMOFLEX model. Figure 4.6 shows the implementation of the modifications.

1. The CCGT exhaust temperature was aimed at 80 °C.
2. Adding a water pump to increase the returning pressure of the condensed water.
3. The discharge pressure of the LP-ST is decreased to 0.0184.
4. Insert an IP bleed factor of 0.379 and the CPH water split of 0.086 to supply the heat to the DHN.
5. Insert an HP bleed to the IP of 0.079.
6. Activation of the Calculation block for the DHN water mass flow to achieve the right DHN feed temperature and assure the minimum temperature limit.

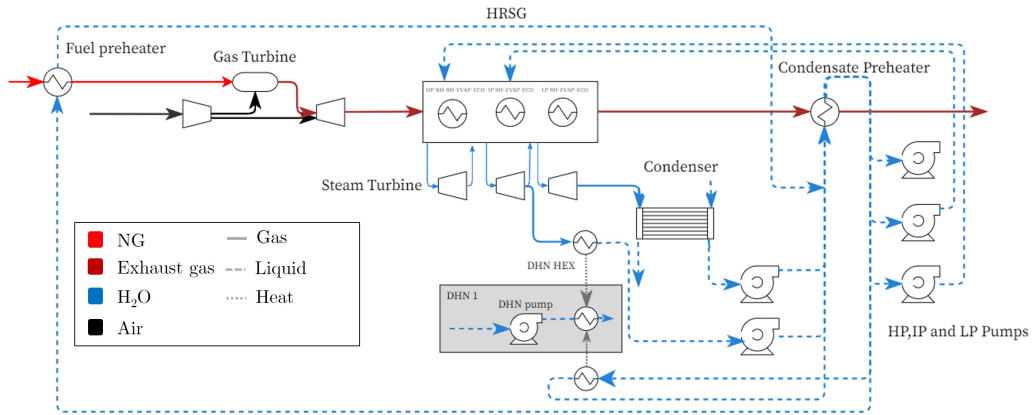


Figure 4.6: Schematic visualization of the planned CCGT CHP Hemweg 9 which defines Base case 1B and 2B.

Validation

Table 4.7 compares the heat reference model with the constructed aspen model. A design point THER-MOFLEX model was provided, which has a net power output of 412.6 MW_e and 100 MW_{th} , found in the Confidential Appendix Page 13. Since the same operating conditions of the GT were applied, the power output of the GT was copied from the simulation of the original CCGT. The total power out differs by $+1.0\%$ while the heat generation is 3% higher. Additionally, the exhaust temperature is slightly below that of the reference model and the efficiency is 1.07% higher.

Table 4.7: Aspen model output with heat production compared with the provided reference heat model. The output is defined as gross power. *The CCGT total power is including Balance of Plant power consumption.

Parameter	Aspen Model	Reference model	Δ [%]
$P_{ST,HP}$ [MW]	30.3		
$P_{ST,IP}$ [MW]	53.3		
$P_{ST,LP}$ [MW]	49.3		
$P_{ST,tot}$ [MW]	132.9		
P_{GT} [MW]	286.6		
P_{CCGT} [MW]	416.8	412.6	1.00
$T_{exhaust}$ [C]	79.7	80.0	0.11
Q_{DH} [MW]	103	100	3.00
η_{CGross} LHV [%]	57.2	56.6	1.07

Output Hemweg 9 CCGT CHP: Full Load Operation (Used in Base Case 1B and 2B)

The simulation of the planned Hemweg 9 CCGT CHP at full load has an exergy efficiency of 57.7% , it produces 416.6 MW electricity and 102.7 MW heat while emitting $0.285 \text{ CO}_2e \text{ [t/MWh]}^2$.

²The calculation includes the electricity and heat generation

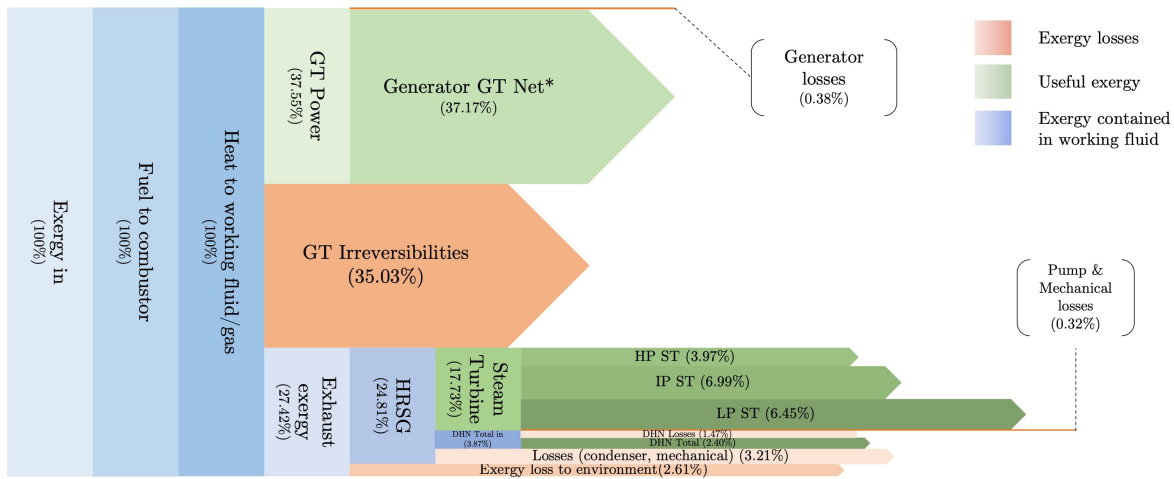


Figure 4.7: Sankey exergy diagram Hemweg 9 CCGT CHP full load, used in Base Case 1B and 2B. *Net = The power consumption subtracted from the power generation.

4.2. rSOC

The zero-dimensional rSOC model of Hauck et al. [16] forms the basis of the model and has been extended to meet the requirements of this work. Hauck et al. calibrated the model by comparing experimental data found in the literature. The resulting model perfectly simulates the cell behavior under various operating conditions and fuel compositions. Because of this flexibility, the model allowed sensitivity analyses to determine the optimal operating conditions. Thereby, it suits the requirements for the optimization study. Matlab was linked to the process modulation in Aspen Plus to produce the voltage analysis. The linked models managed to generate a realistic representation of the system behavior and could analyze various operating conditions.

4.2.1. Stack Assumptions

The following list summarizes the assumptions regarding the SOC model:

- The SOC operates at steady state conditions.
- Zero-dimensional cell representation.
- Uniform SOC operating temperature. A variable sweep gas flow maintains the temperature of the cell. The system energetically balances the exothermic and endothermic reactions.
- Uniform SOC operating pressure. Negligible pressure drop in the cell for the electrochemical model so that the difference in the inlet and outlet pressure does not affect the cell voltage.
- Ideal gas law.
- The SOC and heat exchangers are isolated.
- Homogeneous and isotropic material properties.
- Negligible potential and kinetic energy effects.
- No gas leakage.
- The bulk concentrations determine the concentration overpotential. The bulk concentration is assumed to be constant along the fuel channel and equal to the average of the intake and outlet concentrations.
- The average temperature of the inlet and outlet of the cell determine the ohmic resistance.

4.2.2. Power

Hauck et al. [16] constructed a zero-dimensional rSOC which allowed the model to simplify the electrochemical calculations while producing representative results. The current J [A] and the difference in Gibbs energy flow [J/s] between the cell's incoming and outgoing streams determine the Nernst voltage:

$$\Delta\dot{G} = \dot{G}_{FE,in} - \dot{G}_{FE,out} + \dot{G}_{OE,in} - \dot{G}_{OE,out} \quad (4.1)$$

$$U_{Nernst} = \frac{\Delta\dot{G}}{J} \quad (4.2)$$

Equation 4.3 states the calculation of the current by multiplying FU , the fuel flow \dot{n} [mol/s] at the input of the cell (H_2 and H_2O for SOFC and SOEC mode respectively), the stoichiometric value (two electrons per mole of H_2 OR H_2O), and the Faradaic constant F [C/mol].

$$J_{cell} = \dot{n}_{H_2} * 2 * F * FU \quad (4.3)$$

Adding the calculated overpotentials to U_{Nernst} makes the cell voltage V_{cell} [V]. Multiplying the calculated cell voltage to the current flowing through the cell J_{cell} [A] results in the electrical power of a cell $P_{e,cell}$ [W].

$$P_{e,cell} = J_{cell} * V_{cell} \quad (4.4)$$

The required stack power is achieved by placing the SOCs in series, resulting in an increase in the stack voltage. The total stack power is calculated by multiplying the cell voltage with the number of cells N :

$$P_{e,stack} = J * N * V_{cell} \quad (4.5)$$

It is assumed that total surface area does not affect the performance of the cell when all other operating conditions are maintained [16]. Therefore, the total surface area will be used to scale the systems' required power while maintaining the current density j [A/m²](Equation 4.6). The quantity of the supplied fuel at the inlet of the system scales accordingly to the total area to maintain the current density. The system was optimized to operate at this determined load. The variation of fuel mole flow is used to determine the current density during part load operation while maintaining the total cell area.

$$P_{e,stack} = j * A_{cell} * N * V_{cell} \quad (4.6)$$

4.2.3. Operating Conditions

The operating conditions - current density, temperature, pressure, fuel composition and sweep gas composition - strongly correlate with the performance of the SOC. Hence the determination of these operating conditions plays a central role in the optimization process. Except for the latter operating conditions, all other conditions are assumed to be fixed. The operating conditions of the Base case are listed in Table 4.8. The operating conditions were retrieved from Hauck et al. (2017) [16] and the conclusions from Chapter 3.

Table 4.8: Operating conditions validation SOC.

Parameter	Value	Unit
Stack temperature	850	C
Stack pressure	1.013	Bar
Current density	10.000	A/m ²
Fuel utilization	0.8	-
Fuel composition	1 H_2 : 1 H_2O	-

4.2.4. Cell Parameters

Hauck et al. [16] based the geometric parameters on the experiments performed by Tjaden et al. [83]. However, Hauck et al. changed the thickness of the cell parameters to adjust for the strong deviations of the diffusion losses. The large difference in the electrolyte layer overestimates the concentration overpotential. Tjaden et al. modeled the support layer of the fuel electrode similar to that of the oxygen

electrode, which proved to be incorrect because the support layer of the fuel electrode is significantly more porous to compensate for the thinner electrolyte layer. Therefore, the fuel electrode thickness of the model was fitted with the results of the experiments by Kazempoor et al. [1]. The single cell active area is adjusted to 0.01 m^2 so that the number of cells is reduced [72]. Since the active area of the cell does not affect the performance of the system [17], the adjustment has no further consequences. Table 4.9 lists the cell parameters after correcting for the overestimation of the concentration overpotentials.

Table 4.9: Input parameters SOC [16], except of the A_{tot} [17].

Parameter	Value	Unit
r_{ohmic}	0.057	$\Omega \text{ cm}^2$
$\sigma_{0,el}$	333.3	$\Omega^{-1} \text{ cm}^{-2}$
$E_{act,el}$	85,634	J/mol
δ_{el}	$1.25 \cdot 10^{-5}$	m
$\delta_{fuel,eff}$	$3.2 \cdot 10^{-5}$	m
δ_{oxygen}	$1.75 \cdot 10^{-5}$	m
A_{tot}	100	cm^2
r_p	$1 \cdot 10^{-6}$	m
η	0.3	-
τ	5	-
γ_{fuel}	$1.344 \cdot 10^6$	A cm^{-2}
γ_{oxygen}	$2.051 \cdot 10^5$	A cm^{-2}
$E_{act,fuel}$	$1 \cdot 10^5$	J/mol
$E_{act,oxygen}$	$1.2 \cdot 10^5$	J/mol

4.2.5. SOFC Computer Model

The constructed SOFC model exists of a composition of several flowsheets found in the literature that are adjusted to conform to the needs of a hydrogen-based SOFC. The schematic flowsheet of the SOFC is depicted in Figure 4.8. A mixture of hydrogen and steam enters the system at the fuel electrode, and the required oxygen - supplied by pure oxygen or air in the sweep gas - enters at the oxygen electrode.

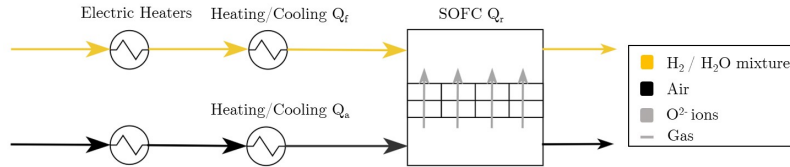


Figure 4.8: SOFC schematic overview.

Electrochemical

In contrast to the work of Hauck [16], the SOC in this work solely converts hydrogen instead of multiple hydrocarbons. Unlike a hydrocarbon-based system, a hydrogen-based SOFC does not have to reform its fuel to prepare for the electrochemical reaction. Consequently, the reformer was removed. By omitting the reforming reaction, the system requires more cooling capacity because the endothermic reforming reaction no longer absorbs heat. The extra cooling capacity results in a larger sweep gas flow rate.

The required oxygen mole flow for the formation of water depends on the hydrogen flow, fuel utilization factor FU and the stoichiometric factor 0.5 which is expressed by Equation 4.7. Since the required sweep gas, consisting of air or oxygen, exceeds the required mole flow of oxygen for sustaining the reaction, the incoming sweep gas stream was split to resemble the oxygen ions permeating the electrolyte required for the reaction (Equation 4.8). The split factor ensures that the outflow of the fuel electrode contains no oxygen molecules. This simulates the driving force of the permeation of oxygen ions into the electrolyte whereby only the right amount of oxygen ions diffuse through the electrolyte relative to the amount of reacting hydrogen. The remaining oxygen leaves the SOFC at the outgoing oxygen

electrode stream.

$$\dot{O}_{2,required} = \dot{H}_2 * FU * 0.5 \quad (4.7)$$

$$SF = \dot{O}_{2,required} / \dot{O}_{2,OE,in} \quad (4.8)$$

The Aspen Gibbs Reactor performs the electrochemical reaction of hydrogen and oxygen ions forming water. The Gibbs Reactor minimizes the Gibbs free energy of the mixture. The concentration of the mixture leaving the Fuel Electrode depends on the incoming gas compositions and the fuel utilization factor FU . The FU determines the amount of converted hydrogen (or water in the case of SOEC mode). The ratio of the unreacted fuel affects the system efficiencies because the residual hydrogen possesses chemical exergy that leaves the system's boundary, thus contributing to the exergy losses. The optimal setup minimizes these losses and utilizes the residual hydrogen. However, the FU is considered an immutable design specification and was set according to Hauck et al. [16].

$$FU = \frac{\dot{n}_{H_2,converted}}{\dot{n}_{H_2,supplied}} \quad (4.9)$$

Thermal Management

The thermal management of a SOFC ensures the maximum temperature gradient in the cell. The brittle material in the SOCs is unable to withstand large temperature distributions. Therefore, the cell maintains a maximum temperature gradient of 100 °C to avoid impermissible thermal stresses [67]. The cell's temperature is maintained by varying the sweep gas flow rate and sweep gas temperature. During SOFC mode, a large amount of heat is released during the electrochemical reaction ($\Delta g - \Delta h = 13.24$ kJ/mol under standard conditions). During SOFC mode, the cell always operates in the exothermic region regardless of the cell voltage. To cool the cell, both the incoming fuel and airflow enter the system at 100 °C below the operating voltage of the SOFC [67]. The heat of reactions Q_r is compensated by the heating of the fuel Q_f and air Q_a by cell walls. The required sweep gas flow rate follows from Equations 4.10, 4.11 and 4.12. The gasses leave the system at exactly the desired operating temperature.

$$Q_a = -(Q_f + Q_r) \quad (4.10)$$

$$Q_a = \dot{m}_{air} (h_{SG,\Delta T=-100} - h_{SG,\Delta T=0}) \quad (4.11)$$

$$Q_f = \dot{m}_{fuel} (h_{Fuel,\Delta T=-100} - h_{Fuel,\Delta T=0}) \quad (4.12)$$

$$Q_r = \Delta G - \Delta H \quad (4.13)$$

The conducted adjustments of the flowsheet of Hauck et al. separates the thermal management from the electrochemical section. The electric heaters increase the temperature of the incoming gasses to $\Delta - 100$ °C compared to the operating temperature. The Heating/ Cooling heat exchanger in Figure 4.8 represent the heating of the gas by the walls Q_a and Q_f . The Gibbs Reactor produces the heat of Reaction Q_r . The heat management of Amaldi [84] inspired the construction of this work's flowsheet. However, this works flowsheet did not require a reformer for internal cracking since solely hydrogen was inserted.

4.2.6. SOEC Computer Model

The SOEC was constructed following the same approach as the SOFC. In contrast to the model of Hauck, the electrochemical active CO_2 was left out, leaving steam as the only electrochemical active specie. The components resembling the reverse water-gas shift were discarded. The reverse water-gas-shift reaction produced heat that was utilized by the heat-consuming water electrolysis reaction. Consequently, the heat management required a careful design ensuring the maximum allowable temperature gradient and

providing enough heat to sustain the reaction.

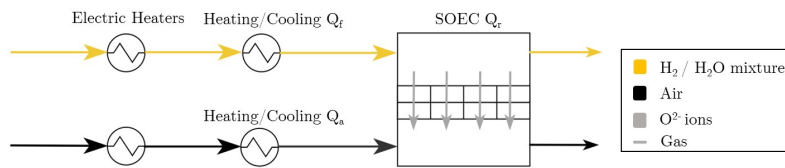


Figure 4.9: SOEC schematic overview.

Electrochemical

The electrochemical reaction of the formation of water and oxygen of water occurs in the SOEC block of Figure 4.8. The amount of water split is proportional to the fuel molar flow \dot{n}_{H_2O} of the incoming H_2 / H_2O stream and the fuel utilization factor FU . The amount of transported oxygen ions from the FE through the electrolyte to the OE is calculated by an oxygen splitter block. The calculation ensures that no oxygen molecules leave the fuel electrode stream so that the Nernst voltage and concentration-dependent overpotentials are not incorrectly affected. Oxygen molecules form at the OE and leave the cell by the Oxygen Electrode outgoing stream. The formed hydrogen and unconverted water are leaving the SOEC at the fuel electrode.

The SOEC is fed by a mixture of water and hydrogen. The insertion of hydrogen sounds controversial, however, it lowers the degradation rate [17] as was discussed in Chapter 3. Section 5.1.1 investigates the implication of the fuel composition on the performance of the cell and the system.

Heat Management

The SOEC operates in endothermic, exothermic or thermoneutral mode depending on the operating conditions which complicate the thermal management of the cell. Again, an incoming sweep gas stream controls the thermal management. The cell's heat consumption or production depends on the cell voltage V_{cell} relative to the thermoneutral voltage V_{tn} . When $V_{cell} < V_{tn}$, the sweep gas exceeds the operating temperature by 100 °C, providing the cell with the required heat to maintain a constant cell temperature.

If the SOEC is operating at $V_{cell} > V_{tn}$, the internal resistance generates heat that exceeds the required heat to sustain the reaction. In this case, the sweep gas must cool the cell to maintain the operating temperature. This is accomplished by varying the sweep gas mass flow and decreasing the gas temperature by 100 °C relative to the operating temperature.

When $V_{cell} = V_{tn}$ the sweep gas only needs to compensate for the heating of the fuel to operate at the prescribed operating temperature. The fuel inlet temperature remained in all cases 100 °C below operating temperature. Only the temperature and the mass flow of the sweep gas affect the performance of the cell.

4.2.7. Validation

The model resulting was, similarly to the work of Hauck et al. [16], compared to the model based on a comparison with Kazempoor's experiments to validate the system. The validation results are depicted in Figure 4.10. The model proved to be capable of approximating the actual behavior of a hydrogen SOC. Thus, the necessary modifications - of changing the heat management and discarding the internal reformers to convert the SOC to a hydrogen-based cell - were successfully conducted. The maximum error is less than 2%.

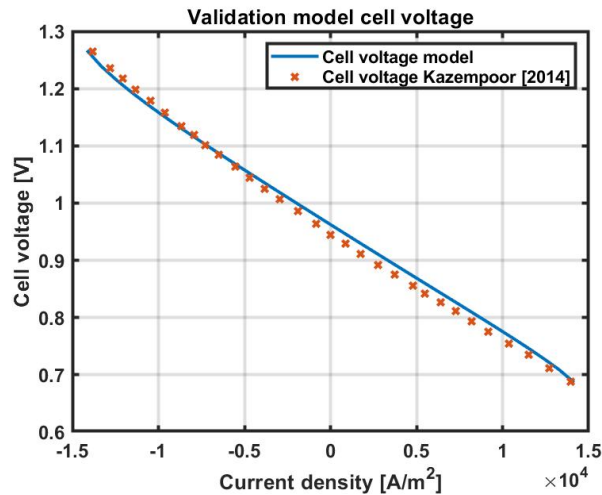


Figure 4.10: Comparison model and experiments [1].

4.3. System level

The components downstream to the SOC, differ from each system since the SOFC is coupled with a CCGT to generate more electricity, and the SOEC is to purification unit to purify the produced hydrogen. The coming sections argue the construction and assumptions of the resulting Base case model. The component-specific assumptions that recur in multiple modules are listed in Table 4.10. All heat exchangers are counter-current flow heat exchangers with a minimum pinch of 5 °C and are assumed to be isolated. External cooling is achieved by cooling water from the environment of 25 °C.

Table 4.10: Assumptions components and storage conditions.

Component	Value	Source
Efficiency [%]		
Pump isentropic	75	[38]
Turbine isentropic	85	[38]
Compressor isentropic	85	[72]
AC/DC converter	95	[38]
Pressure drop [%]		
Heat exchanger	2	[43]
Afterburner	5	[43]
SOC	2	[43]

4.3.1. System Modules

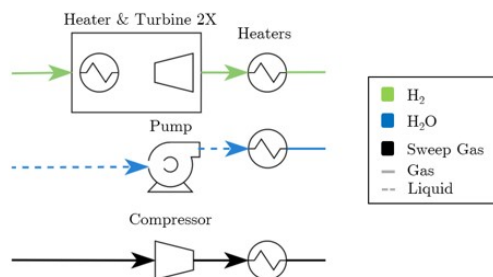
The Balance of Plant is grouped according to their collective function and position relative to the SOC. The following modules divide the entire system: Grid to Stack, Purification, Purification to Grid, and Afterburner. Table 4.11 summarizes the modules with the grouped components. The following paragraphs discuss all assumptions regarding the modeling of the modules.

Table 4.11: Overview of system modules with the consisting system components.

Module	Function	Components
Grid to stack	<ul style="list-style-type: none"> • Applicable for SOFC and SOEC • Aligns the incoming hydrogen, water and air with the operating conditions of the SOC 	<ul style="list-style-type: none"> • Series of turbines and heaters for the hydrogen stream • Pump for the water stream • Heater for the water stream • Air compressor
Purification	<ul style="list-style-type: none"> • Applicable for SOEC • Separates the hydrogen and water 	<ul style="list-style-type: none"> • Condenser • Flash drum • Compressor • Purification membrane • Steam turbine
Purification to Storage	<ul style="list-style-type: none"> • Applicable for SOEC • Pressurizes the hydrogen for the hydrogen backbone 	<ul style="list-style-type: none"> • Series of coolers and compressors
Afterburner	<ul style="list-style-type: none"> • Applicable for SOFC • Burns the residual hydrogen to increase temperature of the exhaust stream 	
Inlet/outlet system	<ul style="list-style-type: none"> • Applicable for SOC • Conditions for the inlet and outlet of fuel, air and water to the system and environment 	<ul style="list-style-type: none"> • Hydrogen • Natural Gas Grid • Electricity grid • District heating network

Grid to Stack

The module Grid to Stack prepares the incoming flows for the SOC. This module ensures the outflow matches the required inflow conditions of the SOC. The flowsheet of the SOEC and SOFC is designed to correspond with each other, so the same components can be used for both functions, decreasing the initial investments.

**Figure 4.11:** Grid to Stack system overview.

Hydrogen Stream The hydrogen originating from the hydrogen grid at 30 bar [85] is brought to the desired operating pressure of the SOC. A series of turbines take advantage of the high incoming pressure by generating power by expanding the incoming hydrogen. The turbines expand the hydrogen with a maximum pressure ratio of 4, resulting in a distributed heat duty and consistent minimum temperatures. The two to three turbines, depending on the operating pressure, distribute the total pressure ratio. Heaters ensure the temperature of the hydrogen not dropping below the ambient temperature so that any impurities do not condense. Initially, electric heaters supply the heat to the hydrogen. Later on, the optimization examines the extent to which heat can be recovered from the system. Electric heaters accommodate the residual heating when the heat exchanger network is incapable to supply sufficient heat.

Water Stream Ambient water enters the system after which a pump pressurizes the water to a pressure slightly exceeding the SOC's operating pressure to compensate for the pressure losses. An electric heater vaporizes the water at 100 to 180 °C depending on the operating pressure. The heaters

ensure that the hydrogen and steam have the same temperature so that mixing exergy destruction is minimized. After mixing, the stream enters the SOC stack. The heat required for the SOC's operating temperature attributes to the SOC's heat duty.

Sweep Gas Stream The sweep gas requires a compressor, no heaters or internal coolers are required. The flow enters the system under ambient conditions. The compression causes the air temperature to increase which partly substitutes for the heating power in the SOC stack. Hence, increasing the operating pressure increases the compression power but simultaneously decreases the heat duty of the cell.

Purification

Pressure swing adsorption (PSA), cryogenic distillation and membrane separation are considered the general methods to purify hydrogen [86]. Commercially available techniques include PSA and cryogenic distillation. However, both are energy intensive in comparison to membrane separation techniques. Membrane separation is a promising solution that produces high-purity hydrogen while limiting energy consumption. Primarily, a series of condensers and vapor-liquid separators was examined but the configuration failed to achieve sufficient purity. Therefore a membrane-based purification system will be adopted that sufficiently approximates the energy requirement and exergy losses based on the flowsheet of Amladi [84].

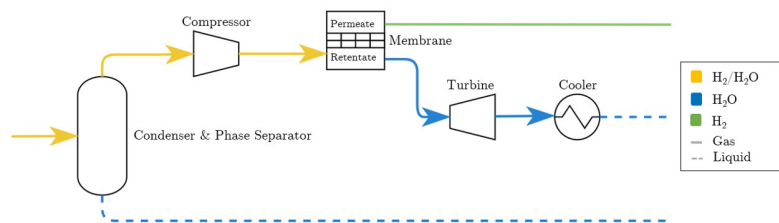


Figure 4.12: Purification system overview.

A condenser and phase separator are used to reduce the amount of steam entering the compressor and membrane. Minimizing the steam leads to lower compression power and pressure losses. The condenser cools the outgoing stream of the SOEC with ambient water resulting in exergy losses. The minimum heat exchanger temperature difference (5 °C) and ambient temperature of the cooling water (25 °C) limits the outgoing condenser streams to 30 °C. Depending on the pressure, water partially condenses at this temperature.

A single compressor ensures the hydrogen/water mix enters the membrane at the specified operating pressure of 10 bar. The incoming hydrogen/water mixture split into the permeate and the retentate stream. The permeate - the purified hydrogen stream that diffused through the membrane - suffers a pressure drop by a ratio of 10 [87]. The retentate - the separated water - leaves the system with a pressure loss of 15 mbar. The membrane conducts a total separation of hydrogen and steam.

A ST recovers the outgoing retentate steam - of 10 bar minus pressure losses - to atmospheric pressure. Before the water steam mixture is disposed of, a condenser reduces the temperature to 30 °C by using ambient water.

Note the impact of the SOC's operating pressure on the purification module power consumption. Higher pressure in the condenser leads to more condensation. More condensate means less steam, reducing the compression power. In addition, a higher incoming pressure reduces the pressure ratio of the purification compressor.

Purification to Grid

The purified hydrogen is cooled and compressed by a series of compressors and coolers. As in the Grid to Stack module, the model maintains a maximum pressure ratio of 4 and the pressure ratio is divided between the two/three turbines. Given the isentropic efficiency, the pressure ratio in combination with the intermittent cooling maintains the temperature below 250 °C for the reduction of compressor power and safety reasons. The hydrogen is fed to the hydrogen grid at 25 °C at a pressure of 30 bar.

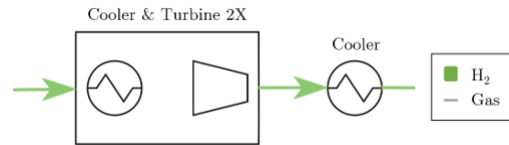


Figure 4.13: Purification to Grid module system overview.

Afterburner

The afterburner uses of the chemical energy stored in the unconverted hydrogen leaving the SOFC to increase the exhaust stream temperature by combustion. The system utilizes the resulting high-temperature exhaust via downstream heat integration. The SOFC converts 80% of the hydrogen which means that 20% of the chemical energy is not being utilized. The streams exiting the oxygen and fuel electrode are mixed in the afterburner and oxidized.

Like the electrochemical reaction, the combustion reaction generates heat. In contrast to the electrochemical reaction, the combustion reaction does not capture the electron transport. As a result, the potential for generating electricity - which is pure exergy - is lost. The afterburner is therefore a major source of exergy loss [34]. However, the afterburner is a relatively simple and inexpensive solution to exploit the unconverted hydrogen [38].

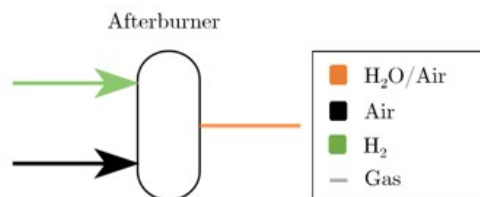


Figure 4.14: Afterburner system overview.

Feed and Product Conditions

Table 4.12 summarizes the feed conditions and product requirements set by the industry. In the Netherlands, Gasunie plans to construct a connection of industries, hydrogen storage facilities, manufacturing areas, and adjacent nations[79]. Therefore, it is assumed that produced and consumed hydrogen can be pumped into and from the hydrogen grid. Determining the best hydrogen storage system falls out of the scope of this work. This assumption simplifies the system by solely considering the expected operating conditions of the hydrogen grid. The transportation temperature is assumed to be the same as a large-scale H₂ tank [72].

Table 4.12: Input and output conditions of streams entering and leaving the system.

Input/output	Parameter	Value	Unit
Natural Gas	Pressure	40 bar	THERMOFLEX reference model
	Temperature	15 C	THERMOFLEX reference model
Hydrogen	Pressure	30 bar	[85]
	Temperature	25 C	[72]
	Purity (minimum)	99.95 Mole %	[85]
DHN	Pressure	10 bar	THERMOFLEX reference model
DHN Supply	Temperature	110 C	THERMOFLEX reference model
DHN Return	Temperature	60 C	THERMOFLEX reference model

4.3.2. Resulting flowsheet

All of the above assumptions result in the initial flowsheet of the SOFC shown in Figures 4.15 and the SOEC in Figure 4.16. In the next chapter, this setup is used to measure the response of the performance of the stack and system to the variation of the operating conditions. During optimization, the flowsheet is modified so that the same components are used for both systems if not mentioned otherwise.

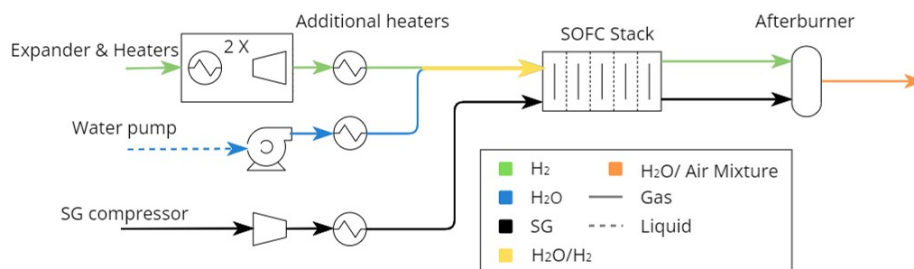


Figure 4.15: Schematic SOFC system overview. During the optimization, the SOFC exhaust flow is connected to the CCGT.

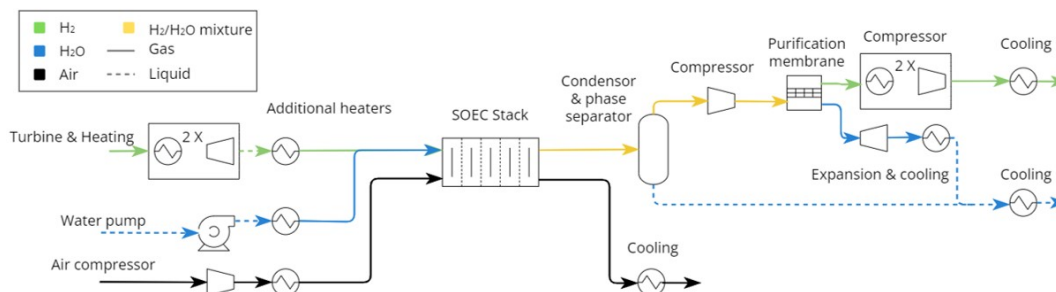


Figure 4.16: Schematic SOEC system overview.

4.4. Aspen Solution Sequence

Figure 4.17 visualizes the summary of the system’s solution methodology for the SOFC-CCGT and SOEC systems. The figure is divided into sequential blocks with an accompanying explanation below the figure. The calculation methodology regarding the SOC is very similar for both modes. Only the cell’s heat strategy - when to use heating or cooling - differs in these blocks. The calculations and convergence of the SOEC end after block 5 from which the results are produced by the tenth block. The SOFC based system is more complicated due to the coupling with the CCGT which requires additional convergence blocks (6 through 9). After this, the result is also computed in block 10.

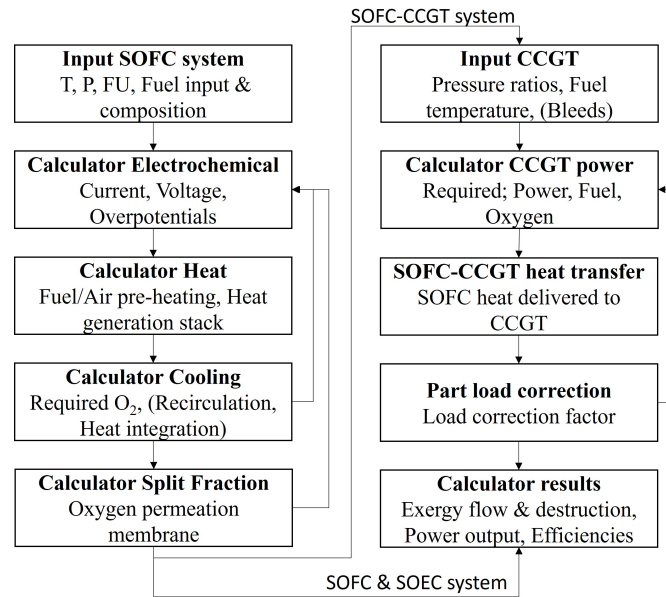


Figure 4.17: Model convergence and solution sequence. Before the heat integration of the SOFC-CCGT the 'SOFC-CCGT heat transfer' is equal to zero indicating that the systems operate separately.

1. **Input** - Through the input block, the operating conditions - required temperatures and corrected pressures due to pressure differences - are distributed throughout the system. In addition, the input block determines the required amount of hydrogen and water based on the total desired Gibbs free energy, fuel utilization factor and fuel composition.
2. **Calculator Electrochemical** - Based on the previous definitions, the current density can be determined. The calculator block calculates the Nernst voltage and the voltage losses from the current density and operating conditions. The outgoing molar concentrations can be determined by the Fuel utilization factor and the incoming concentrations. The calculator block searches for a stable solution using a loop in case of a recirculation stream.
3. **Calculator Heat** - The block calculates the required heat or cooling of the cell by subtracting V_{cell} from V_{th} and multiplying by the current.
4. **Calculator Cooling/Heating** - The model attempts to balance the heat in the stack by varying the incoming sweep gas flow rate. The model repeats the previous two blocks until the heat balance is met.
5. **Calculator Split Factor** - The split factor determines the exact amount of oxygen ions diffusing through the electrolyte to meet the desired fuel utilization. This adjustment changes the outlet concentrations which in turn changes the voltages. A while loop repeats the previous calculations until a solution is found.

From this point, the SOFC and SOEC are different. The exhaust gasses of the SOFC enter the Afterburner but the SOEC outgoing streams are purified and discarded. The SOEC model already possesses all the necessary information to produce the results. The SOFC model continues with the following steps:

6. **Input CCGT** - This input block determines the pressure ratios of the turbines, the fuel preheater temperature and the bleed of the Intermediate Pressure ST. The bleed depends on the amount of heat production for DH. Until the system includes the DHN, the bleed factor of 0 is maintained.
7. **Calculator CCGT power** - The examined Base case or Optimization case affects the fuel consumption. The fuel consumption is adjusted to maintain the GT exhaust temperature to avoid heat crossover effects. During the Cases 'A'³ during exclusive power production, the model maintains 91 °C conforming to the original simulation of the Hemweg 9 CCGT. At the Cases 'B'⁴

³(Base case 1A, Base case 2A, Optimization case 1A, Optimization case 2A)

⁴(Base case 1B, Base case 2B, Optimization case 1B, Optimization case 2B)

during CHP operation, the temperature is decreased to 80 °C. The model adjusts the amount of air to maintain the Turbine Inlet Temperature.

8. **SOFC-CCGT heat transfer** - Heat integration provides the CCGT with heat originating from the SOFC exhaust stream. The Aspen model takes measures to effectively incorporate this heat transfer which is discussed in the next chapter during the heat integration. Without the integration, this step can be neglected. The additional heat results in an increase in downstream GT exhaust temperature that leaves the system.
9. **Part load correction** - When deviating from the Base case models, the model corrects for the part load operation by the application of the isentropic load correction factors for the GT's compressor and turbine, and individual STs. The modification affects the heat balance causing the system to iterate back to 'Calculator CCGT power' to find a stable solution.
10. **Calculator results** - The model possesses all the data to prepare the results.

4.5. Performance Indicators

The system is optimized according to the exergy efficiency. Exergy analysis is a useful tool for effectively optimizing a system, as the system is improved by the further improvement of the major exergy-destructing components. Ranking the components and optimizing the component with exergy efficiency, allows for an effective, systematic approach to increasing system efficiencies and improving cost-effectiveness [47]. Besides, exergy is a perfect parameter to use in combination with economic and environmental impact studies [45].

4.5.1. Exergy Efficiency

The exergy efficiency is derived from the exergy rate balance from Equation 2.34. It is defined as a ratio of the useful recovered exergy divided by the total supplied exergy. The exergy efficiency and exergy destruction form the basis of the exergy analysis. It is used in the parametric analysis to examine the effects of the operating conditions and for determining the optimal system component setup.

Research commonly refers to functional exergy involving the exergy flows that matter in the particular component [88]. The useful exergy is component-specific and thus is the exergy efficiency. This allows for a better analysis of the desired exergy from the relevant input sources. For example, when looking at the useful output of the system, the exergy of the discarded sweep gas (SG) is excluded but the hydrogen produced is included. The useful exergy is component-specific and thus is the exergy efficiency. In this analysis, the relevant exergy flows are explained by component. Electric power is defined as pure exergy. This means that the electricity produced and consumed by the system components is considered directly as exergy. In the Aspen model, the exergy destruction of each component was determined. The total exergy destruction of each module summed the individual components. The different modules correspond to the basic model discussed above.

SOFC-CCGT System

Table 4.13 summarizes the exergy efficiency and exergy destruction of the SOFC-CCGT system. The subscripts *SG*, *NG*, *DH*, *env* and *AB* denote the Sweep Gas, Natural Gas, District Heating, Environment and Afterburner. The rest of the subscripts can be deducted from the System module name. Exergy destruction is defined in [MW].

Table 4.13: Exergy efficiency and exergy destruction of the SOFC-CCGT system.

System module	Variable	Calculation
Exergy efficiency		
SOFC stack	ψ_{SOFC}	$P_{e,SOFC,net}/(\dot{E}x_{H_2/H_2O,stack,in} + \dot{E}x_{SG,stack,in}) - (\dot{E}x_{H_2/H_2O,stack,out} + \dot{E}x_{SG,stack,out})$
SOFC system	$\psi_{SOFC,sys}$	$P_{e,SOFC,sys,net}/\dot{E}x_{H_2,sys,in}$
SOFC-CCGT system	$\psi_{SOFC-CCGT,sys}$	$(P_{e,SOFC,sys,net} + P_{e,CCGT})/(\dot{E}x_{H_2,sys,in} + \dot{E}x_{NG,sys,in})$
SOFC-CCGT +DH system	$\psi_{SOFC-CCGT,sys}$	$(P_{e,SOFC,sys,net} + P_{e,CCGT} + \Delta\dot{E}x_{DH,water})/(\dot{E}x_{H_2,sys,in} + \dot{E}x_{NG,sys,in})$
Exergy destruction		
Grid to Stack	Ed_{GtS}	$P_{e,GtS} + \dot{E}x_{H_2,sys,in} - \dot{E}x_{H_2/H_2O,stack,in} - \dot{E}x_{SG,stack,in}$
Stack	Ed_{Stack}	$P_{e,SOFC,net} + \dot{E}x_{H_2/H_2O,stack,in} + \dot{E}x_{SG,stack,in} - \dot{E}x_{H_2/H_2O,stack,out} - \dot{E}x_{SG,stack,out}$
Afterburner	Ed_{AB}	$\dot{E}x_{H_2/H_2O,stack,out} + \dot{E}x_{SG,stack,out} - \dot{E}x_{AB,out}$
CCGT	Ed_{CCGT}	$P_{e,CCGT,net} + \dot{E}x_{NG,sys,in} + \Delta\dot{E}x_{Cond} + \dot{E}x_{AB,out} - \dot{E}x_{CCGT,exhaust} - \dot{E}x_{HRSOFC,out}$
Exergy losses	Ed_{env}	$\dot{E}x_{CCGT,exhaust} + \dot{E}x_{HRSOFC,out} + \dot{E}x_{Cooling}$

SOFC Stack The exergy efficiency and destruction of the SOFC stack maintain the system boundary of Figure 4.8. The electric power $P_{e,SOFC}$ consists of the power supplied by the stack $P_{e,stack}$ in Equation 4.6 and the additional electric heating $P_{th,SOFC}$ to attain the operating conditions Equation 4.14. When heat integration substitutes for electric heating, a physical exergy flow replaces electric power according to the amount of substituted heat. At $\psi_{SOFC,stack}$, the incoming and outgoing sweep gas and water are included in the formula because of the high temperatures and pressures that possess a significant amount of physical exergy. In contrast to $\psi_{SOFC,sys}$, that excludes the incoming sweep gas and water which are at ambient conditions and thus possess negligible.

$$P_{th,SOFC} = P_{th,SOFC,FE} + P_{th,SOFC,OE} \quad (4.14)$$

$$P_{e,SOFC,net} = P_{e,SOFC} - P_{e,GtS} - P_{th,SOFC} \quad (4.15)$$

CCGT The net energy produced by the CCGT $P_{e,CCGT,net}$ consists of the gross power of the GT $P_{GT,net}$ and ST $P_{ST,net}$ multiplied by the generator efficiency η_{gen} . The $\Delta\dot{E}x_{Cond}$ is the difference between the incoming and outgoing exergy of the condensed water streams. $\dot{E}x_{CCGT,exhaust}$ is the exergy stream leaving the system. In addition, the afterburner supplies the CCGT with heat that is represented by the difference between $\dot{E}x_{AB,out}$ and $\dot{E}x_{HRSOFC,out}$

$$P_{e,CCGT} = P_{GT,net} + P_{ST,net} \quad (4.16)$$

$$P_{GT,net} = P_{Turb} - P_{Com} \quad (4.17)$$

$$P_{ST,net} = (P_{ST,HP} + P_{ST,IP} + P_{ST,LP}) - \sum P_{pumps} \quad (4.18)$$

Balance of Plant The BOP GtS gross power is the sum of the generated power by the three upstream turbines, the required power of the water pump and the air compressor. The total heat required is the sum of heaters $\sum(Q_{e,GtS,heater})$ to increase the hydrogen's temperature and vaporize the water.

$$P_{e,GtS} = \sum(W_{Turbines}) + W_{pump} + W_{SG,comp} - \sum(P_{th,GtS,heater}) \quad (4.19)$$

SOFC-CCGT System Level The net generated electric power of the SOFC CCGT system is expressed as:

$$P_{SOFC-CCGT} = P_{e,SOFC,sys,ne} + P_{e,CCGT} \quad (4.20)$$

SOEC System

Table 4.14 summarizes the exergy efficiency and exergy destruction of the SOEC system. The subscripts correspond to those of the SOFC system, the rest of the subscripts can be derived from the name of the system module.

Table 4.14: Exergy efficiency and exergy destruction of the SOEC system

System module	Variable	Calculation
Exergy efficiency		
SOEC stack	$\psi_{SOEC,stack}$	$(\dot{E}x_{H_2,stack,out} - (\dot{E}x_{H_2/H_2O,stack,in} + \dot{E}x_{SG,stack,in}))/P_{e,SOEC}$
SOEC system	$\psi_{SOEC,sys}$	$(\dot{E}x_{H_2,sys,out} - \dot{E}x_{H_2,sys,in})/P_{e,SOEC,net}$
Exergy destruction		
Grid to Stack	Ed_{GtS}	$P_{e,GtS} + \dot{E}x_{H_2,sys,in} - \dot{E}x_{H_2/H_2O,stack,in} - \dot{E}x_{SG,stack,in}$
Stack	Ed_{Stack}	$P_{e,SOEC,net} + \dot{E}x_{H_2/H_2O,stack,in} + \dot{E}x_{SG,stack,in} - \dot{E}x_{H_2/H_2O,stack,out} - \dot{E}x_{SG,stack,out}$
Purification	Ed_{Pur}	$P_{e,Pur} + \dot{E}x_{H_2/H_2O,stack,out} - \dot{E}x_{H_2,membrane,out} - \dot{E}x_{H_2O,pur,out}$
Purification to Grid	Ed_{PtG}	$P_{e,PtG} + \dot{E}x_{H_2,membrane,out} - \dot{E}x_{H_2,sys,out}$
Exergy losses	Ed_{env}	$\dot{E}x_{SG,sys,out} + \dot{E}x_{H_2O,sys,out} + \dot{E}x_{Cooling}$
CCGT	Ed_{CCGT}	$\dot{E}x_{NG,sys,in} + \Delta\dot{E}x_{Cond} + \dot{E}x_{AB,out} - \dot{E}x_{CCGT,exhaust} - \dot{E}x_{HRSG,SOFC,out}$
Exergy losses	Ed_{env}	$\dot{E}x_{CCGT,exhaust} + \dot{E}x_{HRSG,SOFC,out} + \dot{E}x_{Cooling}$

SOEC The exergy efficiency of the SOEC is calculated similarly to the SOFC exergy efficiency except that the desired product is the chemical exergy in the form of hydrogen and the exergy input is the electricity required for the electrochemical reaction. Again the stack is considered first, whereby the system boundary is defined as Figure 4.9. The $P_{e,SOEC}$ is the total required electrical power for the electrochemical reaction plus the required electrical heating. For the exergy efficiency of the SOEC stack, the hydrogen produced is considered the desired exergy product. From the outgoing hydrogen exergy flow $\dot{E}x_{H_2,stack,out}$, the incoming hydrogen and sweep gas exergy flows are subtracted $\dot{E}x_{H_2/H_2O,stack,in}$.

Balance of Plant The upstream Grid to Stack module is constructed similarly to during the SOFC mode. The Purification and Purification to Grid system boundaries are defined according to Figure 4.12 and 4.13. The condenser in the purification module, and the intermediate chillers in the Purification to Grid module, use which add up to the environmental exergy losses $\dot{E}x_{Cooling}$. The variables are all in [MW], the subscripts *Turb*, *GtS*, *pump*, *SG*, *Comp*, *Pur* and *PtG* represent the turbine, Grid to Stack module, Pumping power, Sweep Gas, Compressor, Purification module, Purification to Grid module respectively

$$P_{e,GtS} = \sum (P_{Turb,GtS}) + P_{Pump} + P_{SG,Comp} \quad (4.21)$$

$$P_{e,Pur} = P_{e,Turb,PtG} - P_{Com,PtG} \quad (4.22)$$

$$P_{e,PtG} = \sum (P_{Turb,PtG}) \quad (4.23)$$

System Level The net electrical power of the modules added together makes the total electrical power used by the SOEC $P_{e,SOEC,net}$. Hydrogen is the desired product of the SOEC system which makes all other exergy flows leave the system as exergy losses. Therefore, only the exergy flow of hydrogen leaving the system $\dot{E}x_{H_2,sys,out}$ defines the system's exergy efficiency $\psi_{SOEC,sys}$.

$$P_{e,SOEC,net} = P_{e,SOEC} + P_{e,GtS} + P_{e,Pur} + P_{e,PtG} \quad (4.24)$$

4.5.2. Energy Efficiency

The first-law efficiency is derived from the energy balance. The first-law efficiency is system-level specific, so the definition varies per component. This work assumes a stationary control volume so that the kinetic energy can be neglected. Additionally, a negligible change of elevation of the control volume is assumed, which cancels the potential energy term (Equation 4.25).

$$0 = \dot{Q} - P + \sum_i \dot{m}_i h_i - \sum_e \dot{m}_e h_e \quad (4.25)$$

The performance of a system undergoing a power cycle is defined as the ratio of energy output to energy input. In this work, useful energy input and output are component-specific. It is defined as

one or a combination of the following forms of energy; heat \dot{Q}_{th} , electricity P_e and chemical energy \dot{Q}_f . The energy efficiency of the combined system is described as the total work delivered and usable heat extracted divided by the HHV_f or LHV_f . The difference between the LHV and the HHV is equal to the latent heat of the vaporization of the fuel. The HHV is maintained throughout this work unless mentioned otherwise, allowing for comparing results from the literature.

4.5.3. GHG Emissions

The emitted GHGs to the atmosphere relative to the total equivalent impact of Carbon dioxide CO_2e represents the negative environmental effects of all GHG emissions to one single parameter, based on the global warming potential of the gas relative to that of CO_2 [89]. The global warming potential was developed to examine and compare the impacts of the emissions of different GHGs on the global warming of the atmosphere. The global warming potential is defined as the amount of absorbed energy of a ton of CO_2 over 100 years time [90]. The GHG emissions of a system relative to the delivered power are calculated by the following equation [89]:

$$\epsilon = \frac{\sum CO_2e}{P_{net} + \dot{Q}_{net}} \quad (4.26)$$

4.6. Optimization Sequence

The structure of the optimization can be divided into four different sections:

1. rSOC operating conditions analysis

- Only the cell is considered. This analysis results in an overview of the electrochemical effects due to the variation of the operating conditions. This analysis helps defending the design considerations during the optimization at the system level, as then the source of the affected performance can be distinguished from those due to electrochemical or Balance of Plant effects.

2. rSOC system operating condition analysis

- The same analysis is applied at the system level in which the Balance of Plant are also considered. From this analysis, the largest exergy destruction sources are determined which allows subsequent rounds to effectively seek to minimize these sources. This optimization round determines the operating conditions by which the following flowsheet optimizations are performed.

3. rSOC system flowsheet optimization

- Through the previous analysis, the benefits and simultaneously the downside of particular operating conditions becomes visible. The next optimizations tackles this downside while still utilizing the benefits by modifying the system design. The addition of system components minimizes the exergy losses and decreases the power consumption of the Balance of Plant. At the end of this section, the final SOEC and SOFC system flowsheets are established.

4. rSOC system optimal operating conditions

- As the flow schedule is modified, the system responds differently to variations in operating conditions. In the last rSOC optimization, operating conditions are reviewed to reflect the latest adjustments while considering the upcoming indirect heat coupling of the SOFC-CCGT systems.

5. SOFC-CCGT integration

- After the rSOC system optimization, the optimal coupling between the SOFC and CCGT is investigated. The outcome results in Optimization case 1A: SOFC-CCGT at full load, and Optimization case 2A: SOFC-CCGT at equal total load as the original CCGT.

6. SOFC-CCGT CHP

- Finally, it is examined whether the coupling between the SOFC and heat generating CCGT results in performance improvement. The outcome results in the Optimization case 2B: SOFC-CCGT CHP at full load, and Optimization case 2B: SOFC-CCGT at equal total heat production as the planned CCGT CHP.

5

Optimization

In this chapter, the system is optimized from a separate set of components to an integrated cooperating system. Several techniques are applied with the goal to increase the exergy efficiency of the system. In the first part of Section 5.1.1, the rSOC that Hauck et al. [16] designed is analyzed to determine the performance response of the cell to different operating conditions. Determining the electrochemical consequences of modifications on cell- and system-level modifications which helps with the justification the future system modification.

After the analysis of the rSOC, the same analysis is performed while considering the Balance of Plant in Section 5.1.2. From this analysis, the first selection of operating conditions, which are maintained during the first process design optimizations, will be evaluated. The largest exergy destruction sources will be eliminated in turn. After adjusting the system by adding components in Section 5.2, the optimal operating conditions are revised which takes into account the system-level modifications.

This will conclude the optimization of the rSOC where after the focus will be on integration between the SOFC and CCGT in Section 5.3. This optimization round results in the optimized power producing SOFC-CCGT of *Optimization case 1A* and *Optimization case 2A*, which will be compared to the current CCGT plant of *Base case 1A & 2A*. The latest Section 5.3 will be devoted to the investigation of whether the exergy efficiency increases when considering the combined heat and power plant of *Base case 1B & 2B*. The chapter ends by defining *Optimization case 1B* and *Optimization case 2B*. The actual results of the resulting optimized models are compared with the *Base cases 1A, 2A, 1B & B* in Chapter 6.

5.1. Operating Conditions Analysis

5.1.1. Stack Level

Table 5.1 shows the overview of the variables studied and the range in which the variables are varied. These variables were selected because they are freely adjustable while exerting significant influence on the Nernst voltage and overpotentials. It is assumed that the SOEC and SOFC both operate under the same operating conditions to avoid mechanical and thermal stress gradients.

The studied pressure range is limited to 10 bar because of the counteracting effect on the performance of both SOC modes [16]. The cell degradation limits the maximum operating temperature to 1000 °C and the declining performance of the cell by a decreasing temperature defines the minimum of 700 °C [17]. Finally, the exponential relationship between voltage losses and current density maximized the current density at ± 15000 A/m². Only one operating condition is varied at a time, if not mentioned otherwise.

Table 5.1: Variations of the operating conditions. The constant operating conditions are based on the experiments of Kamzempoor et al. [1]. * Fuel utilization factor determines the current density. ** Concentration definition is dependent on the SOC mode: SOFC mode; $[H_2]$, SOEC mode; $[H_2O]$.

Parameter	Varying	Constant	Unit
Current density*	0 - 15000	10000	A/m^2
Temperature	700 - 1000	850	$^{\circ}C$
Pressure	1-10	1	Bar
Fuel concentration**	0.5 - 1	0.5	-
Sweep gas	Air / pure oxygen	Pure oxygen	-

Current Density

The main consideration for determining the current density is a consideration between increasing voltage losses and the associated heat duty on the one hand, but on the other hand, the power density and the consequent total cell area required of the system.

Figure 5.1a shows the relationship between the current density, with the Nernst voltage and cell voltage. The graphs confirm the hyperbolic relationship of the current density j with the cell voltage V_{cell} . During SOFC mode at increasing current densities, the overpotentials increase, which results in larger heat production. In the case of the SOEC, the required electrical power increases while the external heat duty decreases.

The cell potential remains below the thermal neutral voltage given the current set of operating conditions. Determining the operating voltage relative to the thermoneutral voltage strongly relates to the availability of an external heat source or the possibility to recover heat from downstream components.

The difference between the cell voltage and Nernst voltage is the total overpotential which Figure 5.1b figure splits into the individual voltage losses. The resulting total overpotential consists of about half of the ohmic overpotential because high-temperature cells gain from sharply reduced activation and ohmic overpotentials. The figure also shows the exponential relation of the concentration overpotentials and the current density approaching $1.5 \cdot 10^4 A/m^2$ which should be avoided.

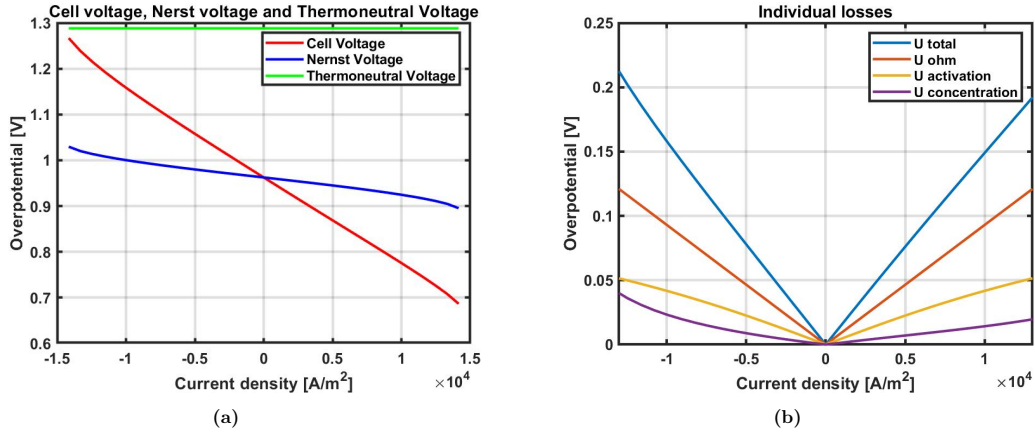


Figure 5.1: Current density [A/m^2] versus a) Cell voltage [v], b) Overpotentials [V]. The graph depicts the current density during SOFC mode as positive, the reverse is true during SOEC mode.

Based on these findings and the results found in the literature, the current density of $5000 A/m^2$ is preferred. The highest round trip efficiencies are achieved at low current densities of $500 A/m^2$ [61]. However, a larger area must compensate for the relatively low current density if the same amount of hydrogen or electricity is to be produced. The maximum power density is around $5000 A/m^2$ for hydrogen cycles [43] resulting in a reasonable amount of power without enlarging the plant size [61] which significantly decreases the capital costs of the stack [62].

Temperature

The operating temperature influence the Nernst voltage by affecting the standard equilibrium potential V_{Nernst}^0 by Δg^0 and $\frac{R \cdot T}{2 \cdot F}$ in Equation 5.1. Uniformly for both modes, an increase in temperature leads to a decrease in Nernst voltage as is depicted in Figure 5.2a and 5.2b.

$$V_{Nernst} = V_{Nernst}^0 + \frac{R \cdot T}{2 \cdot F} \ln \left(\frac{X_{H_2,b} \cdot \sqrt{X_{O_2,b}}}{X_{H_2O,b}} \right) + \frac{R \cdot T}{2 \cdot F} \ln \left(\sqrt{\frac{P_{stack}}{P_0}} \right) \quad (5.1)$$

The temperature affects the cell voltage mainly through the activation overpotential and the ohmic overpotential. The increasing temperature reduces the required activation energy of the electrochemical reaction represented by the Butler-Volmer Equation 2.5. In addition, operating temperature profoundly affects ionic and Ohmic resistance of ceramic materials of the electrolyte (Equation 2.8). Figure 5.2a shows clearly that the Nernst voltage and the total overpotentials both fall as temperature rises. Temperatures exceeding the 700 ° are preferred to stimulate the Oxygen ion permeation speed and thermal activation of the reaction [91].

For the SOFC, the decrease in overpotentials exceeds the decline in Nernst voltage at increasing temperatures which results in a higher cell voltage. Figure 5.2a shows the temperature at 900 °C maximizes the cell voltage. Comparing Figure 5.2a and 5.2b indicates that the operating temperature has a greater effect on the SOEC than on the SOFC. During SOEC mode the reduction in Nernst voltage and overpotentials complement each other rather than the substitution during SOFC mode. The increase in temperature is advantageous for the SOEC mode which now needs less electrical power to perform the electrochemical reaction.

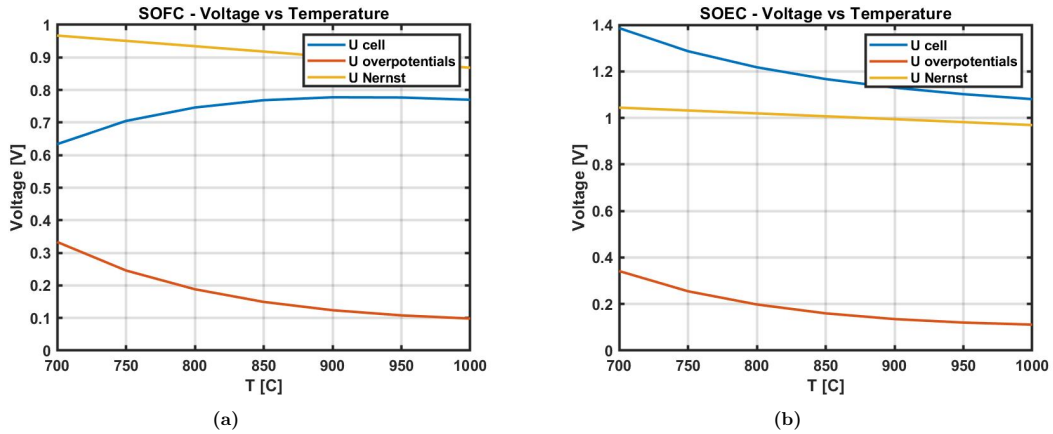


Figure 5.2: Operating temperature versus Cell voltage, Overpotentials, and Nernst voltage for a) SOFC and b) SOEC.

Pressure

The variation of pressure mainly influences the cell voltage through the increase of the Nernst voltage by influencing the pressure-related term $\left(\ln \sqrt{\frac{P_{stack}}{P_0}} \right)$ in the Nernst equation (Equation 2.3). Due to the logarithmic relationship, the impact on the Nernst voltage diminishes. The concentration and activation increase slightly by 0.9% over the 4 bar increase while the Nernst voltage increase 6% over the same range.

The increase in pressure similarly affects the cell voltage of both SOC modes as is depicted in Figure 5.3a and 5.3b. However, the accompanying consequence differs because a higher cell voltage negatively impacts the SOEC performance, which now requires more electrical power, while benefiting the SOFC performance, which generates more electricity.

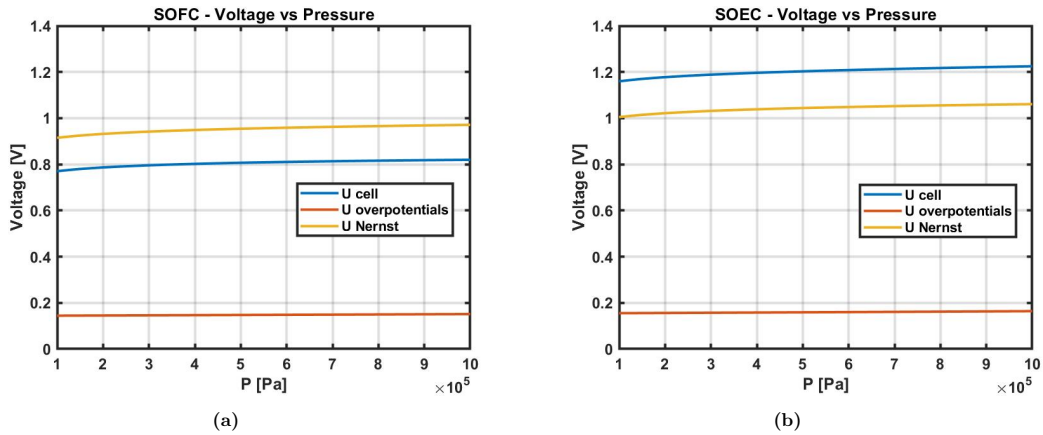


Figure 5.3: Pressure versus the cell voltage, overpotentials, and Nernst voltage for a) SOFC, and b) SOEC.

Combining Temperature and Pressure

The resulting figure - when both temperature and pressure varied simultaneously - reveals the operating window in which the SOC function is exothermic or endothermic. The figures show the optimal operating conditions when only considering the Cell Voltage. The SOFC mod, depicted in Figure 5.4a, prefers a simultaneous high temperature and pressure to maximize the cell voltage. However, at moderate pressures, smaller than 3 bar, the SOFC maximizes the cell voltage at 900 °C which moves simultaneously to 1000 °C with increasing operating pressure. In the current operating window, the cell voltage remains below the thermoneutral region.

But in the same analysis for the SOEC, the thermoneutral region does play an important role resulting in an interesting visualization in Figure 5.4b. The black plane indicates the thermoneutral limit. Above this plane, the SOEC operates exothermic, below it endothermic, and on it thermoneutral. The figure highlights the effect of the selected operating conditions on the heat management of the cell. This research aims for an operation below the thermoneutral point to allow the system's recovered waste heat to be used for the heat duty of the cell which hypothetically increases system efficiency.

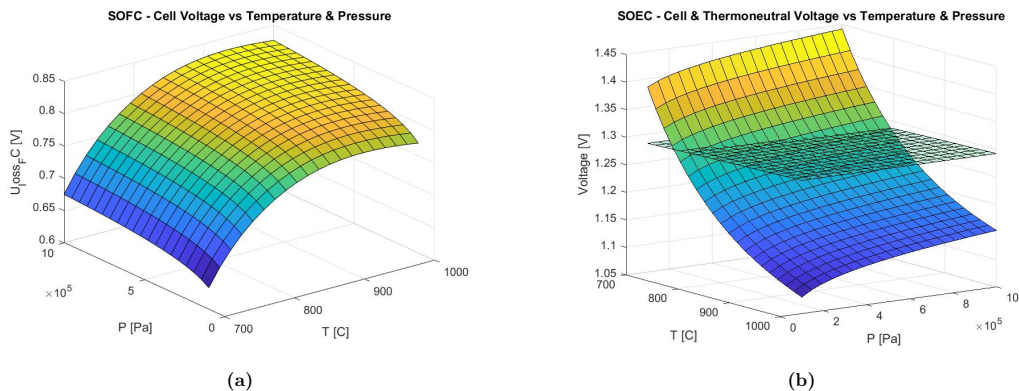


Figure 5.4: a) SOFC - Cell voltage versus Temperature and Pressure. b) SOEC - Cell voltage versus Temperature and Pressure. The black plane represents the thermoneutral region at a specified Temperature and Pressure.

In summary, a high temperature for both modes leads to a higher cell voltage. Pressure, however, has the opposite effect on SOFC as on SOEC. This means that the effects partly cancel each other out causing the pressure to have less impact compared to the temperature in the examined range. Although pressure has less effect on cell voltage, it is expected to play a significant role in the BOP and heat management [17], which will be examined in the next paragraphs. This is because the input feeds (hydrogen, water, and air) enter the system at different pressure levels that are managed by using turbomachinery. Besides, the pressure determines the thermal neutral behavior of the SOEC.

Fuel Composition

The fuel composition mainly affects the Nernst voltage and to a lesser extent the concentration overpotential. Figure 5.5a shows the minimum of the total overpotential of the SOFC at the hydrogen concentration of 0.68 on a molar basis. The overpotentials do not outweigh the improvements of the Nernst voltage at higher concentrations. The SOEC shows in Figure 5.5b the strictly decreasing cell voltage and overpotentials at higher steam concentrations. Similarly to the SOFC, the effects of the overpotential are relatively small in comparison to the change in the Nernst Voltage.

It seems obvious to choose the highest possible concentration of hydrogen or water for the SOFC and SOEC respectively. However, in practice, a sub-optimal concentration is chosen because the presence of steam in the SOFC, and hydrogen in the SOEC, results in a significant lower degradation rate of the cell [17] [92]. On the one hand, the maximum concentration of hydrogen during SOFC mode invokes microstructural changes in the electrochemical materials. On the other hand, the maximum concentration of water during SOEC mode slows down the initiation of an electrochemical reaction which results in deteriorated power output. In order to maximize performance while taking degradation into account, the concentration ratio 97/3 and 10/90 mol% H_2/H_2O should be chosen for the SOFC and SOEC respectively [17].

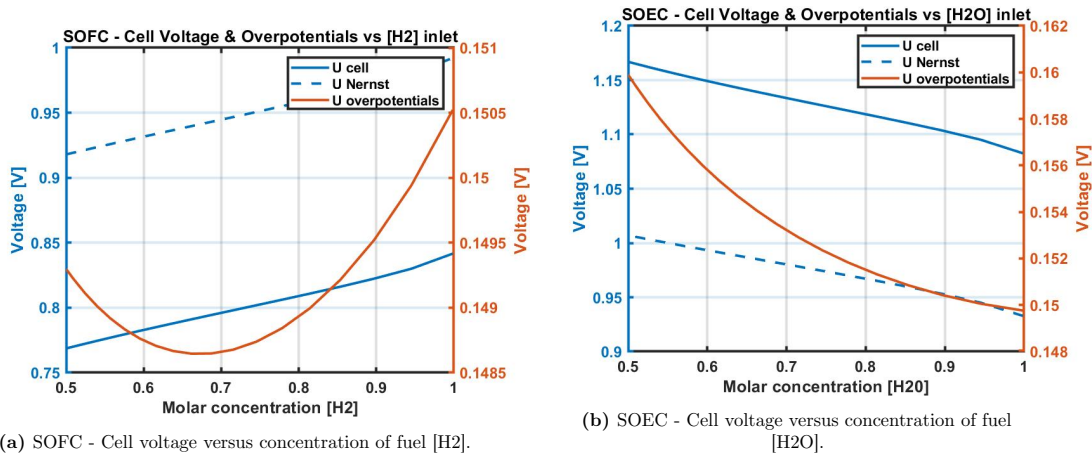


Figure 5.5: SOEC Cell Voltage vs concentration of fuel.

Sweep Gas

Figure 5.6 compares the effect on cell performance of using air and pure oxygen as the sweep gas. The decrease of Nernst Voltage when using pure oxygen improves the performance of the SOFC but the reverse is true for the SOEC. The figure shows that the SOFC's performance, enhanced by using oxygen, is just slightly higher than the loss of the SOEC's performance at the same magnitude, and negative current densities. The slight difference causes a minimal gain.

However, the minimal gain does not outweigh the additional cost of supplying pure oxygen [17]. Because a large quantity of sweep gas is required, for heating and cooling when operating in the exothermic or endothermic region, the use of pure oxygen is impractical since the system needs oxygen storage or simultaneous oxygen production. Besides, air promotes operating conditions that lower the risk of material failures while minimizing parasitic power [1] and is commonly used in practice for an rSOC [17]. Atmospheric air, or alternatively a mixture of oxygen-enriched air, is thus preferred when considering the entire system's performance.

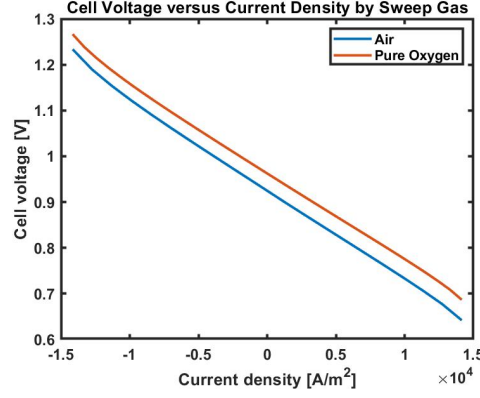


Figure 5.6: SOC - Cell voltage versus Current Density at different sweep gasses.

5.1.2. System Level

It is now time to apply the same variation of pressure, temperature, and fuel composition, to the performance of the system. The exergy efficiency of the system is based on the useful exergy as defined in Equation 5.2. In the case of the SOEC, the total useful exergy $\dot{E}x_{useful}$ corresponds to the outgoing exergy of the hydrogen, the incoming exergy to the power consumption E_{input} . Similar to the SOFC, the $\dot{E}x_{useful}$ corresponds to the generated power, and the E_{input} is the exergy of the consumed hydrogen. The total produced or consumed hydrogen will be maintained, until the SOFC-CCGT system integration in Section 5.3, promoting the comparison of results of the coming optimization rounds.

$$\psi_{system} = \frac{\dot{E}x_{useful} - \dot{E}x_{destruction}}{E_{input}} \quad (5.2)$$

Pressure - SOEC

Power The cell and system total energy requirement rise with the higher pressure as can be noted from Graph 5.7. It is remarkable that the total power¹ requirement of the cell decreases with increasing pressure because the cell analysis showed that increasing pressure leads to a higher power requirement for the cell.

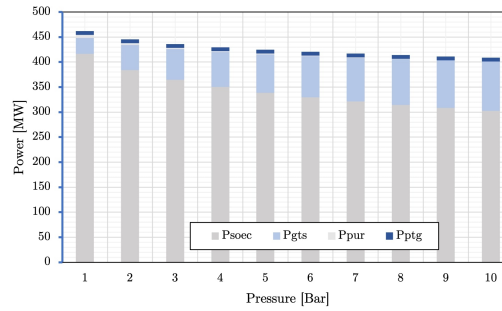


Figure 5.7: SOEC Pressure versus System Power. The four system modules are depicted: SOEC, Grid to Stack, Purification, and Purification to Grid. During the SOEC analysis, power consumption is defined as positive, and power production as negative. The cumulative of the bars is the total power consumption.

This is explained by the reduction in the heat demand of the cell by operating closer to the thermoneutral point. The compression of the air dominates the power requirements of the Grid to Stack module. The air required to cool the stack is significantly less at higher pressures. When expressing the reduction in the molecular ratio of air versus hydrogen water mixture it is of factor 11 at a pressure of 10 bar and a factor of 15 at 1 bar. The reduction of the airflow will reduce the required compression

¹The total power requirement of the cell equals the total of the required electricity and the heat.

power and at the same time reduce the required heating power of this airflow.

Besides, the increase in pressure leads to an increase in the temperatures of the incoming flows. The compression of the air is responsible for the majority of it. Pressurizing ambient air to 10 bar without intermittent cooling raises the temperature to 298 °C. The additional compression power partially substitutes the heat requirement of the SOEC. The water flow needs a considerable amount of power to vaporize the water. The power required to evaporate the water becomes more present as the pressure increases. The heat duty for the Grid to Stack module takes over the heat duty of the cell.

But also downstream at the purification module, the variation of pressure affects the power consumption. The energy requirement of the purification module drops substantially by 98% at the maximum pressure. The pressure of the incoming stream equals the membrane operating pressure, which eliminates the need for compression.

Exergy The exergy analysis, shown in Figure 5.8, reveals similar reactions at the system level. The system's exergy efficiency increases with higher operating pressures due to the steady exergy destruction drop of the SOEC. However, the exergy losses to the environment increase at higher pressures by exhausting the increased physical exergy airflow at elevated pressure. At 3 bar the environmental exergy loss exceeds the SOEC exergy destruction and becomes the largest contributor to the total exergy losses. The environmental exergy losses consist largely of the physical exergy flow of air (98.2 to 96.8% depending on operating conditions), the rest is the exergy flow of cooling the water.

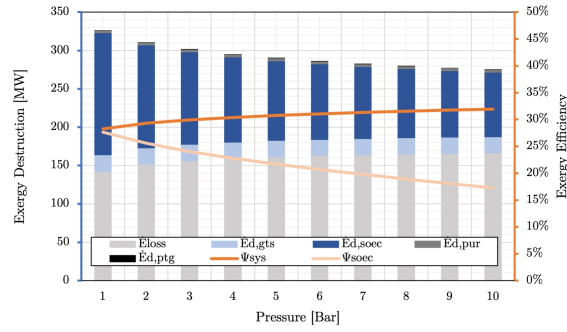


Figure 5.8: SOEC Pressure versus System Exergy Destruction and Exergy Efficiency. The exergy destruction of the four system modules is depicted (left y-axis): SOEC, Grid to Stack, Purification and Purification to Grid. Ψ_{sys} represents the exergy efficiency of the SOEC system including the Balance of plant, and Ψ_{SOEC} and represents the exergy efficiency of the cell. The cumulative equals the total exergy losses.

At increased pressures, the cell exergy efficiency decreases although the total required power and the stack exergy destruction decrease. This can be explained by the definition of the useful exergy (discussed in Chapter 4.5) and the exergy efficiency which is repeated in Equation 5.3 below. The outgoing airflow is not understood as useful exergy so the term is excluded in the numerator of exergy efficiency. Because the higher pressures increase the physical exergy of the term $\dot{E}x_{air,stack,in}$ more than the useful product $\dot{E}x_{H_2,stack,out}$ increases, and the $P_{e,SOEC}$ decreases, it results in a decrease in exergy efficiency.

$$\psi_{SOEC,stack} = \frac{\dot{E}x_{H_2,stack,out} - (\dot{E}x_{H_2/H_2O,stack,in} + \dot{E}x_{air,stack,in})}{P_{e,SOEC}} \quad (5.3)$$

Pressure - SOFC

Power Similar to the SOEC mode, the net power consumption of the cell and system decreases by the increasing pressure, shown in Figure 5.9. Because the electric power consumption of the fuel cell for heating the airflow is higher than the power generated by the fuel cell, the net generated power by

the P_{sofc} is sums up to a negative value.

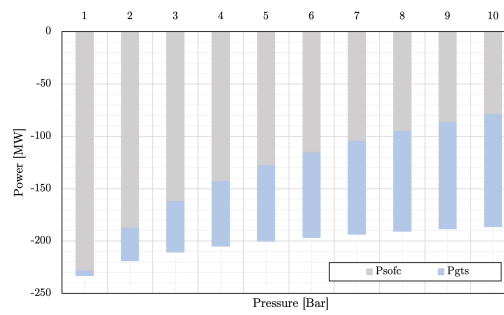


Figure 5.9: SOFC Pressure versus Power. P_{SOFC} and P_{GtS} represent the power production of the SOFC and the Grid to Stack module. During the SOFC analysis, power consumption is defined as negative, and power production as positive. The total of the bars equals the cumulative power production.

Due to the similar system configuration of the GtS module of both modes, the GtS module also behaves similarly: increasing the pressure results in a larger compression duty. The expansion of the incoming hydrogen from the hydrogen grid from 30 bar to operating conditions does not compensate for the higher air compression cost, because the mass airflow is more than an order of magnitude greater than the hydrogen flow. At low SOFC operating pressures, the recovery of pressure from hydrogen generates more than the air compressor needs. The SOFC operates further from the thermoneutral operation than the SOEC. As a result, the SOFC requires proportionally a larger airflow for cooling the stack, which results in larger compression power and greater heat duty.

But at the same time, the amount of electrical heating in the cell decreases at increasing pressures which is reflected in the decreasing power consumption of the P_{SOFC} . Again, the electric heating power shifts to the P_{GtS} , as the temperatures of the incoming flows increases by compression and the higher vaporization temperature of the water.

Exergy The operating pressure determines the heat duty of the cell by determining the cell voltage relative to the thermoneutral voltage. A higher operating pressure means less required air for cooling resulting in a large decrease in the exergy destruction in the cell.

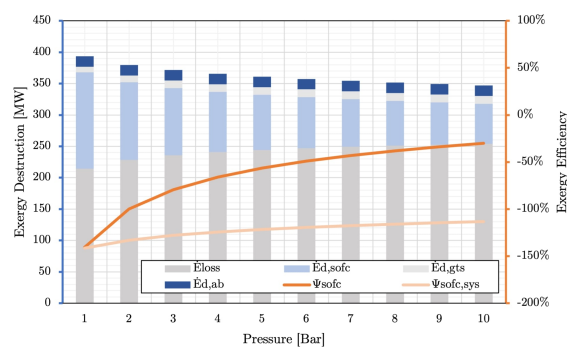


Figure 5.10: SOFC Pressure versus System Exergy Destruction and Exergy Efficiency. The cumulative of the bars is the total exergy destruction [MW].

However, the physical energy of the outgoing flow is paired with the pressure leading to more environmental exergy losses. From the environmental exergy losses point of view, without pressure recovery, the pressure must be maintained to a minimum. Although, the afterburner utilizes the chemical exergy losses to the environment by the complete combustion of the hydrogen converting it to heat. Without

heat recovery, the system discards the additional generated heat to the environment.

Temperature - SOEC

Power Looking at Figure 5.11 the temperature increase mainly affects the power requirements of the SOEC. The total SOEC power requirement increases significantly due to the more distant position from the thermoneutral point (Figure 5.4b). The additional power for heating substitutes the electrical power saving by a lower cell voltage. Without heat integration, the SOEC system discards the hot exhaust gasses and thus wastes the additional heating. The temperature does not affect the Grid to Stack components because the electric heaters in the stack provide the correct operating temperature.

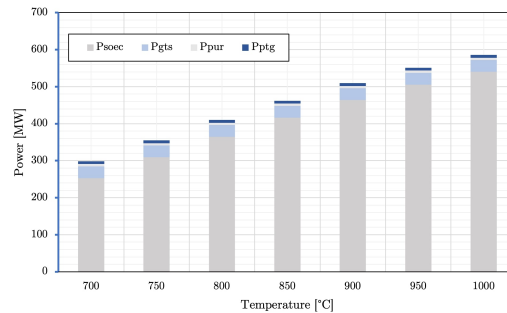


Figure 5.11: SOEC Temperature versus System Power. Power consumption is defined as positive.

Exergy The exergy losses grow by the increased temperature caused by the increase in the physical exergy of the outgoing flows (Figure 5.12). In addition, exergy destruction in the SOEC increases substantially because of the dependency on additional electric heating. Without heat integration, heating the cell is disastrous for the performance of the system.

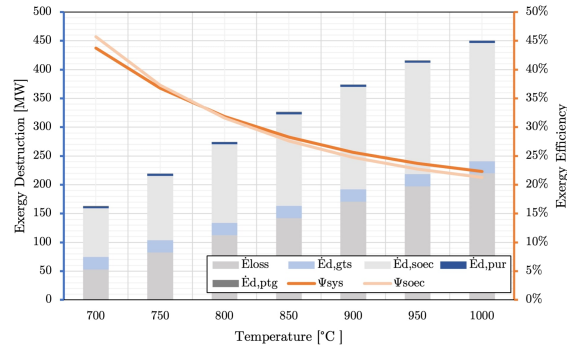


Figure 5.12: SOEC Temperature versus system Exergy Destruction and Exergy Efficiency.

Temperature - SOFC

Power Similar results are observed with the SOFC system. Higher temperatures increase the total power demand (which still exceeds electricity production). However, the temperature increase now causes lower heat generation by the electrochemical reaction through reduced voltage losses. At the cell level (see Figure 5.2a), an increase in temperature would lead to more electric power generation, less heat production by voltage losses, and thus less cooling requirements because V_{cell} is closer to V_{th} . Due to decreased heat production, less air is needed to cool the cell which reduces compression power. But again, the gas streams must be brought to a higher operating temperature, requiring a larger heat duty from the electric heaters. Figure 5.13 shows negative SOFC net power requirements, indicating the electric heating still exceeds the electric power generation.

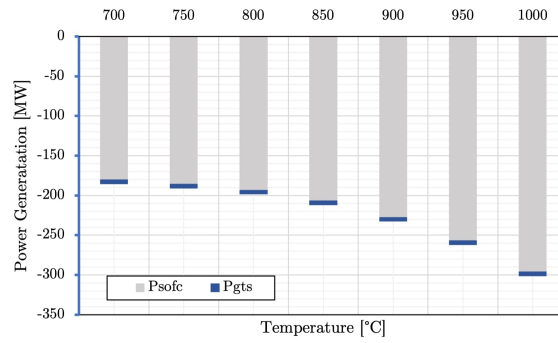


Figure 5.13: SOFC Temperature versus System Power. Power generation is defined as positive.

Exergy Again, exergy losses increase due to the greater amount of discarded physical exergy. The exergy destruction is less affected compared to the SOEC because the temperature rise in the SOFC leads to a higher Nernst voltage with less heat production while the SOEC requires more heat.

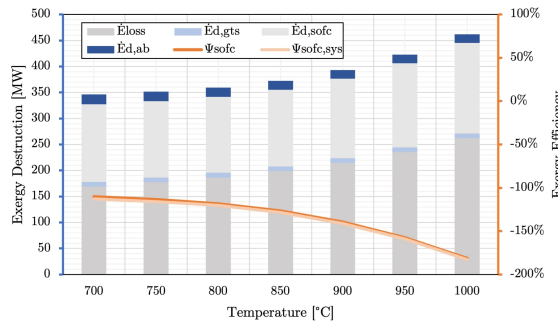


Figure 5.14: SOFC Temperature versus system exergy destruction and exergy efficiency.

Fuel Composition

The fuel composition can be changed by mixing steam and hydrogen in the Grid to Stack module. Although mixing leads to exergy destruction, the composition of the incoming steam can lead to additional heat or cooling to the cell. During the analysis, the concentration is determined by maintaining the molar flow of the electrochemically active component while increasing the diluent. Consequently, the required or generated current for electrochemical conversion remains constant while the total molar flow changes.

SOEC The water molar concentration determines the cell voltage (as shown in Figure 5.5) and sequentially the required power for the reaction and electric heating. Besides, the concentration determines the size of the hydrogen flow which is to be expanded and preheated to the operating conditions. At higher concentrations, the cell voltage moves away from the thermoneutral point resulting in a larger heat duty (increasing P_{SOEC}) but reduces the mass flow of the hydrogen which has to be preheated (decreasing P_{SOEC}). This opposite relationship is reflected in Figure 5.15 by the appearance of a minimum at 0.70 [H₂O]. The external heating and compression of the residual modules drop due to the diminished total mass in the system. In addition, the reduced mass flow results in an absolute reduction of the total pressure drop, reducing exergy destruction.

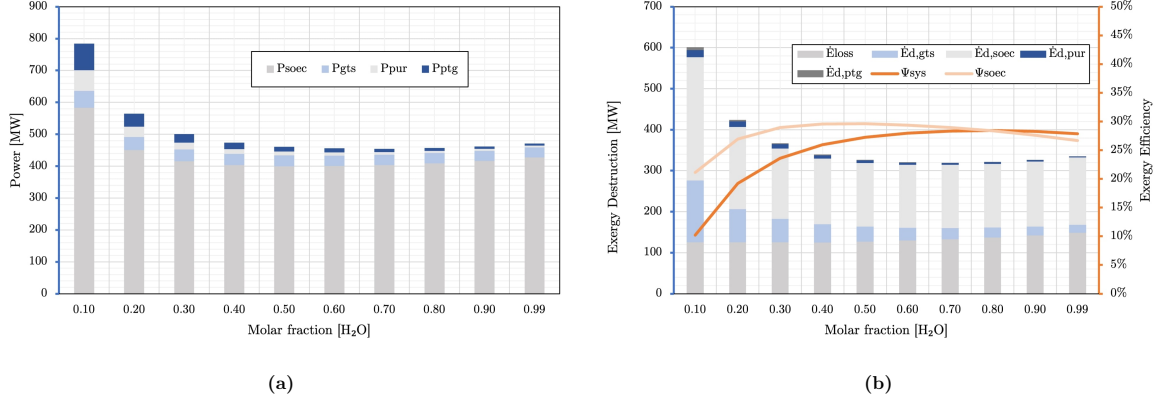


Figure 5.15: SOEC Molar Fraction [H₂O] versus a) System Power, b) System Exergy Destruction and Exergy Efficiency.

SOFC From the stack analysis, it was found that a higher hydrogen molar ratio leads to a higher Nernst voltage while having a negligible effect on the voltage losses. This resulted in a higher cell voltage and power output. This is also reflected in Figure 5.16. Next to the increasing Nernst voltage, decreased water mass flow reduces the required heat to vaporize the water. Decreasing the required water flow leads simultaneously to lower exergy destruction due reduction of pressure drops.

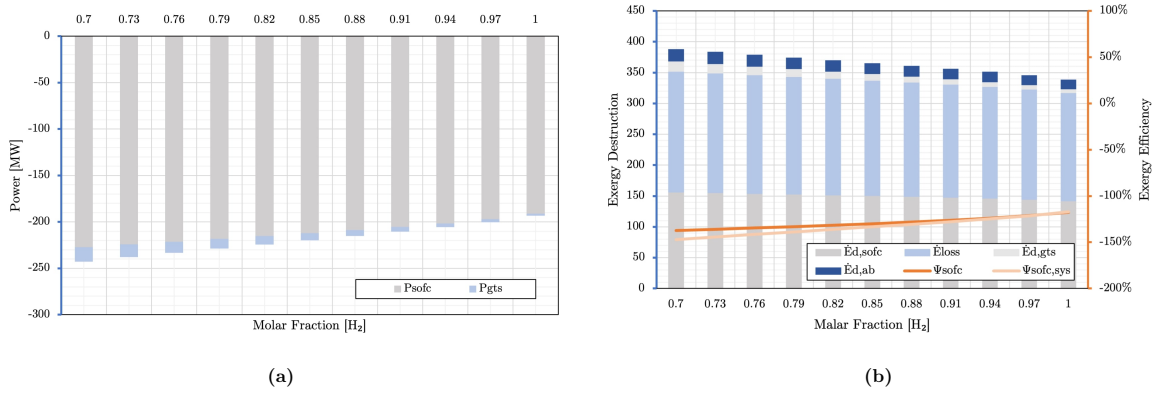


Figure 5.16: SOFC Molar Fraction [H₂] versus a) System Power, b) System Exergy Destruction and Exergy Efficiency.

5.1.3. Conclusion Operating Conditions

The examined operating conditions often appeared to cut both ways for the performance of the SOFC and SOEC modes. While the variation of the operating conditions enhance the performance of the SOFC mode, it deteriorated the performance of the SOEC, the opposite also holds. Besides, the design choices determined by looking purely at the optimization of the exergy efficiency often go against the findings in the literature study defending the practical aspects. These differences will be outlined and operating conditions will be determined by making a consensus. These operating conditions will be maintained until the rSOC is fully optimized. Thereafter, the optimal operating conditions will be reviewed. Concluding from the above findings, the following operating conditions are adopted in further analysis of the system:

- Current density = 5000 A/m². Lower current densities would decrease the overpotentials, affecting the stack's efficiency and the heat management of the SOC. However, a larger area must compensate for the relatively low current density. The maximum power density is around 5000 A/m² for hydrogen cycles [43] which significantly decreases the capital costs of the stack [62].
- Temperature = 850 °C. At the cell level, it was found to be advantageous to maximize temperature. Elevated temperatures decrease the overpotentials and Nernst Voltage. However, the increase in temperature led to decreasing system exergy efficiencies which were explained by increasing exergy losses. This emphasized the importance of heat recovery, which is expected to decrease

when heat recovery is applied. As a result, an average temperature of 850 °C is maintained for the optimization of the flowsheet until all the exergy losses are utilized.

- Pressure = 5 bar. The pressure mainly affected the Nernst and had an opposing effect on the cell performance of the modes. Nevertheless, increasing the pressure proved to be advantageous for both systems. A trade-off has to be made between the heat duty, the exergy destruction caused by the differences in pressure ratios of successive modules, and the exergy losses to the environment. To include both cell and system effects during the flowsheet optimization, a pressure of 5 bar is used. After the flowsheet optimization, the pressure will be verified again.
- Fuel concentration [H_2/H_2O] for the SOFC & SOEC = 97/3 & 10/90. Maximum concentration led to maximum performance at the cell level and for the SOFC on the system level. For the SOEC system, exergy efficiency was found to peak at 0.7 [H_2O] but differed little with maximal contraction. Yet for practical reasons, the concentration should be maximized. The small gain in efficiency from adding large amounts of hydrogen does not outweigh the additional cost of the hydrogen. In addition, when heat integration is applied, the disadvantages of the additional heat duty would likely vanish. Concluding, the concentration is finally set at the maximum concentration while considering the degradation effect and reaction initiation problems that were found in the literature study.
- Sweep gas = Dry air. In the cell analysis, the performance of the reversible system was not much affected due to the opposing impact on both modes. In the literature study, dry air was determined to be the most practical and performed best for heat management in the cell.

The results of implementing the selected operating conditions are shown in Table 5.2 and 5.3 for cell level and system level respectively. Based on these results, the following optimization will be compared. The amount of hydrogen and water remains the same throughout the rSOC optimization, so the amount of power per hydrogen can be compared. However, the amount of air varies as the heat management determines the amount of required air to heat or cool the stack.

Table 5.2: Results SOC voltages and power output. Input Stack temperature 850 C, pressure 5 bar, Current density 5000 A/m², Fuel Utilization 0.8, Fuel composition 0.97 & 0.9 for SOFC and SOEC respectively, Sweep gas Air.

Parameter	SOFC	SOEC	Unit
V_{cell}	905	1040	mV
V_{nernst}	990	962	mV
V_{loss}	84.5	78.3	mV
V_{con}	46.5	46.5	mV
V_{act}	22.5	22.5	mV
V_{ohm}	15.4	9.24	mV
P_{total}	1234	1234	W
P_{el}	906	961	W
P_{th}	328	273	W

Table 5.3: Preliminary results after examining the operating conditions: Input and output, exergy efficiency, and exergy destruction.

SOFC system	Value	SOEC system	Value
Gas (kg/s)		Gas (kg/s)	
H ₂ in	1.363	H ₂ (Net out)	1.090
H ₂ O	0.377	H ₂ O	12.19
Air	320.9	Air	254.5
Power Generation [MW]		Power Consumption [MW]	
Total	-170.9	Total	424.6
Stack	-101.9	Stack	337.6
Grid to Stack	-68.99	Grid to Stack	77.76
		Purification	1.504
		Purification to Grid	7.731
Exergy efficiency [%]		Exergy efficiency [%]	
SOFC	-45.35	SOEC	21.69
SOFC system	-103.7	SOEC system	30.78
Exergy destruction [MW]		Exergy destruction [MW]	
Total	316.5	Total	293.9
Grid to Stack	10.19	Grid to Stack	21.40
Stack	81.05	Stack	104.1
Exergy loss	209.0	Exergy loss	164.1
Afterburner	16.28	Purification	3.691
		Purification to Grid	0.689

5.2. Flowsheet Optimization

The flowsheet of the rSOC system is modified by four consecutive rounds after which the previously determined operating conditions are reviewed. The order of the optimization rounds is determined by the magnitude of the contribution to total exergy destruction.

With the help of the previous system analysis, it turned out that the heat demand of the cell accounted for the largest amount of external heat duty. But at the same time, the extra heat supplied left the system boundary downstream resulting in exergy losses. Because of this, the first optimization is devoted to cell heat recovery.

Subsequently, it was found that the amount of air required to heat or cool the cell, strongly affects the total power requirements and exergy losses. The literature studied repeatedly mentioned that implementing air recirculation would lead to a reduction in exergy destruction, so the second round explores the implication of this solution.

The third round focused on regaining the applied pressure. It appeared, from the previous analysis, that the system improved when the pressure was increased, but at the same time the exergy losses to the environment increased significantly.

Finally, after completing the adjustments that adjust the mass and heat balance of the system, methods are sought to supply the upstream heat requirement with the downstream exergy heat losses. Through pinch analysis, a heat exchange network is constructed that achieves optimal exergy efficiency.

During the optimization process of the Stack, the amount of hydrogen or water is maintained. Only after finalizing the rSOC optimization, the SOFC stack system is scaled to produce 100 MW P_e . In the coming optimization rounds, the SOEC is scaled so that the current density is equal to that of the SOFC. After determining the optimal operating conditions of the rSOC system, the optimal integration of the SOFC-CCGT is investigated. This will be further explained when the research reaches that point.

To lighten the upcoming sections from too much data, all the data the optimization rounds of exergy efficiency P_{si} , exergy destruction/losses Ed_{system} and power consumption/generation P_e of the rSOC system are presented in the Appendix A.2. The effect of the optimization round on the variables can

be observed from the graphs. The coming section frequently refers to these graphs.

The conclusion of the optimization rounds highlights only the changes in relevant variables.

5.2.1. Flowsheet Optimization 1: Cell Heat Integration

The first optimization round focuses on the SOEC's exergy losses caused by the high SOFC exhaust gas and the large required additional electric heating. The current incoming cell streams are of relatively low temperature (140 °C at 5 bar). These streams need to be increased to 750 °C or 950 °C (± 100 °C the operating temperature), depending on the endothermic or exothermic mode. Without heat recovery, electric heaters provide all of the required power. After the conversion of the fuel, the high-temperature stream is led out of the SOEC. Countercurrent heat exchangers - placed between the outgoing SOEC flows and the incoming flows - recover the heat.

SOEC

The heat integration of the downstream outgoing flows of the cell is individually integrated with the upstream flows. The flowsheet of the cell is depicted in Figure 5.17. In order to maintain an overview, the figure depicts the heat transfer by an arrow but the system employs a heat exchanger. The outgoing fuel electrode stream heats the incoming fuel electrode stream and the same happens with the oxygen electrode streams. A calculator block maximizes heat transfer. The electric heater supplies additional heat when the heat exchanger cannot provide enough heat to reach the required operating temperature. During endothermic mode, the incoming oxygen electrode stream always needs additional electric heating because the incoming stream is 100 °C above the operating temperature to energetically balance the heat.

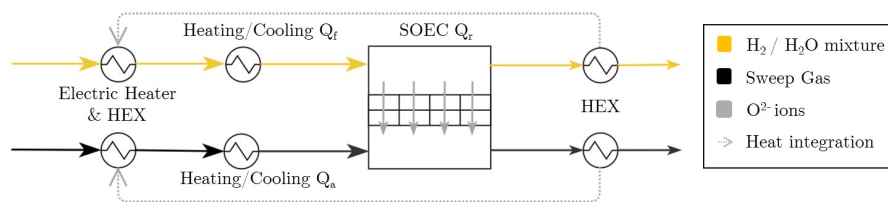


Figure 5.17: SOEC Optimization 1: Cell heat integration.

SOFC

The heat integration of the SOFC greatly improves the performance because large amounts of heat can be recovered. The outgoing temperature is always 100 °C higher than the incoming temperature. Figure 5.18 shows the flowsheet, which shows the identical construction of the heat exchange network as for the SOEC. Eventually, it will be shown whether the volume flows match allowing the same system components to be used.

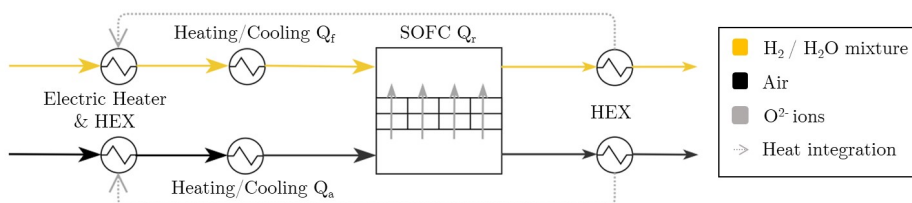


Figure 5.18: SOFC Optimization 1: Cell heat integration.

Conclusion

The heat integration reduces the SOEC's power requirements by 61% by reducing electric heating power by 204 MW but the stack still requires 25.8 MW. In addition, the exergy losses to the environment decrease significantly as the temperature of the outgoing airflow decreases, and so does the physical

exergy. Figure 5.19b summarizes the main reduction of exergy destruction sources. The temperature of the outgoing OE stream still exits the system at 203 °C at around 5 bar. The Oxygen Electrode stream contributes to a single-handily exergy loss of 45.3 MW, indicating potential improvements. Due to the cell's heat recovery the $\Psi_{SOEC,system}$ increases from 30.8 % to 59.3%.

The SOFC shows similar results, the reduction in electric heating power and environmental losses turns the negative efficiency Ψ_{SOFC} and $\Psi_{SOFC,system}$ to a positive efficiency. Figure 5.19a denotes the reduction of exergy losses of the SOFC. The reduction in the externally required preheating of the SOFC causes a decrease of 78% in of the SOFC stack exergy destruction. The largest absolute decrease results from the reduction in the temperature of the exhaust stream. In the system without cell heat integration, the required electric heating and compressor power exceeds the generated power of the SOFC. After heat integration, this is no longer the case.

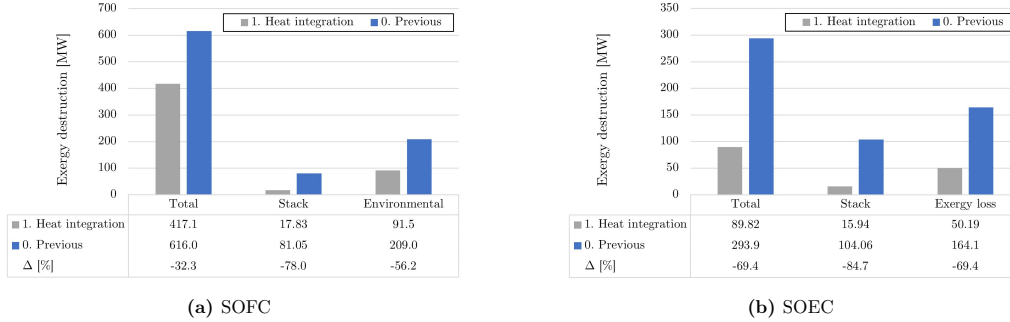


Figure 5.19: Results and improvement of optimization 1: Cell heat integration. The blue bars indicate the results from the previous flowsheet, the grey bars indicate the results after the applied heat integration.

5.2.2. Flowsheet Optimization 2: Air Circulation

The amount of air entering the system dominates the power consumption of the Grid to Stack module and the exergy losses to the environment. Air circulation affects the system performance by the following five aspects which all will be examined:

- It would decrease the required fresh air flow, thus decreasing the compression power of the Grid to Stack module and the electric preheating power of the Stack.
- It would decrease the outgoing airflow, thereby decreasing the discarded hot air to the environment.
- The energy confined in the hot recirculated air would replace the electric preheating in the stack.
- The additional air compressor would increase the stack power consumption to compensate for the pressure losses.
- The recirculation of the air stream would change oxygen concentration at the oxygen electrode, thus influencing the performance on electrochemical level.

The air circulation is applied immediately after the airflow from the Oxygen electrode leaves the cell. The recirculation factor determines the portion of the flow returning to the incoming airflow from there with the total amount of recirculating energy. Originally, the recirculated flow meets the airflow before heat integration. The position where the two streams are mixed has an effect on heat integration. The optimal position is also investigated in this optimization round.

SOEC

First of all, the air recirculating affects the required heat because a large quantity of air is able to reheat the incoming stream by mixing with the hot splitted stream. Caused by the pressure drop, the recirculated stream was pressurized again, which heats the gas by compression. At the currently optimized conditions; an isentropic efficiency of 85% and a pressure ratio - that ensures the operating pressure again after the pressure drops - of 1.04, the temperature rises from 850 to 863 °C (the same applies to the SOFC).

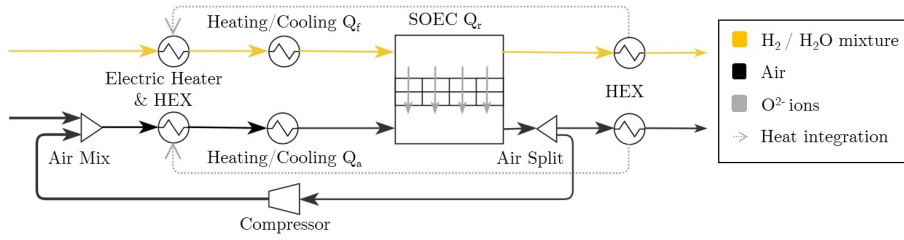


Figure 5.20: SOEC Optimization 2: Air recirculation.

A larger air recirculation ratio (ARR) means a smaller proportion of required fresh air. Because the recirculated air has a higher temperature than the fresh air after heat integration (in the current setup 863 versus 198 °C), the temperature of the mixed incoming air stream increases depending on the ARR factor. This increase leads to a reduction in the additional electrical heating required, thereby reducing the SOEC power requirements. This is offset by the additional compression requirements of the SOEC recirculation compressor. Especially with high-temperature gases, which are associated with larger volumes, it takes a relatively large amount of power to increase the pressure. These opposing effects can be seen in Figure 5.22a where first the power requirement of the SOEC (P_{SOEC}) increases after which it decreases again after an ARR of 0.55. The power requirements of the SOEC at the maximum ARR of 0.95 slightly exceed the ARR of 0.

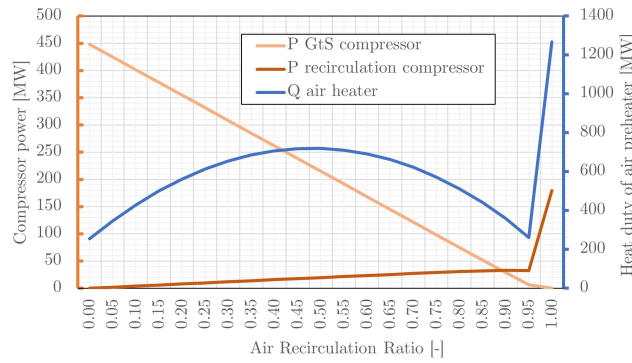


Figure 5.21: SOEC Air recirculation ratio versus Compressor power of the recirculation compressor and the Grid to Stack compressor P (Orange y-axis), and the heating/cooling duty of the air preheating Q (Blue y-axis).

However, the total power requirements decrease at higher ARR s due to the decrease of the compression power of the fresh air to the SOEC's operating conditions. While the recirculated airflow only has to make up for the 4% pressure difference because of the pressure losses, the fresh air is brought from atmospheric pressure to operating pressure, which is currently a pressure ratio of 5.

Figure 5.22b also shows a clear consequence of the ARR on exergy losses. The hot outgoing airflow from the SOEC with a substantial mass flow needs to be cooled before it is discarded to the environment, and is therefore a large contributor to exergy loss. With an increased ARR , this outgoing airflow decreases resulting in a decrease of over 90% at the selected ARR .

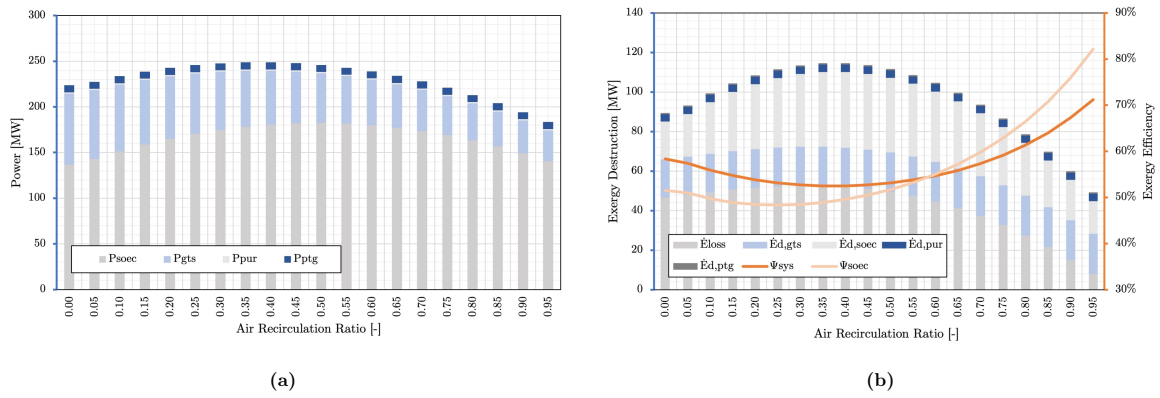


Figure 5.22: SOEC Air recirculation factor versus a) System Power, b) System Exergy Destruction and Exergy Efficiency.

At the electrochemical level, air recirculation also has significant implications due to the effects of changing concentrations. The O₂ molecules formed at the oxygen electrode permeate through the oxygen electrode and mix with the cooling air. This increases the concentration of O₂ in the outgoing stream. This increase is minimal in the case where the system recirculates no air. The influence on the concentration grows when the ARR increases as the ratio of recirculated air to fresh air increases. In the cell analysis in Section 5.1.1, it was shown that a higher concentration of O₂ leads to a higher cell voltage which penalizes the performance of the SOEC.

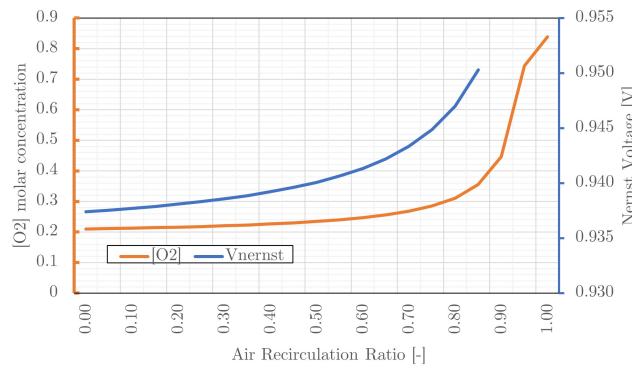


Figure 5.23: SOEC - Air recirculation ratio versus Oxygen concentration and Nernst Voltage.

SOFC

Three aspects must be considered when applying the SOFC's ARR which was not necessary for the SOEC. The first relates to the cooling function of the airflow that limits the temperature of the incoming airflow to -100 °C compared to the operating temperature. Secondly, the SOFC reacts differently in the electrochemical domain to the changing oxygen concentration than the SOEC mode. Finally, the environmental losses tend to react less severe due to the SOFC's downstream system configuration compared to that of the SOEC.

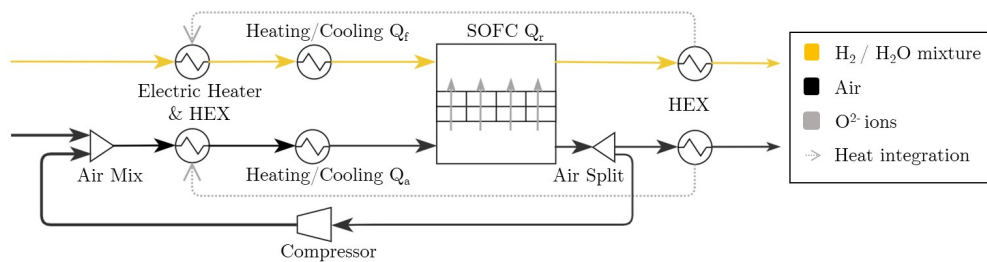


Figure 5.24: SOFC Optimization 2: Air recirculation.

The incoming air must be 100 °C lower than the operating conditions to cool the cell during the exothermic SOFC reaction as compared to 100 °C higher to provide the cell with the required heat during the SOEC endothermic reaction. The temperature of the SOFC's outgoing airflow (850 °C) is already higher than the required incoming airflow (750 °C) but is additionally raised by the recirculation compressor. With an increasing ARR, the incoming SOFC temperature could exceed the required temperature of 750 °C which would prevent the stack from being cooled.

If the ARR is set too high, the cooling requirements should be solved in two very detrimental ways: By feeding the stack with a relatively large fresh airflow which increases the total airflow intensively, or by cooling the incoming air externally which leads to pure exergy destruction. It turned out that the second option was preferred over the first option, but still should never be considered. This can be confirmed by Figure 5.25, which depicts the exponential cooling requirement at an ARR higher than 0.87. In addition, it can also be noticed that the compressor power of the incoming fresh air flow decreases sharply at higher ARR because less air is needed to cool the SOFC. However, there is an increase in the recirculation compressor in its place but this does not exceed the decrease in the relevant ARR range. Looking at the performances in Figure 5.27a and 5.27b, the ARR below 0.85 is preferred. Above this, the external cooling increases and so the exergy destruction in the SOFC increases. As a result, the exergy efficiency implodes.

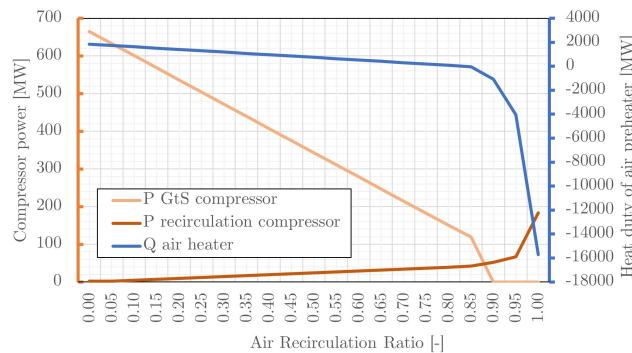


Figure 5.25: Air recirculation ratio versus Compressor power of the recirculation compressor and the Grid to Stack compressor P (Orange y-axis), and the heating/cooling duty of the air preheating Q (Blue y-axis). A negative Q means the cooling which is pure exergy loss.

This consequence can be generalized to any SOFC system that uses an ARR and cools the cell by the incoming airflow. This phenomenon becomes increasingly important as the operating pressure increases because the absolute pressure losses increase with higher operating pressure. This results in an increase in the temperature of the recirculating air stream. Consequently, the higher operating pressures result in a lower optimum recirculation factor.

The second difference was the relation of the oxygen concentration with the ARR depicted in figure 5.26. The hydrogen on the fuel electrode side pulls the oxygen ions through the electrolyte to form a current. Consequently, the concentration of oxygen drops slightly at the outgoing stream of the oxygen electrode. The recirculation amplifies this decrease in concentration. This is in contrast to the SOEC where the oxygen concentration increases with the addition of formed oxygen. Figure 5.6 showed the negative consequence of decreasing oxygen concentration on the SOFC's presence. A low concentration of oxygen is associated with a lower Nernst Voltage and slightly higher overpotentials, and thus a lower generated electrical power.

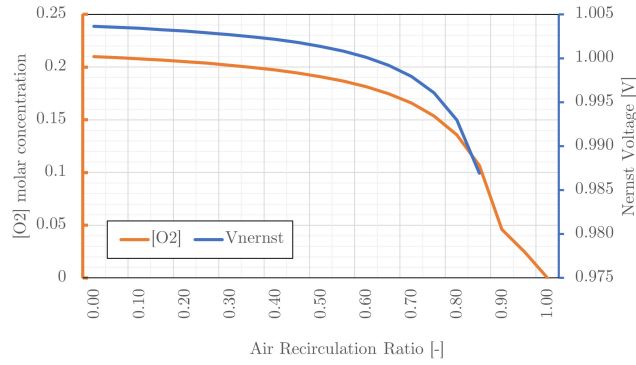


Figure 5.26: Air recirculation ratio versus Oxygen concentration and Nernst Voltage.

Finally, the afterburner burns the residual hydrogen along with the incoming air and steam. These two flows ultimately make up the environmental losses. The big spike in environmental losses, at the ARR greater than 0.85, occurs because the oxygen concentration is too low to oxidize all the hydrogen due to the high ARR. As a result, not all the chemical exergy is converted to physical exergy which ends up being discharged into the environment.

At a lower ratio of the amount of air, the temperature of the afterburner exhaust gasses increases (from 880 °C at an ARR of 0 to 1203 °C at 0.83) with the result that the physical exergy per mole increases. The increase in outgoing temperature has consequences for the heat integration with the CCGT and the exergy destruction caused by the larger temperature difference in the counter-current flows of the heat exchangers. These consequences are discussed during the system heat integration optimization.

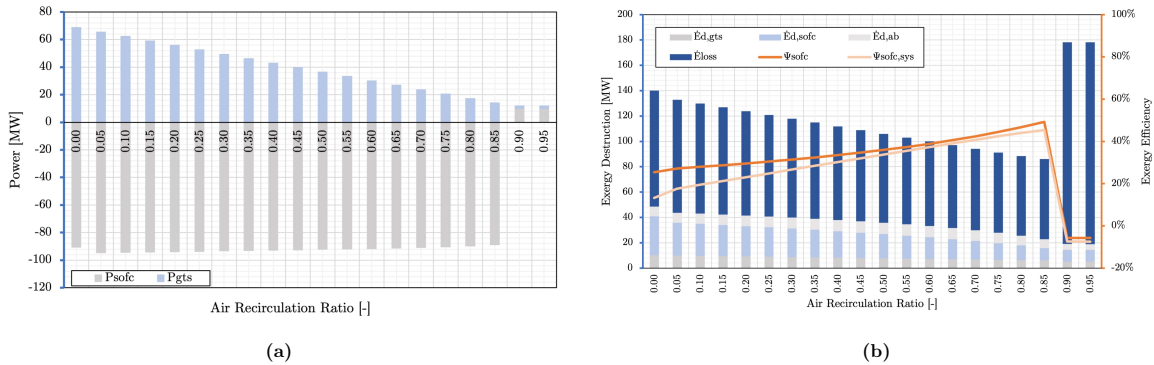


Figure 5.27: SOEC Air recirculation factor versus a) System Power, b) System Exergy Destruction and Exergy Efficiency.

Conclusion

In summary, a higher ARR benefits the SOC's performance due to: A lower additional heat requirement, a decrease in the compression cost of Storage to Stack P_{GTS} that ultimately exceeds the higher SOEC air circulation compression cost, and in a decrease the environmental exergy losses (as is depicted in Appendix A.2). However, the variation of oxygen concentration deteriorates the SOC's performance due to a disadvantageous variation in Nernst voltage depending on the SOC mode. During SOFC mode, a higher ARR than 0.85 showed poor results due to exceeding the required cooling temperature.

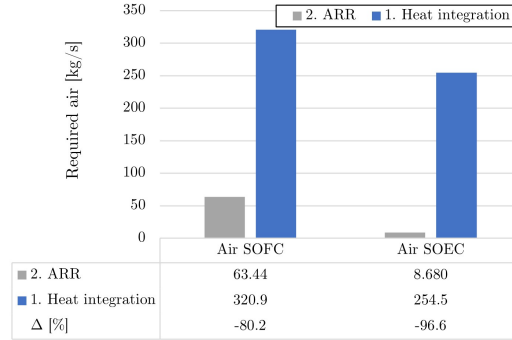


Figure 5.28: Reduction of fresh air. The current air consumption (grey) is compared to the system after Flowsheet optimization 1: Cell heat integration (blue).

Considering all phenomena, the ARR should be set close to its maximum. The SOEC uses an ARR of 0.93 and the SOFC one of 0.83. At these two points, just below the allowed maximum, the heat duty of the heat exchangers is 0. As a result, both heat exchangers are no longer needed which avoids the pressure drop of 2% over a large airflow, and would save on investing in a large airflow heat exchanger.

This optimization round results in great improvements to the performance parameters. The exergy efficiency and exergy destruction of this round compared to the previous setup are depicted in Appendix A.2. The produced power of the SOFC system increases by 183% which is mainly explained by the 77.3% decrease of the P_{GtS} air compression power. In addition, the SOFC exergy efficiency increases by over 80%, from 27% to 48% compared to the previous setup. The exergy destruction of all modules decreases. The biggest absolute improvement can be seen in the exergy losses with almost 30 MW.

The SOEC shows similar improvements, visualized in Appendix A.2. With air circulation, the fresh air stream is significantly reduced by 96.6%. Consequently, the increased ARR reduces the compression power of P_{GtS} by more than half compared to the previous setup (Table 5.20). Overall, 15% less electricity is needed to generate the same amount of hydrogen. Additional compression power and increases in operating voltage increase the SOEC power consumption by 8%. However, the decrease in compression power of the GtS module by 56% makes up for these losses. The exergy efficiency impressively increases from 22% to nearly 80% as the ARR allows the exergy losses to be used to heat the incoming air stream. The ARR of 0.93 reduced the exergy losses by 92%.

5.2.3. Flowsheet Optimization 3: Downstream Turbines

After bringing down the exergy losses caused by the stack's heat management and heat losses, the exergy losses by discarding pressurized flows are investigated. Adding a downstream turbine to the system utilizes the physical exergy of the pressure and temperature by converting the exergy into electricity. The pressure ratio of the turbine is slightly below the required ratio to achieve ambient pressures to account for the heat integration pressure drop. The positions of the turbines vary by mode due to the differences in the downstream modules. The generator efficiency of the turbines is assumed at 99%, which corresponds to the same generator efficiency of the Hemweg 9 CCGT in the Base case.

SOEC

For the SOEC, the position is simple, namely directly behind the oxygen electrode outlet as is depicted in Figure 5.29. At an isentropic efficiency of 85 % and a pressure ratio of 4.6, the temperature decreases from 850 °C to 543 °C while the turbine generates 5.8 MW P_e . As a result, exergy losses go down by 43%, and 3.1% less electricity is needed (Figure 5.31b). The combined reductions cause a 3.2% increase in the SOEC system's exergy efficiency which is depicted in Appendix A.2.

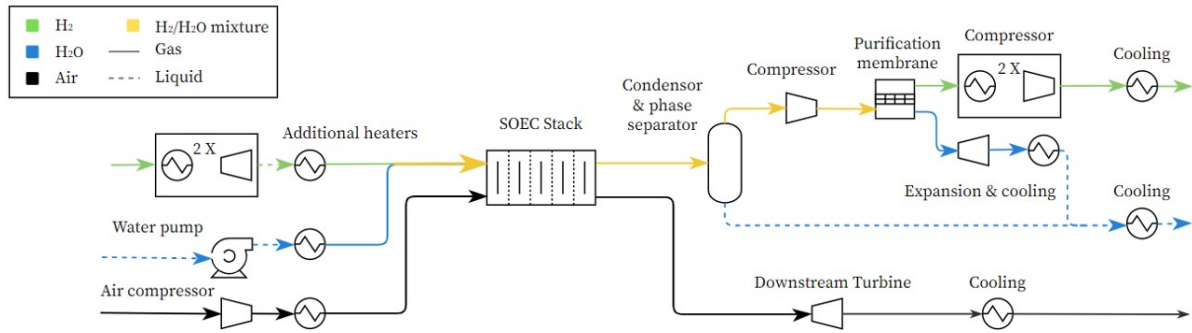


Figure 5.29: SOEC Optimization 3: Downstream turbine

SOFC

The determination of the optimal position of the turbine in the SOFC system is not so straightforward. Three factors play a role in determining the optimal position: the limited exhaust temperature, exergy destruction of heat integration, and the turbine inlet temperature.

The first concerns the limited pressure ratio to meet the proper exhaust temperature. The expansion is accompanied by a temperature decrease, with the current setup, this is not a problem but when heat coupling between the SOFC and the CCGT is applied, the exhaust temperature must match the temperature required for integration. This seems controversial because the exhaust temperature should be brought to a minimum to reduce the exergy losses. Therefore, during the analysis of the results, the proposed system is also compared to the decoupled systems. During the coupled systems, crossing the minimum temperature would limit the amount of heat that can be extracted, increasing the exergy losses and the required additional electrical heating. To ensure maximum heat transfer the turbine should be placed completely downstream (even after the HRSG of the CCGT when the SOFC-CCGT is considered).

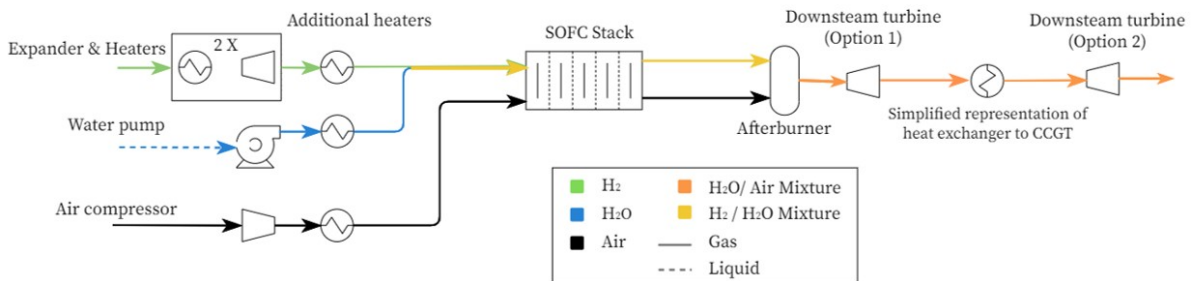


Figure 5.30: SOFC Optimization 3: Downstream turbine. Comparison position of Option 1 and 2. The heat integration is included in the flowsheet to substantiate the explanation of the dependency on the following heat integration.

Concerning the second factor, the exergy losses increase with the spread of temperature between the hot side and cold side of a heat exchanger [50]. The temperature difference between the two streams must be minimized to achieve minimal exergy destruction. The average temperature on the hot side of the heat exchangers is lower when the turbine is positioned immediately after the afterburner. The last factor to consider is the relation between the turbine inlet temperature and the turbine power output, which was explained in Chapter 2. When the turbine is placed immediately after the afterburner, before the heat integration, the inlet temperature is higher than when the turbine is placed downstream.

Table 5.4 shows the affected variables. The exergy destruction of the SOFC has indeed decreased, because the temperature difference between the hot and cold sides of the heat exchanger are closer together. The turbine is positioned sequential to the afterburner, the turbine inlet temperature is 1203 °C and the exhaust gas is 890 °C which would be sufficient for the heat integration with the HRSG or the fuel preheater. Besides, the temperature difference between the working fluid of the HRSG and that of the SOFC exhaust flow is reduced. When the turbine is positioned after the HRSG, with the

assumption of a small heat transfer of 7 MW to the steam in the HRSG (2% of the total heat extracted from the exhaust flow of the GT) the turbine inlet temperature would be 873 °C.

The configuration directly positioned after the afterburner results in a slightly higher efficiency of the SOFC. The effect of the temperature difference is reflected in the system exergy efficiency which is an absolute increase of 0.26% relative to the downstream configuration. The pressure ratio had to consider the forthcoming pressure drop in the HRSG making the increased power not as large as expected. The benefits of the selected position will become more apparent during integration with the CCGT due to the reduced heat integration exergy losses.

Table 5.4: Comparison positions downstream turbine. DST end is positioned all the way downstream, and DST Aftb is positioned directly after the afterburner.

SOFC system	DST end	DST Aftb.
Power [MW]		
Downstream Turbine	-29.40	-29.83
Exergy Efficiency [%]		
SOFC system	62.18	62.44
Exergy destruction [MW]		
Stack	10.43	9.732
Afterburner	7.390	7.389
Downstream Turbine	1.644	1.384
Exergy loss	32.73	33.69

Conclusion

Figure 5.31 shows that the exergy losses decrease by 46% and 43% for the SOFC and SOEC respectively. The optimal position for the downstream turbine turned out to be directly behind the afterburner while for the SOEC only one option was possible. Apart from the exergy losses, the turbine additionally generates 30 MW of power and 5.8 MW for the SOFC and SOEC respectively. The combined reductions cause a 3.2% increase in the SOEC system's exergy efficiency.

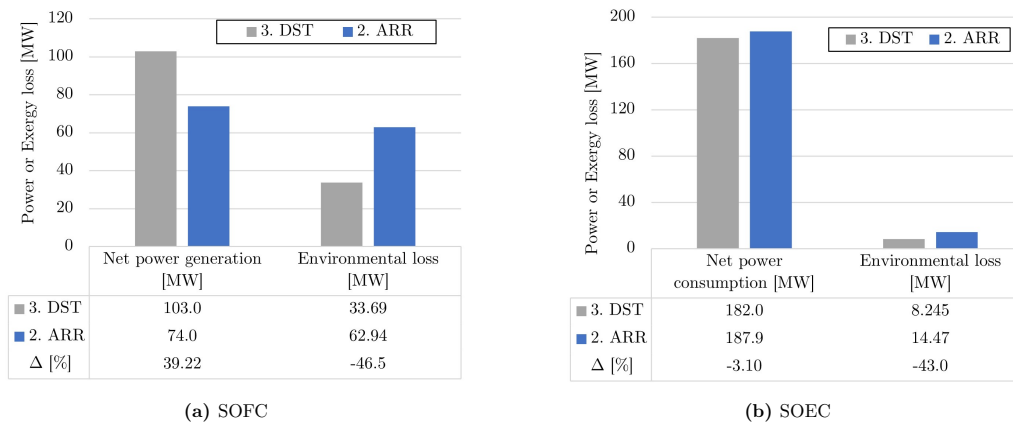


Figure 5.31: Power generation or consumption, and decreased environmental exergy losses of optimization 3: Downstream turbine (grey) vs optimization 2:ARR (blue).

5.2.4. Flowsheet Optimization 4: System Heat Integration

Now that all mass balances are defined, heat integration will be optimized at the system level. For both systems, the electric heaters of the Grid to Stack module consume power to prepare the incoming stream to the proper operating temperature, and the downstream modules (Purification, Purification to Grid, but also the exhaust gasses) require cooling before the system discharges the flows or is allowed to be fed into the hydrogen grid. A pinch analysis determines the optimal heat integration network of the downstream modules² with the upstream module Grid to Stack.

²for SOEC: Purification, Purification to Grid and the exhaust air stream; for the SOFC: Afterburner and the exhaust stream

Redesigning Stack Heat Integration

In the current setup, the air recirculation ratio prevents the outgoing oxygen electrode stream from providing heat to the incoming oxygen electrode current. The high temperature associated with the ARR limits the amount of heat that can be exchanged from the exhaust stream and the incoming fresh air stream (Figure 5.32). To increase the potential heat to be recovered, the downstream turbine is placed between the cell heat integration to enhance the heat duty. The setup in Figure 5.33 can be applied to the SOFC and SOEC.

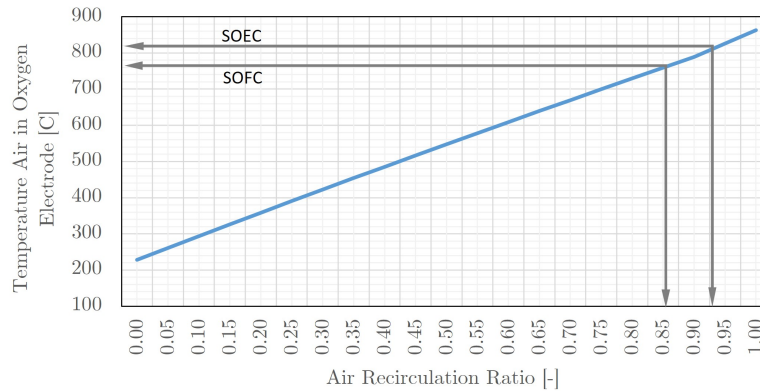


Figure 5.32: Current ARR and corresponding Oxygen Electrode inlet temperature [C].

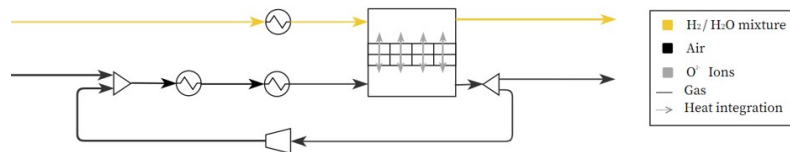


Figure 5.33: Redesigning the SOEC heat integration.

SOEC By moving the heat exchanger to the flow prior to the air mixer, it becomes possible to add more heat to the incoming flow. This lowers the additional electric heating requirements as the addition of heat, together with the increased temperature of the air recirculation flow, causes the incoming stream's temperature to increase even beyond the 850 °C. Figure 5.34 visualizes the SOEC heat exchanger network. In addition, the volume flow of the incoming preceding the mixer than the volume flow after the mixer due to the large ARR airflow and temperature. This can reduce the size of the heat exchanger, reducing the investment cost. In addition, the decreased flow reduces the amount the exergy losses by pressure losses.

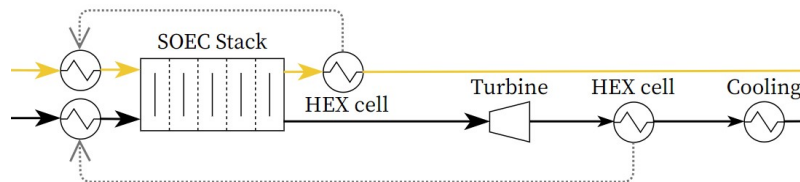


Figure 5.34: SOEC Optimization 4: Cell heat integration.

SOFC Because this work is dedicated to designing a reversible system, this heat exchanger integration is also applied to the SOFC. For equal reasons, the exergy efficiency of the SOFC increases. However, there is a limitation on the amount of heat that can be supplied because the temperature may not

exceed the set limit ($-100\text{ }^{\circ}\text{C}$ below the operating condition). If this limit is exceeded, the same detrimental efficiency drops occur, as shown during the optimal ARR optimization round. To avoid this, an additional Design Specs block is introduced into Aspen Plus that extracts the optimal amount of heat depending on the operating conditions and the ARR. The Design Specs block reduces the external heat demand to 0. Preheating the air before mixing also reduces the exergy destruction of mixing. The cell heat integration of the SOFC is depicted in Figure 5.35.

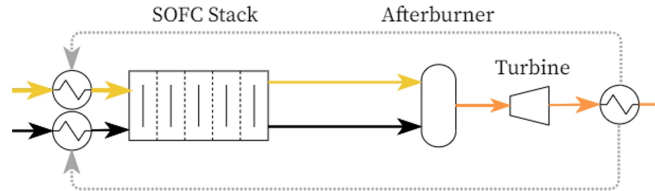


Figure 5.35: SOFC Optimization 4: Cell heat integration.

Upstream and Downstream Pinch Analysis

SOEC In the Grid to Stack module, the required hydrogen must be heated as two successive turbines in order to expand the hydrogen to the required operating pressure at a current pressure ratio of 5. As a result, the hydrogen must be heated which prevents the temperature of the hydrogen from dropping below environmental temperatures to avoid impurities to condensate, and allows the hydrogen to be mixed with the steam with minimal mixing exergy destruction. The incoming water needs to be converted into steam at the dew point so that it can be mixed with hydrogen. The latent heat is the largest contributor to the total heat requirement of the Balance of Plant.

In the current setup, the water cools the hot downstream streams with environmental temperatures. The heat duties are depicted in Table 5.5. The reduction in exergy at these streams is considered pure exergy loss. The hydrogen and water vapor mix are condensed in the purification module by the condenser. The cooling of the disposed air requires the largest amount of cooling.

Table 5.5: SOEC pinch analysis input.

Cooler	T_{in} [C]	T_{out} [C]	Q [MW]	Heater	T_{in} [C]	T_{out} [C]	Q [MW]
Condenser	154	30.0	-8.47	Hydrogen heater 1	25.0	150	0.27
Exhaust air	542	25.0	-9.14	Hydrogen heater 2	56.9	153	0.25
Purification cooler 1	113	30.0	-1.49	Water evaporator	25.1	153	31.5
Purification cooler 2	238	30.0	-3.74				
Purification cooler 3	252	30.0	-3.99				
Purification cooler 4	101	30.0	-0.04				
Total			-26.87	Total			32.0

Figures Appendix A.1 and A.2 show the Aspen Plus pinch analysis results when all the above heat requirements are incorporated into a pinch analysis. The pinch analysis uses hot utility electric heating and cold utility cooling water. Because the incoming water has to be heated from $25\text{ }^{\circ}\text{C}$ to $153\text{ }^{\circ}\text{C}$, it is utilized to lower all downstream streams to $30\text{ }^{\circ}\text{C}$. This heat integration reduced the total external heat requirement of the cooling water from 32.0 MW to 5.13 MW . With this arrangement, the waste heat of the downstream modules supplies all the required heat of the Grid to Stack module. The relevant part of the flow sheet is depicted in Figure 5.36.

stack heat integration. All combined improvements enhance the exegetic performance by 6.4%.

The utilization of the downstream waste heat provided 84% of the total external electric heating duty of the Grid to Stack module. The heating of the incoming water provides all downstream cooling of the SOEC. The system heat integration improved the system tremendously, as is depicted in Figure 5.38b by the four parameters. Ultimately, the system achieves an exergy efficiency of 84.2% (Figure A.3.b in the Appendix A.2).

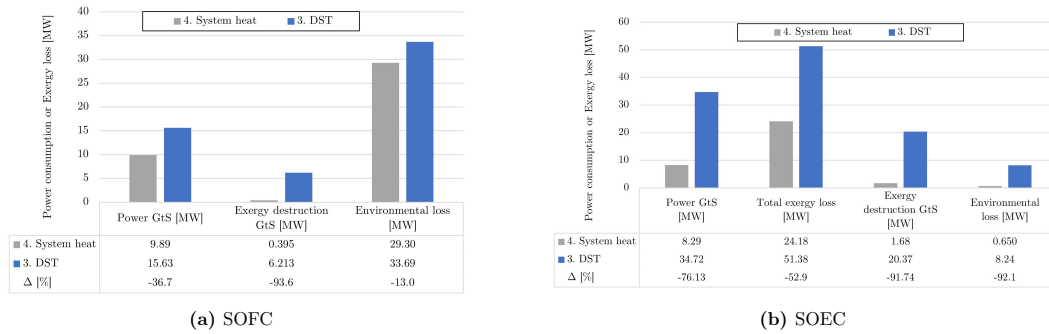


Figure 5.38: Results and improvement of optimization 4: System heat integration (grey) vs. optimization 3: Downstream Turbines.

5.2.5. Revised: Optimal Operating Conditions

Since the analysis of the preliminary results, the past four flowsheet optimizations have significantly modified the flowsheet. The current optimized system is able to recover most of the physical exergy confined in the pressurized and heated streams. The air recirculation reduced the compression power, but affected the cell on an electrochemical level by changing the oxygen concentration. Therefore, it is necessary to analyze the behavior of the current system and review the optimal conditions.

Temperature - SOEC

The P_{SOEC} increases, as higher temperatures demand more external electric preheating to heat the incoming oxygen electrode stream which is visualized in Figure 5.39a. As the temperature of the air recirculation flow increases, so does its volume flow and its compression power required.

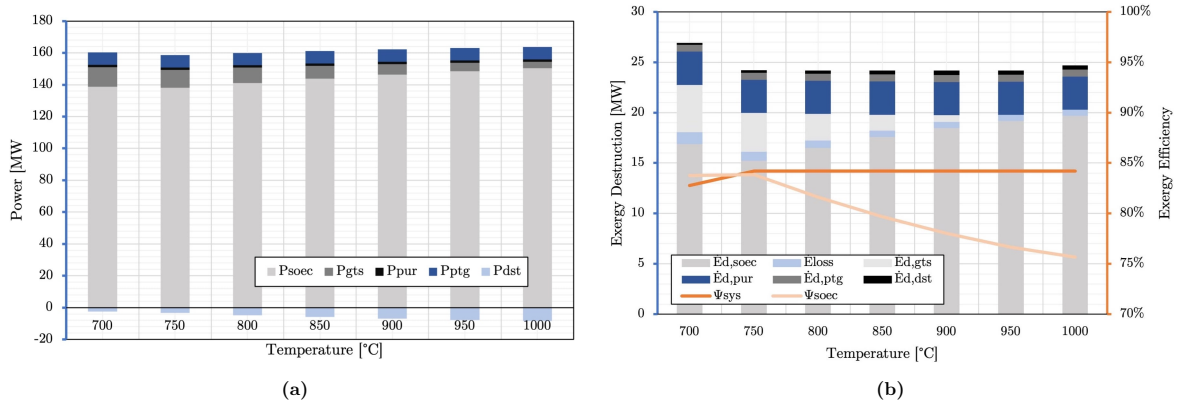


Figure 5.39: SOEC Temperature versus a) System Power, b) System Exergy Destruction and Exergy Efficiency.

Still, the system benefits from the high temperature by reducing the overpotentials of the SOEC, but also by the increased generated power of the downstream turbine. At a lower temperature, the cell is closer to the thermoneutral point, reducing heat duty. Exceeding the exothermic mode at 700 °C causes an increase in the required power of the P_{SOEC} because the cell needs additional cooling. In contrast to the temperature analysis prior to the flowsheet optimizations, the heat can be recovered

causing the increased temperature to have a smaller negative impact than before the optimization.

Figure 5.39b shows the exergy destruction of the modules versus the operating temperature. The total exergy destruction is lowest at $T = 750\text{ }^{\circ}\text{C}$ due to the increased heat duty of the cell. However, the difference between the maximum total exergy destruction at $1000\text{ }^{\circ}\text{C}$, excluding the exothermic mode at $700\text{ }^{\circ}\text{C}$, exceeds the minimum exergy destruction by merely 1.4%.

Temperature - SOFC

The SOFC system benefits from a higher temperature by improving the total power output (Figure 5.40a) while the total exergy destruction decreases (Figure 5.40b). Due to the implemented heat recovery, a higher temperature does not lead to higher heating requirements. The decrease in overpotentials decreases the exergy destruction in the SOFC, thus lowering the heat duty, which results in less required cooling air. Even the increased compression power per mole of the recycled air was compensated by the decrease in the required amount of gas. The diminished total recirculating air reduced exergy destruction across the entire chain of the modules due to reduced pressure losses. Yet the system cannot recover all exergy losses in the form of heat because all upstream heat requirements are met. Therefore, the optimum exergy efficiency is not at the maximum temperature ($1000\text{ }^{\circ}\text{C}$) but between 900 and $950\text{ }^{\circ}\text{C}$.

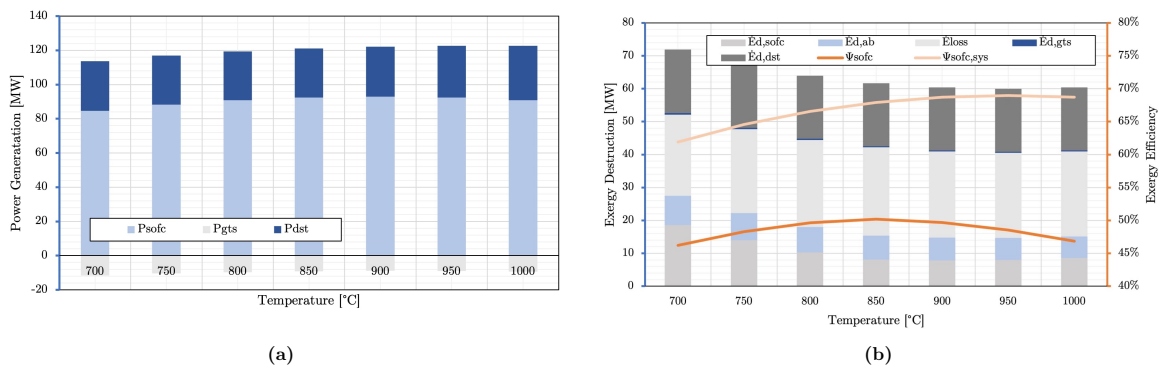


Figure 5.40: SOFC Temperature versus a) System Power, b) System Exergy Destruction and Exergy Efficiency.

Pressure - SOEC

Figure 5.41 shows the relationship between power consumption and pressure. The P_{pur} benefits from increasing pressure because the purification membrane operates at 10 bar. A compressor in front of the membrane compresses the outgoing fuel electrode flow to 10 bar. When the SOEC's operating pressure approaches this required 10 bar, the required power of the compressor decreases.

However, the increased pressure is disadvantageous for the Grid to Stack module which can be noted from Figure 5.41. At 1 bar, the Grid to Stack module actually produces electricity by expanding the incoming hydrogen from 30 bar using turbines (indicated with a negative value). At higher operating pressures this power generation diminishes. The heat exchanger network provides the necessary heat to keep the hydrogen above environmental temperatures. At 1 bar, the generated power exceeds the required electrical heating, resulting in a net power generating Grid to Stack module instead of power consuming.

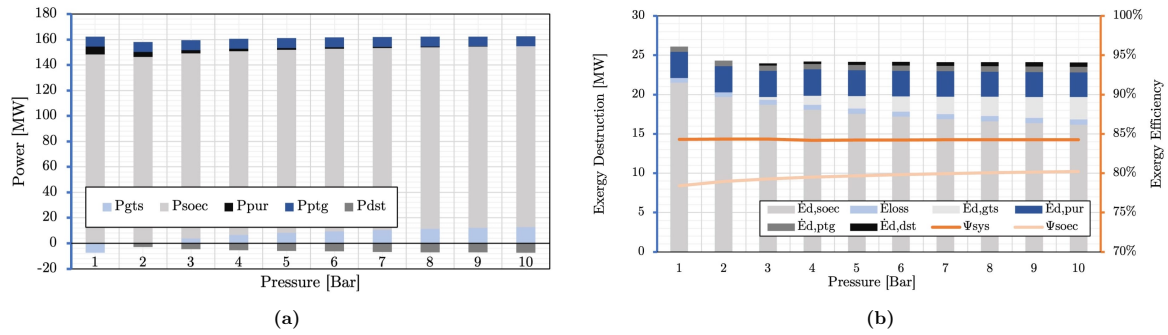


Figure 5.41: SOEC effect of Pressure on a) Power and b) Exergy.

The exergy destruction Ed_{GTS} and Ed_{SOEC} move in opposite directions, as the pressure affects the incoming temperature of the SOEC stack. With higher pressure, the evaporation temperature of water rises, and the temperature of the incoming air increases through compression. The additional compression power thus substitutes for the required heating of the incoming flows in the SOEC stack which benefits the SOEC stack because, during the previous system heat integration optimization round, the heat duty of the Grid to Stack module was shown to exceed the downstream available heat.

Pressure - SOFC

With the current system setup, the system can recover the increased pressure. This enables the system to take advantage of the pressure-related benefits while the physical exergy is not lost to the environment. As is depicted in figure 5.42a, the SOFC is able to increase the power production resulting from the increased cell voltage and electric heating. The downstream turbine simultaneously increases its power output due to the increased pressure ratio, exceeding the power consumption of the Grid to Storage module.

Graph 5.42b shows the relationship between pressure and exergy efficiency. Based on the system’s exergy efficiency, the pressure must be maximized. However, continuing to increase the pressure leads to unfavorable consequences on the Stack level. High pressure leads to higher airflow return temperatures due to the absolute increase of pressure losses. After mixing fresh and recirculated air, the temperature exceeds the required temperature requiring cooling either by extra oxygen or the use of cooling water. This consequence is strongly related to the ARR leading to further exploration of this relation in the next paper.

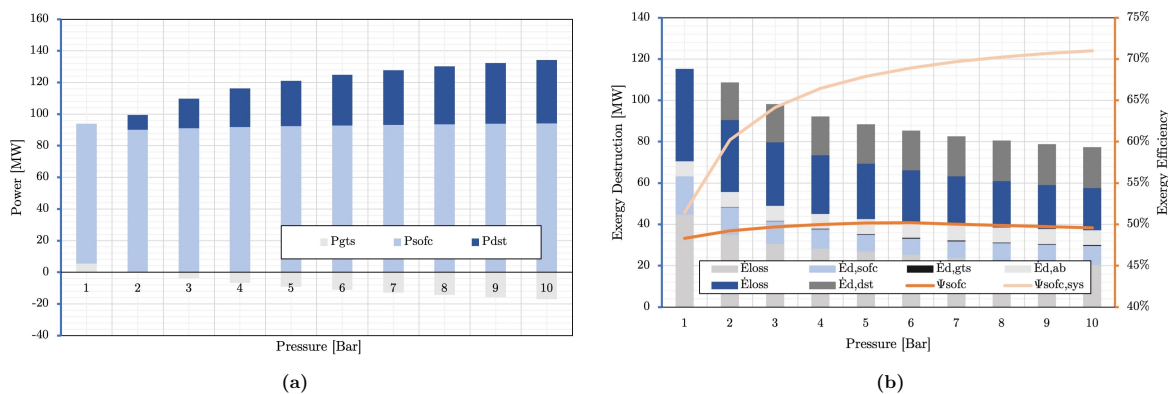


Figure 5.42: SOFC Pressure versus a) System Power, b) System Exergy Destruction and Exergy Efficiency.

Optimal Air Recirculation

The variation of the ARR affects the whole system through multiple relations that were already detected at the air recirculation flowsheet optimization and at the latter examination of optimal pressure.

1. The optimal ARR depends on the operating pressure. Increasing the pressure leads to a lower allowable ARR due to the heat formation in the recirculating pressure, which deals with the pressure losses.
2. The ARR affects the SOC on electrochemical level due to the variation in oxygen concentration negatively influencing the Nernst voltage and concentration losses.
3. Besides, the ARR affects the Afterburner's output temperature by changing the ratio of oxygen to burned hydrogen. At a high ARR, proportionally less air enters the Afterburner compared to the incoming unconverted hydrogen. Increasing temperatures have negative effects on exergy destruction in the constructed heat exchanger network, because the temperature difference increases.
4. The ARR is limited to ensuring an oxygen concentration that complies with the required oxygen to ensure complete combustion which is essential for minimizing the chemical exergy losses to the environment of the exhaust stream.
5. During the ARR optimization in Section 5.2.2, the ARR allowed the compression power and external heating to go down significantly boosting the efficiency.

Optimizer An Aspen optimizer³ is able to process these complex relationships and constraints to determine the optimal ARR. The tool optimizes the SOFC's system exergy efficiency where the tool varies the pressure and the ARR simultaneously. Two boundary conditions are set: 1) the temperature of the mixed incoming oxygen electrode air stream must not exceed the SOFC cooling temperature and 2) the temperature of the outgoing flow from the downstream turbine must be 5 °C higher than the incoming fuel electrode flow to ensure maximum heat transfer.

The optimized result for the SOFC system is a pressure of 7 bar with an ARR of 0.745. The system recovers maximum heat because the outgoing temperature of the compressor ends up exactly 5 °C higher than the temperature of the incoming fuel electrode stream: The incoming fuel electrode temperature should be 800 °C at an operating temperature of 900 °C.

In contrast to the SOFC, the SOEC system is not subjected to temperature-related boundary conditions. During SOFC mode operating at 900 °C, the incoming oxygen electrode steam is limited to 800 °C to cool the stack. However, during the SOEC operation, a higher incoming air temperature is beneficial to the SOEC system because it reduces the required electric heating.

Conclusion Optimal ARR

The increasing recirculation compression power is compensated by the decrease in downstream compression power. This allows the SOEC optimization to look primarily at pressure and temperature instead of the ARR. These operating conditions must match those of the SOFC. The optimal ARR was kept at 0.93 at the operating pressure and temperature of 7 bar and 900 °C respectively. The compressors of the SOFC and SOEC are at these conditions of about the same size (33 MW and 38 MW for the SOEC and SOFC respectively). This allows the same compressor to be used for both systems.

The maximization of the multiplication of both exergy efficiencies led to the selection of the current operating conditions which mainly enhance the performance of the SOFC system by 10% while the SOEC increases the SOEC system efficiency with only 0.07%. The increases in fresh air requirements, temperature, and pressure result in an increase in the electricity generated by the stack and turbine. This exceeds the increase in P_{GtS} to prepare the incoming fuels for the stack. The SOEC benefited less than the SOFC from the changed operating conditions because the SOEC system utilized the majority of the environmental exergy losses and therefore responded less vigorously to the changes. Due to the temperature increase, the SOEC operates more distant from the thermoneutral point. The higher temperature harms the performance of the SOEC stack (-2%) but benefits the system (+0.07%).

³Aspen Plus describes the optimization tool as: "A tool to maximize or minimize a user-specified objective function by manipulating flowsheet variables. Equality or inequality constraints may be imposed on the optimization."

5.2.6. Conclusion SOC Optimization

This concludes the SOC system-focused optimization. The optimization modified and improved the standard cell of Hauck et al. [16] by maximizing the performance of the entire system. It started with a SOFC system that required 171 MW with an exergy efficiency of -104% and total exergy destruction of 317 MW. The final optimized SOFC system ends up generating 120.7 MW of power, at an exergy efficiency of 73.1% with a reduction of 89% of the exergy destruction, as can be seen from Table 5.6a.

As can be seen from Table 5.6b, the SOEC system operates at an exergy efficiency of 84.3%. The minimization of physical exergy losses by the applied heat integration and pressure recovery, reduced the exergy losses by 99% and the total exergy destruction to 24 MW. For the same amount of hydrogen produced, the SOEC demands 155 MW instead of 425 MW.

Table 5.6: Comparison of the current system after the five optimization rounds and the systems prior to the flowsheet optimization.

(a) SOFC				(b) SOEC			
SOFC system	5. Revised	0. Start	Δ	SOEC system	5. Revised	0. Start	Δ
Gas (kg/s)				Gas (kg/s)			
H2 in	1.363	1.363	-	H2 (Net out)	1.090	1.090	-
H2O	0.377	0.377	-	H2O	12.19	12.19	-
Air	80.4	320.9	-240	Air	10.50	254.5	-244
Power Generation [MW]				Power Consumption [MW]			
Total	120.7	-170.9	292	Total	155.1	424.6	-270
Stack	95.10	-101.9	197	Stack	145.2	337.6	-192
Grid to Stack	-18.57	-68.99	50.4	Grid to Stack	9.165	77.76	-68.6
Downstream Turbine	44.13	-	44.1	Purification	0.772	1.504	-0.73
				Purification to Grid	7.731	7.731	-
				Downstream Turbine	-7.841	-	-7.84
Exergy efficiency [%]				Exergy efficiency [%]			
SOFC system	73.14	-103.7	177	SOEC system	84.27	30.78	53.5
Exergy destruction [MW]				Exergy destruction [MW]			
Total	36.35	316.5	-280	Total	24.05	293.9	-270
Grid to Stack	0.771	10.19	-9.42	Grid to Stack	1.290	21.40	-20.1
Stack	6.217	81.05	-74.8	Stack	17.69	104.1	-86.4
Exergy loss	18.89	209.0	-190	Exergy loss	0.616	164.1	-163
Downstream Turbine	2.226	-	2.23	Downstream Turbine	0.533	-	0.53
Afterburner	8.241	16.28	-8.03	Purification	3.230	3.691	-0.46
				Purification to Grid	0.689	0.689	-

With the optimized system, the system lower the total exergy destruction significantly while considering the bifunctional mode. All the heat required by the SOFC could be provided by the system itself with the current setup. In addition, the environmental losses of the SOEC in the form of heat were almost reduced to zero. The optimized operation conditions are shown in Table 5.43.

Parameter	SOEC	SOFC	Unit
Current density	5000	5000	A/m ²
Fuel concentration	0.90	0.97	-
Temperature	900	900	C
Pressure	7.00	7.00	bar
ARR	0.930	0.745	-

Figure 5.43: Final operating conditions after optimized SOC. Concentration definition is dependent on the SOC mode: SOFC mode; [H₂], SOEC mode; [H₂O].

Scaling

Before these optimization rounds start, the size of the SOFC system is downscaled. Prior to the optimizations, the SOFC system consumed a fixed amount of hydrogen that equaled 100 MW of Δ Gibbs

free energy. The current system is able to generate more power with the same amount of hydrogen. Before integrating the system into the CCGT, the SOFC is scaled to 100 MW to match the desired power output. After scaling, the rSOC flowsheet and the system capacities are fixed. The scaling has no effect on the performance, only after the moment that the system is presumed to be fixed will the deviation from these capabilities influence the performance.

The SOFC system net generation of 100 MW was achieved by reducing the hydrogen consumption by 20.7%. The number of cells of both modes is scaled down accordingly to maintain the current density of 5000 A/m². In order for the SOEC to change with the same amount of cells while maintaining the current density, the systems input and thus the power output was also decreased by 20.7%, resulting in a capacity of 128.7 MW.

5.3. SOFC CCGT

Now that all the upstream SOFC optimizations have been implemented, the SOFC-CCGT integration is examined. The afterburner, which is positioned sequentially to the SOFC, converts the chemical energy conserved by the residual hydrogen into heat. When appropriately modeled, the CCGT utilizes the heat to enhance the combined system performance. The optimization is performed while considering the operating conditions of the original CCGT that matches the validated models in Chapter 4. The constructed models result in the Optimization cases 1A, 2A, 1B and 2B, which will be used to compare with the original CCGT. The models are divided into full- or part load, and the power generating plant or the combined heat and power plant. A recap is listed below. The execution of the heat integration will be discussed in this Chapter. However, the comparison of the resulting models with the Base cases is done in the following Chapter 6.

- Optimization case 1A ensures the CCGT to operate at full load while considering the SOFC heat integration. This allows to properly compare the decoupled systems (separate SOFC and CCGT of Base case 1A) to the new proposed system (SOFC-CCGT of Optimization case 1A).
- Optimization case 2A equals the total generated power of the SOFC-CCGT to the generated power of the original CCGT (Base case 2A), so that the SOFC-CCGT systems are compared while generating the same power output.
- The same is applied for the SOFC-CCGT CHP plant at full load (Optimization case 1B). The performance of the decoupled systems (SOFC and CCGT CHP of Base case 1B) is compared with the coupled systems.
- The last system Optimization case 2B ensures that the heat generation of the coupled SOFC-CCGT CHP matches the original CHP (Base case 2B) while the power generation is allowed to differ.

Heat can be inserted at multiple locations of the CCGT flowsheet. Two locations are applied in this work which was based on the findings in the literature review [34][38][66]: the heat transfer to the working fluid of the downstream ST, and to the GT's fuel preheater. The capacity of heat transfer was leading to the determination of the implementation sequence of implementing this optimization.

5.3.1. SOFC-CCGT HRSG

The SOFC exhaust stream provides additional heat to the HRSG that is conventionally supplied by the GT exhaust gases. The additional heat transmitted would be discharged to the environment by the condenser without any improvements to the system. Besides, adding heat would disturb the heat balance in the HRSG, which makes it impossible to ensure the proper operation of the CCGT with the current Aspen model.

Consequently, the system must find a method to absorb the SOFC's heat without structurally deviating from the ST operating conditions. There are two design considerations, either the heat originally supplied by the GT to the HRSG must be reduced in order to decrease the heat supplied by the GT exhaust flow, or the total heat absorption of the HRSG must increase by increasing the recirculating water and steam. During the full load operation in Optimization case 1A, the latter is not possible

because the STs are running at full load. As a result, the first option is applied causing the load of the GT to slightly deviate from its normal operating conditions. The consequences of deviation are discussed in the coming section. The additional heat addition of the SOFC ensures the operation of the STs remains as its original setup. The schematic flowsheet is depicted in Figure 5.44.

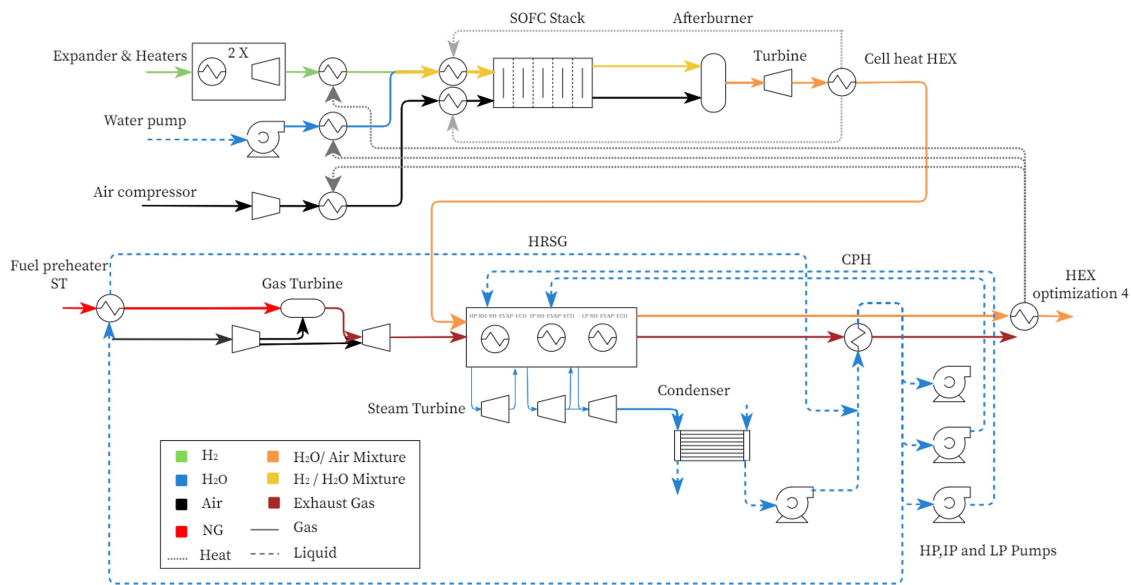


Figure 5.44: SOFC-CCGT flowsheet with heat transfer from the SOFC exhaust flow to the HRSG.

Model Modification

As a response, the required fuel to supply the HRSG with sufficient heat ensuring the operating conditions of the original ST needs to be slightly reduced. The addition of heat supplied by the SOFC is intended to serve as a substitute for the heat generated by the GT. The reduction of gas depends on the amount of total heat supplied by the SOFC. Still, the residual heat confined in the exhaust gasses of the 100 MW SOFC is small, compared to the 440 MW CCGT.

To ensure the original heat and mass balance in the STs, the model initially maintains the GT system exhaust temperature of 91 °C, which corresponds to the original configuration. This exhaust temperature is assumed to ensure the HRSG is supplied with sufficient heat. To approximate the effect of SOFC heat integration, minor adjustments are assumed to be allowed when taking into account the part load operating conditions provided THERMOFLEX models, the load correction curve (discussed in Chapter 4), and the assured flexibility of the SGT5-4000 GT at non-standard conditions [93] [13].

The Aspen model calculates the proper gas supply that maintains the original exhaust temperature and scales the air accordingly to match the fuel-to-air ratio of the reference models. This replaces the heat source of the HRSG from the combustion of natural gas to the combustion of the remaining hydrogen. Since the applied setup ensures the same load and system operating conditions for the STs, the isentropic efficiency correction only needs to be applied to the GT's compressor and turbine.

Decreasing the GT load affects the performance of the system by two opposing relations. The reduced gas consumption affects the GT by the decrease in load due to the load correction. However, the heat supply by the SOFC increases the produced power while simultaneously decreasing the natural gas fuel consumption. These two opposing effects play a key role during the optimization of the SOFC-CCGT integration. Nevertheless, this work attempts to match the operating conditions of the original setup while modifying the heat source. The reduction of gas, the resulting power output and correction factors are depicted in Table 5.7.

The heat is supplied after the first reheater of the HRSG to match the temperature of the GT exhaust stream (514 °C) and the SOFC exhaust stream (547 °C) to prevent exergy destruction. This work does not discuss further the optimal location of the heat integration in the HRSG, due to the assumed simplification of the heat exchangers, no conclusions can be drawn on this matter. The boundary conditions are related to the heat duty and the minimum exhaust temperature of the SOFC. The SOFC must still be able to supply heat to the Grid to Stack module. The Grid to Stack module requires temperatures of up to 185 °C and a total of 5.2 MW. In addition, the SOFC exhaust stream must be able to provide the incoming water flows of the three pressure levels of the HRSG after the CPH at 149 °C.

Implication SOFC-HRSG

Table 5.7 compares the system with the HRSG heat integration to the uncoupled system. The implications of integration are briefly discussed, but the results are elaborated on in the next Chapter. The heat exchangers transfer a total of 27.3 MW to the HRSG while still being able to deliver heat to the Grid to Stack module. The heat transfer lowers the exergy losses of the fuel cell by 65% by reducing the exhaust gas from 453 °C to 120 °C. Heat coupling induces a reduction the of natural gas required by 7% to accommodate heat absorption of 27 MW along the length of the HRSG. This means an isentropic efficiency correction of the GT by 0.83% when applying the load correction curve of Brouwer et al. [15]. The next Chapter elaborates on these synergies by comparing the exergy flows. The operating pressure and pressure ratios are the same as mentioned in the original simulation of the Hemweg 9 CCGT which can be found in Table 4.3.

5.3.2. SOFC-CCGT Preheater

Because the exergy losses of the SOFC have not yet been minimized, the exhaust flow after heat integration with the HRSG and Grid to Stack module is still 120 °C, the possibility of supplying heat to the GT is being considered.

The literature review provided two options for the SOFC-GT heat integration. The first is air preheating which is applied after the compression of air [38][34]. However, tapping the compressed airflow to preheat cannot be accomplished without major modifications to the turbine. Therefore, this adjustment is very unlikely in a retrofitted GT. Heating the air stream before it enters the compressor deteriorates the system's performance because heated air streams require more compressor power. Besides, heating an airflow of 671 kg/s requires a huge heat exchanger, increasing the component costs and plant size.

The second heat integration technique is the preheating of GT's fuel. The fuel preheating takes place before it enters the GT, which allows the optimization to be applied without major modifications [94][38]. In the current CCGT, the fuel is preheated to 156 °C to avoid the Joule-Thomson effect, which prevents the condensation of the fuel during the decrease of the fuel's pressure when entering the combustion chamber. Expanding the amount of transferred heat to the fuel improves the system efficiency and could reduce the fuel consumption [94].

Model Modification

Preheating the incoming GT fuel increases the Turbine Inlet Temperature, resulting in an increase of generated power [38]. With the increase in the total supplied heat of the SOFC, the gas consumption should decrease accordingly to maintain the exhaust temperature.

In the current GT, the incoming fuel is already preheated to 156 °C by a stream of water tapped from the stream after the CPH at the Intermediate Pressure level. The Hemweg 9 GT allows a maximum fuel preheating temperature of 200 °C [77] which allows using the exhaust stream from the SOFC after the SOFC-HRSG. This stream has a temperature of 219 °C. The modified flowsheet is depicted in Figure 5.45.

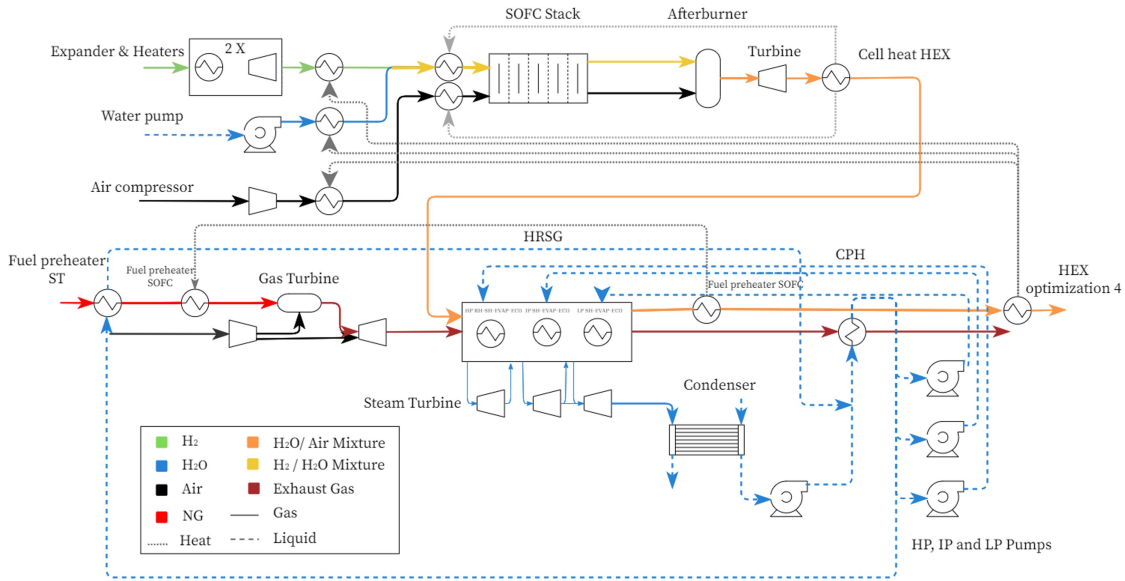
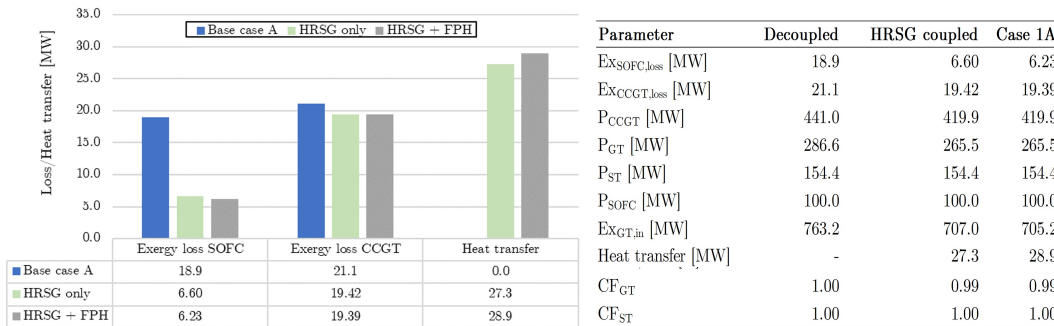


Figure 5.45: SOFC-CCGT flowsheet with heat transfer to from the SOFC exhaust flow to the HRSG and fuel preheater. The fuel preheater is positioned after the HRSG.

Implication SOFC-HRSG-FPH

With a heat transfer of 1.46 MW, the fuel increases from 156 °C to the permitted 200 °C. The hot side of the heat exchanger goes from 219 °C to 201 °C. The fuel preheating enhances the total heat transfer between the SOFC and the CCGT by 5.9 % to 28.9 MW, which reduces the gas consumption by 0.35%. The exergy losses of the SOFC decrease by another 5.6%. Although the GT isentropic correction factor was decreased, the exergy efficiency of the system improves by 0.20%.

Table 5.7: Comparison between the system of Base case 1A (two SOFC and CCGT decoupled systems), the integration with HRSG, and the integration with the HRSG and the fuel preheater (FPH). The latter defines Optimization case 1A. All units are in [MW]. CF is the isentropic correction factor of the turbomachinery.



5.3.3. Part Load SOFC-CCGT

For part load, the operating conditions of the 290 MW reference case are maintained as is described in Chapter 4.1.1. However, the coupling between the 290 MW CCGT at part load and the 100 MW SOFC does not result in the required 441 MW for the comparison between the Base case 2A. To accommodate this, mass flows in the GT and ST are scaled proportionally to achieve the total capacity of the integrated system to 441 MW. To approximate the deviations in the system’s performance, the isentropic efficiency correction is applied to the compressor, GT and STs. The consequences of the downscaling of Optimization case 1A and 2A on the turbomachinery is depicted in Table 5.9. The deviation of the residual components is unaffected. Nevertheless, it was assumed after the validation in Chapter 4.1.1 that the correction sufficiently approximated the performance of the system.

Table 5.8: Fuel input, Turbine power output and applied turbomachinery isentropic efficiency for the original CCGT simulation and optimized Cases 1A and 2A.

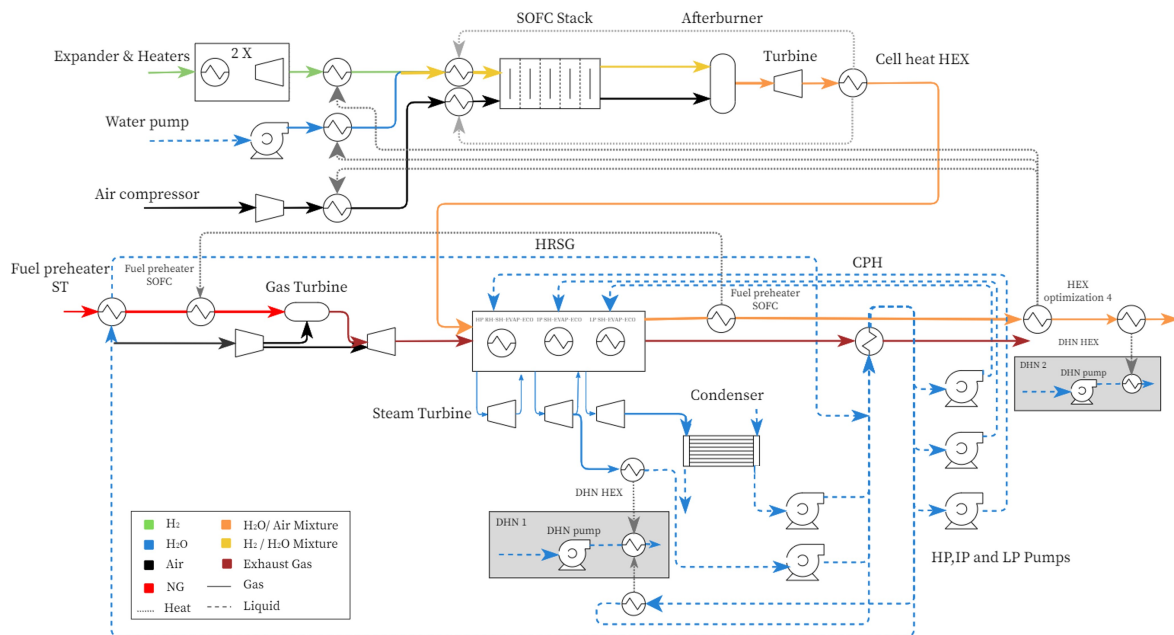
Parameter	Original CCGT		Case 1A		Case 2A	
Gas consumption [kg/s]	15.9		14.7		12.6	
Turbine	Net P _e [MW]	Isentropic efficiency	Net P _e [MW]	Isentropic efficiency	Net P _e [MW]	Isentropic efficiency
GT	284	Compressor = 87.0% Turbine = 92.5%	263	Compressor = 86.1% Turbine = 91.6%	195	Compressor = 84.6% Turbine = 89.9%
LP-ST	31.0	92.0%	31.0	92.0%	30.3	91.6%
IP-ST	50.9	94.5%	50.9	94.5%	48.1	94.0%
HP-ST	75.0	91.7%	75.0	91.7%	67.5	90.5%

5.4. SOFC CCGT CHP

Finally, the integration of the SOFC with the CCGT CHP plant is also being investigated. Because the CHP employs a connection to the DHN, the system can transfer more heat, lowering its exhaust temperature. This presumably allows the SOFC to dissipate more heat and lower its exhaust temperature to the return temperature of the DHN. The added value will be demonstrated from the following analysis.

5.4.1. Model Modification

The SOFC is coupled similarly to the previous analyses, but this time the SOFC gets an additional heat exchanger added at the very end of its exhaust stream, which represents the connection to the DHN. The resulting SOFC CCGT CHP plant utilizes the downstream SOFC environmental exergy losses by cooling down the SOFC exhaust gasses to supply the DHN. With the construction of the connection to the DHN in the CCGT CHP plant of Base cases B, the SOFC could also be connected to the same grid. Figure 5.46 depicts the final flowsheet of the SOFC-CCGT CHP plant.

**Figure 5.46:** Resulting SOFC-CCGT CHP flowsheet. DNH1 receives heat from the bleed between the IP- and LP- ST, and from the CPH splitted water flow. DNH2 utilizes the SOFC's downstream exhaust gas.

Heat Alignment

The temperatures of the heat integration network connected to the Grid to Stack module need to be modified in order to supply heat to the DHN. Consequently, the temperatures of the Grid to Stack heat exchanger network were adjusted from 180 °C to 160 °C, which is just above the vaporization temperature of water at the operating pressure of 7 bar. This slightly reduces the generated power of

the turbines but this allows the downstream heat integration to be able to deliver all the heat.

By adjusting the upstream heat integration temperatures to 160 °C, the exhaust temperature of the SOFC (115 °C) is sufficient for supplying the DHN with heat. Considering the minimum pinch temperature of 5 °C and a DHN return temperature of 60 °C, the heat transfer is maximized if the SOFC exhaust gas is 65 °C. The Aspen model automatically calculates the right amount of water flow to achieve this temperature. This minimizes exergy destruction by the heat integration with the DHN.

Adjustments to ARR and temperature were also considered to increase the total amount of potential heat. Both adjustments resulted in lower efficiency despite the additional heat delivered. The effect of changing the temperature resulted in the increased heat duty of the SOFC electrode preheaters, preventing the increased temperature from reaching downstream heat integration. In addition, the higher temperature led to increased compression power of the SOFC's recirculation compressor, decreasing the system efficiency.

The selected ARR by the Aspen optimizer proved to be optimal, the reduction in SOFC exergy efficiency outweighed the improvement of the CCGT. If the ARR was reduced, increasing the exhaust flow but at the same time decreasing the temperature, the heat integration could no longer meet the boundary conditions. An increase led to increased compression power that reduced the efficiency.

Implication and Part Load

Similarly to the previous model, the GT operates at nearly full load to enable the addition of residual heat from the SOFC. The same small gas reduction was applied as with the power plant. This provides the DHN with an additional 5.94 MW_{th}.

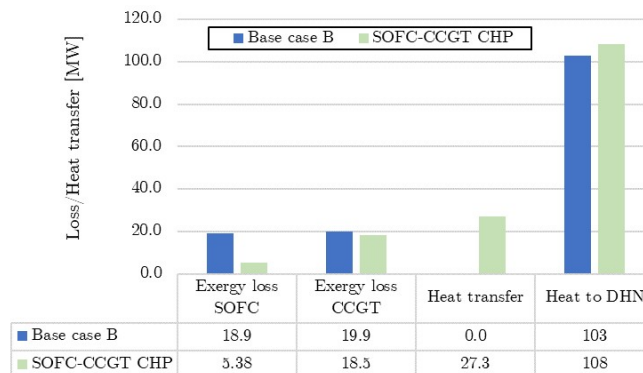


Figure 5.47: Comparison between the decoupled SOFC and CCGT CHP systems (Base case 2B), and the optimized SOFC-CCGT CHP. The latter defines Optimization case 1B. All units are in [MW].

The part load of the CHP plant of Optimization case 2B differentiates from the power plant of Optimization case 2A, because it does not scale to the generated power, but to the generated heat. The original 103 MW is obtained by scaling the load of the CCGT CHP to match the total heat generation of the SOFC-CCGT CHP. The consequences of the downscaling of Optimization case 1B and 2B on the turbomachinery is depicted in Table 5.9. The in-depth comparison is covered in the next chapter.

Table 5.9: Fuel input, Turbine power output and applied turbomachinery isentropic efficiency for the original CCGT CHP simulation and optimized Cases 1B and 2B.

Parameter	Original CCGT CHP		Case 1B		Case 2B	
Gas consumption [kg/s]	15.9		14.8		13.9	
Turbine	Net P _e [MW]	Isentropic efficiency	Net P _e [MW]	Isentropic efficiency	Net P _e [MW]	Isentropic efficiency
GT	284	Compressor = 87.0% Turbine = 92.5%	264	Compressor = 86.1% Turbine = 91.6%	249	Compressor = 85.6% Turbine = 90.9%
HP-ST	30.3	91.9%	30.3	91.9%	28.6	91.6%
IP-ST	53.3	94.5%	53.3	94.5%	50.4	94.1%
LP-ST	49.3	90.0%	49.3	90.0%	46.5	89.0%

6

Results and Discussion

With all optimizations being completed, the optimized systems can be compared to the original systems. The four systems 1A, 2A, 1B and 2B were designed to contribute to the final comparison of the exegeric performance and weighed CO₂e emissions with the original system. To clarify, Table 6.1 restates which systems are compared to one another and what parameters are adhered to.

Table 6.1: Comparisons overview with system power and heat output.

Comparison	Base case	Optimization case
1A	CCGT & SOFC <u>full load</u> decoupled	CCGT-SOFC <u>full load</u> coupled
Power [MW]	CCGT: 441, SOFC 100	CCGT + SOFC: 518
Heat [MW]	-	-
2A	CCGT full load	CCGT-SOFC part load coupled
Power [MW]	CCGT: <u>441</u>	CCGT + SOFC: <u>441</u>
Heat [MW]	-	-
1B	CCGT & SOFC <u>full load</u> decoupled	CCGT-SOFC <u>full load</u> coupled
Power [MW]	CCGT: 417, SOFC 100	CCGT + SOFC: 497
Heat [MW]	CCGT: 103, SOFC 0	CCGT: 103, SOFC 5
2B	CCGT full load	CCGT-SOFC part load
Power [MW]	CCGT: 417	CCGT + SOFC: 474
Heat [MW]	CCGT: <u>103</u>	CCGT + SOFC: <u>103</u>

In comparison 1A and 2A, the systems generate no heat. In comparison 1A, the systems operate at full load. The decoupled system (Base case 1A) is compared to the coupled system (Optimization case 1A). In comparison 2A, the power output of the coupled system (Optimization case 2A) is matched to the original CCGT (Base case 2A). In comparison 1B and 2B, the systems generate heat. In comparison 1B, the systems operate at full load. The decoupled system (Base case 1B) is compared to the coupled system (Optimization case 1B). In comparison 2B, the heat output of the coupled system (Optimization case 2B) is matched to the original CCGT CHP (Base case 2B).

6.1. Assessing the Benefits Based on Exegeric Performance (Subjective 1)

In the next four comparisons, the exergy flows of the base cases and the optimized models are compared using exergy Sankey diagrams and tables. Because the Sankey diagrams are expressed in relative numbers to the input exergy, the tables give the absolute numbers. Appendix A.4 also contains tables showing the relative differences to which this chapter also frequently refers.

6.1.1. Results Optimization Case 1A: Full Load

The exergy Sankey diagram Figure 6.1 visualizes the results of the SOFC-CCGT integration at full load, where the exergy flows are expressed relative to the total exergy input of the gas and hydrogen.

From the figure, the exergy efficiencies can be deduced. The useful exergy (visualized in green arrows and for the SOFC also the purple arrows) relative to the exergy input of the individual system (blue blocks) define the exergy efficiency of the individual systems¹.

The SOFC benefits the most from integration, the SOFC operates at an exergy efficiency of 83.91%, while the stand-alone CCGT also increases the exergy efficiency to 58.00%. The SOFC delivers 11.77%² of its exergy to the CCGT through the indirect heat coupling, which accounts for 1.91% of the total exergy input. About 10% of the total transferred heat is lost due to heat transfer exergy destruction. The exergy efficiency of the system is calculated by counting the green arrows as useful exergy divided by the exergy of the fuels (blue blocks).

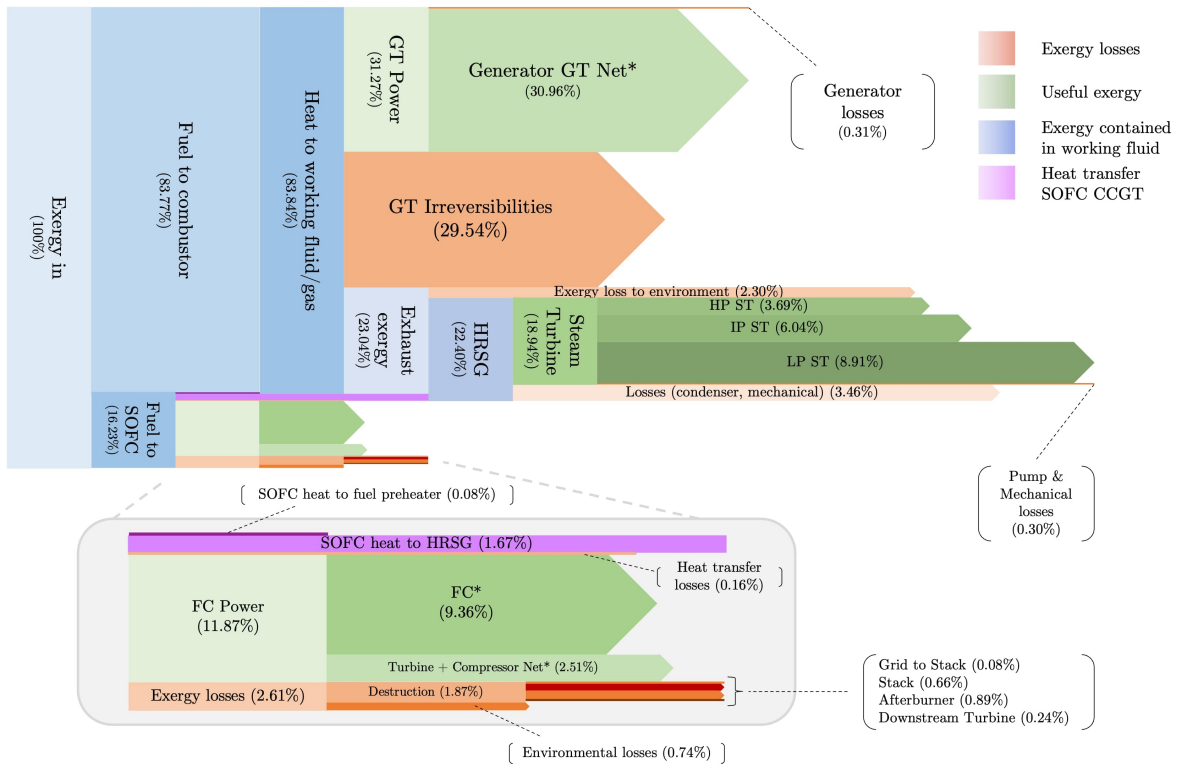


Figure 6.1: Sankey exergy diagram Optimization case 1A: SOFC-CCGT full load. *Net = The power consumption subtracted from the power generation.

Comparison with Base Case 1A

To properly measure the effect of the integration at full load, the SOFC was included in the comparison at Base case 1A but without heat coupling. Thus, the SOFC and the CCGT operate independently of each other. During the integration of the SOFC with the CCGT in Optimization case 1A, the gas consumption had to be reduced to accommodate the heat provided by the indirect heat coupling. This results in an absolute gas reduction of 7.6%, while the absolute power reduction of the CCGT only decreases by 5.24% 6.2. The implication of the applied isentropic correction factor on the turbomachinery of the GT is reflected when comparing the GT's irreversibilities to the reduction of gas consumption. The correction factor results in a lower absolute reduction in GT irreversibilities (-7.00%) than gas consumption decreases (-7.60%), meaning relative losses have increased.

In order to compare the two systems with different capacities, the relative differences must also be considered, expressing exergy flows relative to the total exergy input of the specific system in Appendix A.3. The total exergy destruction decreased by 9.7% (Table 6.2). However, as can be seen in Appendix

¹ $\Psi_{SOFC} = (FC\ Power + SOFC\ heat\ to\ HRSG + SOFC\ heat\ to\ fuel\ preheater) / Fuel\ to\ SOFC$ and $\Psi_{CCGT} = (Generator\ GT\ Net + ST - Pump\ \&\ Mechanical\ losses) / (Fuel\ to\ combustor + SOFC\ heat\ to\ HRSG + SOFC\ heat\ to\ fuel\ preheater)$
² $(1.67+0.08+0.16)/16.23$

A.3, the relative exergy destruction decreases by 1.39%, caused by the large reduction of exergy destruction of the SOFC. Furthermore, heat integration reduces the environmental losses of the SOFC by 67.1%. The environmental losses of the SOFC decoupled system in Base case 1A are used for heat integration with the CCGT in Optimization case 1A.

In addition, the Grid to Stack module benefits from the system integration (-84.2% relative exergy destruction) as the temperatures of the hot and cold side of the SOFC system heat integration are brought closer together because of the heat integration of the SOFC and the CCGT, which is positioned upstream of the SOFC system heat integration. In the decoupled system, the incoming hot stream temperature is 512 °C and leaves at 453 °C, while the maximum cold outgoing stream is 200 °C. In the coupled system, the incoming hot stream temperature is 165 °C and leaves at 99 °C, while the maximum cold outgoing is 160 °C.

Table 6.2: Absolute exergy differences of Base case 1A and Optimization case 1A.

Exergy input/losses [MW]	Base case 1A	Case 1A	Δ%
Exergy in	900	842	-6.44
Natural gas	763	705	-7.60
Hydrogen	137	137	-
Exergy out	541	518	-4.28
Power	541	518	-
CCGT	441	418	-5.24
SOFC	100	100	-
Exergy destruction	359	324	-9.7
CCGT	323	302	-6.26
Irreversibilities GT	267	249	-7.00
Generator losses	2.87	2.63	-8.13
Pump + mechanical losses	2.54	2.54	-
Environmental GT	21.1	19.4	-8.12
Condenser + irreversibilities ST	28.7	29.1	1.62
SOFC	36.7	20.6	-43.7
Grid to Stack	3.96	0.63	-84.2
Stack	5.10	5.10	-
Afterburner	6.83	6.83	-
Turbine	1.85	1.85	-
Environmental	18.9	6.23	-67.1
Exergy integration	-	16.1	-
Exergy exchanged HRSG	-	14.1	-
Exergy exchanged FPH	-	0.66	-
Exergy losses integration	-	1.36	-
Exergy efficiency [%]	Base case 1A	Case 1A	Δ
SOFC	73.14	83.91	10.76
CCGT	57.74	58.00	0.27
SOFC-CCGT	60.08	61.47	1.39

Conclusion Comparison 1A

The above advantages outweigh the decreased isentropic efficiency of the gas turbomachinery. The integrated SOFC-CCGT system has an exergy efficiency of 61.47% which is an increase of 1.39% over the two separate systems at full load. The CCGT also performs 0.27% better if the heat supplied by the SOFC is considered (58.0%) than the CCGT without the heat supply of the SOFC (57.7%). To find out whether the exergy efficiency of Optimization case 1A is higher than that of Base case 1A, the exergy efficiency of the stand-alone CCGT (57.74%) was compared with the SOFC-CCGT (61.47%). The indirect coupling of the retrofitted SOFC-CCGT improves the exergy efficiency of the stand-alone CCGT by 3.74% and with this improvement, it can be concluded that Optimization case 1A outperforms Base case 1A based on its exergy efficiency.

6.1.2. Results Optimization Case 2A: Part Load

For the following analysis, it was ensured that the total capacities of the two systems matched each other. Figure 6.2 shows the relative exergy flows of the scaled model, Optimization case 2A. The total power generated by the SOFC is maintained at 100 MW, but the CCGT is scaled to generate 441 MW, which corresponds to the standalone CCGT at full load (Base case 2A). This comparison allows examination of the effect of the applied part load operation of the CCGT to enable the integration of the SOFC, while keeping the total power equal to that of the original CCGT.

Figure 6.2 shows that the SOFC has a capacity that is relatively larger when compared to the CCGT than the latter Optimization case 1A in Figure 6.1. The scaled down CCGT capacity will have an opposite effect: On the one hand, the SOFC has a higher exergy efficiency, so that proportionally the weighted efficiency ought to go up. On the other hand, the part load operation of the CCGT degrades the CCGT's performance, because it operates at a sub-optimal point away from the full load design point. Additionally, the decreased capacity of the CCGT may limit the heat that the CCGT could potentially absorb due to the disturbed relative capacities of the systems which would increase the environmental exergy losses. In Optimization case 2A, the SOFC supplies 0.08% of the total exergy in the form of heat to the FPH and 1.90% to the HRSG while 0.19% being destroyed by the heat transfer (depicted in purple in Figure 6.2).

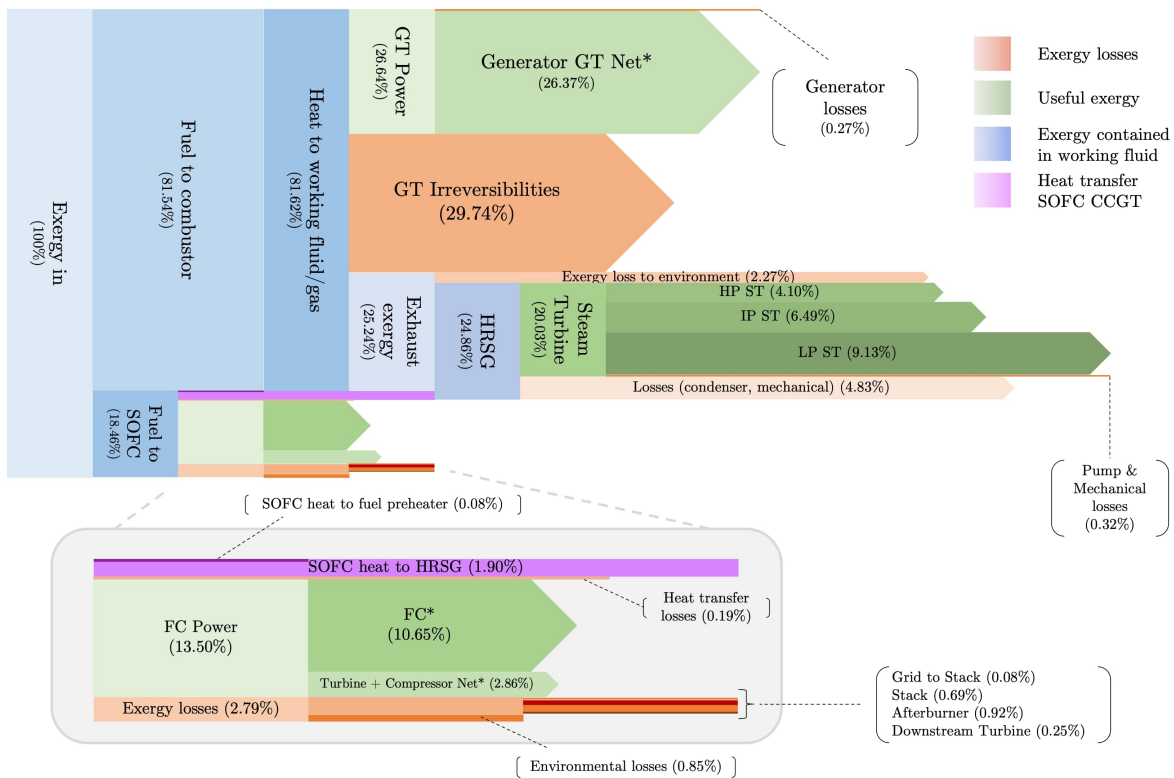


Figure 6.2: Sankey exergy diagram Optimization case 2A: SOFC-CCGT part load. *Net = The power consumption subtracted from the power generation.

Comparison with Base Case 2A

Because the absolute power capacity is the same in Optimization case 2A compared to Base case 2A, the comparison between absolute differences gives a better comparison than the relative comparison. Table 6.3 shows the improvement when the exergy inputs of the two systems are compared considering the equal exergy outputs. Replacing 160 MW of exergy confined in natural gas with only 137 MW of hydrogen accounts for a 23 MW reduction in total exergy input.

The decreased efficiency of the CCGT due to the part load operation is more apparent than in the previous analysis. Although the natural gas consumption decreases by 20.9%, the GT irreversibilities

only decrease by 17.7% and the total power output of the CCGT decreases by 22.6%. The negative effect is greater, in terms of exergy losses and power drop, than the reduction of exergy input of natural gas. The same is noted with the ST, where pump and mechanical losses decrease by only -6.79%.

Even more significant is the increased losses originating from the steam turbine at +7.1 MW (condenser + irreversibilities ST). The decreased isentropic efficiency of the three STs decreased by an average of 0.70% on average compared to the STs at full load, mentioned in Table 5.8. In addition to the efficiency degradation, the additional heat supplied by the SOFC is condensed whenever there is an excess of heat. With the additional heat transfer of the SOFC to the HRSG, proportionally more heat is supplied by the SOFC to the HRSG compared to Optimization case 1A during full load operation. This difference can be seen when comparing the amount of heat from the SOFC to the HRSG in Figure 6.1 and in Figure 6.2, or the tables in Appendix A.3 and A.4.

Table 6.3: Absolute exergy differences of Base case 2A and Optimization case 2A.

Exergy input/losses [MW]	Base case 2A	Case 2A	$\Delta\%$
Exergy in	763	740	-3.01
Natural gas	763	604	-20.9
Hydrogen	-	137	-
Exergy out	441	441	-
Power	441	441	-
CCGT	441	341	-22.6
SOFC	-	100	-
Exergy destruction	323	299	-7.25
CCGT	323	277	-14.1
Irreversibilities GT	267	220	-17.7
Generator losses	2.87	1.97	-31.2
Pump + mechanical losses	2.54	2.36	-6.79
Environmental GT	21.1	16.8	-20.3
Condenser + irreversibilities ST	28.7	35.8	24.8
SOFC	-	20.7	-
Grid to Stack	-	0.63	-
Stack	-	5.10	-
Afterburner	-	6.83	-
Turbine	-	1.85	-
Environmental	-	6.28	-
Exergy integration	-	16.0	-
Exergy exchanged HRSG	-	14.1	-
Exergy exchanged FPH	-	0.58	-
Exergy losses integration	-	1.39	-
Exergy efficiency [%]	Base case 2A	Case 2A	Δ
SOFC	-	83.85	-
CCGT	57.74	55.18	-2.56
SOFC-CCGT	-	59.59	-

Conclusion Comparison 2A

All the effects added together result in a decreased efficiency of the CCGT of 2.56%, yet the SOFC-CCGT still outperforms the stand-alone CCGT despite the additional losses associated with the part load operation. This also confirms that Optimization case 2A outperforms Base case 2A based on its exergy efficiency. Comparing Optimization case 1A with 2A show that the synergies between the SOFC and the CCGT are decreasing. Even though the ratio of the SOFC to the CCGT is greater, as well as the efficiency of the SOFC compared to the stand-alone CCGT, the SOFC-CCGT efficiency still decreases. The attenuation of the synergies originates from the failure of the model to fully convert the

addition of heat to useful exergy. The sum of the condenser losses and the ST irreversibilities increased by 24.8% although that the CCGT capacity was down-scaled by 22.6%.

6.1.3. Results Optimization Case 1B: Full Load

The following comparison between Optimization case 1B with Base case 1B includes heat in the equation. Similar to Optimization case 1A, the comparison examines both systems operating at full load. Figure 6.3 shows the exergy Sankey diagram where the exergy flows are expressed relative to the total amount of exergy input. The figure shows that useful exergy consists not only of electricity, but also physical exergy contained in the heat supplied. Although, the supplied heat expressed in energy sums up to 108 MW, expressing the heat in exergy equals 19.1 MW. The heat to the DHN is 2.27% of the total exergy input. The SOFC extends its system boundary by the implementing three system heat connections. The first and second are the same as in the previous analysis, to the fuel preheater (0.08%) and to the HRSG (1.61%). The heat is converted into generated power and losses, but also contributes indirectly to the heat supply of the DHN. The exergy confined in the steam of the HRSG is tapped by 16.1%³ to feed the DHN. Besides the indirect contribution of the SOFC to supply the DHN indirectly by the heat transfer to the working fluid of the HRSG, the SOFC contributes directly to the supply of heat to the DHN (0.12%). The major difference between the power-only cases is that the system now has a method of achieving lower exhaust temperatures that allows for recovering more environmental exergy losses. In this case, the SOFC discharges the exhaust gas at a temperature of 65 °C instead of 99 °C which should be noticeable in the efficiency.

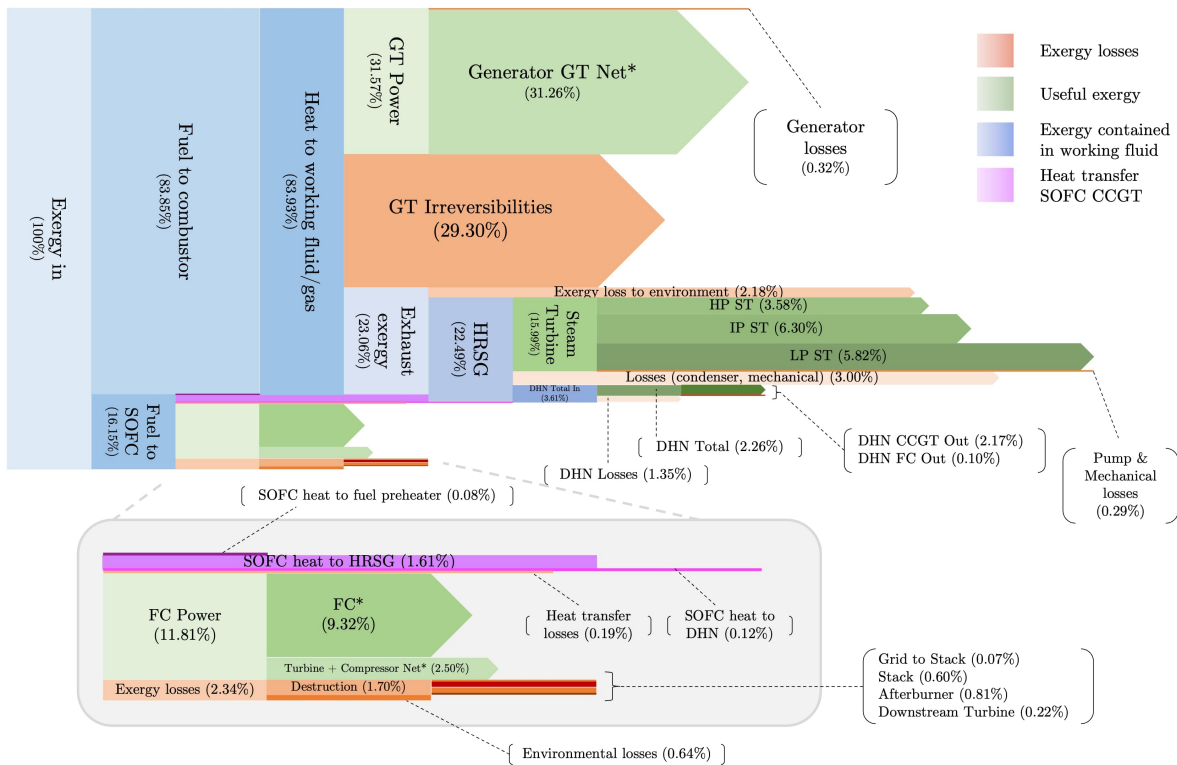


Figure 6.3: Sankey exergy diagram Optimization case 1B: SOFC-CCGT CHP full load. *Net = The power consumption subtracted from the power generation.

Comparison with Base Case 1B

To clearly demonstrate the improvements caused by making the DHN connection, the SOFC was added to Base case 1B during the comparison. In this case, the SOFC and the CCGT CHP operate independently of each other, and the DHN connection of the SOFC was omitted. To make the heat transfer possible, the gas consumption of the CCGT was reduced by 7.0%. However, the power of the CCGT decreases by a smaller amount of 4.6%, indicating the effective substitution of the heat released by the

³ $(3.61\%/22.49\%)*100\%$

gas combustion with the exhaust heat of the SOFC. The exergy transferred to the fuel preheater of 0.69 MW and to the HRSG of 13.6 MW, partially compensates for the decreased gas consumption that would otherwise be discharged to the environment.

The SOFC provides an additional 4.4% of heat (+0.81 MW), which reduces the environmental losses of the SOFC by 71.6% to 5.38 MW. In Optimization case 1A, where the system is not coupled to the DHN, the environmental losses are higher at 6.23 MW. The reduction of environmental losses in Optimization case 1B reduces the total losses of the SOFC by 45.5%. Because the heat delivered to the DHN is also considered as useful exergy, the SOFC efficiency increases to 84.21%.

Table 6.4: Absolute exergy differences of Base case 1B and Optimization case 1B.

Exergy input/losses [MW]	Base case 1B	Case 1B	Δ%
Exergy in	900	846	-5.98
Natural gas	763	709	-7.04
Hydrogen	137	137	-
Exergy out	535	516	-3.45
Power	517	497	-3.73
CCGT	417	397	-4.6
SOFC	100	100	-
Heat	18.3	19.1	4.4
CCGT	18.3	18.3	-
SOFC	-	0.81	-
Exergy destruction	365	330	-9.7
CCGT	328	308	-6.2
Irreversibilities GT	267	248	-7.3
Generator losses	2.87	2.67	-6.8
Pump + mechanical losses	2.41	2.41	-
DHN losses	11.2	11.2	-
Environmental GT	19.9	18.5	-7.2
Condenser + irreversibilities ST	24.5	25.4	3.72
SOFC	36.7	20.0	-45.5
Grid to Stack	3.96	0.63	-84.2
SOFC	5.10	5.10	-
Afterburner	6.83	6.83	-
Turbine	1.85	1.85	-
DHN losses	-	0.20	-
Environmental	18.9	5.38	-71.6
Exergy integration	-	15.9	
Exergy exchanged HRSG	-	13.6	-
Exergy exchanged FPH	-	0.69	-
Exergy losses integration	-	1.60	-
Exergy efficiency [%]	Base case 1B	Case 1B	Δ
SOFC	73.14	84.21	11.06
CCGT	56.99	57.43	0.45
SOFC-CCGT	59.44	61.04	1.60

Conclusion Comparison 1B

Whether Optimized case 1B outperforms Base case 1B is tested when the original CCGT CHP is compared with the integrated SOFC-CCGT CHP system. The exergy efficiency improves from 56.99% to 61.04%. Because the stand-alone SOFC already has a higher efficiency than the CCGT, the comparison between the paired SOFC-CCGT CHP and stand-alone CCGT CHP may create unjust conclusions. Comparing the separate CCGT CHP and SOFC with the coupled SOFC-CCGT CHP gives insights in the synergies of the systems. This comparison also results in an improvement of as much as 1.6%. It can therefore be concluded that Optimized case 1B indeed outperforms Base case 1B based on its

exergy efficiency.

6.1.4. Results Optimization Case 2B: Part Load

The last system being analyzed is the scaled system Optimization case 2B where the heat production is equal to that of the planned CCGT CHP of Base case 2B. The supplied heat to the DHN was scaled from 108 MW to 103 MW in terms of energy. The relatively small scaling does not change the system much, except that with the down scaling of the CCGT the relative capacity of the SOFC becomes larger and the part load losses become greater. For comparison with Base case 2B, the SOFC is now excluded from consideration, which, with equal heat output, makes the inputs more comparable.

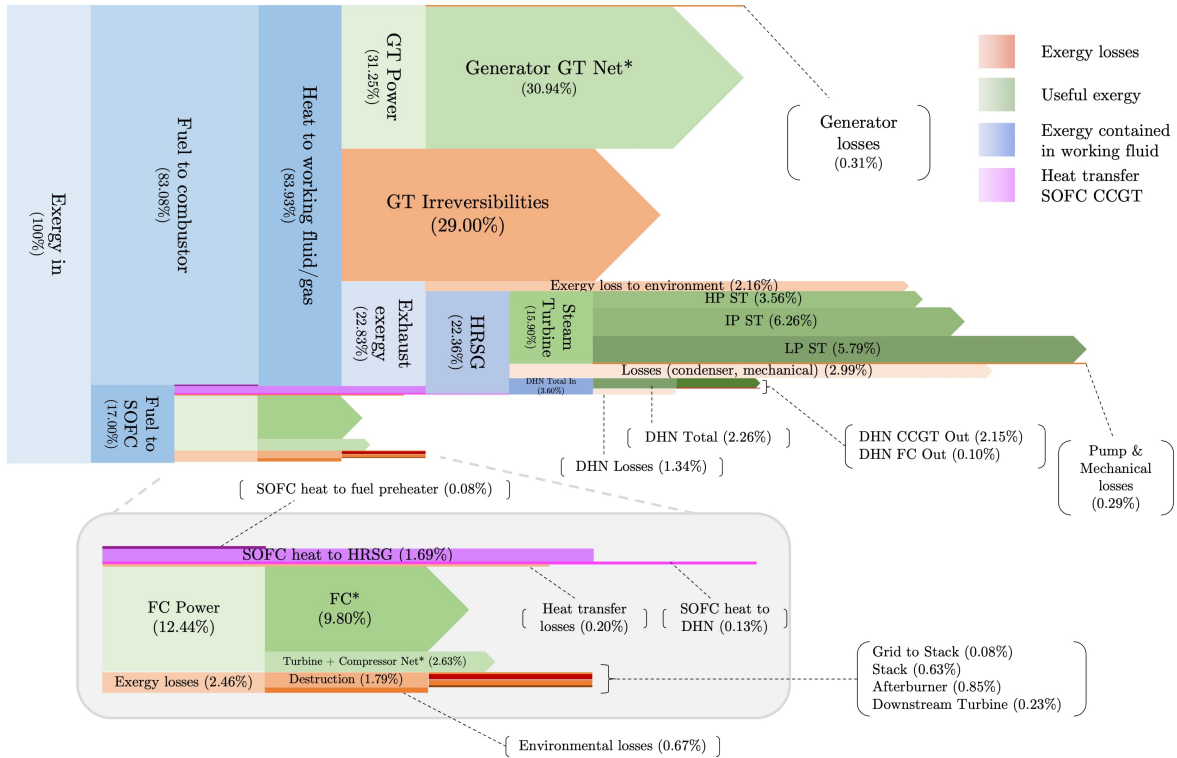


Figure 6.4: Sankey exergy diagram Optimization case 2B: SOFC-CCGT CHP part load. *Net = The power consumption subtracted from the power generation.

Comparison with Base Case 2B

Even though the same amount of heat goes to the DHN, the heat transfer from the SOFC to the DHN loses 0.21 MW of exergy, which explains the difference between the total exergy to the DHN. In addition, it is notable that the increase in inserted exergy of the fuels (+5.33%) is a lot smaller than the increase in useful exergy (+13.20%). The gain of incorporating the SOFC exceeds the loss of the isentropic efficiency correction of the turbomachinery for a reduction of 12.6% natural gas (which is -1.4% for the compressor and -1.5% for the turbine, mentioned in Table 5.9).

Compared to Optimization case 2A, where synergies declined due to part load operation due to the increase environmental losses through the condenser, Optimization case 2B loses less heat through the condenser. In Optimization case 2B, a larger proportion, of the supplied heat by the SOFC, is converted in useful exergy. The bleed after the IP ST of 38% allows the excess heat to be used for heat supply to the DHN. This results in a reduction in condenser losses of 1.9% instead of an increase of 24.8% in Optimization case 2A. Thus, the SOFC-CCGT CHP is able to efficiently utilize the heat provided by the SOFC under the current operating conditions.

Table 6.5: Absolute exergy differences of Base case 2B and Optimization case 2B.

Exergy input/losses [MW]	Base case 2B	Case 2B	Δ%
Exergy in	763	804	5.33
Natural gas	763	667	-12.6
Hydrogen	-	137	-
Exergy out	435	492	13.20
Power	417	474	13.82
CCGT	417	374	-10.2
SOFC	-	100	-
Heat	18.3	18.1	-1.07
CCGT	18.3	17.3	-5.55
SOFC	-	0.82	-
Exergy destruction	328	312	-5.09
CCGT	328	290	-11.7
Irreversibilities GT	267	233	-12.8
Generator losses	2.87	2.51	-12.3
Pump + mechanical losses	2.41	2.30	-4.66
DHN losses	11.2	10.6	-5.55
Environmental GT	19.9	17.4	-12.7
Condenser + irreversibilities ST	24.5	24.0	-1.93
SOFC	-	20.0	-
Grid to Stack	-	0.63	-
SOFC	-	5.10	-
Afterburner	-	6.83	-
Turbine	-	1.85	-
DHN losses	-	0.21	-
Environmental	-	5.38	-
Exergy integration	-	15.9	-
Exergy exchanged HRSG	-	13.6	-
Exergy exchanged FPH	-	0.66	-
Exergy losses integration	-	1.61	-
Exergy efficiency [%]	Base case 2B	Case 2B	Δ
SOFC	-	84.19	-
CCGT	56.99	57.45	0.47
SOFC-CCGT	-	61.24	-

Conclusion Comparison 2B

Optimization case 2B outperforms Base case 2B, the exergy efficiency of the SOFC-CCGT CHP system is higher than the original CCGT CHP whereby the heat output is equalized. At the same time, the efficiency of Optimization case 2B is higher than the system examined in Optimization case 1B, because the relative larger capacity of the more efficient SOFC than the CCGT outweighs the part load losses of the CCGT. Besides, the additional heat supplied can be well absorbed in the DHN because a portion of the heat is now conducted past the condenser by applying the bleed of the IP ST, instead of being discarded by the condenser.

6.1.5. Summary

Table 6.6 summarizes results from the systems studied. Each optimized system is better than the compared original or decoupled case. Of all Optimized cases is the exergy efficiency of Optimization case 1A the highest. The full load optimized cases (1A and 1B) define the proposed systems that will be used in the MES case study.

Table 6.6: Summary of exergy efficiency results of all Cases.

Case	Base case Ψ_{system} [%]	Optimization case Ψ_{system} [%]	Δ
1A	60.0	61.5	1.47
2A	57.7	59.6	1.85
1B	59.4	61.0	1.60
2B	57.0	61.2	4.26

6.2. Assessing the Benefits Based on GHG Emissions (Sub-objective 2)

The combination of the higher efficiency and the addition of hydrogen results in a lower amount of GHG emissions per unit of useful exergy. Table 6.7 shows that the relative CO_{2e} [t/MWh] emissions compared to the original CCGT (Base case 2A) and original CCGT CHP (Base case 2B) for the cases A and B respectively. The benefits of coupling, without including the additional hydrogen, can be seen when the GHG reductions of the optimized systems are compared to the GHG reductions of the uncoupled systems in Base cases 1A and Base case 1B. Noting from the table, it appears that the relative reduction of the coupled systems is always greater than the relative reduction of uncoupled systems.

The optimized cases decreases the relative CO_{2e} emissions by 21.3% and 21.0% for Optimization case 1A and Optimization case 2A respectively compared to the original CCGT. Relative GHG emissions continue to decrease when heat is also included. But when compared to the simulation of the planned CCGT CHP, it is 20.3% and 21.3% for Optimization case 1B and 2B respectively.

Table 6.7: Summary of CO_{2e} results of all Cases. The variable CO_{2e} includes the total of the heat and electricity generation of the system. *Relative to Base case 2A and Base case 2B for the Cases A and B respectively.

Case	P_e [MW]	P_{th} [MW]	CO _{2e} [t/MWh]	Δ [%]*
Base case 1A	541	-	0.274	-18.5%
Base case 2A	441	-	0.336	-
Optimization case 1A	518	-	0.264	-21.3%
Optimization case 2A	441	-	0.266	-21.0%
Base case 1B	517	103	0.239	-16.2%
Base case 2B	417	103	0.285	-
Optimization case 1B	497	108	0.227	-20.3%
Optimization case 2B	474	103	0.224	-21.3%

7

Multiple Energy System: Case Study

The exergetic performance of the optimized SOFC-CCGT systems exceeded the Base case models of the original power plant and planned CHP plant. They emit less CO_{2e} per produced power and heat, and require less natural gas. Yet the added financial value of integrating an rSOC with the CCGT to also enable the SOEC mode has not been demonstrated. For this purpose, the third research sub-objective is to assess the benefits of retrofitting an rSOC to an existing CCGT based on the gross profit. The integration of an rSOC with a CCGT would increase the weighed gross profit [€/MWh] compared to the current Hemweg CCGT.

By utilizing various energy carriers, the integration of an rSOC with a CCGT would be able to respond to price fluctuations of the energy network. The relative gross profit is expected to increase because the proposed system can adjust its operating mode depending on the energy price, whereas the original system was solely able to produce power. Even though the proposed system is more efficient, the price of the same amount of energy in hydrogen is higher compared to that in natural gas, so the cost per MWh produced is not guaranteed to go down. To account for any increased total output of the system, the relative gross profit per unit of energy is considered. To account for time-related effects, the net present value (NPV) of the gross profit was calculated.

Finally, the effect of adding a TES to the MES on the weighted gross profit is also examined. The TES is expected to decouple the production and demand of heat, giving the system more freedom to anticipate price volatility, while still meeting the required heat demand.

The financial benefits of retrofitting an rSOC to an existing CCGT are assessed by inserting the system into a dispatch model that represents the energy system of the Amsterdam metropolitan area. The following section will discuss the construction of the model with the assumptions made, followed by a comparison of the systems. Finally, sub-objective 3 will be concluded.

7.0.1. Dispatch Model

The dispatch model is a mixed-integer programming model that calculates the optimal dispatch solution for the whole energy asset portfolio. The dispatch model aims to maximize the total gross profit of the entire energy system. Covering the heat and electricity demand of the portfolio is the main constraint, which is based on a database of Amsterdam's predicted heat and electricity demand on an hourly basis until the year 2050. The output generated by the model is the full dispatch profile for the whole portfolio, but specific assets can be highlighted. The output includes operating data (electricity-, heat- and hydrogen production; fuel consumption; and CO_{2e} emissions) and financial data (electricity-, heat- and hydrogen revenues; fuel costs; and variable Operating & Maintenance costs).

The dispatch model simulates the energy system by representing it with interconnected nodes. Each node represents an Asset (such as a CHP, TES, an electric boiler, or a biomass power plant) or a consumer of the energy carrier (such as electricity, gas, heat, or hydrogen). The heat network of the metropolitan area of Amsterdam is visualized in Figure 7.1a as an example. The dispatch model has

converted this network to the interconnected nodal network of Figure 7.1b. The dispatch model processes the electricity, gas, and hydrogen grid in the same manner. Each connection between nodes is equipped with boundary conditions, based on the pipe capacity and flow direction. The model calculates the optimal distribution of resource and energy flows by the hour while respecting these boundary conditions.

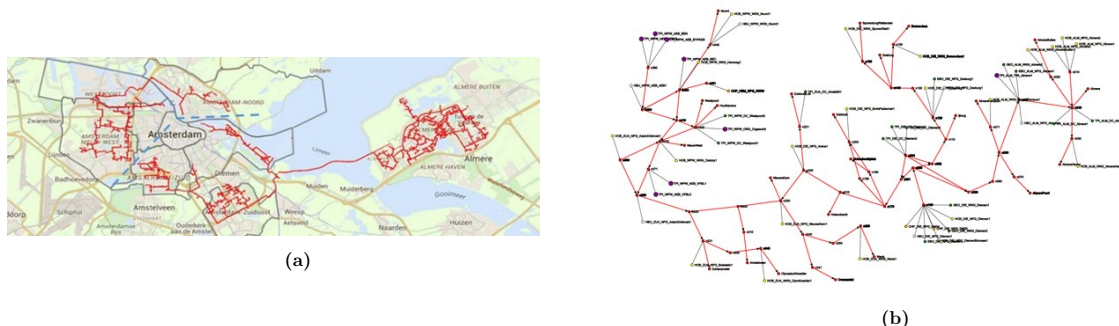


Figure 7.1: a) District Heating Network Metropolitan area Amsterdam and Almere. b) Interconnected nodal representations of DHN of the Heating Network Metropolitan area Amsterdam and Almere by the dispatch model.

Current System and Opportunities

The current CCGT in the Hemweg area solely produces electricity. A heat grid is present due to the neighboring incineration plant that supplies the North and West Amsterdam areas. In 2018, the DHN supplied 1.7 PJ of heat to 19 thousand residential houses. It is expected that the DHN will supply 2.2 PJ of heat to 32 thousand residential houses by the year 2023 [95]. The growing heat network creates opportunities for the proposed CHP system. The power plant in Diemen (natural gas CHP CCGT plant) is the main heat supplier of the DHN in Amsterdam's South, East, and Zuidas districts, and to the cities Almere and Amstelveen. The Diemen power plant is on the other side of the city and will thus not conflict with the proposed system due to the losses associated with transportation heat losses.

The energy mix of Vattenfall in 2020 consisted of 52.4% wind energy and 2.9% solar energy [96]. Additionally, Vattenfall is expanding its offshore wind farms significantly in the coming years. The rSOC balancing system is expected to become competitive when the proportion of renewable energy sources in the energy mix is increased [32] because of the intermittent behavior of RESs[27]. In the future, the Hemweg area will become a fossil-free hub for electricity and heat, and it will become Vattenfall's center for the production of green hydrogen [78]. Moreover, the government of the Netherlands is planning to construct a hydrogen grid that will be accessible from the Hemweg area [79]. Amsterdam plans on implementing this hydrogen grid by the year 2025 [97].

In summary, the growing demand for the DHN and the expansion of Vattenfall's renewable energy mix create opportunities for making a profit through the proposed setup. The Hemweg area exhibits an electricity grid, a connection to the DHN, and an assumed hydrogen grid.

Input

The financial input consists of the commodity bidding and selling prices, and the CO₂ tax. It is assumed that the bid and offer prices of the commodities are equal. The commodity prices for the examined years are listed in the Confidential Appendix Page 16. The model only studies the years 2025 through 2045 in five-year increments, due to the large required computing power. The intermediate years were approximated by applying linear interpolation.

The following years and system setups are examined:

- *Years:* 2025, 2030, 2035, 2040 and 2045
- *Energy system setups:* Current system setup (Hemweg 9 CCGT), Proposed system (rSOC-CCGT CHP), Proposed system + TES (rSOC-CCGT CHP + TES)

The model predicts electricity prices on an hourly basis, gas prices on a monthly basis, and heat and hydrogen prices on an annual basis. The standard deviation SD in the Confidential Appendix Page 16 shows the volatility over a year of the commodity prices. It was assumed that the consumed hydrogen was classified as green hydrogen, meaning it did not increase GHG emissions in the total energy system.

Research on the CHP mode of the Hemweg 9 CCGT by Siemens and Vattenfall concluded that the imposed bleeds of the ST enable the system to scale the power and heat output [77]. Therefore, it is assumed that the system can freely vary between its power mode and its heat and power mode. It can also vary the capacity of both modes. The efficiency decrease of part load operation is considered in the model. The optimized systems (Optimization case 1A and 1B) are implemented in the energy network, allowing the system to deliver heat at a variable capacity depending on the demand constraints. The dispatch model considers startup time and ramp-up speeds, which was based on the original model provided by Vattenfall. The ramp rate for the CCGT is set to 1000 MW/h, while the heat ramp rate is 55 MW/h. The dispatch model was adjusted to enable the implementation of the varying electricity and heat production by reading a Power-Heat diagram shown in Figure 7.2. The PQ diagram describes the electricity and heat operating area of the CHP unit. This diagram shows four coordinates from which the model calculates the optimal operating coordinate by conducting a linear interpolation.

The total switching time from the SOEC to SOFC would only take 10 minutes [39]. The transient response of the rSOC was sufficient for grid balancing purposes [39][63], so the ramp up rate of the CCGT would be the limiting factor [63]. With the implementation of the CCGT ramp rate, the SOEC ramp rate would have little effect.

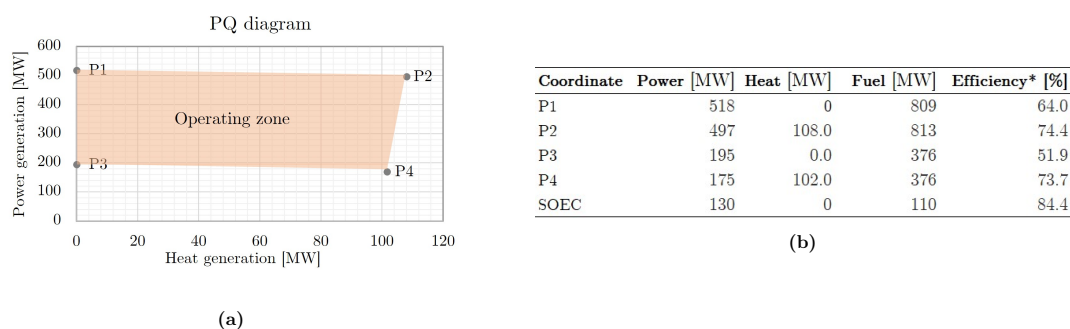


Figure 7.2: a) PQ diagram of SOFC-CCGT CHP system. The highlighted area shows the operating zone of the proposed system b) PQ coordinates and SOEC input/output in LHV. The SOEC can operate at any point between 130 and 0 MW which is determined by an interpolation.*First-order LHV efficiency which includes power and heat.

The four coordinates are the maximum and minimum of heat and power generation, which are based on the results obtained with the optimization of the system. For the coordinates P1 and P2, the results of Optimization case 1A and Optimization case 2B are applied. Points P3 and P4 are retrieved from the existing model Hemweg 9 CHP of Vattenfall. Because this work did not investigate the complete operating window of part load performance, it was assumed that the SOFC load scales proportionally with the CCGT. This assumption results in a constant fuel ratio $H_2/NaturalGas$ based on the chemical energy input based on the LHV [W], which was maintained at 20.1%. The available operating points P3 and P4, applied in this model, account for the efficiency drop during the part load operation. Table 7.2b defines the hydrogen production of the SOEC based on the LHV. It is assumed that the SOEC can scale its production proportionally to the applied load.

The gross profit is calculated by the model. The income of the model includes the sales from electricity production (SOFC,CCGT), heat production (SOFC,CCGT), and hydrogen production (SOEC). The expenses include electricity consumption (SOEC), natural gas consumption (CCGT), hydrogen consumption (SOFC), CO₂ tax (CCGT), and variable operating and maintenance costs (CCGT).

7.1. Assessing the Benefits Based on Gross Profit (Sub-objective 3)

To explain the mechanisms that influence the gross profit of the system, the results of the year 2030 will be highlighted. From the analysis, it will become clear how the proposed multi-energy system utilizes the different energy carriers and thus increases the gross profit. After this analysis, the TES will be added to the system showing how the TES decouples the production and consumption of heat thereby increasing the gross profit. After the analysis, the resulting system will be used to determine research sub-objective 3.

rSOC-CCGT CHP

The four Figures 7.3 depict the utilization of the four energy carriers used by the proposed system in the first two weeks of January 2030. The figures indicate the flexibility of the system of being able to change from mode and energy carrier. The first figure shows the use and production of hydrogen by the SOFC and SOEC respectively. Because the system can switch modes it increases the total operating hours which it presumably responds to the electricity price. This will be investigated shortly. The variable heat production and the flexibility of the system to follow the heat demand constraints are shown in Figure 7.3.3. The last figure, Figure 7.3.4, shows the gas consumption of the CCGT which follows the same curve as the hydrogen consumption.

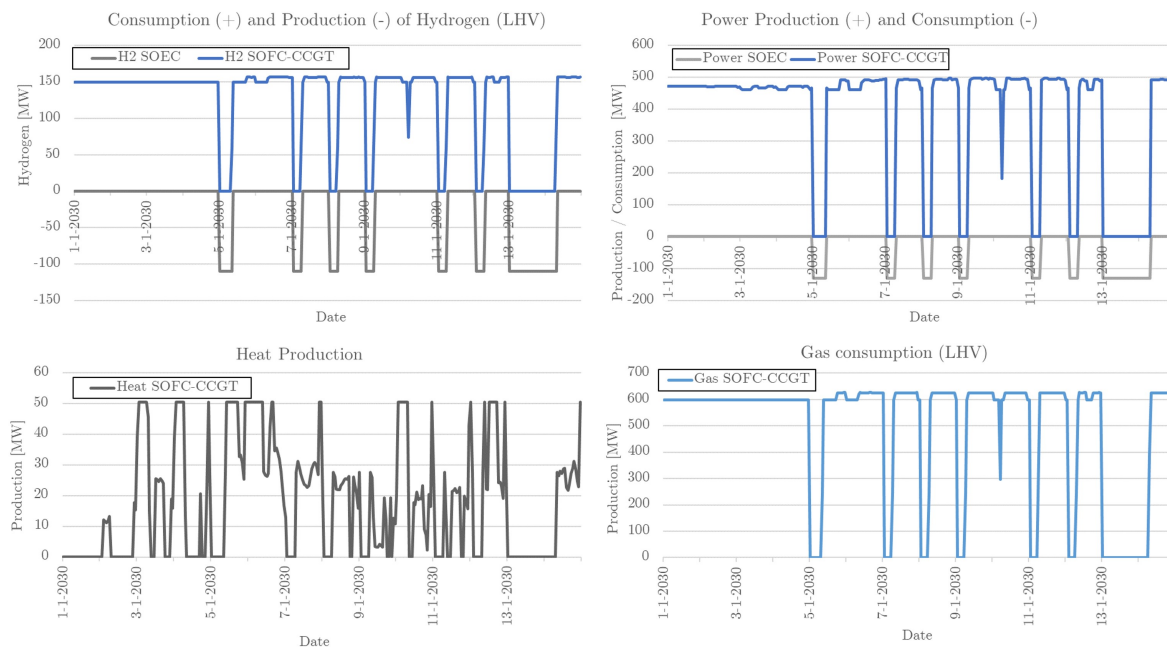


Figure 7.3: Utilization of energy carriers by the rSOC-CCGT CHP in the first two weeks of January 2030. 1) Hydrogen, 2) Power, 3) Heat, 4) Natural Gas.

The major advantage of the proposed system is shown in Figure 7.4 where the adaptability of the system to the APX price¹ is demonstrated. The normalized APX price is shown in orange and the hydrogen production and consumption of the rSOC are shown in the two shades of blue, be aware of the two different y-axes. When the price is high, for example in the first five days, the SOFC-CCGT converts hydrogen and gas to electricity. However, when the price is low, and it is not profitable to produce power, the SOEC exploits the low electricity price by using it to generate hydrogen and sell it on the hydrogen market which provides opportunities for increased profitability.

¹Spot market price for electricity in the Netherlands, the United Kingdom, and Belgium.

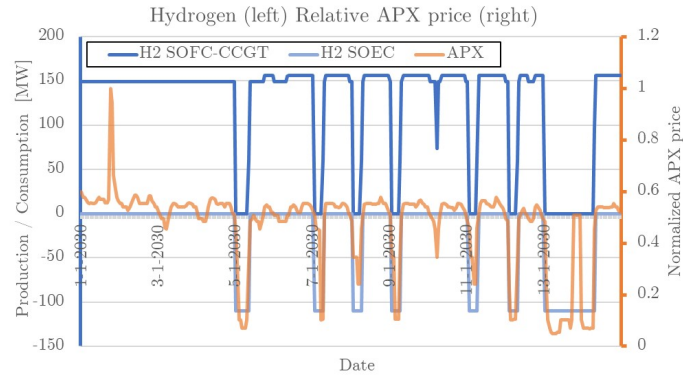


Figure 7.4: Adaptability of the rSOC-CCGT system to the APX price. The price is normalized for confidentiality purposes.

The results of the year 2030 are compared with the simulation of the current 442 MW CCGT Hemweg 9 power plant in Table 7.1². The rSOC-CCGT CHP system shows the impressive growth of the gross profit by an increase of 141%. The revenues from the SOFC-CCGT are considerably higher due to the additional revenues from the generated heat (+74 GWh) and electricity (+756 GWh). The relative fuel costs [€/GWh] did increase because the relatively expensive hydrogen was used to substitute for the NG. But the substitution simultaneously reduces the relative CO₂ [kt/GWh] emission from 0.345 to 0.253 (-26.6%) which reduces costs regarding the CO₂ tax by €1.86 M.

In addition, the SOEC contributes to a substantial portion of the gross profit with 18.9%. The SOEC generates hydrogen with a high gross profit margin³ (80.0%) because the SOEC benefits from the volatile electricity prices by activating the SOEC when electricity prices are low, as was depicted in Figure 7.4. The SOEC produces in total 321 GWh of hydrogen (HHV), which equals 43.9% of the SOFC's hydrogen consumption. However, the hydrogen is assumed to be fed into the grid instead of stored on-site.

²The gross profit is not depicted for confidentiality purposes. These results can be found in the Confidential Appendix Page 17

³(Sales - Costs of goods sold)/Sales

Table 7.1: Results 2030 rSOC-CCGT CHP in comparison to CCGT Hemweg 9. *Listed in HHV.

Parameter	rSOC-CCGT CHP	CCGT Hemweg 9	Δ [%]
Financials [M€]			
Gross profit	(Confidential)	(Confidential)	140.8
Revenue	(Confidential)	(Confidential)	66.7
SOFC-CCGT	(Confidential)	(Confidential)	53.4
SOEC	(Confidential)		
Costs	(Confidential)	(Confidential)	53.4
SOFC-CCGT	(Confidential)	(Confidential)	49.8
SOEC	(Confidential)		
Commodity [GWh]*			
Generated	3213	2043	57.3
Electricity	2799	2043	37.0
Heat	74		
Hydrogen	340		
Consumed	5368	3848	39.5
Natural Gas	3971	3848	3.18
Hydrogen	1056		
Electricity	341		
Other			
Operating hours [h]	8524	4978	71.2
SOFC-CCGT	5691	4978	14.3
SOEC	2833		
CO2 emission [kt]	727	704	3.18
CO2 [kt/GWh]	0.253	0.345	-26.6

To assess the third sub-objective, the NPV of the gross profit needs to be compared to the original setup. The difference in NPV of the gross profit of the original CCGT and the proposed rSOC-CCGT CHP indicates the available budget that may be invested to convert the original CCGT to the proposed system and reinvested throughout the lifetime of the systems. The calculation of the NPV of the gross profit (GP) in Equation 7.1 assumes an interest rate of 2%, calculates back to the year 2023, and excludes degradation effects. The results are listed in Table 7.2. The years in between the examined years are approximated by linear interpolation. The proposed system generates an NPV of gross profit that is 118% higher than the original system. Furthermore, it can be concluded from Table 7.2 that each year's gross margin and NPV increase, which is not the case for the original CCGT. The difference can be explained by the increasing hydrogen production, presumably due to rising CO₂ tax and volatility of electricity prices, which benefit the profitability of the SOEC.

$$NPV_{GP} = \sum_{t=0}^T \frac{GP_t}{(1+r)^t} \quad (7.1)$$

Table 7.2: NPV, gross profit, revenue, and costs of examined years of the rSOC-CCGT CHP and the original Hemweg 9 plant. The absolute numbers are confidential (Confidential Appendix Page 19), the relative difference is provided.

Energy System	Year	NPV 2023	2025	2030	2035	2040	2045
rSOC-CCGT CHP	Gross profit [M€]	(Conf.)	(Conf.)	(Conf.)	(Conf.)	(Conf.)	(Conf.)
	Revenue		(Conf.)	(Conf.)	(Conf.)	(Conf.)	(Conf.)
	Costs		(Conf.)	(Conf.)	(Conf.)	(Conf.)	(Conf.)
CCGT Hemweg 9	Gross profit [M€]	(Conf.)	(Conf.)	(Conf.)	(Conf.)	(Conf.)	(Conf.)
	Revenue		(Conf.)	(Conf.)	(Conf.)	(Conf.)	(Conf.)
	Costs		(Conf.)	(Conf.)	(Conf.)	(Conf.)	(Conf.)
+ Δ [%]	Gross profit	118	60	135	143	115	109
	Revenue		72	66	65	72	67
	Costs		75	53	49	59	52

To assess the third sub-objective, whether the implementation of the proposed MES achieves a higher gross profit [€/MWh], the NPV of the gross profit was divided by the total generated energy of

the commodities (Table 7.3). Because the number of operating hours has gone up, and the system now also produces heat and hydrogen, the gross profit is weighted by the total generated energy to assess the profitability. This calculation also includes the hydrogen generation expressed in HHV.

Table 7.3: Total generated energy [TWh] of the two systems and energy carrier over the years 2025 to 2045.

System	Commodity	Energy [TWh]
rSOC-CCGT CHP	Power	53.2
	Heat	1.18
	Hydrogen	10.1
	Total	64.5
Original CCGT	Power	37.8

When the outcome of Equation 7.2 of the proposed rSOC-CCGT CHP is divided by that of the original Hemweg 9 plant, the ratio is 1.28. This ratio indicates that the weighted gross profit [NPV_{GP}/MWh] of the proposed rSOC-CCGT CHP system is indeed higher than that of the original CCGT.

$$\text{Weighted } NPV_{GP} = \frac{NPV_{GP,2023}}{\sum MWh_{\text{Power, Heat, Hydrogen}}} \quad (7.2)$$

$$NPV_{ratio} = \frac{\text{Weighted } NPV_{GP, \text{ rSOC-CCGT CHP}}}{\text{Weighted } NPV_{GP, \text{ Original CCGT}}} \quad (7.3)$$

rSOC-CCGT CHP + TES

TES is added to the rSOC-CCGT energy system and the system is thereafter compared to the previous energy system. Besides, Vattenfall applied sensible TES in the Diemen area. Therefore, the same TES asset is adopted as at the Diemen power plant with the same maximum capacity of 1600 MWh_{th} (depending on the return and supply ΔT) and a maximum pump load of 225 MW_{th} . This storage is unnecessarily large when compared to the capacity of the proposed system, however, it is only used to demonstrate the usefulness of the TES in the MES system. Because the rSOC is only being tested at a small scale to date compared to the 100MW proposed in this research, it is difficult to make statements about the system's CAPEX. These are therefore not included in this study.

The advantages of adding the TES can be deducted from Figure 7.5. The addition of the TES to the MES system enables the MES to decouple heat production and consumption. In the period between the 13th and 15th of January, indicated with the black arrow on the right, the MES provides heat to the DHN by discharging the TES while the SOEC takes advantage of low electricity prices to generate hydrogen (which was illustrated in Figure 7.4). Besides, the TES enables that when the CHP produces heat, the CHP operates at full load, resulting in a higher system efficiency. This situation may occur during periods in which renewable energy sources are overproducing, while connected users of the DHN require heat.

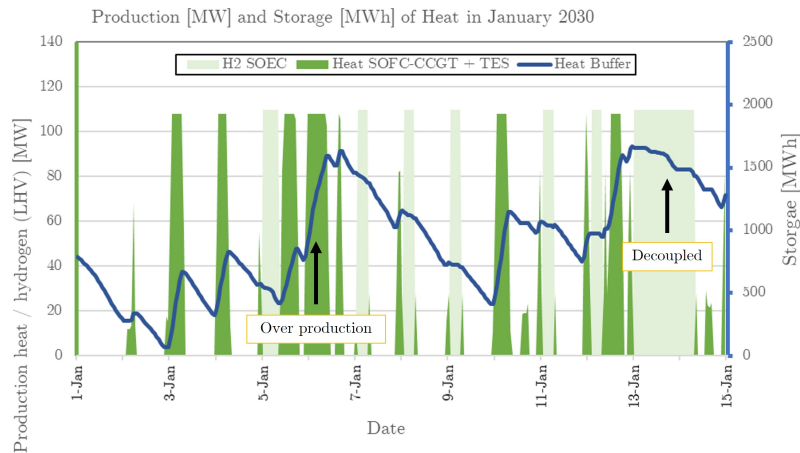


Figure 7.5: Production of hydrogen HHV [MW] (light green, left y-axis), heat [MW] (dark green, left y-axis) and total heat stored (blue, right y-axis). Arrows indicate the regions of interest.

Table 7.4 displays the same gross profit NPV analysis, but compares the rSOC-CCGT CHP with and without TES. Ultimately, NPV of the gross profit of the system increases by 1.44%, which is dominated by the differences in the year 2025. The comparison between the system with and without TES of the produced commodity quantities, operating hours and CO₂ emissions of the year 2030 can be found in Appendix A.2.

Table 7.4: NPV, gross profit, revenue and costs of examined years of the rSOC-CCGT CHP and rSOC-CCGT CHP + TES. The absolute numbers are confidential (Confidentiality Appendix Page 19), the relative difference is provided.

Energy System	Year	NPV 2023	2025	2030	2035	2040	2045
rSOC-CCGT CHP + TES	Gross profit [M€]	(Conf.)	(Conf.)	(Conf.)	(Conf.)	(Conf.)	(Conf.)
	Revenue		(Conf.)	(Conf.)	(Conf.)	(Conf.)	(Conf.)
	Costs		(Conf.)	(Conf.)	(Conf.)	(Conf.)	(Conf.)
rSOC-CCGT CHP	Gross profit [M€]	(Conf.)	(Conf.)	(Conf.)	(Conf.)	(Conf.)	(Conf.)
	Revenue		(Conf.)	(Conf.)	(Conf.)	(Conf.)	(Conf.)
	Costs		(Conf.)	(Conf.)	(Conf.)	(Conf.)	(Conf.)
Δ [%]	Gross profit	1.44	2.85	0.33	0.12	0.15	0.08
	Revenue		0.61	0.11	-0.02	0.38	0.10
	Costs		0.08	0.05	-0.07	0.47	0.10

7.2. Conclusion

The NPV of the gross profit of the proposed rSOC-CCGT CHP system has increased by 118% compared to the current CCGT. If this result account for the increased energy production by dividing the NPV by the total amount of energy produced, the increase is still 27%. This concludes the third sub-objective. Adding a TES to the system results in a slight increase of the NPV by 1.44%.

8

Conclusion

This chapter discusses the conclusions of this research. The main findings based on the optimization process, comparison and energy system analysis are reviewed. Finally, the limitations of this work are addressed. Recommendations for future research to overcome these limitations will be proposed.

8.1. Research Objectives

While the performance of various SOFC-CCGT cycles has been widely explored, few research was found on the retrofitted hybrid system by applying an existing gas cycle, and no research examined the integration of an rSOC with a CCGT. This study aims to determine the enhancement of performance caused by coupling the SOFC to an existing CCGT while taking into account the bifunctional SOEC operating mode.

The research objective was to assess the benefits of retrofitting an rSOC to an existing CCGT by simulating its exergetic performance, relative GHG emissions and gross profit, and comparing these results to those of the existing CCGT.

This main research objective was then divided into three sub-objectives, namely:

- *The first research sub-objective was to assess the benefits of retrofitting an rSOC to an existing CCGT based on the exergetic performance.*
- *The second research sub-objective was to assess the benefits of retrofitting an rSOC to an existing CCGT based on the relative GHG emissions.*
- *The third research sub-objective was to assess the benefits of retrofitting an rSOC to an existing CCGT based on the gross profit.*

8.2. Summary and Conclusion of Research Process

First, a brief summary and the main conclusions of the optimization process of the rSOC. Then the coupling between the SOFC and the CCGT will be presented. Finally, the results from the MES analysis are discussed.

8.2.1. Summary and Conclusion of rSOC Optimization Process

On cell level, both rSOC modes favored a high temperature, high fuel concentration and low current density. Pressure had a contrary effect on the different modes, however, the heat duty of the cell dropped at increasing pressures, which reduced the additional required electric heating. Nevertheless, on the system level the increased pressure and temperature were detrimental for the system's exergetic performance. This is caused by the increased compression power and environmental exergy losses, which relate to the large airflow, high exhaust temperature and pressure. To minimize the exergy environmental losses and exergy destruction, several optimizations were proposed.

Reducing the need for fresh air proved to be the most effective method to reduce heating and compression power. The air recirculation re-utilized the warm and pressurized outgoing airflow. A trade-off had to be made between the reduced compression power of the fresh air compressor and the increased compression power of the recirculation compressor. Besides, by reducing the fresh air, the SOFC's and SOEC's Nernst voltage was negatively affected through the decreased (SOFC) or increased (SOEC) oxygen concentration. The optimal air recirculation factor varied per SOC mode due to the difference in endothermic and exothermic cell operation, and the affected cell voltage.

Two heat exchanger networks per mode were constructed, one for the stack and the other for the systems Balance of Plant. The imposed heat exchanger network provided all the SOFC stack's required heat, while the additional heat duty of the SOEC was reduced to 16% compared to the system without heat integration. A downstream ST was introduced to expand the outgoing gas streams. In the case of the SOFC, the best position for the downstream turbine was shown to be immediately after the afterburner, because this maximized the turbine inlet temperature and reduced the exergy destruction of the downstream heat exchangers.

The resulting rSOC was used for the integration with the CCGT. The optimized SOEC system achieved an efficiency of 84.3% which required 129 MW to produce 0.903 kg/s of hydrogen. The SOFC operates at an exergy efficiency of 73.1%, with an electrical power output of 100 MW while consuming 1.13 kg/s of hydrogen.

8.2.2. Summary and Conclusion of SOFC-CCGT Coupling

To utilize the exergy losses of the SOFC, an indirect coupling of the SOFC-CCGT system was imposed. The heat was inserted in the CCGT at two locations, the higher temperatures at the HRSG and the lower at the GT fuel preheater. To effectively transfer the heat of the SOFC into the CCGT system, the heat of combustion of natural gas was substituted by the heat of the SOFC's exhaust stream.

The heat integration reduces the environmental losses of the SOFC by 65% while enhancing the performance of the CCGT. A reduction of 3.0% of total exergy input was achieved when the SOFC-CCGT generated the same power output as the original CCGT. Nevertheless, the synergies of the SOFC-CCGT diminish when operating at part load due to the limited absorption of heat. The environmental losses were reduced by incorporating the heat transfer to the DHN in the system, while the exergetic performance of the CCGT CHP was increased. Maintaining the heat output resulted in an increased efficiency, due to the ability to supply the additional heat to the DHN instead of discharging it to the environment.

8.2.3. Summary and Conclusion about MES

The gross profit of the proposed MES was analyzed with an energy system optimization model of the Amsterdam Metropolitan Area. The proposed MES, consisting of the rSOC-CCGT CHP, was able to adjust its operating mode to anticipate on the variations in the energy grid. The proposed model took advantage of low electricity prices by operating at SOEC mode, which resulted in a large gross margin of 80.0%. The gross profit of the MES was increased compared to the original CCGT due to the high gross margin of the SOEC, the increased efficiency of the system, and the increased total energy produced hours. The NPV of the gross profit of the years 2025 to 2045 was calculated to take time dependency into account. Additionally, the NPV of the gross profit was corrected for the increased amount of energy produced, by dividing it by the total amount of energy. This was used to assess sub-objective 3.

The addition of the TES showed that heat production and consumption could be decoupled. This allowed the system to run at full load more frequently, which is advantageous because the full load has higher efficiency than part load. In addition, it was found that the addition of TES allowed to operate the SOEC while still meeting the heat demand, which increased the total heat supplied. The NPV of the gross profit of the system with TES is 2.85% higher than the system without TES.

8.3. Main Findings

In this section, a conclusion will be drawn about each of the sub-objectives. From the three sub-objectives, a conclusion can then be drawn about the main research objective.

8.3.1. Assessing the Benefits Based on Exegetic Performance (Sub-objective 1)

The benefits of the rSOC-CCGT based on exegetic performance can be assessed using the results of the exergy analysis, summarized in Tables 8.1 and 8.2. The exegetic performance of the system increases when a SOFC is coupled with an existing CCGT and CCGT CHP, while respecting the operating conditions of the SOEC. Thus, in both cases, it can be assumed that there are benefits of retrofitting an rSOC to an existing CCGT based on the exegetic performance.

8.3.2. Assessing the Benefits Based on GHG Emissions (Sub-objective 2)

The benefits of the rSOC-CCGT based on GHG emissions can be assessed using the results of the exergy analysis, summarized in Tables 8.1 and 8.2.

As can be seen from the table, the reduction of CO₂e in Optimized case 1A is 21.3% compared to the CO₂e of the original CCGT. When the CHP is included in the consideration, the reduction of CO₂e in Optimized case 2B is 13.2% over the CO₂e of the original CCGT CHP. Thus, in both cases, it can be assumed that there are benefits of retrofitting an rSOC to an existing CCGT based on the GHG emissions.

Table 8.1: Concluding results Sub-objective 2 Cases A: Exergy efficiency and relative GHG emissions

Case	System	Ψ System [%]	CO ₂ e [t/MWh]
Original CCGT (Base case 2A)	CCGT full load CCGT: 441 [MW _e]	57.7	0.336
Optimization case 1A	CCGT-SOFC full load coupled CCGT + SOFC: 518 [MW _e]	61.5	0.264
Difference		3.80	-21.3%

Table 8.2: Concluding results Sub-objective 2 Cases B: Exergy efficiency and relative GHG emissions

Case	System	Ψ System [%]	CO ₂ e [t/MWh]
Original CCGT CHP (Base case 2B)	CCGT full load CCGT: 417 [MW _e] CCGT: 103 [MW _{th}]	57.0	0.258
Optimization case 2B	CCGT-SOFC part load CCGT + SOFC: 474 [MW _e] CCGT + SOFC: 103 [MW _{th}]	61.2	0.224
Difference		4.20	-13.2%

8.3.3. Assessing the Benefits Based on Gross Profit (Sub-objective 3)

As can be seen from table 8.3, the NPV of the gross profit of the proposed MES case was found to be 118% higher than the original CCGT. Corrected for the increased amount of energy produced, by dividing it by the total amount of energy, this resulted in a 28% increase from the original CCGT to the Proposed MES case. It can therefore be concluded that there are also benefits of retrofitting an rSOC to an existing CCGT based on the gross profit.

Table 8.3: Concluding results Sub-objective 3: NPV of gross profit [M€], Total energy of carriers generated [TWh], Weighted NPV [€/MWh]

Case	NPV [M€]	Energy [TWh]	Weighted NPV [€/MWh]
Original CCGT (Base case 2A)	(Conf)	(Conf)	(Conf)
Proposed MES case (Combined Optimization case 1A and 1B)	(Conf)	(Conf)	(Conf)
Difference	118%	71%	28%

8.3.4. Assessing the Benefits Based on All Performance Parameters (Main Research Objective)

Using the three sub-objectives, a conclusion can be drawn about the main research objective: Exergy efficiency increases, GHG emissions decrease and gross profit increases, when a retrofitted rSOC is coupled with an existing CCGT. The proposed systems outperform the original CCGT system on each performance parameter.

8.4. Research limitations and recommendations for future research

Although the outcomes of this research are valuable, the reader is advised to take into account the limitations while interpreting the results. These limitations provide opportunities for future research.

8.4.1. Simulation software

The first limitation of this work stemmed from the software used to model the combination of the rSOC and the CCGT systems. No simulation software currently is known to be capable of perfectly mapping both an electrochemical process of an electrolyzer and gas cycles. Although several studies have managed to get the rSOC to match experiments with Aspen Plus, Aspen plus is generally not used for modeling CCGTs but for chemical process simulations.

In addition, Aspen plus has no ability to correct for part load operation of a system such as in the engineering mode in THERMOFLEX or in the simulation software Cycle Tempo. In this work, the losses in part load operation were approximated with an isentropic correction of the turbomachinery. However, the other parts, such as the heat exchanger, also suffer efficiency losses. Again, with the current simulation software a trade-off has to be made.

Through the stack analysis, it was found that in the range of current densities ($<10,000$ A/m²) and pressures (<10 bar), mainly the temperature and the oxygen concentration the cell voltage. If these operating conditions are not exceeded, relationships in the literature are available where the cell voltage can be corrected depending on the operating temperature and current density. This allows adopting the electrochemical cell in a gas cycle focused simulation software such as THERMOFLEX, thereby enabling the part load analysis while accounting for the largest electrochemical implications. Because this work opted for detailed mapping of the electrochemical process of the rSOC, thereby compromising on the detail of the CCGT, future work is recommended to investigate the reverse.

8.4.2. Model

The electrochemical model has been validated and calibrated with respect to small-scale experiments. However, the current system is of MW scale. It was assumed that scale does not affect performance. However, it does appear to do so when looking at more mature electrochemical techniques such as alkaline electrolysis. The SOC's are expected to be applied on various scales but the scaling effects of cells and stacks on performance remain to be explored.

The degradation can significantly affect the performance of the system. Besides maintaining the temperature gradient and maximum fuel concentrations, little attention was paid to the degradation effects of the SOC. The determination of optimal operating conditions and the financial analysis would likely be different if these effects were taken into account. Future research that determines the degree to which degradation affects long-term exergetic performance, and incorporates these effects into the thermodynamic optimization and into the dispatch model would be a valuable addition to this work.

The fuel consumption of 0.8 was assumed based on experiments discussed in the literature. This factor has a strong effect on efficiency: the higher, the better. However, other papers often assume a higher utilization factor than was used in this work. This could increase the efficiency of the system since the afterburner - which receives the residual 20% unconverted hydrogen - is the major source of the SOC's system exergy destruction. SOC technological improvements in the coming decades, such as

an increasing fuel utilization factor, when SOC system majors were not considered in this work.

It was assumed that a hydrogen grid will be in place when the proposed system will be manufactured. However, the hydrogen grid will not be constructed everywhere, so the majority of the CCGTs around the world do not comply with the current system requirements. Considering hydrogen storage instead of the hydrogen grid will expand the scope of this work, making the system applicable to more CCGTs. However, the scale of the proposed system would make the implementation of storage unlikely. Other energy carriers than hydrogen could be the solution. Storage would also have beneficial effects on the system configuration. The SOFC features a maximum allowable hydrogen concentration of 97%. This means that a series of flash drums can be deployed to facilitate the fuel of this purity, rather than the assumed membrane technology to meet the 99.97% purity required for the hydrogen grid. Therefore, the effect of hydrogen storage on the exergetic and financial performance of the system would be an interesting follow-up study.

In this work, the same system components are used for the SOFC and SOEC to access the rSOC mode. However, this research has not considered whether the same components could be used. To determine this, the efficiency losses associated with deviating operating conditions must be taken into account and balanced against the required investments. Future work could contribute with a technological economic analysis of the rSOC's Balance of Plant.

Based on recommendations from the literature, an indirect heat integration of the SOFC and the retrofitted CCGT was imposed, because a direct integration would excessively affect the normal operation of existing CCGTs. However, a direct hybrid system shows better thermodynamic performance. Future work should examine the extent to which direct integration can be applied to existing cycles and how off-design performance affects the system.

Bibliography

- [1] P Kazempoor and RJ Braun. “Model validation and performance analysis of regenerative solid oxide cells for energy storage applications: Reversible operation”. In: *international journal of hydrogen energy* 39.11 (2014), pp. 5955–5971.
- [2] Vikrant Venkataraman et al. “Reversible solid oxide systems for energy and chemical applications—review & perspectives”. In: *Journal of Energy Storage* 24 (2019), p. 100782.
- [3] Alexander Buttler et al. “A detailed techno-economic analysis of heat integration in high temperature electrolysis for efficient hydrogen production”. In: *International journal of hydrogen energy* 40.1 (2015), pp. 38–50.
- [4] Christopher H Wendel, Pejman Kazempoor, and Robert J Braun. “A thermodynamic approach for selecting operating conditions in the design of reversible solid oxide cell energy systems”. In: *Journal of Power Sources* 301 (2016), pp. 93–104.
- [5] Abed Saria, Khir Tahar, and Ben Brahim Ammar. “Thermodynamic and energy study of a regenerator in gas turbine cycle and optimization of performances”. In: *2014 5th International Renewable Energy Congress (IREC)*. IEEE. 2014, pp. 1–5.
- [6] Lalatendu Pattanayak. “Thermodynamic modeling and exergy analysis of gas turbine cycle for different boundary conditions”. In: *Int. J. Power Electron. Drive Syst.* 6.2 (2015), pp. 205–215.
- [7] Yaşar Demirel. “Energy conversion”. In: *Energy*. Springer, 2016, pp. 241–319.
- [8] Katsuya Hayashi et al. “Solid oxide fuel cell stack with high electrical efficiency”. In: *NTT Technical Review* 7.10 (2009), pp. 1–5.
- [9] L Barelli, G Bidini, and A Ottaviano. “Part load operation of SOFC/GT hybrid systems: stationary analysis”. In: *International journal of hydrogen energy* 37.21 (2012), pp. 16140–16150.
- [10] Stef Boesten et al. “5th generation district heating and cooling systems as a solution for renewable urban thermal energy supply”. In: *Advances in Geosciences* 49 (2019), pp. 129–136.
- [11] Ishai Olikier. *Retrofitting Single Purpose Electric Power Plants to CHP district energy*. Aug. 2021. URL: <https://www.power-eng.com/coal/retrofitting-single-purpose-electric-power-plants-to-chp-district-energy/#gref>.
- [12] Fiammetta Rita Bianchi et al. “Multiscale modeling for reversible solid oxide cell operation”. In: *energies* 13.19 (2020), p. 5058.
- [13] Siemens AG. *Siemens Gas Turbine Package sgt5-pac 4000F - siemens energy*. 2009. URL: <https://www.yumpu.com/en/document/read/10004068/siemens-gas-turbine-package-sgt5-pac-4000f-siemens-energy>.
- [14] F.S.C. Van Den Oudenalder. *Natural gas displacement by wind curtailment utilization in combined-cycle power plants*. Nov. 2016. URL: <http://resolver.tudelft.nl/uuid:fef26f7d-eab7-42dc-a7f7-63e21f5e284b>.
- [15] Anne Sjoerd Brouwer et al. “Operational flexibility and economics of power plants in future low-carbon power systems”. In: *Applied Energy* 156 (2015), pp. 107–128.
- [16] Maximilian Hauck, Stephan Herrmann, and Hartmut Spliethoff. “Simulation of a reversible SOFC with Aspen Plus”. In: *International Journal of Hydrogen Energy* 42.15 (2017), pp. 10329–10340.
- [17] Fiammetta Rita Bianchi and Barbara Bosio. “Operating principles, performance and technology readiness level of reversible solid oxide cells”. In: *Sustainability* 13.9 (2021), p. 4777.
- [18] Jan Szargut. *Exergy method: technical and ecological applications*. Vol. 18. WIT press, 2005.
- [19] Michael J Prather and Jennifer A Logan. “Combustion’s impact on the global atmosphere”. In: *Symposium (International) on Combustion*. Vol. 25. 1. Elsevier. 1994, pp. 1513–1527.

- [20] United Nations. *The Paris Agreement*. Dec. 2015. URL: <https://unfccc.int/process-and-meetings/the-paris-agreement/the-paris-agreement>.
- [21] EU Council. *Council adopts regulation on reducing gas demand by 15% this Winter*. Aug. 2022. URL: <https://www.consilium.europa.eu/en/press/press-releases/2022/08/05/council-adopts-regulation-on-reducing-gas-demand-by-15-this-winter/>.
- [22] Goldman Sachs. *Europe's energy crisis is at a tipping point*. Sept. 2022. URL: <https://www.goldmansachs.com/insights/pages/europe-energy-crisis-is-at-a-tipping-point.html>.
- [23] William F Lamb et al. "A review of trends and drivers of greenhouse gas emissions by sector from 1990 to 2018". In: *Environmental research letters* (2021).
- [24] International Energy Agency. *The netherlands 2020 – analysis*. Feb. 2020. URL: <https://www.iea.org/reports/the-netherlands-2020>.
- [25] Bas Van Ruijven and Detlef P Van Vuuren. "Oil and natural gas prices and greenhouse gas emission mitigation". In: *Energy Policy* 37.11 (2009), pp. 4797–4808.
- [26] European Commission. *Taxes, charges and fees*. Oct. 2021. URL: https://environment.ec.europa.eu/economy-and-finance/ensuring-polluters-pay/taxes-charges-and-fees_en.
- [27] GAM Van Kuik et al. "Long-term research challenges in wind energy—a research agenda by the European Academy of Wind Energy". In: *Wind energy science* 1.1 (2016), pp. 1–39.
- [28] Elisa Guelpa and Vittorio Verda. "Thermal energy storage in district heating and cooling systems: A review". In: *Applied Energy* 252 (2019), p. 113474.
- [29] Katharina Koch, Bastian Alt, and Matthias Gaderer. "Dynamic modeling of a decarbonized district heating system with CHP plants in electricity-based mode of operation". In: *Energies* 13.16 (2020), p. 4134.
- [30] Pierluigi Mancarella. "MES (multi-energy systems): An overview of concepts and evaluation models". In: *Energy* 65 (2014), pp. 1–17.
- [31] FM Mulder. "Implications of diurnal and seasonal variations in renewable energy generation for large scale energy storage". In: *Journal of Renewable and Sustainable Energy* 6.3 (2014), p. 033105.
- [32] Markus Millinger et al. "Electrofuels from excess renewable electricity at high variable renewable shares: cost, greenhouse gas abatement, carbon use and competition". In: *Sustainable Energy & Fuels* 5.3 (2021), pp. 828–843.
- [33] Yousef Haseli, Ibrahim Dincer, and GF Naterer. "Thermodynamic modeling of a gas turbine cycle combined with a solid oxide fuel cell". In: *International journal of hydrogen energy* 33.20 (2008), pp. 5811–5822.
- [34] Annamaria Buonomano et al. "Hybrid solid oxide fuel cells–gas turbine systems for combined heat and power: A review". In: *Applied Energy* 156 (2015), pp. 32–85.
- [35] Diamantis P Bakalis and Anastassios G Stamatias. "Incorporating available micro gas turbines and fuel cell: Matching considerations and performance evaluation". In: *Applied Energy* 103 (2013), pp. 607–617.
- [36] Kamal IM Al-Malah. *Aspen plus: chemical engineering applications*. John Wiley & Sons, 2016.
- [37] Søren Højgaard Jensen et al. "Large-scale electricity storage utilizing reversible solid oxide cells combined with underground storage of CO₂ and CH₄". In: *Energy & Environmental Science* 8.8 (2015), pp. 2471–2479.
- [38] Valerie Eveloy et al. "Energy, exergy and economic analysis of an integrated solid oxide fuel cell–gas turbine–organic Rankine power generation system". In: *International journal of hydrogen energy* 41.31 (2016), pp. 13843–13858.
- [39] G Botta et al. "Dynamic modeling of reversible solid oxide cell stack and control strategy development". In: *Energy Conversion and Management* 185 (2019), pp. 636–653.
- [40] Josef Schefold, Annabelle Brisse, and Hendrik Poepke. "Long-term steam electrolysis with electrolyte-supported solid oxide cells". In: *Electrochimica Acta* 179 (2015), pp. 161–168.
- [41] P Kazempoor, V Dorer, and F Ommi. "Modelling and Performance Evaluation of Solid Oxide Fuel Cell for Building Integrated Co-and Polygeneration". In: *Fuel Cells* 10.6 (2010), pp. 1074–1094.

- [42] Haibo Huo et al. “Temperature Gradient Control of the Solid Oxide Fuel Cell under Variable Load”. In: *ACS omega* 6.42 (2021), pp. 27610–27619.
- [43] Mohsen Sadeghi et al. “Size and exergy assessment of solid oxide fuel cell-based H₂-fed power generation system with alternative electrolytes: A comparative study”. In: *Energy Conversion and Management* 228 (2021), p. 113681.
- [44] Zuming Liu and Iftekhar A Karimi. “New operating strategy for a combined cycle gas turbine power plant”. In: *Energy Conversion and Management* 171 (2018), pp. 1675–1684.
- [45] Penyarat Chinda and Pascal Brault. “The hybrid solid oxide fuel cell (SOFC) and gas turbine (GT) systems steady state modeling”. In: *International Journal of Hydrogen Energy* 37.11 (2012), pp. 9237–9248.
- [46] Siemens. *Sgt5-4000F: F-class gas turbine: Gas turbines: Manufacturer: Siemens Energy Global*. URL: <https://www.siemens-energy.com/global/en/offerings/power-generation/gas-turbines/sgt5-4000f.html>.
- [47] Michael J Moran et al. *Fundamentals of engineering thermodynamics*. John Wiley & Sons, 2010.
- [48] Roberto Carapellucci and Lorena Giordano. “Regenerative gas turbines and steam injection for re-powering combined cycle power plants: Design and part-load performance”. In: *Energy Conversion and Management* 227 (2021), p. 113519.
- [49] Stephen A Rackley. *Carbon capture and storage*. Butterworth-Heinemann, 2017.
- [50] Mohsen Mehdizadeh-Fard, Fathollah Pourfayaz, and Akbar Maleki. “Exergy analysis of multiple heat exchanger networks: An approach based on the irreversibility distribution ratio”. In: *Energy Reports* 7 (2021), pp. 174–193.
- [51] Omar Z Sharaf and Mehmet F Orhan. “An overview of fuel cell technology: Fundamentals and applications”. In: *Renewable and sustainable energy reviews* 32 (2014), pp. 810–853.
- [52] Henrik Lund et al. “The role of district heating in future renewable energy systems”. In: *Energy* 35.3 (2010), pp. 1381–1390.
- [53] Ministerie van Economische Zaken en Klimaat, BZK. *Maatregelen voor verduurzamen van de gebouwde omgeving*. Feb. 2022. URL: <https://www.klimaatakkoord.nl/gebouwde-omgeving>.
- [54] Netherlands Enterprise Agency. *Multi-annual Mission-driven Innovation Program (MMIP): Rvo.nl: Rijksdienst*. 2020. URL: <https://www.rvo.nl/subsidie-en-financieringswijzer/meerjarige-missiegedreven-innovatie-programmas-mmip>.
- [55] Ivan Komarov et al. “Combined cycle gas turbine for combined heat and power production with energy storage by steam methane reforming”. In: *Journal of Energy Systems* 5.3 (2021), pp. 231–243.
- [56] Pierluigi Mancarella et al. “Modelling of integrated multi-energy systems: Drivers, requirements, and opportunities”. In: *2016 Power Systems Computation Conference (PSCC)*. IEEE. 2016, pp. 1–22.
- [57] Alexandre Oudalov, Rachid Cherkaoui, and Antoine Beguin. “Sizing and optimal operation of battery energy storage system for peak shaving application”. In: *2007 IEEE Lausanne Power Tech*. IEEE. 2007, pp. 621–625.
- [58] Sheila Samsatli and Nouri J Samsatli. “The role of renewable hydrogen and inter-seasonal storage in decarbonising heat—Comprehensive optimisation of future renewable energy value chains”. In: *Applied Energy* 233 (2019), pp. 854–893.
- [59] Truls Gundersen. “An introduction to the concept of exergy and energy quality”. In: *Department of Energy and Process Engineering Norwegian University of Science and Technology, Version 4* (2011).
- [60] P Kazempoor and RJ Braun. “Hydrogen and synthetic fuel production using high temperature solid oxide electrolysis cells (SOECs)”. In: *international journal of hydrogen energy* 40.9 (2015), pp. 3599–3612.
- [61] Sotiris Giannoulidis et al. “Methanol based Solid Oxide Reversible energy storage system—Does it make sense thermodynamically?” In: *Applied Energy* 278 (2020), p. 115623.

- [62] F Calise, G Restuccia, and N Sammes. “Experimental analysis of micro-tubular solid oxide fuel cell fed by hydrogen”. In: *Journal of Power Sources* 195.4 (2010), pp. 1163–1170.
- [63] Konrad Motylinski et al. “Dynamic modelling of reversible solid oxide cells for grid stabilization applications”. In: *Energy Conversion and Management* 228 (2021), p. 113674.
- [64] Lukas Wehrle et al. “Dynamic modeling of reversible solid oxide cells”. In: *Chemie Ingenieur Technik* 91.6 (2019), pp. 833–842.
- [65] MS Khan et al. “Air electrodes and related degradation mechanisms in solid oxide electrolysis and reversible solid oxide cells”. In: *Renewable and Sustainable Energy Reviews* 143 (2021), p. 110918.
- [66] Marta Gandiglio et al. “Thermoeconomic analysis of large solid oxide fuel cell plants: Atmospheric vs. pressurized performance”. In: *Energy* 55 (2013), pp. 142–155.
- [67] RJ Braun et al. “Highly efficient IGFC hybrid power systems employing bottoming organic rankine cycles with optional carbon capture”. In: *Journal of engineering for gas turbines and power* 134.2 (2012).
- [68] Denver F Cheddie. “Integration of a solid oxide fuel cell into a 10 MW gas turbine power plant”. In: *Energies* 3.4 (2010), pp. 754–769.
- [69] Yingru Zhao, Nilay Shah, and Nigel Brandon. “Comparison between two optimization strategies for solid oxide fuel cell–gas turbine hybrid cycles”. In: *international journal of hydrogen energy* 36.16 (2011), pp. 10235–10246.
- [70] Bram Schouten and Sikke Klein. “The Optimization of Hydrogen Oxygen Cycles”. In: *Turbo Expo: Power for Land, Sea, and Air*. Vol. 84140. American Society of Mechanical Engineers. 2020, V005T06A007.
- [71] Jarosław Milewski, Marcin Wołowicz, and Janusz Lewandowski. “Comparison of SOE/SOFC system configurations for a peak hydrogen power plant”. In: *International Journal of Hydrogen Energy* 42.5 (2017), pp. 3498–3509.
- [72] Chen Bin et al. “Integration of Reversible Solid Oxide Cells with methane synthesis (ReSOC-MS) in grid stabilization”. In: *Energy Procedia* 158 (2019), pp. 2077–2084.
- [73] MATTIA SENSOLI. “Power to gas to power conversion systems with thermal energy storage. Possible applications for reversible solid oxide cells”. In: (2015).
- [74] M Burer et al. “Multi-criteria optimization of a district cogeneration plant integrating a solid oxide fuel cell–gas turbine combined cycle, heat pumps and chillers”. In: *Energy* 28.6 (2003), pp. 497–518.
- [75] H. Bo, E. M. Gustafsson, and F. Setterwall. “Tetradecane and hexadecane binary mixtures as phase change materials (PCMs) for cool storage in district cooling systems”. In: *Energy* 24.12 (1999), pp. 1015–1028.
- [76] Omais Abdur Rehman et al. “Enabling Technologies for Sector Coupling: A Review on the Role of Heat Pumps and Thermal Energy Storage”. In: *Energies* 14.24 (2021), p. 8195.
- [77] D van der Vlist. *Personal interview with D. van der Vlist (Vattenfall): Hemweg 9 operating conditions*. Apr. 2022.
- [78] Vattenfall. *De hemwegcentrale: Van Hero Naar Zero in één generatie*. Feb. 2019. URL: <https://www.vattenfall.nl/sluiting-hemweg/>.
- [79] Gülbahar Tezel. *Final report research project HyWay 27*. 2021, pp. 1–109. URL: <https://www.hyway27.nl/actueel/hyway-27-realisatie-van-het-landelijk-waterstofnetwerk>.
- [80] Vattenfall. *Hemweg 9 - a new gas fired plant*. 2012. URL: <https://powerplants.vattenfall.com/hemweg-9/>.
- [81] Thermoflex. *Thermoflow*. URL: https://www.thermoflow.com/products_generalpurpose.html.
- [82] Kamalakannan Soundararajan, H Kwee, and Bin Su. *A Sankey Framework for Energy and Exergy Flows*. 2013.
- [83] B Tjaden et al. “Small-scale biogas-SOFC plant: technical analysis and assessment of different fuel reforming options”. In: *Energy & fuels* 28.6 (2014), pp. 4216–4232.

- [84] Amogh Amladi. “Process Chain Development of a ReSOC System with ammonia as fuel and steam electrolysis”. In: (2020).
- [85] Guidehouse. *Gas for climate - gas for climate 2050*. July 2020. URL: https://gasforclimate2050.eu/wp-content/uploads/2020/07/2020_European-Hydrogen-Backbone_Report.pdf.
- [86] Sushil Adhikari and Sandun Fernando. “Hydrogen membrane separation techniques”. In: *Industrial & Engineering Chemistry Research* 45.3 (2006), pp. 875–881.
- [87] Yu Huang, Tim C Merkel, and Richard W Baker. “Pressure ratio and its impact on membrane gas separation processes”. In: *Journal of membrane science* 463 (2014), pp. 33–40.
- [88] Andriy Redko, Oleksandr Redko, and Ronald DiPippo. *Low-temperature energy systems with applications of renewable energy*. Academic Press, 2019.
- [89] Ramin Roushenas, Ehsan Zarei, and M Torabi. “A novel trigeneration system based on solid oxide fuel cell-gas turbine integrated with compressed air and thermal energy storage concepts: Energy, exergy, and life cycle approaches”. In: *Sustainable Cities and Society* 66 (2021), p. 102667.
- [90] Keith Shine et al. “Alternatives to the global warming potential for comparing climate impacts of emissions of greenhouse gases”. In: *Climatic Change* 68.3 (2005), pp. 281–302.
- [91] Guo-Bin Jung et al. “Study of reversible solid oxide fuel cell with different oxygen electrode materials”. In: *International Journal of Hydrogen Energy* 41.46 (2016), pp. 21802–21811.
- [92] Lorenz Holzer et al. “Microstructure degradation of cermet anodes for solid oxide fuel cells: Quantification of nickel grain growth in dry and in humid atmospheres”. In: *Journal of Power Sources* 196.3 (2011), pp. 1279–1294.
- [93] Siemens. *Sgt5-PAC4000FGasTurbinePackageAppli.PDF*. Jan. 2018. URL: https://www.academia.edu/35699025/SGT5_PAC_4000F_Gas_Turbine_Package_Appli_pdf.
- [94] F Triesch. “Hybrid combustion air conditioning at Gas Turbines. A new method to optimise the operation of gas turbines; Die hybride Verbrennungsluftkonditionierung an Gasturbinen. Ein neues Verfahren zur Optimierung des Gasturbinenbetriebes”. In: (2007).
- [95] Central Agency for Statistics and Netherlands Organisation for Applied Scientific Research. *Heat monitor 2019*. 2020. URL: <https://www.cbs.nl/nl-nl/achtergrond/2020/35/warmtemonitor-2019>.
- [96] Vattenfall. *Het stroometiket Toont de herkomst Van Stroom*. May 2021. URL: <https://www.vattenfall.nl/stroom/stroometiket/>.
- [97] GasUnie. *The development of the Hydrogen Network in the Netherlands*. 2021. URL: <https://www.gasunie.nl/en/expertise/hydrogen/the-development-of-the-hydrogen-network-in-the-netherlands>.

A

Appendix Tables

A.1. Theoretical Background

Table A.1: Relevant molecules in the system and the molecule standard exergy [18]

Molecule	Exergy ₀ ^{ch} [J/mol]
H2	2.35E+05
H2O _{vapor}	9.50E+03
H2O _{liquid}	9.00E+02
O2	3.97E+03
N2	6.90E+02
CH4	8.31E+05
CO2	1.95E+04
C2H6	1.50E+06
C3H8	2.15E+06
C4H10	2.80E+06
CO	2.75E+05
NO	8.89E+04
NO2	5.56E+04

A.2. Appendix Optimization

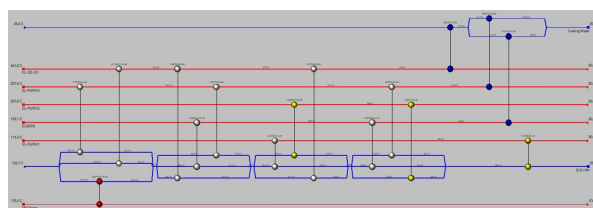


Figure A.1: Pinch analysis for SOEC system, cooling water at cold utility and electric heating at hot utility

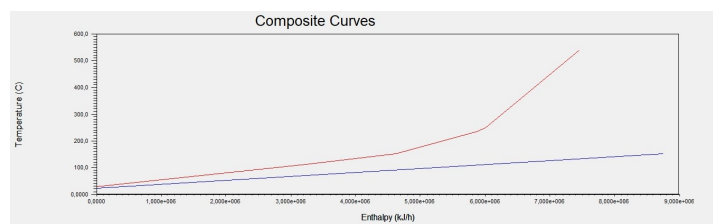


Figure A.2: Pinch analysis for SOEC system, Temperature vs. heat load diagram

Figure A.3: SOEC system optimization rounds results



Figure A.4: SOFC system optimization rounds results



Figure A.5: SOFC Graphs

A.3. MES analysis

Parameter	+TES	rSOC-CCGT CHP	Δ [%]
Financials [M€]			
Gross profit	(Confidential)	(Confidential)	0.32
Revenue	(Confidential)	(Confidential)	0.11
SOFC-CCGT	(Confidential)	(Confidential)	0.11
SOEC	(Confidential)	(Confidential)	0.07
Costs	(Confidential)	(Confidential)	0.05
SOFC-CCGT	(Confidential)	(Confidential)	0.04
SOEC	(Confidential)	(Confidential)	0.31
Commodity [GWh]*			
Generated	3253	3213	1.24
Electricity	2790	2799	-0.34
Heat	123	74	66.57
Hydrogen	340	340	0.07
Consumed	5370	5368	0.04
Natural Gas	3972	3971	0.04
Hydrogen	1057	1056	0.04
Electricity	341	341	0.07
Other			
Operating hours [h]	8526	8524	0.02
SOFC-CCGT	5691	5691	0.00
SOEC	2835	2833	0.07
CO2 emission [kt]	727	727	0.04
CO2 [kt/GWh]	0.250	0.253	-1.32

Table A.2: Results 2030 rSOC-CCGT CHP with and without TES. *Listed in HHV

A.4. Appendix Results and discussion

Exergy input/losses [%]	Base case 1A	Case 1A	Δ
Exergy in	100	100	-
Natural gas	84.8	83.8	-1.05
Hydrogen	15.2	16.2	1.05
Exergy out	60.1	61.5	1.39
Power	60.1	61.5	1.40
CCGT	49.0	49.6	0.63
SOFC	11.1	11.9	0.77
Exergy destruction	39.9	38.5	-1.39
CCGT	35.8	35.9	0.07
Irreversibilities GT	29.7	29.5	-0.18
Generator losses	0.32	0.31	-0.01
Pump + mechanical losses	0.28	0.30	0.02
Environmental GT	2.35	2.30	-0.04
Condenser + irreversibilities ST	3.19	3.46	0.27
SOFC	4.07	2.45	-1.6
Grid to Stack	0.44	0.07	-0.4
Stack	0.57	0.61	0.04
Afterburner	0.76	0.81	0.05
Turbine	0.21	0.22	0.01
Environmental	2.10	0.74	-1.4
Exergy integration	-	1.91	-
Exergy exchanged HRSG	-	1.67	-
Exergy exchanged FPH	-	0.08	-
Exergy losses integration	-	0.16	-
Exergy efficiency [%]	Base case 1A	Case 1A	Δ
SOFC	73.14	83.91	10.76
CCGT	57.74	58.00	0.27
SOFC-CCGT	60.08	61.47	1.39

Table A.3: Relative exergy differences of Base case 1A and Case 1A

Exergy input/losses [%]	Base case 2A	Case 2A	Δ
Exergy in	100.00	100.00	-
Natural gas	100.00	81.54	-18.5
Hydrogen	-	18.46	-
Exergy out	57.74	59.59	2
Power	57.74	59.59	1.85
CCGT	57.74	46.08	-11.7
SOFC	-	13.50	-
Exergy destruction	42.26	40.41	-1.85
CCGT	42.26	37.43	-4.8
Irreversibilities GT	35.03	29.74	-5.3
Generator losses	0.38	0.27	-0.1
Pump + mechanical losses	0.33	0.32	-0.01
Environmental GT	2.77	2.27	-0.5
Condenser + irreversibilities ST	3.76	4.83	1.1
SOFC	-	2.79	-
Grid to Stack	-	0.08	-
Stack	-	0.69	-
Afterburner	-	0.92	-
Turbine	-	0.25	-
Environmental	-	0.85	-
Exergy integration		2.16	-
Exergy exchanged HRSG	-	1.90	-
Exergy exchanged FPH	-	0.08	-
Exergy losses integration	-	0.19	-
Exergy efficiency [%]	Base case 2A	Case 2A	Δ
SOFC	-	83.85	-
CCGT	57.74	55.18	-2.56
SOFC-CCGT	-	59.59	-

Table A.4: Relative exergy differences of Base case 2A and Case 2A

Exergy input/losses [%]	Base case 1B	Case 1B	Δ
Exergy in	100	100	-
Natural gas	84.8	83.8	-0.97
Hydrogen	15.2	16.2	0.97
Exergy out	59.4	61.0	1.60
Power	57.4	58.8	1.37
CCGT	46.3	47.0	0.7
SOFC	11.1	11.8	0.7
Heat	2.04	2.26	0.2
CCGT	2.04	2.17	0.1
SOFC	-	0.10	-
Exergy destruction	40.6	39.0	-1.6
CCGT	36.5	36.4	-0.1
Irreversibilities GT	29.7	29.3	-0.4
Generator losses	0.32	0.32	0.0
Pump + mechanical losses	0.27	0.29	0.02
DHN losses	1.25	1.32	0.1
Environmental GT	2.21	2.18	0.0
Condenser + irreversibilities ST	2.72	3.00	0.28
SOFC	4.07	2.36	-1.7
Grid to Stack	0.44	0.07	-0.4
SOFC	0.57	0.60	0.0
Afterburner	0.76	0.81	0.0
Turbine	0.21	0.22	0.0
DHN losses	-	0.02	-
Environmental	2.10	0.64	-1.5
Exergy integration	-	1.88	-
Exergy exchanged HRSG	-	1.61	-
Exergy exchanged FPH	-	0.08	-
Exergy losses integration	-	0.19	-
Exergy efficiency [%]	Base case 1B	Case 1B	Δ
SOFC	73.14	84.21	11.06
CCGT	56.99	57.43	0.45
SOFC-CCGT	59.44	61.04	1.60

Table A.5: Relative exergy differences of Base case 1B and Case 1B with the decoupled SOFC

Exergy input/losses [%]	Base case 2B	Case 2B	Δ
Exergy in	100	100	-
Natural gas	100.0	83.0	-17.00
Hydrogen	-	17.0	-
Exergy out	57.0	61.2	4.26
Power	54.6	59.0	4.40
CCGT	54.6	46.6	-8.0
SOFC	-	12.4	-
Heat	2.4	2.26	-0.15
CCGT	2.4	2.15	-0.2
SOFC	-	0.10	-
Exergy destruction	43.0	38.8	-4.3
CCGT	43.0	36.1	-6.9
Irreversibilities GT	35.0	29.0	-6.0
Generator losses	0.38	0.31	-0.1
Pump + mechanical losses	0.32	0.29	-0.03
DHN losses	1.47	1.32	-0.2
Environmental GT	2.61	2.16	-0.4
Condenser + irreversibilities ST	3.21	2.99	-0.22
SOFC	-	2.49	-
Grid to Stack	-	0.08	-
SOFC	-	0.63	-
Afterburner	-	0.85	-
Turbine	-	0.23	-
DHN losses	-	0.03	-
Environmental	-	0.67	-
Exergy integration	-	1.98	-
Exergy exchanged HRSG	-	1.69	-
Exergy exchanged FPH	-	0.08	-
Exergy losses integration	-	0.20	-
Exergy efficiency [%]	Base case 2B	Case 2B	Δ
SOFC	-	84.19	-
CCGT	56.99	57.45	0.47
SOFC-CCGT	-	61.24	-

Table A.6: Relative exergy differences of Base case 2B and Case 2B without the decoupled SOFC